# **Exploring radio-loud AGN with large datasets**

Author:
Siddhant Pinjarkar

Supervised by: Prof. Martin J. Hardcastle

Centre for Astrophysics Research

Department of Physics, Astronomy and Mathematics

University of Hertfordshire

Submitted to the University of Hertfordshire in partial fulfilment of the requirements of the degree of Doctor of Philosophy.

January 2025

### Abstract

In this thesis, I use recent high sensitivity surveys that provide multi-wavelength information, to study and explore the key phenomenon of Radio-loud Active Galactic Nuclei (RLAGN). This thesis carries out in-depth investigations of three core aspects of these objects in order to understand the properties and evolution of AGNs. The studies herein make use of recent high sensitivity and resolution surveys, such as MIGHTEE, superMIGHTEE, LOFAR, and GMRT, to achieve better constrained estimates of spectral age distribution, uncover robust trends in the spectral index, redshift, and radio luminosity relationship, and critically test the unification model using new methods.

In the thesis I have used the new sensitive and high-resolution MeerKAT MIGHTEE survey of the XMM-LSS field, along with data from the Low Frequency Array (LOFAR), the Giant Meterwave Radio Telescope (GMRT), and upgraded GMRT (uGMRT) surveys. These datasets include radio images and measurements at several frequencies such as 144, 390, 460, 610, 688, and 1400 MHz along with their narrow band, broad band, and deep field information. The first study focuses on the spectral age distribution of RLAGNs in the XMM-LSS field. This is important as jets of energetic particles, seen in FR type-I and FR type-II sources, ejected from the centre of radio-loud AGN affect the sources' surroundings and the intracluster medium/intergalactic medium. Placing constraints on the age of such sources is important in order to measure the jet powers and determine the effects on feedback. To evaluate the age of these sources I have used spectral aging models where high-resolution multi-wavelength data is required, which is provided by the MIGHTEE, LOFAR, and GMRT surveys. I present a sample of 28 radio galaxies with their best-fitting spectral age distribution analyzed using the Jaffe–Perola (JP) model on a pixel-by-pixel basis. The fits are generally good, and the objects in our sample show maximum ages within the range of 2.8 to 115 Myr with a median of 8.71 Myr. Some key conclusions of the study include that the use of high-resolution maps over a range of frequencies are required to observe detailed age distributions for small sources, and that high-sensitivity maps will be needed in order to observe fainter extended emission. In the study I also explore other parameters such as size and age correlation and comparison with dynamical age models. I do not observe any correlation between the total physical size of the sources and their age, and speculate that both dynamical models and the approach to spectral age analysis may need some modification to account for observed discrepancies in the results of the two models. The outcomes of the study can be used to place constraints on jet powers and comment on the extent of their influence on the environment.

In the second study, I explore the trend previously observed between spectral index ( $\alpha$ ) and redshift for high-redshift radio galaxies (HzRG) and investigate the overall trend observed between spectral index, redshift, and radio luminosity along with the trends observed in previous studies.

The study uses data from the new sensitive and high-resolution MeerKAT MIGHTEE survey of the XMM-LSS field, along with data from the Low Frequency Array (LOFAR), the Giant Meterwave Radio Telescope (GMRT), and upgraded GMRT (uGMRT) surveys, at frequencies 144, 390, 610, 688, and 1400 MHz, where the data is used for both pairwise and multi frequency analysis. The apparent trend observed between spectral index and redshift has been used for many years to select high-redshift objects by searching for radio sources with steep spectra. I use the surveys above to investigate this relationship in detail by selecting compact sources over a wide range of redshifts and luminosities. My results suggest that there is a correlation between  $\alpha$  and z in the observed sample over some frequency range pairs, although there is a clear offset between the  $\alpha$ -z relations in the observed sample and those derived previously from samples of more luminous objects. The relationships between  $\alpha$  and luminosity are also weak in the observed sample but in general the most luminous sources are steeper-spectrum and this trend is extended by samples from previous studies. In detail, I have argued in the study about both a  $\alpha$ -luminosity relation and an  $\alpha$ -z relation which can be found in the data, but it is the former that drives the apparent  $\alpha$ -z relation observed in earlier work, which only appears because of the strong redshift-luminosity relation in bright, flux density-limited samples. One of the conclusions of the study is that steep-spectrum selection must be applied with caution in searching for high-z sources in future deep surveys. A careful selection of HzRG incorporating effects of luminosity can further help to select unbiased complete population of sources, to be used for studying the properties of such galaxies and the effect they have in the early universe.

In the final study, I test and investigate the orientation based unification model that argues that radio loud quasars and radio galaxies are part of the same population, observed at different angles. In this study I use the data provided by the LoTSS deep field survey in the Lockman Hole and ELAIS-N1 field. The key predictions of the model are that quasars are seen at smaller angles to the line of sight and so should be more projected, and hence apparently physically smaller, than corresponding radio galaxies, but this has not always been found to be the case in earlier studies. Using data from the LOFAR LoTSS deep fields, I test the unification model by measuring the critical angle and linear size ratio of quasars to radio galaxies for different redshift bins. I also argue that the interpretation of my (and all others') observations requires a less simplistic model for the effects of projection, which takes into account the fact that real radio sources are of finite width and have an intrinsic axial ratio distribution. Using this model, I present simulations that predict the size ratio of observed lengths in the presence of a distribution of intrinsic physical sizes and axial ratios that are derived from observation, and compare the outputs with the observed results from the LoTSS data. For homogeneously selected sample in the study, the sample size is relatively small and the naive interpretation of the linear size ratio is not always consistent with the simplest expectations from the unified model. However, simulations show that the LoTSS sample, in common with every other sample so far used in the literature, is too small to carry out a reliable test. I conclude that to test the unified scheme, the

sample size should be greater than  $\sim 500$  sources and homogeneously selected samples must be compared with the expectations from a realistic projection model. Using realistic models for testing orientation based unification scheme further helps modeling of AGN feedback which is known to affect the environment, and should also lead to a more refined understanding of processes involved in AGN activity.

### **Declaration**

I declare that no part of this work is being submitted concurrently for another award of the University or any other awarding body or institution. This thesis contains a substantial body of work that has not previously been submitted successfully for an award of the University or any other awarding body or institution.

The following parts of this submission have been published previously and/or undertaken as part of a previous degree or research programme:

- Chapter 2: This chapter has been published as Pinjarkar, S., Hardcastle, M.J., Harwood, J.J., Lal, D.V., Hatfield, P.W., Jarvis, M.J., Randriamanakoto, Z., Whittam, I.H., 2023. Spectral age distribution for radio-loud active galaxies in the XMM-LSS field. *Monthly Notices of the Royal Astronomical Society*, 523(1):620.
- Chapter 3: This chapter has been published as Pinjarkar, S., Hardcastle, M.J., Lal, D.V., Smith, D.J., Afonso, J., Barbosa, D., Hale, C.L., Jarvis, M.J., Kolwa, S., Murphy, E., Vaccari, M., Whittam, I.H., 2025. MIGHTEE: exploring the relationship between spectral index, redshift, and radio luminosity. *Monthly Notices of the Royal Astronomical Society*, 537(4):3481.
- 3. Chapter 4: This chapter has been submitted for publication at Monthly Notices of the Royal Astronomical Society and is under review.

Except where indicated otherwise in the submission, the submission is my own work and has not previously been submitted successfully for any award.

## Acknowledgements

#### "Ph.D is not a race, it's a marathon"

This has definitely been a journey for me. When I started 4 years ago, everything was unsure and hazy, partly because this was the start of something new, and partly because I had to start from a foreign land, in the midst of COVID. The time was changing quickly and I had to learn to adapt as fast, although the feelings about research and astronomy have always remained the same. I am as excited and curious about the subject now, as I was before, when I first got admitted into the course. There have been a lot of struggles but they are complimented by as many achievements and cherishable moments. So, I wouldn't call it a "bitter sweet" journey, rather a sweet journey with hints of sourness.

A lot of people needed to be thanked and there are many things I am grateful about, although the very first person I would like to thank is my supervisor, Martin Hardcastle. This was not possible without his immense support, guidance and understanding. He has always been available to guide me, teach me, and help me through the good and bad times of the Ph.D. I am very grateful and glad to have had the chance to work with him. I would also like to extend my thanks to Jeremy Harwood and Dharam Vir Lal for providing the scientific inputs and research opportunities. I am also very much grateful for the comments and input from the collaborators of the publications I have made so far.

I would also like to thank my Father and Mother for supporting me through out the process and being my constant rock that has helped me overcome a lot of hardships over the course of my Ph.D. Last but not the least I would like to give myself a big pat on my back to have always followed through the complications and struggles, and not giving up until the end. This has been a very memorable journey, which I hope will continue in the form of research in the future.

## **Contents**

Abstract				Í	
A	cknow	vledgem	ients	V	
C	ontent	ts		vi	
Li	st of l	Figures		ix	
Li	st of ]	<b>Fables</b>		X	
1	Intr	oductio	n	1	
	1.1	Brief I	History	1	
		1.1.1	Active Galaxies Discovery and Timeline	1	
		1.1.2	Types of AGN	5	
		1.1.3	Radio Loud AGN	6	
	1.2	Observ	vations	8	
		1.2.1	Morphology	8	
		1.2.2	High and Low Excitation Radio Galaxies	10	
		1.2.3	High Redshift Radio Galaxies	12	
		1.2.4	Multi-wavelength observations	14	
			1.2.4.1 Radio Waves	14	
			1.2.4.2 Optical	14	
			1.2.4.3 X-ray	15	
		1.2.5	Selection and Identification	16	
	1.3	Physic	s	18	
		1.3.1	Synchrotron Radiation	18	
		1.3.2	Power Law distribution of Electrons	20	
		1.3.3	Spectral Age	21	
		1.3.4	Relativistic Beaming	22	
		1.3.5	Polarization	23	
	1.4	Host C	Galaxy Environments and Feedback	24	
		1.4.1	Host Galaxies	25	
		1.4.2	Large Scale Environment	26	
		1.4.3	Feedback	27	
	1.5	Survey	78	29	
		1.5.1	MIGHTEE	31	
		1.5.2	LOFAR	32	

<u>Contents</u> vii

		1.5.3	GMRT				
	1.6	Questi	ons to answer				
2	_	pectral age of Radio-loud AGNs					
	2.1		action				
		2.1.1	Radio-loud active galactic nuclei				
		2.1.2	Spectral ageing models				
	2.2	2.1.3	Questions to answer				
	2.2		deduction and Analysis				
		2.2.1	Data Extraction and Organization				
		2.2.2	Creation of the sample				
		2.2.3	Data Processing				
		2.2.4	Parameter Determination				
	2.2	2.2.5	Spectral Analysis				
	2.3		8				
		2.3.1	Morphology				
		2.3.2	Resolution and sensitivity				
		2.3.3	Beam size and source size				
		2.3.4	Source environment				
	2.4	2.3.5					
	2.4	2.4.1	sion				
		2.4.1	Sensitivity and redshift limits				
		2.4.2	Injection index				
		2.4.4	What are the age estimates?				
		2.4.5	What can we say about extended emissions?				
		2.4.6	What is the total size and age correlation?				
		2.4.7	What can we say about the spectral age model?				
		2.4.8	What is the relationship between the age distribution maps and the source				
		2.4.0	morphology?				
	2.5	Summa	ary and Conclusions				
3	Spec	ctral Inc	dex, Redshift, and Radio Luminosity Correlation 66				
	3.1 Introduction		action				
	3.2	Data re	eduction and analysis				
		3.2.1	Data description				
		3.2.2	Data extraction				
		3.2.3	Parameters and analysis				
		3.2.4	Data from legacy radio surveys				
	3.3	Results	s and Discussion				
		3.3.1	Two-frequency analysis				
		3.3.2	Multi-frequency analysis				
		3.3.3	Interpretation of the correlations				
	3.4	Conclu	sions				
4	Revi	isiting R	Barthel's Unification Scheme 90				
-	4.1	_	action				

Contents

Bi	bliogr	aphy	1	133	
	A.2	α-z an	d α-L for compact 3CRR sources	130	
	A.1	_	e	130	
A	App	Appendix		130	
	5.4	Conclu	sion and Future Work	128	
	5.3	_		124	
	5.2	Spectral index, redshift and Radio luminosity correlation			
	5.1	Spectral Age Distribution analysis			
5	Summary and Conclusions				
	4.4	Conclu	sions	114	
		4.3.6	1	113	
		4.3.5		112	
		4.3.4	,	110	
		4.3.3	Mean Length Ratio	109	
		4.3.2	Construction of an unbiased sample	107	
		4.3.1	Critical Angle and Sample Size	107	
	4.3	Results	* *	106	
		4.2.6	1	103	
		4.2.5		102	
		4.2.4		رو 101	
		4.2.2 4.2.3	Radio selection	99 99	
		4.2.1	Data description	98	
	4.2		Reduction and Analysis	98	
		4.1.4	This chapter	97	
		4.1.3	Previous tests of unified models	95	
		4.1.2	Consequences of the unification model	91	
		4.1.1	Quasars and radio galaxies	90	

## **List of Figures**

1.1	Radio images of different sources that exhibit FR-I, FR-II and other morphology	9
1.2	A schematic diagram showing the view of a RLAGN	12
1.3	WISE colour–colour diagram for the DR2 sample	16
1.4	Spectral curves obtained by using Tribble model	22
1.5	Image rms, frequency, and angular resolution of LoTSS-DR1 in comparison to	
	a selection of existing surveys	30
2.1	Spectral age maps of target 1 to target 4	50
2.2	Spectral age maps of target 5 to target 8	52
2.3	Spectral age maps of target 9 to target 12	53
2.4	Spectral age maps of target 13 to target 16	54
2.5	Spectral age maps of target 17 to target 20	55
2.6	Spectral age maps of target 21 to target 24	56
2.7	Spectral age maps of target 25 to target 28	57
2.8	Maximum age distribution and Size versus maximum age plots	59
2.9	Radio luminosity versus total physical size relation	62
3.1	Area covered by the surveys	69
3.2	Luminosity versus redshift plot for optically identified MIGHTEE sources	72
3.3	Redshift and flux density distribution for the different surveys	73
3.4	Observed distribution of MIGHTEE flux density and spectral index including	
	sensitivity line separation for each survey	74
3.5	The distribution of the spectral index evaluated using different frequency pairs	
	for each detected source	76
3.6	The correlation of the average spectral index with the redshift for each frequency	
	pair	77
3.7	The correlation of the spectral index with the luminosity for each frequency pair	78
3.8	Comparison of observed relationship with De Breuck et al. (2000) sample	81
3.9	Spectral index, redshift, and luminosity relationship observed using multi-frequency	
	information	82
3.10	$\alpha$ -z and $\alpha$ -L relationship comparison using luminosity and redshift binned sample	84
3.11	Correlation between the spectral index obtained for frequency range uGMRT	
	B3 - B4 and uGMRT B4 - MIGHTEE	85
4 1		
4.1	Representation of the cylindrical model for a source tilted at angle $\theta$ from the	0.4
4.2	line of sight.	94
4.2	Quasar versus radio galaxy diagnostics in different models	94
4.3	1 0 0	101
4.4	Color-color plot selection comparison	102

<u>List of Figures</u> x

4.5	Sources actual length versus axial ratio plot comparing simulated sample with	
	Mullin et al. (2008) sample	105
4.6	Full sample and subsample distribution of the redshift and the luminosity	108
4.7	Distribution of size ratios for different sample size and critical angle using sim-	
	ulation	111
A.1	Positive error distribution of age for each source	131
A.2	Distribution of age pixel by pixel with respect to its distance from the core	132
A.3	The correlation of the average spectral index with the redshift, comparing with	
	3CRR sample selected by filtering sources having angular size less than 10 arcsec	133
A.4	The correlation of the spectral index with the luminosity, comparing with 3CRR	
	sample selected by filtering sources having angular size less than 10 arcsec	134

## **List of Tables**

1.1	List of surveys	30
2.1	Baseline and uv coverage information for the MeerKAT, the LOFAR and the	
	GMRT telescopes	43
2.2	Properties of the sources in our sample	46
2.3	Estimates of the age values obtained after performing the analysis	51
2.4	JP, Tribble, and KP model comparison for two sources	52
2.5	Varying injection index analysis	61
3.1	Survey information used to obtain the sample for the spectral index, redshift,	
	and luminosity analysis	71
3.2	Number of sources in the analysis at each frequency range and correlation coef-	
	ficients between spectral index, luminosity and redshift	79
3.3	Correlation analysis for the spectral index, redshift, and luminosity evaluted	
	using multi-frequency information	82
4.1	Previous studies that support Barthel's unification schemes	95
4.2	Previous studies that provide evidence against Barthel's unification schemes	96
4.3	Number of sources in the sample from the LOFAR and SDSS catalogue	104
4.4	Critical angle, expected linear size ratio of the stick model and observed linear	
	size ratio for sources in different redshift bins along with simulated size ratio	
	ranges	106
4.5	Predicted range of length ratio at $3\sigma$ with and without resolution truncation	110

## **Chapter 1**

## Introduction

#### 1.1 Brief History

In this section, we explore the development of our understanding of active galactic nuclei (AGN), focusing on the scientific advancements and discoveries that have shaped the field. By tracing the historical timeline, we highlight the emergence of radio astronomy and its significant role in uncovering the nature of AGN. This historical perspective not only illustrates how AGN evolved from being observational anomalies to central components of modern astrophysics but also provides context for their relevance in studying galactic formation and evolution. Understanding this progression is crucial for appreciating the foundations of current research and for framing AGN within the broader narrative of cosmic evolution. The content of this section is based on insights derived from the study of Shields (1999).

#### 1.1.1 Active Galaxies Discovery and Timeline

The early 20th century marked the beginning of studies of active galactic nuclei (AGN). In 1908, Edward Fath became one of the pioneers in this field. At the Lick observatory Fath was studying the nature of spiral galaxies, known as 'Spiral Nebulae' at the time, trying to figure out if the spirals were nearby gaseous objects (similar to the Orion Nebula) or distant collections of unresolved stars. His study aimed at observing the spectrum of different objects to test the spirals continuous spectrum and gaseous nebulae bright spectrum. He discovered that all but one of the objects exhibited a continuous spectrum, indicative of unresolved solar-type stars. However, one object, NGC 1068, stood out with a spectrum that featured both absorption and bright emission lines. These unusual spectral lines suggested the presence of energetic processes in the nucleus of NGC 1068 that were distinct from normal stellar activity (Fath, 1909). A typical stellar spectrum is characterized by low ionization, narrow absorption lines, and thermal emission at lower

energy wavelengths, such as visible or near-UV, very different from what was observed for NGC 1068. The findings by Slipher (1917) further confirmed that some spiral galaxies harbored energetic centers, with emission spread across a range of wavelengths. Subsequent studies, such as Hubble (1926), also reported the presence of nuclear emission lines in some spiral nebulae. Building on these observations, Seyfert (1943) conducted a pivotal study that identified six galaxies exhibiting broad emission lines with high ionization. The presence of high ionization indicated the presence of high-energy processes, as sustaining such ionization requires photons with sufficiently high energy to excite electrons across multiple levels. Among the six galaxies, NGC 4151 stood out; Seyfert observed narrow forbidden lines and narrow core-permitted lines, suggesting the presence of relatively slow-moving gas at a distance from the center. In addition to this, he observed the presence of broad hydrogen lines (of width 7500 kms<sup>-1</sup>) and missing forbidden lines suggesting high velocity, active, dense region in the galaxy. Similarly, for NGC 1068, he noted comparable profiles of forbidden and permitted lines, with widths of approximately 3000 km s<sup>-1</sup>, further indicating high velocities and energetic processes. Seyfert's work provided compelling evidence of galaxies hosting compact nuclear regions capable of generating high-energy photons. These galaxies are now known as 'Seyfert Galaxies'. The study had become a major stepping stone in astronomy that had provided evidence of high energy processes occurring near the center of the galaxies. Understanding the working of such galaxies, now known as Active Galactic Nuclei (AGN), since early 20th century, has remained a central focus of astrophysical research, catalyzed by Seyfert (1943) groundbreaking discoveries.

The studies above were foundational but not sufficient to fully understand AGN. A major leap in AGN research occurred with the advent of radio astronomy. Karl Jansky in 1932 first laid the foundation for radio astronomy when he identified radio waves originating from the Milky Way and proved the existence of extraterrestrial radio sources (Jansky, 1933). Using a rotatable antenna operating at 14.6 m wavelength, he measured static present in all directions, which he described as "a steady hiss type static of unknown origin". His observations revealed that the strongest radiation came from the center of the Milky Way, with the emission extending along its spiral arms. Building on Jansky's work, Grote Reber constructed the first 31-foot parabolic reflector, allowing him to focus incoming radio waves onto a receiver at the focal point. Reber's efforts led to publication of a radio sky map at 160 MHz, where he noted a much larger ratio of radio to optical flux for the Milky Way compared to the sun (Reber, 1940, 1944).

The search for discrete radio sources began with Hey et al. (1946), who discovered a fluctuating source in Cygnus. While the intensity fluctuations were later attributed to Earth's ionosphere, the discrete nature of the source was still in place, later confirmed by Bolton and Stanley (1948). This led to the publication of a catalog of six discrete radio sources (Bolton, 1948). Optical identification of three radio-emitting sources — Taurus A, Virgo A, and Centaurus A — soon established a critical link between optical and radio sources (Bolton et al., 1949). Subsequent

studies expanded this association, with researchers focusing on optical identification and precise position determination of radio sources (e.g., Ryle et al., 1950; Smith, 1951; Baade and Minkowski, 1954). Further pivotal progress was made by Jennison and Das Gupta (1953), who revealed that the structure of Cygnus A consisted of two blobs of intense radio emissions, separated by 1.5 arcmin. This "double-lobed" morphology, later in the history, was also observed in other extragalactic radio sources (e.g., Dent, 1965; Sholomitsky, 1965; Pauliny-Toth and Kellermann, 1966; Knight et al., 1971; Whitney et al., 1971). The morphology was puzzling although common for many extragalactic radio sources. Throughout the decade, as the sensitivity and resolution of surveys improved, more such double radio sources were observed (Maltby et al., 1963). These discoveries revealed a distinct class of active galaxies which could be further explored. Initially, radio sources were categorized into two classes, "Class I" were sources that were aligned with the plane of the Milky-Way and "Class II" were isotropically distributed sources that were mostly extragalactic, although some had a small angular size and were also considered to be "radio stars".

The acceleration of radio source studies began with the Third Cambridge (3C) survey at 159 MHz (Edge et al., 1959) and its revised version at 178 MHz (Bennett, 1962). Radio sources came to be known by their 3C numbers and the increase in optical identification helped further to get accurate positions for the sources. One of the sources from 3C catalog, 3C 48 was studied by Allan Sandage in 1960, where he obtained a photograph of the source that showed a 16thmagnitude apparently stellar object surrounded by faint nebulosity. What stood out about this observation was the presence of broad emission lines at unfamiliar wavelengths. Additionally, the object exhibited variable photometry and excess ultraviolet emission compared to typical stars. These peculiar characteristics led to the identification of similar objects, which were subsequently termed quasi-stellar sources (QSS), quasi-stellar radio sources (QSRS), or quasars (Matthews and Sandage, 1963). These objects were speculated to be either nearby stars with unusual properties or distant galaxies. The breakthrough came when Schmidt (1963) analyzed the spectrum of the quasar 3C 273. He found that its emission lines resembled the Balmer series of hydrogen but were shifted, corresponding to a redshift of 0.16. This redshift established that 3C 273 was an extragalactic object. Similarly, 3C 48 was later found to have a redshift of 0.37, further confirming its position beyond the boundaries of the Milky Way. In a detailed study of 3C 48 and 3C 273, Greenstein and Schmidt (1964) proposed a model featuring a central optical continuum source surrounded by emission line region, with a radio emitting region located further out. At this point from these studies it was established that quasars were mostly compact and had shown frequently variable radio emission (Dent, 1965). Quasars were added as a new class of radio objects especially when the radio observations were extended to higher radio frequencies and more such extragalactic radio sources were observed. These discoveries indicated that quasars were associated with powerful radio emission and were very luminous and distant objects.

While it was well established that radio sources were highly energetic, the origin of this immense energy remained a critical question. At first, Burbidge (1961) thought that the energy came from a series of chain reaction supernova explosions occurring near the center of the galaxy, as a galactic nucleus has a high central density of stars. Other works had soon emerged, where models that were developed involved dense star clusters (Spitzer and Saslaw, 1966; Arons et al., 1975; Terlevich and Melnick, 1985). Hoyle and Fowler (1963b,a) suggested that a supermassive star was the source of gravitational and thermonuclear energy. They proposed that "a magnetic field wound toroidally between the central star and a surrounding disk" would be able to store large energy eventually leading to an explosion to produce jet like structure. However, it was Salpeter (1964) who identified the actual cause, i.e. presence of supermassive black hole, in which the gas was accreting to produce energy. For an inner radius of the accretion disk equivalent to  $6GM/c^2$ , it can release energy per unit mass of  $0.057c^2$ , reasonable enough for a quasar energy output. The model was later supported by Lynden-Bell (1969), who explored the thermal radiation and fast particle emission which is expected to be present for gas orbiting a black hole for a given magnetic and turbulent energy density. He argued that different combinations of black hole mass and accretion rate could explain large fraction of the observed energetic phenomena. Additionally, Hoyle (1966) also noted that optical and synchrotron radiation emitted by electron could Compton scatter ambient photons leading to larger energies, also known as inverse Compton catastrophe. It was Alfvén and Herlofson (1950) who first proposed the presence of synchrotron emission by suggesting that the emission from so called 'radio stars' involved electrons in a magnetic field. The importance of synchrotron emission in an astrophysical context was later supported by more studies such as Kiepenheuer (1950); Ginzburg (1951). By the late 1950s synchrotron emission was the most widely accepted explanation for the emission from extragalactic sources (for example, Burbidge 1959 and the references therein); these findings underscored the importance of supermassive black holes, and the accretion of mass and relativistic particles in understanding the underlying energetic processes of AGN. By the mid-1960s, it was also known that many radio sources showed structure ranging from subarcsecond to milliarcsecond. Some observations also provided compelling evidence for apparent superluminal motion. For instance, Whitney et al. (1971), who identified a source 3C 279, which, at a redshift of z = 0.538, showed two components whose rate of separation was apparently 10 times the speed of light. This apparent superluminal motion was later explained by Rees (1966), who demonstrated that such speeds could result from relativistic effects when the expansion is nearly aligned with the line of sight, causing the motion to be boosted by relativistic beaming. Ultimately, it had been established that AGN consisted of a central, stationary supermassive black hole, with components being ejected over periods of several years at speeds close to the speed of light.

A new population of quasars was identified by Sandage (1965) using U-B and B-V color plots. Quasars were known to exhibit "ultraviolet Excess" in color-color plots, setting them apart from

stars in the Milky Way. In such plots, stars adhere to the main sequence, and are characterized by their high brightness due to their relative proximity to Earth. However, quasars do not follow same trend; their high redshifts and significant distances cause them to appear much fainter than stars. Sandage observed that objects with magnitudes fainter than 15 occupied the same region of the color-color plot as quasars, while brighter objects aligned with the stellar main sequence. In addition these fainter objects' radio counterparts were not yet detected by the surveys of the time. He had found a population of quasars that showed the same UV excess but were fainter than what had been observed before and showed no radio emission and these objects he named "Quasi Stellar Galaxies" (QSG). These type of objects are now also known as radio-quiet quasars.

#### 1.1.2 Types of AGN

From early studies it became evident that AGN were powerful objects that were driven by accretion of matter on to the supermassive black hole at the center of their host galaxy. Our discussion in Section 1.1.1 highlights at least two types of AGN that were initially discovered. In the mid 20th century, Seyfert (1943) identified the very first type of AGN, which have been divided into two groups. Seyfert 1 are identified based on presence of both broad and narrow emission lines, whereas Seyfert 2 are identified based on narrow emission lines. Notably, Seyfert galaxies are predominantly spiral in morphology. Another major class of AGN discussed in the previous section is quasars, first identified by Allan Sandage while studying the strong radio source 3C 48 in a photograph that showed excess UV. Later, he also identified a population of objects in optical that were fainter than 15 mag and occupied the same region as quasars in the color-color diagram but lacked strong radio emissions. These are termed as radio quiet quasars. Hence, there are now two types of quasars depending on the strength of radio emissions, radio loud and radio quiet quasars.

In addition other AGN populations have been identified that differ in terms of method of observation. For example, DuPuy et al. (1969) and Blake (1970) reported sources that were compact, rapidly variable, and highly polarized but lacked emission lines (Angel and Stockman, 1980). Such objects were collectively termed as 'blazars'. Around the same period it was also found that there was a population of spirals that showed low ionization nuclear emission line regions (LINER), at low luminosity scale Heckman (1980). Since these studies, it has been a common method to identify AGN using emission line spectra, their wide range of ionization, and from presence of permitted lines and forbidden lines. Following the extragalactic optical identification of radio sources carried out by Bolton et al. (1949) and later, Baade and Minkowski (1954) radio galaxies were also identified using their rich emission line spectra where Broad-line radio galaxies (BLRG) showed presence of both broad and narrow emission line regions, similar to Seyfert 1, whereas, Narrow-line radio galaxies (NLRG) showed presence of narrow line regions,

similar to Seyfert 2. In addition to these objects, a class of radio galaxies that are of similar luminosity as other radio galaxies but do not show high ionization and have weak emission line spectra, are Weak-line radio galaxies (WLRG) or Low excitation radio galaxies (LERG), which have optical spectra similar to those of LINERs (Hine and Longair, 1979; Laing et al., 1994).

With advancements in technology, enabling higher resolution and better sensitivities, radio sources could now be classified using their structure or morphology. Based on morphology, Fanaroff and Riley (1974) came up with a classification scheme that could divide the sources in two types, FR Type I and FR Type II. As previously discussed, the primary features of radio sources include presence of relativistic material ejection, also known as jets, puffed up clouds, also known as plumes/lobes, and a central core that is coincident with the supermassive black hole. In the scheme, Fanaroff and Riley (1974) classified sources based on the brightness regions where FR Type I were sources that had high brightness regions close to the galaxy, and FR Type II sources had high brightness regions further from the galaxy. Furthermore, their observations also showed a luminosity based division, where nearly all FR Type-I showed  $L_{178} < 2 \times 10^{25}$  W Hz<sup>-1</sup> sr<sup>-1</sup>, as compared to FR Type-II showing  $L_{178} > 2 \times 10^{25}$  W Hz<sup>-1</sup> sr<sup>-1</sup>. I discuss FR classification in detail in Section 2.3.1.

It is evident that there are different criteria for classification methods, which include, optical emission observations (e.g. Sy1/2, BLRG/NLRG), optical morphology (e.g. BLRG/RLQ), radio morphology (FRI/FRII), variability (BL Lac/ Blazar), and luminosity (WLRG/NLRG). This diversity in classification raises an intriguing question: are these population of AGN interconnected? In an effort to answer this question, Barthel (1989) proposed an unification scheme that unified AGN based on their orientation. He proposed that different observed AGN are from a single population but observed at different lines of sight. Depending on the viewing angle, the observed emission, luminosities, variability, and spectral shape changes, are accounted into projection. If this unification scheme holds true, it would mean that all types of AGN are fundamentally the same objects, only observed at different angles. Such a framework would help at establishing a cohesive classification method and enhance our understanding of the interplay between black holes, host galaxies, and the environment. These are important components of the "Feedback" system which is detailed in Section 1.4.

#### 1.1.3 Radio Loud AGN

By the end of the 20th century, studies of AGN had established that these objects were powered by highly energetic processes occurring at the centers of galaxies. In addition, AGN consisted of relativistic particles being ejected out of supermassive black holes, where many of the observed objects were of high redshift and were bright in the radio wavelengths. AGN that emit significant portion of their energy in the form of radio waves are usually termed Radio-loud AGN

(RLAGN), and these are the type of sources I will be using in the thesis for AGN investigation. Most classifications we have discussed above, such as BLRG, NLRG, WLRG, radio loud quasars, Blazars, and FR Type I and II galaxies, can fall under the radio loud AGN category. Other types of AGN, such as Seyfert galaxies, LINERs, etc show weak radio emission and are usually categorized as radio quiet AGN.

It is important to note that there is no universally robust parameter to definitively separate radioloud and radio-quiet AGN, although strong radio emission, spectral characteristics, and luminosities are some effective indicators of radio loudness. Some examples are:

- The *R* parameter, which is defined as the ratio of flux density as 5 GHz (radio) and flux density in the B-band (optical), can be used as an indicator of radio loudness in objects, like quasars, where radiative emission from the AGN dominates the optical emission. Objects that show values of *R* greater than 10 are said to be radio loud and those where *R* < 10 are said to be radio quiet Kellermann et al. (1989). However, we would not be able to use this definition as most of the object in the analysis are not quasars.
- As it is known that RLAGN have energetic jets and mostly dominate above luminosities (at around 1.4 GHz) of  $10^{24}$  W Hz<sup>-1</sup> (Tadhunter, 2016), this luminosity can be used as a threshold to sample RLAGN. Objects that show luminosities less than  $10^{24}$  W Hz<sup>-1</sup> (at around 1.4 GHz) are mostly dominated by Star Forming Galaxies (SFG). This distinction allows us to sample sources that do not show radio contribution from star formation of a galaxy. However, a drawback of the method is that objects that have higher star formation rates would contaminate our sample, in addition to loss of faint AGN that would fall below the luminosity limit.
- Ideally, selection of RLAGN would involve evaluation of radio excess from a source. The
  radio/FIR excess identifies radio-loud AGN by detecting an excess of radio emission compared to what is expected from the known radio-FIR correlation of star-forming galaxies.
  Galaxies that lie above the radio-FIR relation are classified as radio AGN. However, either
  a FIR measurement or another star formation rate estimate is needed to apply this method.

We do not have information on radio emission from star formation for each source and hence, for this thesis I define RLAGN as objects that show luminosities above  $10^{24}$  W Hz<sup>-1</sup> (at 1.4 GHz), where the effects of SFG contamination are discussed in Chapter 3. However, for Chapter 4, we use sample derived from the Best et al. (2023) classification, which uses the radio excess method to select RLAGN.

#### 1.2 Observations

The observation of RLAGN encompasses a comprehensive approach to understanding both how these systems are studied and what can be learned from their diverse population. This section explores the physical characteristics, energetic processes, and diverse population that helps define RLAGN, drawing on insights gained from their distinct radio emissions and multi-wavelength signatures. Beyond the methodologies of observation, it delves into the intrinsic and extrinsic properties of RLAGN, such as their morphology, emission features, and cosmological distribution. The insights presented in this section are based on the research and review outlined by Hardcastle and Croston (2020) and Magliocchetti (2022).

#### 1.2.1 Morphology

The observations of radio galaxies and radio-loud quasars, collectively referred to as radio-loud AGN (RLAGN), have the shown presence of structures that stretch to lengths ranging from pc to Mpc. These structures, often characterized by prominent large-scale jets and lobes, are defining features of such active galaxies. Northover (1973) was one of the first studies to successfully report these structures for 3C 66B noting that the length of the jets were  $\approx 30$  kpc, linking the nucleus to the extended structures. However, the term "jets" was originally coined by Baade and Minkowski (1954) in their observations of optical knots in M87, extended about 20" from the galactic centre. The early radio studies motivated development of a 'beam model' (Longair et al., 1973; Scheuer, 1974; Blandford and Rees, 1974) which referred to the outflows, of which jets were the observational manifestation. It was the development of large radio interferometers, such as NRAO Very Long Array (VLA), that allowed observations of RLAGN structure in much greater detail due to their high resolution. In fact, radio emission from the structures, being synchrotron emission implied that the structures stored extremely large energies as synchrotron emission reflects the interplay of relativistic particles and strong magnetic fields (Burbidge, 1959) (also see Section 1.3.1). Due to the structural distinction of RLAGN and the strength of radio emission, given the development of high resolution and sensitive interferometers, morphological selection has become an efficient way of selecting these sources where we distinguish radio AGN with respect to their morphology, easily observed in radio maps of high resolution, from other types of extragalactic radio sources, such as star forming galaxies.

As addressed in Section 1.1.2, a structural distinction between different types of RLAGN was first introduced by Fanaroff and Riley (1974), who classified these sources in two types based on their observational differences and links with radio luminosities. Fig. 1.1 shows some radio images of sources that exhibit the different types of morphology, including FR-I and II. The first type, known as FR Type I sources, are center-brightened, with jets that are relativistic near the core but decelerate on kiloparsec scales. The clouds of material ejected by these sources are

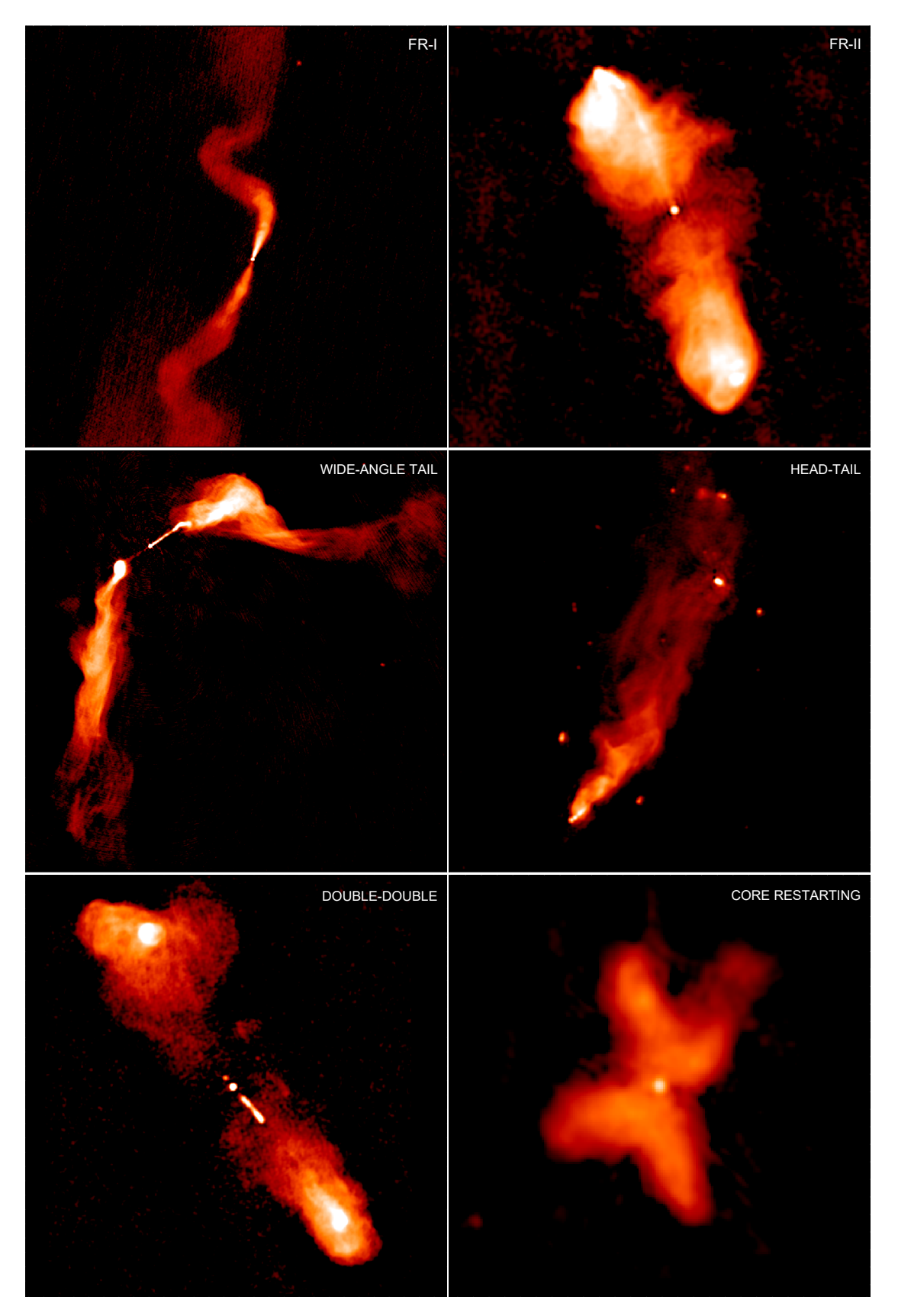


FIGURE 1.1: Radio images of different sources that exhibit FR-I, FR-II and other morphology. Top row left is the FR-I source 3C 31 (image provided by Robert Laing) and top row right is the FR-II source 3C 98 (image taken from Atlas of DRAGNS). Middle row are the wide-angle tail source 3C 465 (left), provided by Emmanuel Bempong-Manful and narrow-angle tail/head-tail source NGC6109 (right), taken from LOFAR data. Bottom row are double-double radio galaxy 3C 219 (left), from Clarke et al. (1992), and core-restarting radio galaxy 3C 315 (right), taken from LOFAR data. Compact 'cores' may be seen in all images, well-collimated jets are visible in 3C 31, 3C 98 and 3C 465, and hotspots in 3C 98, 3C 465 and 3C 219. Images and caption taken from Hardcastle and Croston (2020)

mostly diffuse and are often called plumes. Fanaroff and Riley (1974) also noted that this type of source had  $L_{178} < 2 \times 10^{25} \text{ W Hz}^{-1} \text{ sr}^{-1}$  and showed low brightness regions further from the galaxy. The second type, FR Type II sources, are edge-brightened, with jets that remain relativistic throughout their length and terminate in hotspots. The material in these jets disperses upon termination, forming extended structures known as lobes. These type of sources had high brightness regions further from the galaxy and had  $L_{178} > 2 \times 10^{25} \text{ W Hz}^{-1} \text{ sr}^{-1}$ . Although the energies provided to the ejected particles comes from the central engine, it is believed that the structural difference arises due to the interplay of jet power and the host galaxy environment (Bicknell, 1995). A jet when placed in a dense environment would entrain the inter-stellar medium (ISM) and inter-cluster medium (ICM) to decelerate and expand to form FR I Type plumes. On the contrary, the same jet when placed in a poor, less dense environment will allow the jet to remain relativistic and terminate when higher surrounding gas pressure is induced, giving rise to hotspots and expanding lobes. This interpretation was further supported by Ledlow and Owen (1996), whose findings suggested that FR Type I sources should be associated with more luminous host galaxies in dense environments, potentially resulting in higher radio luminosities. However, this conclusion was derived from a flux-limited sample with differing redshift distributions and environments. Recently, with the help of lower flux limit surveys, some FR Type II have been found to have low radio luminosities (Best, 2009; Miraghaei and Best, 2017; Capetti et al., 2017) where a substantial fraction of these galaxies were found at  $z \sim 0.8$  (Mingo et al., 2019). However the morphology link to the host brightness has not been totally denied by the study of Mingo et al. (2019), as it is believed that these low-power FR Type-II galaxies might occupy poor local environments. Mingo et al. (2022) in their study of the relationship between accretion mode and radio morphology show that the probability of a low power jet becoming an FR-Type I or FR-Type II is dependent on host galaxy stellar mass, and also conclude that FR class is not primarily controlled by the central engine. Overall, there exists a clear morphological distinction for RLAGN explained in the form of FR Type I and FR Type II sources. This type of distinction gives a hint towards the RLAGN possible placement in the host galaxy environment and their jet power. A systematic homogeneous study of these sources in detail can help us understand the underlying population distribution of the two types and the environment they are hosted in, further improving our understanding of the evolution of AGN.

#### 1.2.2 High and Low Excitation Radio Galaxies

Observations of optical spectra have played a crucial role in the identification of RLAGN, understanding their physical properties, and distinguishing between different types of radio galaxies and quasars. As we have seen in Section 1.1, RLAGN have been categorized into different types using presence of narrow line and broad line emission regions. Emission spectra of this

type produce high excitation lines by a gas that has been strongly ionized usually due to strong ultraviolet and X-ray radiation.

Laing et al. (1994) investigated a sub sample of 3CR sources aiming to make optical classifications and observed that RLAGN could be also separated based on galaxy excitation, where high-excitation radio galaxies (HERGs) exhibit strong ionization and include BLRGs and NL-RGs, but a class of galaxies with low-excitation emission lines was also identified. Subsequent research (e.g., Chiaberge et al., 2002; Whysong and Antonucci, 2004; Hardcastle et al., 2006, 2009) suggested that these low-excitation galaxies lacked accretion-driven emission lines, a torus, or a corona. Any nuclear optical and X-ray emission that were seen, came from jets only. Such galaxies were termed as low-excitation radio galaxies (LERG). To explain for the difference between HERGs and LERGs, studies such as, e.g., Ghisellini and Celotti (2001); Merloni and Heinz (2008), proposed that variations in accretion flow regimes result in differing radiative efficiencies. They are governed by the Eddington-scaled accretion rate, given by

$$\dot{M}_{Edd} = \frac{4\pi G M_{BH} c m_p}{\eta \sigma_T c^2} \tag{1.1}$$

where  $\eta$  is mass-energy conversion efficiency,  $\sigma_T$  is the Thomson cross-section,  $M_{BH}$  is the mass of the black hole and  $m_p$  is the mass of a proton. HERGs, including quasars and BLRGs, exhibit narrow-line and broad-line emissions, along with additional features such as X-ray and mid-IR emission from the nucleus. These characteristics are produced by accretion disks radiating at more than a few percent of the Eddington luminosity. Hence, according to the model, LERGs are also referred to as radiatively inefficient (RI) and HERGs are referred to as radiatively efficient (RE) (Hardcastle, 2018a).

After Barthel (1989) proposed the unification of RLAGN based on their orientation, it became evident that radio galaxies and quasars might be intrinsically similar objects, differentiated primarily by the angle at which they are observed. Barthel (1989) had noted for 3CRR objects (for 0.5 < z < 1) that quasars showed smaller projected sizes and brighter kpc-scaled jets. Based on his observations he showed that quasars would fall within 45° of our line of sight. The view was that an AGN would have a central continuum source and a broad line region (BLR) which was surrounded by an opaque torus; a representative diagram of this situation is shown in Fig. 1.2. When the AGN is viewed head-on, within an angle of sight less than  $\approx 45^{\circ}$ , both the BLR and the narrow-line region (NLR) are visible. These objects are classified as Type-I AGN. Conversely, when viewed at an angle greater than  $\approx 45^{\circ}$ , the torus obscures the BLR, leaving only the NLR observable, classifying the object as a Type-II AGN. While Type-I and Type-II objects both have high velocity gas near the AGN, Type-IIs are obscured by torus, preventing the observation of the high velocity gas (Kauffmann et al., 2003). In this framework, when a BLRG is being observed, exhibiting both broad line and narrow emission, it corresponds to a quasar. On the other hand, when an observation of NLRG is made, only narrow line emission are seen,

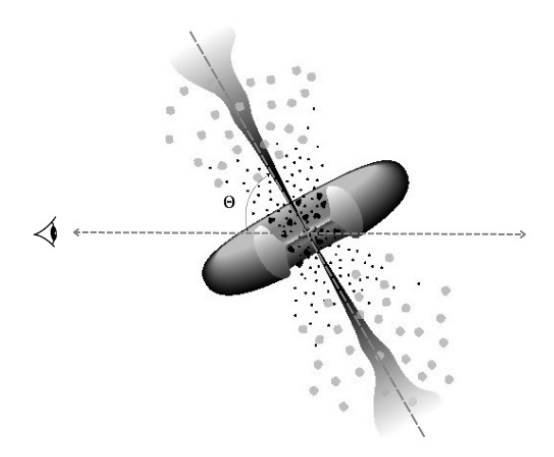


FIGURE 1.2: A schematic diagram showing the view of a RLAGN from different angles. The diagram shows the central black hole surrounded by a luminous accretion disk. The outermost region shows the torus, which obscures the broad line emission produced by the orbiting clouds and the disk, while narrow lines are produced further away from the centre. A hot corona is present above the accretion disk, responsible for production of hard X-rays, and jets are released perpendicular to the plane of the disk, which diffuse further away from the central region. The angle  $\theta$  shows the angle between the jet axis of the source and the line of sight. The diagram is modified from Urry and Padovani (1995).

corresponding to radio galaxy. As BLRGs and NLRGs both have radiatively efficient accretion, radio galaxies and quasars are mostly selected from RLAGN that are also HERGs. AGN that can be divided into Type-I (quasar) and Type-II (radio galaxy) show high ionization and emission such as UV/optical from accretion disk, infrared from the torus, and X-ray emission near the corona and jets. Such emissions are not seen for LERGs, except for some X-ray emission from jets, making it difficult to identify if the AGN is Type-I or Type-II, as the orientation of the objects cannot be known. Hence, LERGs should be excluded from orientation based unification analysis.

#### 1.2.3 High Redshift Radio Galaxies

For quite a few decades now, astronomers have been interested in studying the evolution of galaxies and have wanted to understand their evolution in the early universe. This has motivated searching for sources at higher and higher redshift, with a special focus on radio sources as they are unaffected by gas or dust and are a product of high energy processes. This means that high redshift objects could be easily observed by radio interferometers as compared to optical telescopes. Early studies in the 1980s had started finding sources at much higher redshift than before, where they also noted some peculiar observations in their findings.

The first high redshift radio galaxy discovered by Spinrad (1982), 3C 368, with a redshift greater than 1, showed notable high radio luminosity and strong emission lines, and work cited in that paper also suggested very luminous radio sources to be approximately 300 times more abundant at  $z \sim 1$  compared to the present epoch (Longair, 1980; Peacock and Gull, 1981; Windhorst et al., 1982). This raised the possibility that such galaxies have largely become extinct in the modern universe. Subsequent discoveries, such as Chambers et al. (1988) and Lilly (1988), that found galaxies at z > 2; noted that "powerful high-redshift radio galaxies have unique enigmatic properties and [...] are certainly not normal galaxies" where color versus z plots could be used to determine their intrinsic nature (Chambers et al., 1988) and, in addition, had strong Ly $\alpha$  emission, along with substantial star formation rates (Lilly, 1988). Further, Lilly (1988) observations of absolute V magnitude also indicated a stellar component of age 1-2 Gyr that dominated the mass of the system, which was unlikely for a protogalaxy. More high redshift galaxy discoveries followed, such as Chambers et al. (1990) who found a galaxy at z = 3.8not long after; a common characteristic was that these galaxies had ultra-steep spectral indices (Chambers et al., 1996; Best et al., 1998; Pentericci et al., 1999). A major contribution to detecting high redshift sources came from surveys like 3CR, which observed at 178 MHz, since 3CR was one of the most complete surveys in terms of identification and redshifts. Laing et al. (1983) created the 3CRR sample of 173 sources that overcame the remaining completeness problem in 3CR in terms of inhomogeneous flux measurement and partial resolution and is now completely identified. Surveys such as these were important, as the low frequency observations were effective in detecting distant objects.

Tielens et al. (1979) and Blumenthal and Miley (1979) found a strong correlation between spectral index of sources and identification fraction, in the sense that the optical identification for steep spectrum 4C sources were three times lower than obtained for normal galaxies, of spectra between -0.7 and -0.9 (Tielens et al., 1979). This was later adapted as a selection criterion by Chambers et al. (1988), selecting sources with z > 1. Since then HzRG have been associated with steep spectra, especially at lower frequencies (< 1 GHz), wherein identification of sources with steep spectra has been a method to select distant sources. The origin of this  $\alpha$  - z correlation has been debated ever since. One of the explanations suggests that the  $\alpha$  - z relation is due to an inherent L -  $\alpha$  relation (Chambers et al., 1990; Blundell and Rawlings, 1999) set by particle acceleration processes, details of which are discussed in Chapter 3. Due to Malmquist bias, for a flux limited sample, higher radio luminosity sources would be more distant galaxies, and therefore lead to  $\alpha$  - z relation. In addition,  $\alpha$  - z relation could also be observed because of higher inverse-Compton losses as there are higher number of photons from cosmic microwave background. Furthermore, at higher redshifts, the observed frequency corresponds to higher rest-frame frequency leading to steepening of the spectral index Krolik and Chen (1991). Higher ambient densities are also speculated to be a cause for steeper spectra as ambient density within the lobes increases with redshift leading to higher magnetic fields strengths and increased losses due to particle acceleration Athreya et al. (1998).

Beyond this curious  $\alpha$  - z correlation, HzRG also exhibit other interesting properties such as i) decrease in typical radio sizes, ii) presence in rich clusters, and iii) difference in host galaxies as compared to low redshift galaxies (see review by Miley and De Breuck 2008). The fact that spectral steepness has been used in selecting distant objects, which are a gateway to studying the properties of the early universe, makes HzRG an important subset of radio galaxy population.

#### 1.2.4 Multi-wavelength observations

#### 1.2.4.1 Radio Waves

Since AGN emit radiation across the entire electromagnetic spectrum, only observations at multiple wavelengths can provide a detailed picture of their physical processes. These observations are particularly useful in classifying different types of AGN, revealing their structure, and investigation of jet physics. Observations of AGN can be made over the entire electromagnetic spectrum, and a variety of techniques have been used to make these observations. For RLAGN, observations in radio wavelengths are important. Powerful radio sources offer an unique perspective in understanding AGN activity and are especially helpful in probing energetic phenomena. Radio emission is dominated by synchrotron radiation for RLAGN, discussed in Section 1.3.1. Radio observations help in revealing the AGN structure and dynamics by providing insights into the interactions of the AGN with the intergalactic medium (see Section 1.4 and review, Bridle and Perley 1984). In addition, multi-wavelength radio observations can be used to get insights into the energy distribution of the relativistic electrons, which allows us to study the spectral index of such objects, further detailed in Chapter 3. One application of multiwavelength observation is broad band spectral mapping, used to evaluate the (model-dependent) age of radio-emitting plasma based on different electron energies and their radiation timescales (Burch, 1977; Myers and Spangler, 1985; Alexander and Leahy, 1987; Harwood et al., 2013), and this will be discussed in detail in Chapter 2.

#### **1.2.4.2** Optical

Foundational contributions in AGN studies and observations have been made using optical spectroscopy, where emission lines, especially broad line and narrow line regions, have been used to infer properties of AGN (Schmidt and Green, 1983; Osterbrock, 1989; York et al., 2000; Peterson et al., 2004), discussed in Section 1.1. Optical spectroscopy serves a wide range of purposes, including determining the composition of stars and galaxies, measuring their temperature and density, calculating their velocity and direction of motion, and identifying the presence

of black holes. However, it is particularly well-suited for determining the redshifts of galaxies and studying the intracluster medium (ICM) and intergalactic medium (IGM) through the analysis of emission lines (see book by Appenzeller 2013). This capability is especially valuable in the study of AGN. Optical variability observations use timescale changes to provide insight into the size and structure of the emitting regions (Ulrich et al., 1997; Kelly et al., 2009; Shull et al., 2012). Optical data are especially essential for cross-matching and optical identification for any kind of physical interpretation. Here optical identification is finding optical counterpart for a radio source, which will be discussed in detail later in the thesis (see Chapter 2). The identification involves locating the center of the radio source, which would ideally inhabit core of the AGN, using high resolution maps and matching the coordinates with the best available optical images, where the optical coordinates are usually within few arcseconds radius. Hence, a successful optical identification requires a combination of good radio and optical images, and the lack of such identifications could be a limitation when exploiting radio surveys. The resolution of the radio images should be high enough to be able to distinguish between different optical counterparts and/or the structural parts of radio sources, for which the MIGHTEE survey would be a good candidate (see Section 1.5).

#### 1.2.4.3 X-ray

X-ray radiation from AGN is typically non-thermal in nature and is observed across various regions of the AGN, including the large-scale components, the nucleus, and the surrounding environment. The key mechanism behind this radiation is inverse-Compton scattering. In inverse-Compton scattering, relativistic electrons are responsible for scattering a photon field to high energies, where the photon field could be cosmic microwave background (CMB), synchrotron photons, host galaxy starlight, extragalactic background, or central AGN radiation. The X-ray luminosity thus depends on both the photon field and the low-energy relativistic electrons, offering important constraints on magnetic field strengths and so the dynamics of the source (Hardcastle et al. 2004; Croston et al. 2005, also see Section 1.3.1).

X-rays from synchrotron radiation have also been observed for jets of both FR-I and FR-II sources, which requires the particle energies to be at the TeV level (Hardcastle et al., 2004; Kraft et al., 2007). X-ray observations have also shown bubbles and cavities in cluster gas, which is believed to be produced dynamically by radio structures, implying a heated gaseous atmosphere (Bîrzan et al., 2004). There is even evidence of unambiguous shock features, believed to arise from motion of lobes through the medium that is supersonic in nature (Kraft et al., 2003; Croston et al., 2009, 2011). Overall, X-ray observations reveal how AGN activity affects the surrounding environment and impact the galaxy cluster (Gilmour et al., 2007). I discuss more about effects of AGN activity on host galaxy environment in Section 1.4.

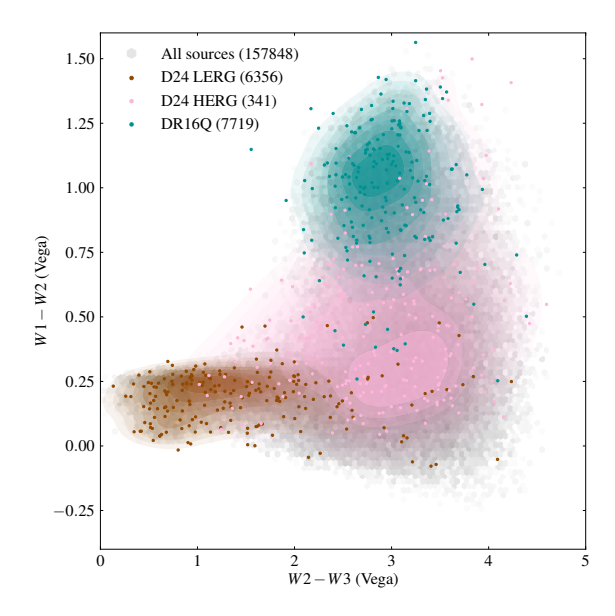


FIGURE 1.3: The observational WISE colour–colour diagram for the DR2 sample. Overlaid on the grey density plot showing the full parent sample with detections in three WISE bands (W1, W2, W3) are the locations of HERGs, LERGs, and DR16 quasars and luminous radio sources. The plot is obtained from Hardcastle et al. (2025)

In the early stages of finding AGN, radio loudness was a significant characteristic used to identify AGN. Surveys like 3C and Parkes helped find strong radio sources which were identified and confirmed as AGN using optical follow-up (Bennett, 1962; Bolton et al., 1964). Other methods include searching for AGN using their morphology, where the presence of the AGN structure, such as lobes and jets, is and has been a crucial factor in the identification of these objects, as they give insights into evolution and energy processes of AGN (Fanaroff and Riley 1974, see Hardcastle and Croston 2020 for a review). In addition, high resolution images of these objects further help in gaining in depth understanding of the driving mechanism of the AGN. By looking at optical surveys and studying the broad and narrow emission lines, AGN can be categorized into Type-I, which show both broad and narrow lines, and Type-II, which only show narrow line emission. In addition, X-rays and infrared have been used to find radiatively efficient AGN, where X-ray surveys have been used to find heavily obscured sources (see review Brandt and Hasinger 2005, Treister et al. 2009). AGN also exhibit distinctive colors in the infrared as the central engine heats the surrounding dust (Stern et al., 2012). AGN produce energy that are radiated in different parts of the spectrum and each part of the spectrum can be used to understand the underlying process of the AGN, in addition to their surroundings and their hosts (see Section 1.4).

#### 1.2.5 Selection and Identification

As extragalactic radio sources are a mix of different populations, the selection of radio AGN has also been a challenge, especially for flux densities below  $\sim 1$  mJy as objects like star forming

galaxies and radio-quiet AGN start dominating the sky (Windhorst et al., 1985; Magliocchetti et al., 2000; Kimball et al., 2012; Condon et al., 2013; Ceraj et al., 2020). This was not a problem until the 1990's but as the sensitivities increased, proper selection of AGN became important to avoid selection bias. As we start moving to much higher redshifts (z > 1.5) we see more star forming galaxies hosting AGN and vice versa, so that it becomes difficult to differentiate between the two populations (Merloni et al., 2004). This means that unless we are able to make use of morphological structure, such as cores, lobes and jets (Morabito et al., 2022), it is difficult to distinguish between the three populations, where both photometric and spectroscopic information is required along with multi-wavelength data. Hence, sophisticated methods and new techniques are required to separate radio AGN and other populations. Some of the techniques used for distinction are, SED fitting, radio continuum slope, mid-infrared (MIR) color, and Radio/FIR excess (Stern et al., 2012; Delvecchio et al., 2017; Alberts et al., 2020; Best et al., 2023). SED fitting uses multi-wavelength information to produce a spectral energy distribution for an object of interest, which is then fitted using different models to infer different properties of a galaxy, including identification of an AGN. Best et al. (2023) used SED fitting models along with data from optical, near-IR, and radio, which helped them compare observed emission from theoretical models. Specific models were used that include contribution from AGN emission which helped in separating AGN and SFGs. The radio continuum slope method uses multi-wavelength information to identify flat spectrum or inverted-spectrum AGN but it is not efficient at distinguishing steep spectrum or star forming galaxies as they tend to have same spectral index. For MIR colors method the Mid-Infrared color is used to distinguish between radio AGN and star forming galaxies, although the method only works for highly luminous and radiatively efficient sources as the method is biased against MIR lower luminosities and high redshifts (Donley et al., 2012). Fig. 1.3, a mid infrared color-color reference plot, shows distinct locations in the plot where LERGs, HERGs, and Quasars are observed using the LoTSS-DR2 survey data. There are other methods, such as, optical/NIR spectroscopy, and X-ray emission, that can be used for AGN selection (see reviews, Padovani 2016; Hardcastle et al. 2019 for different selection methods). However, no single method provides the ultimate selection, as they suffer from different limitations and are only easily applied to high luminosity sources. Therefore, special care has to be taken when selecting radio-AGN. Details of color selection of sources used in the thesis is given in Chapter 4, along with effects of selection of sources discussed in all upcoming chapters.

#### 1.3 Physics

#### 1.3.1 Synchrotron Radiation

Baade (1956) concluded in his study of M87 that the optical radiation emitted by the jets was strongly polarized, thus establishing that it and the radio emission was synchrotron emission. Burbidge (1956) made calculations by assuming equipartition of energy, which is then used to determine magnetic field strengths. The presence of synchrotron emission meant that the particles were moving at relativistic speeds in magnetic fields, and the calculated field strengths combined with the large physical sizes of the sources meant that the sources stored large energies. Furthermore, AGN also emit in shorter wavelengths, such as X-ray, where particles lose energy quickly, further implying a requirement for continuous injection of energy. For the particle of interest, an electron which radiates over a range of frequencies, the central frequency is determined using the Lorentz factor, the cyclotron frequency, and the angle between the net velocity and magnetic field direction, given by the equation;

$$v_c = \left(\frac{E}{m_e c^2}\right)^2 \frac{eB}{2\pi m_e} \sin\theta \tag{1.2}$$

where E is total energy of electron, B is the magnetic field strength, and  $\theta$  is the pitch angle between the velocity vector of the particle and the magnetic field direction. Although, when an ensemble of electrons is considered then the spectrum of an electron is integrated over appropriate distribution function. The energy distribution of electrons is given by a power law;

$$n(E)dE \propto E^{-\delta}dE \tag{1.3}$$

Hence, the emission being synchrotron radiation was an important finding as it not only confirmed the process responsible for radio emission, but was also useful in inferring the energy distribution of sources and their magnetic field strengths. For energy density (U) of a radiating electron in a magnetic field B with power law energy distribution of index  $\delta$ , the total energy is given by:

$$U = kJ(v)B^{-\frac{\delta+1}{2}} + \frac{B^2}{2\mu_0}$$
 (1.4)

where J(v) is volume emissivity and k is a constant. The eq.1.4 shows that for a given emissivity from a radio emitting structure, the only free parameter is the magnetic field strength B. Hence,

at some give value of emissivity, we can obtain the minimum energy contained in a region of radio source, given by;

$$B_{min} = \left(\frac{kJ(\nu)\mu_0}{2}(\delta+1)\right)^{\frac{2}{\delta+5}} \tag{1.5}$$

Substituting the eq. 1.5 into the magnetic field energy  $(U_{mag})$  component and particle energy  $(U_{par})$  component of eq. 1.4, gives;

$$U_{mag} = \frac{\delta + 1}{2} U_{par} \tag{1.6}$$

Hence, we can see that minimum energies are basically equipartition in energies of particles and magnetic field. Here, Spectral index and luminosity are observable quantities, however magnetic fields cannot be observed directly. Also, the critical frequency, given in eq. 1.2, of a particle is directly dependent on both, the particle energy and the magnetic field strengths, so disentangling the two is difficult, unless one of them is known.

In addition to synchrotron radiation, low energy photons are also scattered by high energy electrons, a process known as inverse-Compton scattering. These photons are most easily seen in X-ray, and can be used to determine the magnetic field strengths of the sources. Here, we are mostly concerned with the up-scattering of the cosmic microwave background (CMB) photon and synchrotron photons, as these are the dominant low energy photons present in AGN hotspots and jets, and are usually responsible for X-ray emission from inverse-Compton process Tavecchio et al. (2000); Celotti et al. (2001); Kataoka and Stawarz (2005). For synchrotron radiation the electron loss rate is given by:

$$-\frac{dE}{dt} = \frac{4}{3}\sigma_T c\gamma^2 \frac{B^2}{2\mu_0} \tag{1.7}$$

where  $\sigma_T$  is Thompson cross-section,  $\mu_0$  is permeability of vacuum, and  $\gamma$  is Lorentz factor given by;  $E/m_ec^2$ . We can see that loss rate is proportional to  $\gamma^2$ , hence high energy electrons cool off faster. Whereas, the loss rate for scattering particles in inverse-Compton scattering is given by;

$$-\frac{dE}{dt} = \frac{4}{3}\sigma_T c \gamma^2 \mu_{CMB} \sigma_T \tag{1.8}$$

where  $\mu_{CMB}$  is the energy density of CMB. As we can see from the two equations, eq. 1.7 and 1.8, they are identical except for the fact that energy loss due to inverse-Compton scattering is only dependent on energy density of CMB, which is known for a given redshift. Hence, X-ray emission can be used to provide an estimate of magnetic field strengths if the photon field is known.

#### 1.3.2 Power Law distribution of Electrons

For an ensemble of electrons, with an energy distribution given by N(E) and bound in a region of energies  $E_{min}$  and  $E_{max}$ , the emissivity as a function of frequency J(v) is given by;

$$J(\mathbf{v}) = \int_{E_{min}}^{E_{max}} j(\mathbf{v}) N(E) dE$$
 (1.9)

where j(v) is emissivity of single electron and is a function of E and B. If N(E) follows a power law distribution as given in eq. 1.3, then the eq. 1.9 becomes;

$$J(v) = \int_{E_{min}}^{E_{max}} j(v) N_0 E^{-\delta} dE$$
 (1.10)

where  $N_0$  is normalization factor,  $-\delta$  is initially injected electron energy distribution power law index. Substituting for energy using eq. 1.2 in eq. 1.10, where j(v) is assumed to be strongly peaked at critical frequency  $v_c$ , we find that;

$$J(v) = N_0 v^{-\frac{\delta - 1}{2}} B^{\frac{\delta + 1}{2}}$$
(1.11)

where

$$\alpha = \frac{\delta - 1}{2} \tag{1.12}$$

is the spectral index ( $\alpha$ ) of the observed spectrum. This leads to an observed flux ( $S_v$ ) which is dependent on observed frequency and spectral index, also expressed as;

$$S_{\nu} = \frac{VJ(\nu)}{4\pi D^2} \propto \nu^{-\alpha} \tag{1.13}$$

where V is the volume of the source, D is its distance, and  $\alpha$  can be measured using maps available at two or more frequencies. This means that we can trace the change in spectral index over different frequencies given data for more than two frequencies is available.

#### 1.3.3 Spectral Age

We know that synchrotron radiation is produced when there is interaction between relativistic charged particles and magnetic field. So, for a fixed magnetic field, emission spectrum by a single electron will peak at a critical frequency, given by eq. 1.2. We have also seen in eq. 1.7 that loss of energy of an electron is dependent on Lorentz factor, which means high-energy electrons tend to lose energy faster. This property of synchrotron radiation produces a curvature in the spectrum that can be used to evaluate the age of population of electrons radiating via the synchrotron process and is also known as spectral ageing. If  $\tau_{rad}$  is the radiative lifetime of a particle, then using eq. 1.7,  $\tau_{rad}$  it can be expressed as;

$$\tau_{rad} = E/(-dE/dt) \propto E^{-1}B^{-2}$$
 (1.14)

The equation clearly shows that the energy of electron and the magnetic field play vital role in determination of radiative ages. From eq. 1.13, flux and frequency being observables, we can evaluate spectral index and thus power law index to further evaluate particle energy distribution. Energy distribution and magnetic field strengths can be then used to get estimates for spectral age for given region of a source. Given that energy loss rate is dependent on Lorentz factor, the loss rate preferentially increases for high energy particles, which means that the spectrum gets steeper and strongly curved, assuming no additional particle acceleration occurs.

Several spectral ageing models have been developed that give insights into the age of AGN and processes involved in these galaxies. The two widely known models are Kardashev (1962); Pacholczyk and Roberts (1971) (KP) model and Jaffe and Perola (1973) (JP) model which assume a single particle injection energy distribution. Both models assume power law energy distribution where synchrotron losses occur along lobes/plumes. An electron energy distribution (N) defined by energy (E), pitch angle ( $\theta$ ), and time since acceleration (t), subject to synchrotron and inverse-Compton losses, is given by (Pacholczyk and Roberts, 1971);

$$N(E, \theta, t) = N_0 E^{-\delta} (1 - E_T E)^{-\delta - 2}$$
(1.15)

where

$$E_T = C_2 B^2 (\sin^2 \theta) t \tag{1.16}$$

According to eq. 1.16 isotropic pitch angle ( $\theta$ ) is assumed which is constant over radiative time. In practice we expect that electrons can change their pitch angle over time (so-called pitch angle scattering) and this leads to the JP model, where the energy distribution given by eq. 1.15,  $E_T$  is expressed as;

$$E_T = C_2 B^2 \langle \sin^2 \theta \rangle t \tag{1.17}$$

Here pitch angle is taken to be isotropic over short time scales which is more realistic as compared to KP model's assumption of constant pitch angle. The synchrotron spectra for these two different models can be calculated using the general form given in eq. 1.9. However, both models assume that magnetic field is constant throughout the source, which is not a realistic scenario. Hence, another model was proposed by Tribble (1993), which considers spatially non-uniform magnetic field, making for a realistic magnetic field structure. Fig. 1.4 shows the spectral curve observed for the Tribble model and the respective age for each curve. We discuss these models in more detail in Chapter 2.

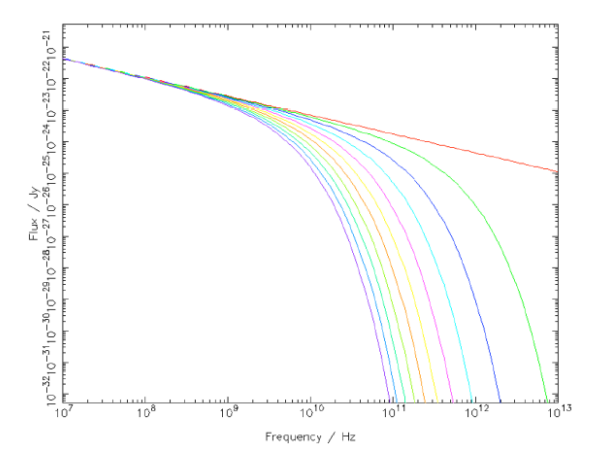


FIGURE 1.4: Flux versus frequency plot showing spectral curves obtained by using Tribble model producing ages between 0 Myr to 10 Myr (Harwood et al., 2013).

#### 1.3.4 Relativistic Beaming

Relativistic beaming, also known as Doppler boosting is a relativistic effect that amplifies or diminishes the observed intensity of light or radiation emitted from a moving source, depending on its velocity and direction relative to the observer. This phenomenon is particularly significant in astrophysical systems with relativistic jets, such as AGN. Blandford and Königl (1979) in their study suggested that the moving components in relativistic jets could have Doppler boosted fluxes, where the effect of the boosting is represented in the form of a Doppler factor ( $\mathcal{D}$ ) applied to the rest frame (see Longair (2010), from where I adapt rest of the discussion in this section). For a source component moving relativistically towards the observer, with velocity v, and at an angle  $\theta$  with respect to line of sight, the rest frame flux density would be;

$$S(v_0) = \frac{L(v_0)}{4\pi D^2} \times \mathcal{D}^{3+\alpha}$$

$$\tag{1.18}$$

where  $\mathcal{D}$  is Doppler factor, given by;

$$\mathscr{D} = \frac{1}{\gamma \left(1 - \frac{v \cos \theta}{c}\right)} \tag{1.19}$$

Now, if we consider a source to have two identical components ejected in opposite direction at same angle, the relative intensities of the components will be;

$$\frac{S_1}{S_2} = \left(\frac{1 + \frac{v}{c}\cos\theta}{1 - \frac{v}{c}\cos\theta}\right)^{3 + \alpha} \tag{1.20}$$

So we would observe different intensities for the two components, with the an approaching component being more luminous than the receding one. Thus, observing a one-sided source would not be a surprise. The jets of the source are closer to the line of sight, we would see higher luminosity differences between the components as opposed to sources that are aligned with plane of sky. Barthel (1989) used the principle to propose the segregation of RLAGN into quasars and radio galaxies based on their orientation as due to beaming effects quasars would show different component luminosities, while radio galaxies would have similar component luminosities. We discuss more about unification in Chapter 4.

#### 1.3.5 Polarization

For relativistic electrons, significant radiation is observed only when the electron's trajectory is within an angle of  $1/\gamma$  relative to observers line of sight (Longair, 2010). This means that the radiation is highly concentrated within the cone of width  $1/\gamma$ , and the observer will detect the radiation if their line of sight is within the  $1/\gamma$  cone. As synchrotron emission is polarized, for electron moving in helical motion along magnetic field, the projection of magnetic field onto plane of sky is dependent on orientation and degree of polarization. Since radiation within  $1/\gamma$  reaches the observer, the observed polarization is the average contribution from all electrons whose cones overlap the line of sight. The fractional linear polarization ( $\pi_L$ ) is independent of frequency and for a power-law distribution of electrons can be determined by using spectral index alone, given by;

$$\pi_L = \frac{3\alpha + 3}{3\alpha + 5} \tag{1.21}$$

As typical spectral index values lie between 0.5 and 1, the fractional polarization given by eq. 1.21 is between 70% and 75%. This calculation assumes that the region consists of highly uniform magnetic field, although the magnetic field in reality are not uniform and lower polarization fractions have been observed for sources. Polarization, coupled with relativistic beaming, is a spectral index dependent property that provides more information into the orientation of the source in the plane of sky. Studies such as Barthel (1989) have used relativistic beaming to describe orientation based unification of radiatively efficient RLAGN, in addition to studies, such as Laing (1988); Garrington et al. (1991), that have explored the one sidedness of AGN jets by studying the polarization and intensity maps to find Doppler enhancement of large scale

jets found in depolarization asymmetry. Here, depolarization asymmetry is unequal depolarization observed in different regions of source. Before diving into depolarization asymmetry, understanding Faraday rotation is essential. In presence of magnetized, ionized medium the polarization angle of the propagating radiation from the components is rotated due to difference in the speeds of propagation. The change is dependent on the frequency, magnetic field strength, and electron density. Hence, in a Faraday-active medium, the measured polarization angle for a single line of sight is given by;

$$\chi = \chi_0 + \phi \lambda^2 \tag{1.22}$$

where,  $\chi_0$  is intrinsic polarization angle and  $\phi$  is given by;

$$\phi = K \int_0^d n_e B \cdot dS \tag{1.23}$$

Here, K is  $2.63 \times 10^{-13} \text{ T}^{-1}$ . In principle, the approaching component of AGN shows higher fractional polarization as compared to the receding component which exhibits greater Faraday rotation. This means that the receding component is being viewed through a denser, more magnetized medium. As different parts of the source can have different polarization angles due to varying levels of Faraday rotation, when a beam of the telescope observes different regions of the source, it averages over these regions, leading to misalignment of polarization vectors, and hence a reduction in observed polarization, also known as depolarization. Overall the depolarization asymmetry is the direct consequence of Faraday rotation differences observed for the components of RLAGN, and the Laing-Garrington effect encapsulates this asymmetry on how orientation of jet influences the polarization properties (Laing, 1988; Garrington et al., 1991). As Faraday rotation is also dependent on the line of sight, so for a source more closely aligned to plane of sky, the effect diminishes, showing similar polarization angles for the components. Due to Doppler enhancement and Laing-Garrington effect, the one sided-ness suggested that if one of the jets is oncoming high velocity then it is closer to us than the opposite side of the jet. These observed properties of AGN emphasize the importance of understanding the unification of different types of AGN.

### 1.4 Host Galaxy Environments and Feedback

Investigations of the AGN environment and the galaxies that host them, are key to exploring the physics behind the AGN process, the feedback, formation of structure, the evolution of galaxies and clusters, and most importantly triggering of AGN. This section discusses the importance of understanding the AGN properties and describes how AGN activity might be affecting their surroundings, such as host galaxies, their environment and the galactic/cluster medium.

#### 1.4.1 Host Galaxies

It has been known for quite a while that majority powerful radio AGN are hosted by massive galaxies (Matthews et al., 1964), with stellar masses up to  $10^{11}M_{\odot}$ , at  $z \sim 1$  (Jenkins, 1982; Jarvis et al., 2001; Willott et al., 2003; Best et al., 2005; Mauch and Sadler, 2007; Smolčić et al., 2009; Sabater et al., 2019). This was also subsequently confirmed by studying rest-frame  $1.6\mu$ Jy and  $4.5\mu$ Jy photometry where radio AGN hosts show high masses, at up to  $z \sim 3$  (Seymour et al., 2007; De Breuck et al., 2010; Drouart et al., 2016). There is evidence that star formation occurs earlier for massive galaxies than for less massive ones (Di Matteo et al., 2005; Best et al., 2005; Springel et al., 2005a; Best, 2007). Furthermore, studies such as Lin et al. (2017); Mo et al. (2020), have shown that radio AGN fraction increases within galaxies residing at cluster centers, and has higher dependency on stellar mass (Sabater et al., 2019). Overall, these studies have noted that most radio AGN are observed in galaxies with rich environments, high stellar mass and black hole mass, or high episodes of star formation. Furthermore, the Fanaroff and Riley (1974) classification has been shown to have links with galaxy mass, irrespective of the accretion mode, for samples that are matched in radio luminosity (Mingo et al., 2019).

While exploring the triggers of the AGN activity, signatures of disturbances have been observed in some cases. Evidence indicates that HERGs often display disturbed host galaxy morphologies, which are also correlated with radio luminosity (Best et al., 1997; Ramos Almeida et al., 2012). Disturbed features are more prevalent in high luminosity HERGs and have lower prevalence in lower luminosity radio samples (Pierce et al., 2019). This could mean that processes in high luminosity HERGs are able to affect the morphology of the galaxies or the disturbed morphology of galaxies could be the signature of the conditions that trigger HERGs. Additionally, there is evidence that neighboring galaxies could be triggering AGN activity, especially for LERGs (Pace and Salim, 2014; Sabater et al., 2015). However interactions cannot be the only contributing factor for LERG activity, since halo mass and stellar population properties also have an effect on the AGN activity of LERGs (Ellison et al., 2015). These results indicate the several pathways through which AGN can be activated wherein for HERGs cold gas from galaxy mergers and interactions could be the fuel, while LERGs mostly rely on intrinsic properties like halo mass and hot gas availability (Hardcastle et al., 2007). Overall, AGN can use combination of different fuels, such as cold/hot gas, halo mass, and or merger/iterations, to start AGN activity. Even in terms of host morphology, not only elliptical but spiral galaxies are also seen hosting AGN, and a number of spirals have been found to host radio AGN of scales larger than kpc (Ledlow et al., 2001; Croston et al., 2008; Hota et al., 2011; Mao et al., 2015; Mulcahy et al., 2016). Even if a relationship is observed between radio AGN and host morphology, other factors, such as black hole and stellar mass difference, evolutionary state along with presence of hot gases seem to be governing the AGN activity (Krause et al., 2019).

Observations also suggest that RLAGN hosts are often massive galaxies that lie below the main sequence, the "red and dead" region, part of color bi-modality, which refers to observation of cluster of two distinct groups of galaxies (red and blue) when plotted on a color-magnitude diagram (Strateva et al., 2001; Baldry et al., 2004). In the "red and dead" region the star formation rates are low or have ceased (Gürkan et al., 2015). This is noteworthy because, in normal galaxies, entry into the "red and dead" region typically coincides with the cessation of star formation, reflecting the end of the expected proportional relationship between star formation rates and galaxy mass. Hence, evidence of massive RLAGN falling in the "red and dead" region suggests that AGN activity is affecting the star formation rates. However, within RLAGN, HERGs and LERGs show different star formation rates, where HERGs are hosted by bluer galaxies that have comparatively higher star formation rates (Baldi and Capetti, 2008; Smolčić et al., 2009; Best and Heckman, 2012; Janssen et al., 2012; Hardcastle et al., 2013). There is also evidence of simultaneous AGN activity and star formation triggering which could be due to gas in-flow or jet-induced star formation (Mahabal et al., 1999; Mannering et al., 2011). From the discussion it is clear that AGN, star-formation rates and the galaxy morphology affect one another, while showing correlations with galaxy/stellar masses and using their surroundings, such as gas, neighboring galaxies interaction, and halos as fuel for the activity.

# 1.4.2 Large Scale Environment

Evidence of large-scale environment affecting radio galaxy properties, especially for the local universe (Best, 2004; Ineson et al., 2015) is extensive. For instance, it has been found that FR Type II are not usually observed in rich environments whereas sources like Wide-Angle tail (WAT) and Narrow-Angle tail (NATs) are present in richer environments (Mingo et al., 2019; Garon et al., 2019). These galaxies are thought to traverse through the intracluster medium (ICM) causing bending of jets and tails, making them effective indicators of dense environments (Johnston-Hollitt et al., 2015; Paterno-Mahler et al., 2017). Environmental effects also impact outflows: as noted above, in rich environments jets decelerate, entrain ISM gas and form FR-I turbulent plumes, whereas in poor environments the jets remain relativistic. External pressure, such as that exerted by a group or cluster environment, is essentially confining the radio-lobe plasma, seen in X-ray images in the form of cavities or bubbles (also discussed in Section 1.2.4), where without external pressure the lobes/plumes would diffuse into their surroundings.

There are links observed between the accretion mode and the large-scale environments (Tasse et al., 2008; Lin et al., 2010), X-ray observations provide stringent constraints on cluster richness, showing that radio sources such as HERGs avoid rich environments and LERGs span through out the environment richness scale (Ineson et al., 2013, 2015). There are also links found between radio luminosity and environmental richness which suggests a strong correlation

between ICM properties and jet power that is not commonly driven by black hole mass (Ineson et al., 2015; Ching et al., 2017).

Environmental investigations have been performed most extensively for local universe, but at higher redshifts, studies of RLAGN environment have only been possible for rare objects belonging to high luminosity population (see Miley and De Breuck 2008 for a review). These galaxies are usually found in rich galaxy clusters where large Faraday rotation measurements (see Section 1.3.5) gave indications of hot magnetized cluster gas surrounding the host galaxies (Carilli et al., 1997; Athreya et al., 1998). In addition, excess of companion galaxies were found near HzRGs (Roettgering et al., 1996; Pascarelle et al., 1996; Le Fevre et al., 1996), which suggested that the HzRG hosts are dominant cluster galaxies, implying that these galaxies are possibly the progenitors of massive galaxies in the local universe. These objects thus help in understanding the evolution and formation of the massive galaxies, black holes and rich clusters that are also observed in the local universe.

#### 1.4.3 Feedback

It is clear from the prior discussions that RLAGN have profound connection with their hosts and galaxy environment, along with other properties such as star formation rates, accretion rates, and luminosity. Feedback from the AGN jets is one of the most studied aspects and evidence of energetic impact from RLAGN jet is extensive (McNamara and Nulsen, 2007). A key piece of evidence is the detection of radio lobes that produce shock fronts and ripples that transfer injected energy into the ICM gas, affecting a range of environments (Kraft et al., 2003; Croston et al., 2011; Randall et al., 2015). There is evidence that show that jets can compress the interstellar gas, leading to conditions conducive to star formation (Gaibler et al., 2012). Observations from X-rays suggest that AGN activity can heat the ICM (McNamara and Nulsen, 2007; Fabian, 2012). In X-ray, there are cavities seen that are excavated by expanding lobes, which provide work done on surrounding medium and these have sufficient energy that they could offset cooling rates of gasses (Boehringer et al., 1993; Dunn et al., 2005; Hlavacek-Larrondo et al., 2015), although these cavities are observed for local universe due to observational and selection limits and it has been difficult to obtain population wide conclusions (Bîrzan et al., 2012). In addition, as discussed above, massive RLAGN are seen in the "red and dead" region, which is consistent with the idea that the activity is inhibiting star-formation in these galaxies (see Section 1.4.1). Other evidence for direct AGN impact on their environment includes the fact that AGN outflows show transportation of metals into the ICM, enriching it with heavy elements (Simionescu et al., 2009).

AGN feedback is invoked because mismatches between the models and observations have been seen. Without something similar to AGN feedback, models show rapid gas cooling due to

radiative processes, leading to excessive star formation and overly luminous galaxies (Croton et al., 2006), whereas observations of massive galaxies have exhibited low star formation rates (Baldry et al., 2004). In addition, models also predict high rates of cooling in galaxy clusters, accumulating gas at the center, forming stars (Fabian, 1994) but X-ray data observations show otherwise; reduced cooling rates and minimal central star formation are observed for galaxy clusters (Sakelliou et al., 2002; Peterson et al., 2003; McNamara and Nulsen, 2007). Invoking AGN feedback hence helps in understanding the suppression of star formation in massive galaxies and prevention of cooling flows into clusters. AGN feedback is also invoked in the study of black-hole bulge mass correlation, evolution of galaxy mass fraction of dark matter halos, and or thermodynamic properties of gas in clusters (Silk and Rees, 1998; McCarthy et al., 2011; Le Brun et al., 2014; Davies et al., 2019). Additionally, AGN feedback can provide insights into the color bi-modality of galaxies, where the distinction requires rapid quenching of star-formation (Springel et al., 2005b).

The observations discussed in Section 1.4.1 and 1.4.2 are suggestive of coupling of host galaxies and large-scale environment with AGN activity, indicating an interplay between the three factors. The interplay is understood in terms of a process called 'feedback' in which the surrounding gas is channeled to the central region of the galaxy, helping fuel the process. For the local universe, the material from massive cluster/group galaxies' atmospheres becomes the fuel for the AGN activity (Gaspari et al., 2013, 2017), whereas at high redshifts it is observed that these sources inhabit high-density massive galaxy formation regions (Miley and De Breuck, 2008). The RLAGN activity is highly energetic in nature and such process can have profound effect on the environment of the galaxies that these AGN inhabit, heating the gas that surrounds them and preventing the gas from cooling, leading to low star formation rates. Cooling causes condensation of clumps that rain on AGN by losing angular momentum to accrete on to central black hole which further leads outward flow of energy and thus forms self-regulated cycle (Pizzolato and Soker, 2005; Gaspari et al., 2012). These series of activities are important to be understood as they are vital parameters that affect the radiative efficiency, morphology, and most probably jet power. The outward flow of energy further transports energy to the surrounding and forms a cycle which becomes an important part of the 'feedback' process (Somerville and Davé, 2015; Naab and Ostriker, 2017). Efforts are being made to understand, computationally and observationally, the extent to which feedback can explain the processes involved in star-formation, black-hole growth, and galaxy evolution where feedback from AGN are invoked into models.

# 1.5 Surveys

Since the development of the first single dish radio telescope by Reber (1940) radio telescopes and later interferometers have undergone remarkable advancements, culminating in the upcoming Square Kilometer Array (SKA), which promises unprecedented sensitivity and resolution. Radio surveys have played a transformative role in exploring celestial phenomena that are mostly invisible to optical telescopes.

A rapid evolution in radio telescope technology took place after world war II, when the first large radio survey was published, the 2C survey at Cambridge (Shakeshaft et al., 1955). This survey catalogued 1936 discrete radio sources at 81 MHz although it turned out to contain many spurious sources. The subsequent survey, 3C survey (Edge et al., 1959), catalogued 471 sources at 159 MHz and had achieved higher resolution and sensitivity, as compared to the 2C, with better rejection of spurious sources. A more almost complete survey was later published, called 3CR (Bennett, 1962). Almost 2 decades later, another survey was published, derived from the 3C and 4C surveys, called 3CRR (Laing et al., 1983), which was complete and overcame problems with the 3C survey that arose due to confusion, inhomogeneous flux measurements and partial resolution. The sample lists 173 sources, and has been widely used by radio investigators because all sources have optical identifications. Although, before 3CRR, a successor had already been published, called 4C survey (Scott and Ryle, 1961), which observed at 178 MHz and has a flux density limit of 2 Jy. Another survey of the time was the Molonglo Reference Catalogue (MRC) survey (Large et al., 1981) containing around 12,000 sources observed at 408 MHz, many of which were galaxies at higher redshifts. The survey uses a flux density cutoff of 1 Jy. Other surveys were also developed around the period that had contributed to the advance of our knowledge of radio sources, these are listed in Table 1.1. The surveys listed in Table 1.1 collectively published millions of extragalactic radio sources, observing at different frequencies, providing multi frequency data and helped in understanding different properties of radio sources. We do not go into details of these surveys as they are out of scope for the thesis and hence, we only introduce them to provide a context on the expanse of surveys that have taken place, although we do refer to the 3CRR and MRC survey in the Chapter 3.

Surveys like 3C and Parkes (Bennett, 1962; Bolton et al., 1964) provided some of the early catalogues that were constructed to study physics of individual AGN or small samples, though wide sky surveys were also used to obtain a representative population. The nature of RLAGN was poorly understood in the early days of radio astronomy, as discussed above and hence, wide field radio telescopes were used; however, these telescopes were of low sensitivity. An advantage of using low frequencies is and has been that RLAGN are often dominated by steep-spectrum emissions which are also presumed to be isotropic (unaffected by relativistic beaming). More sensitive surveys, such as those with the Very Large Array (VLA) (Thompson et al., 1980) have been used in the recent past to get a detailed look at the RLAGN. These surveys use

TABLE 1.1: List of surveys wit	n their frequencies, resolution,	noise levels and number of
	sources observed.	

Survey Name	Date	Telescope	Reference	Frequency (MHz)	Resolution (")	Noise Level (mJy/beam)	No. of Sources
4C	1958- 1962	Cambridge Radio Telescope	Scott and Ryle (1961)	178	1200	200	4081
Bologna B2	1960	Northern Cross	Colla et al. (1973)	408	180 × 600	50	9929
Parkes 2700 MHz	1993	Parkes	Griffith and Wright (1993)	2700	600	100	1178
Westerbork Northern Sky Survey (WENSS)	1991- 1996	Westerbork Synthesis Radio Telescope (WSRT)	Rengelink et al. (1997)	327	54	3.6	230,000
NRAO VLA Sky Survey (NVSS)	1993- 1996	Very Large Array (VLA)	Condon et al. (1998)	1400	45	0.45	1,800,000
Faint Images of the Radio Sky at Twenty- Centimeters (FIRST)	1993- 2004	Very Large Array (VLA)	Becker et al. (1995)	1400	5	0.15	800,000
Sydney University Molonglo Sky Survey (SUMSS)	1997- 2003	Molonglo Cross	Bock et al. (1999)	843	45	1.0	211,000

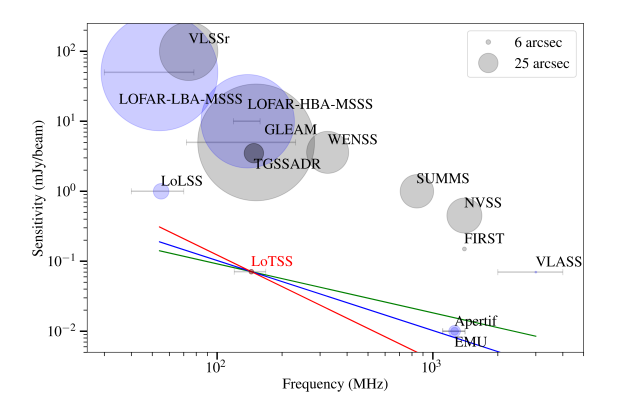


FIGURE 1.5: Image rms, frequency, and angular resolution (linearly proportional to the radius of the markers) of LoTSS-DR1 in comparison to a selection of existing wide-area completed (grey) and upcoming (blue) radio surveys. The horizontal lines show the frequency coverage for surveys with large fractional bandwidths. The green, blue, and red lines show an equivalent sensitivity to LoTSS for compact radio sources with spectral indices of 0.7, 1.0, and 1.5, respectively. The plot is obtained from Shimwell et al. (2019).

GHz frequencies to generate larger samples than before as they have higher spatial resolution and lower noise. Where wide area surveys can be used to get large numbers of sources in the local universe, deep surveys with a narrow field of view can be used to find high redshift RLAGN (Smolčić et al., 2018). Fig. 1.5 shows a comparative plot of resolution and rms for new upcoming surveys and existing wide area surveys, depicting the change in resolution and sensitivity of older to newer surveys. As deep field surveys are sensitive they often detect not just RLAGN but emission from star forming galaxies, as the sensitivity of these surveys extend to the low-level radiation emitted by star formation processes within galaxies, and separating RLAGN emission in the host galaxy can be a concern, thus cross-match from multi-wavelength observations and selection effects need to be taken into account while a study is conducted. More recent surveys and telescopes with ability to get samples at wide areas and deep fields with higher sensitivity will provide data and images at multiple frequencies. The Low Frequency Array (LOFAR), designed to observe the sky at low frequencies (10 - 240 MHz) and LOFAR Two meter Sky Survey (LoTSS) is mapping the northern sky (Shimwell et al., 2017, 2019). Similarly, the Giant Meterwave Radio Telescope with frequency range between 150 MHz to 1.4 GHz is also available (Swarup et al., 1991) and has conducted both wide and deep sky surveys. In addition, data from the MIGHTEE survey with the MeerKAT telescope early science data and data release I provides images and sample of RLAGN that are probed with very high sensitivity and resolution (Jarvis et al., 2016), compared to previous surveys. More forthcoming surveys include the Australian Square Kilometre Array Pathfinder (ASKAP), that will provide more insights in to the working of AGN and Square Kilometer Array (SKA), which will be the world's largest radio telescope and 50 times more sensitive than ASKAP (Dewdney et al., 2009; Norris et al., 2011).

Since then many advancements have been made in terms of resolution and sensitivity which have helped astronomers study the sources and their properties in greater detail and obtain better insights into AGN processes and their lifetimes. We discuss such surveys below, which have also been used in the thesis, discussed in the upcoming chapters.

#### **1.5.1 MIGHTEE**

The MIGHTEE survey is the MeerKAT international GHz Tiered Extragalactic Exploration survey and observes using the MeerKAT telescope, based in South Africa. The MeerKAT telescope is an array of 64 interlinked antennas, where each antenna consists of reflector, sub-reflector, and receivers. The telescope was originally called Karoo Array Telescope (KAT) and had 20 receptors, but was later upgraded to 64 antennas. The MIGHTEE survey aims to cover 20 deg $^2$  of area at  $\mu$ Jy sensitivity at GHz frequencies. The goal is to provide excellent multi-wavelength data of simultaneous radio continuum, spectral lines, and polarization information. The survey targets two bands, L-band (900 MHz - 1.6 GHz) and S-band (2.2 - 3 GHz). The pointings target

four well studied fields, XMM-LSS, E-CDFS, ELAIS-S1 and COSMOS. The MIGHTEE survey aims to answer a range of scientific questions, with various science goals in mind. These goals include, understanding the evolution of AGN and star formation activity, evolution of neutral hydrogen and how effectively it can fuel AGN activity, and properties of magnetic fields (see Jarvis et al. 2016 for more details). Given MIGHTEE's sensitivities and ability to produce ultra-deep images, the catalogues and maps are excellent to conduct multi-wavelength analysis. MIGHTEE, being a highly sensitive survey, is also the best candidate to be used as a reference dataset to select and visually identify sources. Until now two sets of data have been released by MIGHTEE, MIGHTEE early science data (Heywood et al., 2022) and MIGHTEE data release I, (Hale et al., 2024). This is the data, specifically within the XMM-LSS field, that we will be using within the thesis and the details are discussed in the upcoming chapters.

#### **1.5.2 LOFAR**

The Low-Frequency Array (LOFAR) is a large radio telescope network developed and operated by ASTRON, the Netherlands Institute for Radio Astronomy. The idea behind LOFAR is to observe the sky at low frequency to offer insights into Epoch of Reionisation, cosmic magnetism, high energy cosmic rays, and deep extragalactic surveys. Under collaboration of several European countries and the United Kingdom, the project began scientific operations in 2010 and since then many different survey have been conducted or are underway. The surveys carried out by LOFAR include the LOFAR Multifrequency Snapshot Sky Survey (MSSS) (Heald et al., 2015), the LOFAR Two-metre Sky Survey (LoTSS) for wide area (Shimwell et al., 2017), LoTSS deep field survey (Best et al., 2023), and the WEAVE-LOFAR survey which makes use of the preceding two. The MSSS was the first wide area survey which had depth of 10 mJy/beam and resolution of 2 arcmin. The LoTSS wide area survey is an ongoing wide area survey that operates between 120-168 MHz with resolution of 6 arcsecond and declination dependent sensitivity of around 100 µJy/beam. The LoTSS deep field survey observes the northern hemisphere for three fields, Boötes, ELAIS-N1 and Lockman Hole with the depth of 10  $\mu$ Jy/beam. The WEAVE-LOFAR is a spectroscopic survey which will provide with spectroscopic redshifts for the two wide and deep tiers of LOTSS. In the thesis we will make use of the LoTSS wide area survey which has observed in the XMM-LSS field and the LoTSS deep field survey. Including data from the LOFAR survey grants us the ability to conduct multi-wavelength analysis, specially for data obtained at lower frequencies.

#### 1.5.3 **GMRT**

The National Centre for Radio Astrophysics (NCRA) located in India, set up a radio astronomy research facility which surveys the sky at meter wavelength ranges, known as Giant Metrewave

Radio Telescope (GMRT). The telescope is made up of 30 parabolic dishes of diameter 45m spread over distances of 25km. One of the reasons for choosing meter-wavelength ranges for observations is that man-made interference is lower at these frequencies and this part of the wavelength had not been exploited for sensitive observations at the time of the construction of the GMRT. Out of 30 dishes, 14 are arranged in a Y-shape and the others form a central square that gives the instrument good sensitivity to extended emission. GMRT operates is in 6 frequency bands centered around 50, 153, 233, 325, 610 and 1420 MHz where the highest resolution is 60 arcsecs and the lowest is about 2 arcsecs for the band at 1.4 GHz. One of the objectives of the telescope is to observe extragalactic sources, and as part of this it carried out a 610-MHz survey of the XMM-LSS field, which is used in Chapters 2 and 3. 15 years after it commenced operation, major upgrades were made to the telescope to improve its sensitivity by a factor  $\sim$  3. A collaboration between the MIGHTEE project and NCRA staff using the upgraded GMRT (uGMRT), will co-observe the MIGHTEE deep fields from 250-850 MHz; the collaboration is called superMIGHTEE, and it aims to provide information about  $\mu Jy$  sources at resolutions close to few arcseconds. Within the thesis we use uGMRT data from band-3 and band-4 in the XMM-LSS field. The GMRT 610 MHz survey provides a mosaic of approximately 30 deg<sup>2</sup> in the XMM-LSS, lowest sensitivity of 200  $\mu$ Jy/beam and highest sensitivity of 45 µJy/beam for a resolution of 6.5 arcsecs (Smolčić et al., 2018). However, the uGMRT superMIGHTEE data in the band-3 (centred on 390 MHz) and band-4 (688 MHz) are of much higher sensitivity (16 µJy/beam and 8 µJy/beam), observing the XMM-LSS at resolution of 10 arcsecs (Lal, Taylor, et al., submitted). Together, the GMRT and uGMRT surveys provide multi-wavelength data at 3 different frequencies in the XMM-LSS field. Further details about the data are discussed in the upcoming chapters.

Overall, we have large datasets from the three surveys that have observed the XMM-LSS field at high sensitivity and provide data at a resolution of a few arcseconds resolution. The key step forward is that we have up to 5 distinct frequencies (LOFAR, MIGHTEE, and three GMRT bands) and such a dataset for a single field has not been available before over such a substantial frequency ranges. This gives us a chance to study RLAGN at multi-wavelengths and understand spectral properties such as spectral age and spectral index curve. Furthermore, the availability of the large dataset provides us with statistically large sample that can offer significant results and gives insight into the overall RLAGN population, such as extended sources and sources at high redshifts. By including data from lower frequencies such as provided by the LOFAR survey, we can account for steep spectrum sources where older, larger and more extended sources can be used for analysis, as sources mostly show emission from lobes and diffuse halos, while data from high frequencies, as provided by MIGHTEE, probes emission from structure such as inner jets, hotspots and cores. High frequencies are mostly generated due to presence of high energy particles, which helps in understanding the flat spectrum sources and provides a wide range for multi-wavelength analysis.

# 1.6 Questions to answer

Studies until now have explored and analyzed different aspects of RLAGN using different surveys (discussed in Section 1.5) to understand the physics of these galaxies. In the thesis, we have underlined different observational and scientific phenomenon of RLAGN that shed some light on the workings of AGN, their structure and the effects they have on their surrounding. We explore the populations of particles responsible for generating radio waves in AGN and their spectrum which could ultimately help in evaluating age of these galaxies. We also describe the structure of AGN, i.e. observed radio morphology, and the different types of sources that have been observed, mostly based on their emission from multiple wavelengths and their emission types, which ultimately might belong to the same population under the orientation based unification scheme. We have also looked into more distant radio sources whose spectral properties are known to show peculiar relationship with redshift of the objects. These aspects of the sources have been extensively studied using different surveys over the period where we are specifically interested in spectral age of AGN, the  $\alpha$ -z correlation, and the orientation based unification scheme. These aspects all require data from multiple wavelengths or can be better studied with multiple large datasets.

Many different studies have been done until now to explore the age of AGN, for example, Katz-Stone and Rudnick (1998); Blundell and Rawlings (2000); Hardcastle and Looney (2001); Orrù et al. (2010); Harwood et al. (2013, 2016, 2017), using different methods such spectral curves, dynamical ageing, or spectral ageing models. The most common problem in the studies is the availability of the data at multiple wavelengths and use of large samples. Until sensitive surveys like MIGHTEE were published it was difficult to make spectral age calculations for multiple sources in a common field of view. Studies such as Harwood et al. (2013, 2017), have only been able to target individual sources for which multi-wavelength data is available but these sources were selected from random parts of the sky rather than a single field of view. In addition, the sample sizes have also been low such that no statistically significant conclusions could be derived for a population of sources. A similar gap also exists for the  $\alpha$ -z correlation studies (for example De Breuck et al. 2010; Saxena et al. 2018; Khabibullina et al. 2023), where most samples produced to explore the relation were from less sensitive surveys (such as 3CRR and MRC) that could mostly detect high luminous sources, or did not have enough multi-wavelength information with respect to optical identification such as redshift, or had lower sample size. These are limiting factors if we want to make a statistically significant analysis, where the selection of sources is homogeneous, unbiased, and sample comes from a representative population. Similarly, for testing the orientation based unification scheme (Barthel, 1989), the studies vouching for the scheme or studies that provide evidence against it lack large enough samples or a homogeneous enough selection of sources to make reasonable conclusions. These studies along with their sample sizes and selection criteria are discussed in detail in Chapter 4. Overall, we

can conclude that availability of large enough datasets has been an issue in the past, and sensitive surveys with high resolution and source information at multiple wavelengths can play a vital role in overcoming that limitation. Hence, in the thesis we explore the physics of RLAGN by performing the spectral age analysis, exploring the  $\alpha$ -z relation, and the orientation based unification scheme, using recent sensitive surveys such as MIGHTEE, LOFAR, and GMRT, as discussed in Section 1.5. All these surveys have information in the XMM-LSS field, along with other fields such as ELIAS-N1, Lockman Hole etc. These surveys also have high number of detections, reporting thousands of sources of varying sizes at high resolution. In addition, these surveys have also produced high resolution radio maps, especially MIGHTEE, which is useful in selecting and visually inspecting sources of desired sizes. Below I give a brief description of the analysis I will be conducting in the upcoming chapters and the possible questions I aim to answer by the end of the thesis.

- 1. For spectral age analysis we use the radio maps provided by the MIGHTEE, LOFAR, GMRT, and uGMRT surveys. Using the MIGHTEE survey as reference we select extended sources that have FR-I and FR-II type structure and cross match these with LO-FAR, GMRT, and uGMRT radio maps. The aim of the cross-matching is to find same sources in different wavelengths which can then be used to infer the spectral curve and in turn obtain spectral age of radio sources. The calculation of spectral age is evaluated by using the BRATS software which utilizes multi-wavelength source maps to conduct pixel-by-pixel analysis in order to obtain age of the source defined by an outlined region. The sample analysis can thus be used to reveal the distribution of ages of sources in the XMM-LSS field and evaluate statistics such as mean, median, maximum, etc. I also try to find the different class of objects within the sample, such as FR-I, FR-II, or any other possible structure, further commenting on the morphology of objects in the sample. I investigate whether any relationship can be observed between the ages of sources, their morphology and their sizes, further discussing about dynamics of the radio sources. The study of the sample and the answers to the questions are discussed in detail in Chapter 2. The study and its results can further help place constraints on the jet power of the sources, which is known to affect the host environment, ICM, IGM, and the cluster/group. The estimates of jet powers will provide an understanding of how much the surroundings and environment are affected by given powers.
- 2. In the investigation of the  $\alpha$ -z relation, I carry out a detailed investigation of the correlation of spectral index, redshift, and the luminosity of the sources. For this study I use the catalogues provided by the MIGHTEE, LOFAR, GMRT, and superMIGHTEE surveys. These surveys provide a range of frequencies that can be used to infer the spectral curve using two frequency pairs or multiple frequency pairs. The values of spectral index obtained using multiple frequency pairs and two frequency pair can be used to observe

correlation with redshift and luminosity of the sources, where I have used MIGHTEE survey as reference to select targets and evaluate luminosity of the radio sources. In this study I try to answer whether an inherent  $\alpha$ -z relation exists within the sample, where the use of recent surveys provides a much larger sample than previously used by other studies. I also explore the trends in the spectral index and luminosity of the samples and provide insight into what physical processes might be responsible for the observations. I also explore other parameters such as sample size and compare the results with the results from previous studies, such as De Breuck et al. (2010) and their use of sample. The study and analysis of the sample along with answers to the questions are detailed in Chapter 3. As HzRGs show different properties, as compared to local universe radio galaxies, in that they show higher stellar mass and star formation rates, have rich environments, and are precursors to present galaxy evolution, selection bias in these objects can affect our understanding of the early universe. Sampling HzRG using the steep spectrum selection criterion can lead to biased inferences about the population. Hence, understanding the correlation using larger samples, derived from sensitive surveys, can help us to take account of data from even low luminosity radio galaxies.

3. I perform a test of the unification scheme, proposed by Barthel (1989), using the sample from the LOFAR deep field observations. The surveys catalogs sources in different fields, such as the Lockman Hole, ELAIS-N1, and Boötes, which are well explored. Using the survey I create a sample of radiatively efficient RLAGN, that can be segregated in to quasars and radio galaxies using different color-color selection methods, outlined in Chapter 4. I also explore the different configurations of orientation, referred to as stick model and cylindrical model in the study, to explore the effects of source axial ratios on the test parameters, such as the critical angle and size ratio. The effects of axial ratio are studied by running simulation on a model that assumes cylindrical shape of a source and uses various distribution of parameters such as true length of a sources and their redshifts. Size ratio and critical angle are most widely used parameters to validate the orientation based unification scheme and thus I study the possible values of these test parameters using different sample sizes. In the analysis, I find the observed critical angles and size ratios obtained from different samples and compare them with values obtained for cylindrical model. The observations obtained from LOFAR sample and simulated sample are also compared with previous studies, where I comment on the unification schemes validity and the test parameters that are used to infer the results. The full details on the analysis and the results obtained are laid out in Chapter 4. Testing and establishing the validity of orientation based unification helps provide support to our understanding of the underlying AGN processes. If sources can be unified using the orientation scheme, it would mean that the process responsible for AGN activity is common for all types of observed AGN, and can be further used in AGN feedback modeling, which describes the effects of AGN activity on the host galaxy and its surroundings.

At the end of the thesis I summarize the results and observations obtained from the three separate analysis described above. These analysis give a deeper understanding of RLAGN population when a large sample size is used where the data obtained is from high sensitivity and resolution surveys, which have not been used before for these purposes. The analysis also give insight into possible physical phenomenon observed for the RLAGN population. In addition, the analysis not only helps in exploring the different aspects of the RLAGN but also lays down the ground work for analysis that can be conducted in future using surveys that will be of much higher sensitivity than MIGHTEE, LOFAR or GMRT, such as the Square Kilometer Array (SKA). The conclusions of the three analysis are detailed in Chapter 5.

# Chapter 2

# **Spectral age of Radio-loud AGNs**

### 2.1 Introduction

## 2.1.1 Radio-loud active galactic nuclei

Active galactic nuclei (AGN) are driven by the accretion of matter onto the central supermassive black hole of a galaxy. In this chapter, we use the term radio-loud AGN (RLAGN) to refer to objects which have strong radio emission related to the active nucleus, in general exceeding the radio emission due to star formation in their host galaxy. Traditionally RLAGNs have been classified morphologically into two different types depending on the jet morphology, namely, Fanaroff-Riley type I and type II (FRI and FRII), named after the Fanaroff and Riley morphological distinction for central brightened and edge brightened sources (Fanaroff and Riley 1974). The jets that terminate in a hotspot and remain relativistic throughout are categorized as edge-brightened FRII radio galaxies, whereas the jets that are relativistic initially and decelerate through kpc scales are categorized as centre-brightened FRI radio galaxies. Hence, the main extended structures that are seen in the RLAGN are: the jet, the hotspot, and the lobes, seen as FRII's and jets which decelerate to form plumes of lobes, seen as FRI's (e.g., Bridle and Perley 1984, Harwood et al. 2015, Blandford et al. 2019, Hardcastle and Croston 2020). These structures can be pc to Mpc in size (e.g., Blandford and Rees 1974, Urry and Padovani 1995, Rafferty et al. 2006).

Energy is dissipated in the jets and hotspots of these sources, which accelerate electrons to relativistic speeds and give rise to intense radio emission. Hotspots advance through the external medium and leave behind the material that forms the lobes (see Begelman et al. 1984 review). The expansion of the lobes does work on the external environment which can heat the gas around it and affect the gas cooling rates; such effects are known as "AGN feedback" processes (e.g., Croton et al. 2006; Bower et al. 2006). These processes in turn transfer energy onto the

intracluster medium (ICM) or intergalactic medium (IGM) (e.g., McNamara and Nulsen 2012), causing the environment around the jets to heat. Hence, it is important to understand the power of AGN mechanism which requires us to focus our attention towards the AGN energetics and the time they spend providing feedback. Furthermore, a constrained plasma age measurement can also give us insights into the dynamics of such powerful radio galaxies.

# 2.1.2 Spectral ageing models

Synchrotron radiation is responsible for the radio emission that is observed in jets and lobes as was first realized in 1956 by examining the polarization and spectrum of the emission (Baade 1956, see Rybicki and Lightman 1979 for details on radiation mechanism). The energy losses for synchrotron radiation producing regions under fixed magnetic field strengths scale directly with frequency, and so they can be expressed in terms of a frequency-dependent volume emissivity (Longair 2010). However to calculate this magnetic field strengths must be known. It is possible to estimate magnetic field strengths by assuming the minimum energy conditions i.e. the field strength that gives the lowest total energy requirement for the system (Burbidge, 1956). The minimum energy conditions are close to the equipartition of energy, where the total particle energy density is equal to the total magnetic energy density (e.g, Longair 2010, Hardcastle and Croston 2020).

We need to observe a range of radio frequencies in order to find the shape of the spectrum (e.g., Alexander and Leahy 1987). As the time scale ( $\tau$ ) of the energy loss for the synchrotron process varies inversely with electron energy ( $\tau \sim 1/E$ ), electrons at higher energies radiate their energy more rapidly as compared to electrons at low energies. This means that an increasingly curved spectrum should be observed over time (e.g., Kardashev 1962, Jaffe and Perola 1973, Harwood et al. 2015).

There are three widely discussed models that assume the generation of single injection electron energy distribution at the jet termination point. The models are named after their originators: Kardashev (1962); Pacholczyk and Roberts (1971) (KP model), Jaffe and Perola (1973) (JP model), and Tribble (1993) (Tribble model). Assuming that the electron population can be described by a power law at the point of acceleration, the electron distribution at acceleration can be given by the normalization factor ( $N_0$ ) and the power law index ( $\delta$ ) of the initially injected electron energy distribution (Pacholczyk and Roberts, 1971);  $N(E) = N_0 E^{-\delta}$ , where N(E) is number of electrons at a given energy. Along the lobes, electrons lose energy through synchrotron losses as they propagate, which allows us to evaluate the age distribution for the AGN

structures (Harwood et al., 2013). For electron energy distribution, defined above, when subjected to synchrotron and inverse-Compton losses, the intensity at given frequency is given by:

$$I(v) = P_c N_0 B \int_0^{\pi/2} \sin^2 \theta d\theta \int_0^{E_T^{-1}} E^{-\delta} \times (1 - E_T E)^{\delta - 2} F(x) dE$$
 (2.1)

where F(x) is the kernel for monoenergetic synchrotron emission and  $P_c$  are constants (Pachol-czyk and Roberts, 1971).  $E_T$  are model losses where the intensity is dependent on the pitch angle  $\theta$ , Energy E, and constant magnetic field B. The injection index  $(\alpha_{inj})$  defines the initial power law spectrum of the electrons where they are accelerated at the hotspots and is related to  $\delta$  by  $\alpha_{inj} = (\delta - 1)/2$ . Here and throughout the chapter we define spectral index  $(\alpha)$  in the sense that flux  $\propto v^{-\alpha}$ . For time t, since acceleration, for an electron under radiative losses, the pitch angle is assumed to be constant for the KP model (Kardashev 1962; Pacholczyk and Roberts 1971), whereas the pitch angle in the JP model is assumed to become isotropic over short time-scales (Jaffe and Perola 1973). The losses and lifetime relation for the KP and the JP model is given by equations 2.2 and 2.3 respectively:

$$E_T \sim B^2(\sin^2\theta)t\tag{2.2}$$

$$E_T \sim B^2 \langle \sin^2 \theta \rangle t \tag{2.3}$$

A third model, the Tribble model (Tribble 1993), evaluates the electron population using the assumption that the magnetic field strength is spatially variable (see Harwood et al. 2013, 2015 for detailed model studies). Harwood et al. (2013, 2015) state that in some circumstances the KP model provides a better description of the observed spectra than the JP model although the JP model is more plausible physically because pitch angle scattering is expected to take place efficiently in realistic magnetic field configurations. Fits using the Tribble model tend to have similar goodness of fit to the KP model while maintaining the physical motivation of the JP model, but its application is computationally expensive.

Observations of the power law index injected by the particle acceleration for hotspots initially showed it to be between 0.5 and 0.6 (Meisenheimer et al. 1989; Carilli et al. 1991) where shock theory limits the value at 0.5 (Bell 1978). Konar and Hardcastle (2013) studied dynamics of Double-Double radio galaxies by measuring the injection index and jet power. They report injection index values between 0.5 to 0.85 and show that the injection index values are strongly dependent on jet power. A broader coverage that includes lower frequencies has shown injection index values between 0.7 and 0.8, suggesting additional acceleration mechanism and/or

absorption processes (Harwood et al. 2013; Mahatma et al. 2020).

Another lifetime estimation method that is used to calculate the ages of the AGN is called dynamical modeling. Such a model uses the radio lobe expansion speeds and the instantaneous source size to determine the dynamical ages (e.g., Machalski et al. 2007; Harwood et al. 2017). Evaluating ages using the two methods, dynamical ageing, and spectral ageing, a discrepancy between the two has been observed (Mahatma et al. 2020). The incorrect use of equipartition magnetic field estimates for the lobes can partly account for the difference in age values for the two methods (Mahatma et al. 2020). Harwood et al. (2016) and Turner et al. (2018) have also suggested electron mixing, the mixing of electron populations over an extended region as a contributing factor. Furthermore, narrow-bandwidth observations (even in sensitive surveys) might not account for the oldest radiating particles which can affect the spectral shape; correction for this requires us to include much more data at low radio frequencies which is often not available. Studies carried out until now (e.g., Harwood et al. 2013, 2015; Mahatma et al. 2020) have pointed out that there are only a limited number of sources available to form a representative sample of RLAGN population for a portion of the sky. In addition there is also a lack of high sensitivity surveys with higher resolution at higher frequencies.

#### 2.1.3 Questions to answer

The aim of the study is to examine the age distribution of the radio galaxy population using spectral age analysis. This requires a large sample of radio sources from sensitive, well-resolved surveys. This study uses a sample systematically extracted from a multi-frequency sky survey, which has not been done before. This study can also be used as an overview of what to expect if we want to perform the spectral age analysis for a larger sample and the different problems that may be encountered (discussed in detail below). In our analysis of the spectral ages, we use data from four surveys at different frequencies, the early science release of the MeerKAT International GHz Tiered Extragalactic Exploration (MIGHTEE) survey of the XMM-LSS field (Heywood et al., 2022), a survey of XMM-LSS with the Low Frequency Array (Hale et al., 2019), a survey of XMM-LSS using the Giant Meter-wave Radio Telescope (GMRT) (Smolčić et al., 2018) and the early science SuperMIGHTEE survey in the XMM-LSS at band 3 (300-500 MHz), also with the GMRT, (Lal, Taylor, et al., submitted). To evaluate the spectral age of the sources, we use the Broadband Radio Astronomy Tools (BRATS<sup>1</sup>) software package (Harwood et al., 2013, 2015). The package evaluates the spectral ages of the radio galaxies on a pixel-by-pixel basis.

Within this chapter we therefore aim to answer the following questions using the spectral age analysis of our sample:

<sup>&</sup>lt;sup>1</sup>http://www.askanastronomer.co.uk/brats/

- i What is the average age, the oldest age and the maximum age distribution observed for resolved sources?
- ii What are the different observable morphologies and how many sources fall into each class?
- iii What is the relationship between the age distribution maps and the source morphology?
- iv What can be a good source selection criterion for a given resolution to perform spectral age analysis?
- v Is there a correlation observed between the source size and the spectral age and what does it say about the dynamics of the radio sources?

Section 2.2 describes the data processing steps applied for the spectral age analysis of the targets. In Section 2.3 and 2.4 we discuss the results obtained from our analysis. The conclusions derived from the analysis are given in Section 2.5. In this study we use a cosmology in which  $H_0 = 70$  km s<sup>-1</sup> Mpc<sup>-1</sup>,  $\Omega_m = 0.3$  and  $\Omega_{\Lambda} = 0.7$ .

# 2.2 Data Reduction and Analysis

#### 2.2.1 Data Extraction and Organization

The MeerKAT International GHz Tiered Extragalactic Exploration (MIGHTEE) (Jarvis et al. 2016) survey is providing radio continuum, spectral line, and polarization information for four (COSMOS, XMM-LSS, ECDFS, and ELAIS-S1) well studied extra-galactic deep fields, using observations with the South African MeerKAT telescope. The MeerKAT is equipped to observe in three bands, namely UHF (544 – 1088 MHz), L-band (856 – 1712 MHz), and S-band (1750 - 3500 MHz), where the dense core region of dishes (three-quarter collecting area) spans over 1 km in diameter and spreads out to provide a maximum baseline of 8 km. The MIGHTEE survey will cover  $\approx 20 \text{ deg}^2$  over the four extragalactic deep fields at a central frequency of  $\approx 1284$ MHz with  $\approx 1000$  h of observations with the L-band receivers. The early science data release provides an area of 3.5 deg<sup>2</sup> in XMM-LSS (a three-pointing mosaic), with the thermal noise of 1.5  $\mu$ Jy/beam (the image is also limited by classical confusion, so the measured noise in the centre of the image is around 4.5  $\mu$ Jy/beam) and a resolution of 8.2 arcsec, where the effective frequency changes across the map. Over 20,000 radio components in the XMM-LSS field were extracted to form a catalog (Heywood et al. 2022 for more information about the MIGHTEE survey and details on data processing steps). The Low Frequency Array (LOFAR) has made observations of the XMM-LSS field at 120-168 MHz. The observations in the field reach a central rms of 280  $\mu$ Jy/beam at 144 MHz and provide a resolution of 7.5×8.5 arcsec (Hale et al. 2019). The GMRT survey is a 610 MHz radio continuum survey covering a 25  $\deg^2$  area in

Telescopes	Frequency (MHz)	Shortest base- line (m)	Longest base- line (m)	Minimum uv distance (λ)	Maximum uv distance (λ)
MeerKAT	1280	20	8000	85	34000
LOFAR	144	320	90000	150	43000
GMRT	610	60	25000	120	51000
GMRT	390	60	25000	80	32000
GMRT	460	60	25000	90	38000

TABLE 2.1: Baseline and uv coverage information for the MeerKAT, the LOFAR and the GMRT telescopes.

the XMM-LSS field and towards the XXL-N field. The rms achieved in the XMM-LSS field is around 200 $\mu$ Jy/beam and the resolution of the mosaic is around 6.5 arcsec (Smolčić et al. 2018). In addition, we use maps from the superMIGHTEE project where the observations target the MIGHTEE XMM-LSS early science region. The region used in this study is covered by a mosaic of 4 pointings at band-3 with a total solid angle of 6.22 deg<sup>2</sup>. The Band-3 radio frequency covers the range 300 to 500 MHz, out of which we use the narrow band data at frequencies 320 MHz, 370 MHz, 420 MHz, and 460 MHz, the resolution of which is 10 arcsec with a flux calibration error of 5% (Lal, Taylor, et al., submitted). LOFAR, the GMRT, and MeerKAT all have shortest baselines that are short enough to sample all of our target sources adequately, also shown in Table 2.1; the three telescopes at our observing frequencies are sensitive to all structure on scales less than  $\sim$  20 arcmin.

Due to MeerKAT's high sensitivity, the data obtained from the survey makes it our obvious choice for mining the radio sources. The MeerKAT data fits well as a reference for sources from other survey frequencies as it is known that spectral curvature is easily observable at GHz frequencies for moderately aged radio sources. Our first task was to look for coordinates of the radio galaxies in the catalogue generated using PYBDSF (Python Blob Detector and Source Finder, Mohan and Rafferty 2015), which contained around 20,000 radio sources, to identify radio galaxies in the image. As the spectral age analysis requires us to look for sources at multiple frequencies, we required sources that are also present in the LOFAR and GMRT surveys. The MIGHTEE survey dataset was searched for extended sources, which we expected to have an elliptical shape due to the elongation of the lobes along the jet axis. Hence all cataloged radio sources which had deconvolved major axis values greater than 10 arcsec in the MIGHTEE survey were identified as potential extended sources. The double lobes of some powerful AGN can be misinterpreted as two different sources and so a visual inspection of the MeerKAT mosaic was conducted to look for any additional sources that could be included in the list of extended sources. We identified 12 sources using visual inspection.

#### 2.2.2 Creation of the sample

A total of 120 extended sources were identified from the catalog and the visual inspection. We next looked for counterparts of MeerKAT sources in the LOFAR and GMRT images. Any point source, or a source that was surrounded by artifacts, in any of the surveys, was removed from the list of extended sources. When the list of extended source coordinates was matched with the LOFAR and the GMRT surveys, using a match radius of 1 arcsec, we found that these comparatively low-sensitivity surveys could not detect the structure that was seen in the highly sensitive MeerKAT images. Hence, any source that did not show the structural features of an extended source in all the surveys was removed from the list, which reduced the sample to 41 radio sources. The position of the sources was listed and FITS cutouts were created, centered at the radio position. For the MeerKAT data, we updated the FITS headers of the cutouts to account for the spatially varying effective frequency, which allows the correct frequency to be used in the spectral age analysis.

We visually inspected these 41 sources and used DS9 (Joye and Mandel, 2003) to find their counterparts in the SDSSr (Sloan Digital Sky Survey), WISE 3.4, and WISE 4.6 (Wide-field Infrared Survey at 3.4  $\mu$ m and 4.6  $\mu$ m). Once we found a counterpart at or around the radio coordinate, we then used NASA/IPAC Extragalactic Database (NED<sup>2</sup>) near position search to look for the counterparts and their recorded redshift. Counterparts that gave spectroscopic redshift information were updated in our sample list; if there was no spectroscopic redshift information present, then we used the photometric redshifts reported by Hatfield et al. (2022). There were some regions absent from the photometric redshift study by Hatfield et al. (2022) which did not report redshift values for some of our sources, such as target 14, and target 22 (see Table 2.2). For such sources, we searched for counterparts in NED to obtain a photometric redshift, described above and added them to the sample list. Hence, apart from the redshifts reported by Hatfield et al. (2022), we additionally obtained redshift values using optical counterparts present in the SDSS, the Cosmic Assembly Near-infrared Deep Extragalactic Legacy Survey-Ultra Deep field (CANDELS-UDS), the Spitzer Wide-area InfraRed Extragalactic Survey (SWIRE) photometric redshift catalog, and the Subaru/XMM-Newton Deep Field (SXDF) survey (Albareti et al. 2017; Galametz et al. 2013; Rowan-Robinson et al. 2008; Simpson et al. 2006). Three sources with optical counterpart but with no available redshift information were excluded from the sample. We finally obtained a sample of 28 targets (see Table 2.2 for target details).

<sup>&</sup>lt;sup>2</sup>https://ned.ipac.caltech.edu/

#### 2.2.3 Data Processing

As the BRATS software package uses a pixel-by-pixel analysis to determine the spectral age which allows us to view spectral features as a function of position, it is important to make sure that the radio maps are aligned accurately in pixel space across all frequencies (Harwood et al. 2013). Using LOFAR's elliptical beam with the circular beam of MeerKAT and GMRT would mean that the radiation received per beam area would be different across frequencies. Hence, the radio maps were smoothed and regridded to give equal beam size for each source using the imsmooth and imregrid commands from Common Astronomy Software Applications (CASA) (McMullin et al., 2007). The resolution obtained after the smoothing and regridding was a circular PSF of FWHM 10 arcsec with a pixel size of 1 arcsec. As a check to see if the smoothing and regridding has worked properly, DS9 was used to verify that the total flux of each source before and after the processing was approximately the same at any given frequency. The typical difference between the total flux values before and after smoothing and regridding was less than 1% for sources at any given frequency. After matching for sky coordinates, to reduce the effects of misalignment we account for frequency-dependent phase shifts and obtain accurate alignment of the radio maps. We used the Gaussian-fitting method which uses a point source around the target to fit a Gaussian at all frequencies and choose an appropriate reference pixel to align the images (refer to Harwood et al. 2013 for a detailed discussion on alignment). As a check for alignment, a Gaussian was again fitted to the same point source in the resulting images and a maximum difference of 0.1 pixels between two maps for any source was set as the threshold to indicate misalignment. No misalignment was observed for the sources.

#### 2.2.4 Parameter Determination

Using BRATS's wide range of spectral age model fitting tools, we can easily determine the on-source properties, evaluate and visualize distributions and run statistical tests on the radio maps. A detailed description of the software package is available in the BRATS cookbook<sup>3</sup>. By using the *load* command in BRATS we loaded the radio maps at each frequency. In order to ensure any background sources were excluded from the model fitting, region files that loosely encompass the target sources were created using DS9. In cases where a bright core was observed (which are not expected to be properly described by models of spectral ageing) an exclusion region was added to ensure that only lobe emission was considered. A background region file was also defined in order to determine the off-source rms thermal noise. Using the rms values, an initial source detection was performed by assuming a  $5\sigma$  cut-off. However, we also wanted to account for the uncertainties arising due to modeling of the extended emission during imaging. As described by Harwood et al. (2013), we assume an on-source noise multiplier of 3. Flux

<sup>&</sup>lt;sup>3</sup>http://www.askanastronomer.co.uk/brats/downloads/bratscookbook.pdf

TABLE 2.2: Properties of the sources in our sample, the radio source name where each name should be prefixed with MGTC to indicate discovery in the MIGHTEE continuum survey (Delhaize et al., 2021), the host galaxy coordinates for the respective radio source, the redshift where P represents photometric redshift and S represents spectroscopic redshift value, the total flux from LOFAR survey, the radio luminosity measured at 144 MHz (LOFAR), the magnetic field strength evaluated using the flux density from the LOFAR survey assuming field at 0.4 times equipartition, source total physical size and the size of the lobes. The total physical size of the radio source was measured using largest extent of the source as seen in the MeerKAT map, given in kpc (column 8) and the size of the two lobes (comma separated) under analysis, measured using MeerKAT maps, is given in arcsec. For sources with single measurement, only one lobe is seen in the MeerKAT maps. The morphology of the sources is given in the superscript of 'Radio source IAU name' column, where FR type-I and type-II are represented as I and II, HT is head-tail source and F is for any unidentified flagged source. The errors on the flux density and radio luminosity are dominated by LOFAR flux calibration uncertainties and so are of order 10%.

Target	MGTC name	Host galaxy (RA, DEC)	Redshift (z)	Total Flux from LOFAR (Jy)	Radio luminosity at 144 MHz (10 <sup>25</sup> W/Hz)	Magnetic Field Strength (×10 <sup>-10</sup> T)	Total source size (kpc)	Lobes size (arcsec)
1	$J021531.81 - 044050.9^{HT}$	02h15m31.25s -04°40′58.9"	0.37 <sup>1</sup> (P)	0.108	4.77	1.55	253	49
2	$J021500.04 - 045346.3^{II} \\$	02h15m00.16s -04°53'47.6"	0.89 <sup>2</sup> (S)	0.845	279	3.98	533	(34, 33)
3	$J021724.39 - 051255.5^{II} \\$	02h17m24.40s -05°12'51.8"	0.92 <sup>3</sup> (S)	0.037	13.30	1.43	1045	(58, 58)
4	$J021953.22 - 051826.9^{II} \\$	02h19m53.02s -05° 18'23.9"	$0.07^{2}(S)$	0.156	0.12	2.84	80	(24, 32)
5	$J021956.07 - 052803.3^{I}$	02h19m56.08s -05°28'08.2"	0.28 <sup>2</sup> (S)	0.179	4.01	1.96	439	(62, 62)
6	$J022050.78 - 051013.4^{I} \\$	02h20m50.62s -05° 10' 18.5"	0.95 <sup>1</sup> (P)	0.032	12.60	2.24	360	(18, 22)
7	$J022334.41 - 045838.5^{II} \\$	02h23m34.30s -04°58'39.5"	$0.17^{2}(S)$	0.063	0.53	1.96	186	(30, 32)
8	$J022349.44 - 041221.6^{II} \\$	02h23m49.47s -04° 12'20.5"	1.74 <sup>1</sup> (P)	0.213	335	5.23	448	(25, 26)
9	$J022325.17 - 042724.3^{II} \\$	02h23m25.30s -04°27'24.4"	0.61 <sup>2</sup> (S)	0.100	14.20	2.83	396	(29, 28)
10	$J022414.01 - 052823.6^{II}$	02h24m13.94s -05°28'19.3"	$0.77^{2}(S)$	0.893	211	3.77	696	(42, 42)
11	$J022511.19 - 045431.7^{II}$	02h25m10.98s -04°54'33.2"	0.23 <sup>2</sup> (S)	0.055	0.82	2.14	206	(26, 22)
12	$J022428.18 - 044952.5^{II}$	02h24m28.00s -04°49'53.3"	0.49 <sup>1</sup> (P)	0.052	4.40	2.29	312	(24, 26)
13	$J021635.17 - 044658.6^{II}$	02h16m35.18s -04°46'58.2"	1.02 <sup>1</sup> (P)	0.090	41.50	3.53	342	(17, 18)
14	$J021827.16 - 045439.2^{I} \\$	02h18m27.16s -04°54'41.6"	0.23 <sup>1</sup> (P)	0.633	9.80	3.10	216	(30, 25)
15	$J021926.45 - 051536.0^{II}$	02h19m26.48s -05°15'34.6"	1.36 <sup>1</sup> (P)	0.019	16.70	3.08	308	(15, 16)
16	$J021943.19 - 043113.3^{II} \\$	02h19m43.26s -04°31'12.8"	0.71 <sup>1</sup> (P)	0.012	2.28	1.80	333	(20, 22)
17	$J022038.83 - 043722.7^{I} \\$	02h20m38.76s -04°37'22.6"	1.19 <sup>1</sup> (P)	0.065	42.60	3.38	311	(19, 19)
18	$J022135.20 - 044855.7^F$	02h21m35.10s -04°48'54.5"	0.80 <sup>1</sup> (P)	0.009	2.26	1.91	311	(15, 17)
19	$J022230.57 - 044706.2^{II}$	02h22m30.43s -04°47'05.2"	1.83 <sup>1</sup> (P)	0.122	217	5.20	346	(20, 20)
20	$J022254.71 - 041358.2^F$	02h22m54.61s -04° 13'59.2"	1.53 <sup>1</sup> (P)	0.047	55.60	3.64	396	(20, 25)
21	$J022256.56 - 042449.9^{II}$	02h22m56.50s -04°24'49.9"	1.18 <sup>1</sup> (P)	0.154	99.60	4.21	319	(14, 21)
22	$J022457.43 - 051656.0^{II} \\$	02h24m57.34s -05°16'55.7"	1.40 <sup>4</sup> (P)	0.199	190	5.00	385	(21, 22)
23	$J022410.08 - 044607.5^{II} \\$	02h24m09.93s -04°46'07.5"	1.45 <sup>1</sup> (P)	0.135	140	5.15	352	(17, 17)
24	$J021600.96 - 043238.5^{II} \\$	02h16m01.01s -04°32'40.8"	0.99 <sup>1</sup> (P)	0.015	6.51	1.11	1171	(56, 75)
25	$J021845.17 - 041438.9^F$	02h18m45.35s -04°14'30.2"	0.79 <sup>1</sup> (P)	0.042	10.70	1.78	831	(39, 54)
26	$J021634.43 - 045507.6^{II} \\$	02h16m34.96s -04°55'06.4"	0.91 <sup>1</sup> (P)	0.033	11.60	1.49	1391	(46, 49)
27	$J021658.68 - 044917.3^{II} \\$	02h16m59.06s -04°49'20.8"	1.32 <sup>5</sup> (S)	0.371	311	3.10	1269	(66, 63)
28	J021944.61 - 044845.9 <sup>I</sup>	02h19m44.64s -04°48'45.1"	0.93 <sup>1</sup> (P)	0.028	10.30	3.03	310	(18, 19)

<sup>1</sup>Hatfield et al. (2022), <sup>2</sup>Albareti et al. (2017), <sup>3</sup>Galametz et al. (2013), <sup>4</sup>Rowan-Robinson et al. (2008), <sup>5</sup>Simpson et al. (2006)

calibration uncertainties were assumed to be 10%; this gives a good match to flux scale uncertainties for the datasets used (Heywood et al., 2022; Hale et al., 2019) and we used consistent flux scale uncertainties for all datasets to avoid bias towards a particular frequency range in the fitting. Using the *setregions* command in BRATS we defined the number of pixels present in the target (see BRATS cookbook for details on the pixel detection techniques, Harwood et al. 2013).

Other parameter dependencies involved the determination of redshifts and magnetic field strength. In order to determine the magnetic field strengths of the radio lobes, we used the PYSYNCH code (Hardcastle et al. 1998), where we defined an elliptical region around the lobes with major and minor axis values and fitted a power law spectrum. With the help of redshifts (see section 2.2.2), lobe flux, and a reference frequency (preferably at low frequency as it is least affected by spectral ageing, we use the LOFAR survey) we were able to determine the fixed magnetic field strengths for the set of target lobes. We also assumed the minimum and maximum Lorentz factor for the particle distribution to be 1 and 100000 respectively. We have assumed no protons and uniform filling factor. The estimated values for the field strengths are calculated at equipartition, although an X-ray study of edge-brightened radio sources (Croston et al. 2005) attempted to evaluate the magnetic field strengths of lobes and the possible lobe particle population, and found that the magnetic field strength lies within 35% of the equipartition value. This estimate was confirmed by Ineson et al. (2017) with a larger representative sample, where they observed the magnetic field strengths to have a median ratio of 0.4 of the equipartition value. Hence we assumed the lobe field strength values to be lower than equipartition by a factor of 0.4. These magnetic field estimates are affected by the statistical uncertainties on the input parameters but also by systematic uncertainties on our input assumptions and so we do not attempt to estimate magnetic field uncertainties or propagate them through our analysis.

We also assumed the value of the injection index as 0.5 for the sources as earlier work eg. Carilli et al. (1991) reported injection index values to be between 0.5 and 0.7. However other works have found steeper injection indices. Harwood et al. (2013) found injection index values greater than 0.8 for two FR type-II sources, 3C 436 and 3C 300. They suggested several reasons for such behavior, such as poor model fit at low frequencies, inclusion of emission from strongly interacting jets, weak shock termination in FR type-II, and single injection particle distribution assumption. Furthermore, studies by Harwood et al. (2015) and Harwood et al. (2017) found similar steeper values of injection index, even when they had included more low-frequency data in their analysis. A recent investigation by Mahatma et al. (2020), a study that attempts to solve the spectral age and dynamical age discrepancy problem by observing two powerful cluster center radio sources using high-resolution JVLA and deep XMM-Newton and Chandra observations, reports the injection index to be around 0.6. In the debate around the true injection index values, it should be noted that the studies conducted until now lack a representative radio source population that can help effectively constrain injection index value using high sensitivity and high resolution radio maps. Until such a population is available, it should be safe to assume a value of 0.5 for the injection index because this is the lowest possible value and has been widely used in the literature until now. The aim of this study is to examine the dispersion in the spectral age distribution of the targets. If the injection index was intrinsically steeper, this would shift the observed age distribution to lower values. The parameter information is summarized in Table 2.2.

#### 2.2.5 Spectral Analysis

We perform the bulk of the spectral age fitting using the JP model due to its physical plausibility, less computational work, and the ability to provide us with the upper limits for the oldest recorded age (Section 2.1.2). However, for a few well resolved sources we also investigate the use of the KP and the Tribble models. For a maximum and minimum age range, flux density values were determined and a  $\chi^2$  test was performed as a check of the goodness-of-fit of the model, given by:

$$\chi^{2} = \sum_{\nu=1}^{N} \left( \frac{S_{i,\nu} - S_{model,\nu}}{\Delta S_{i,\nu}} \right)^{2}$$
 (2.4)

where, at N given frequencies v,  $S_{i,v}$  is the observed flux density in region i,  $S_{model,v}$  is the model flux, and  $\Delta S_{i,v}$  is the total observed region uncertainty that depends on fractional flux calibration error (see Harwood et al. 2013 and the BRATS cookbook for details). The BRATS software package performs a grid search to look for the spectral age that best fits the model. By performing a broad search over a range of defined maximum and minimum ages, we can evaluate a best-fitting age over the grid. For more accurate age evaluation, the software automatically repeats the search for the age interval that produced the best fit in the previous cycle, until the desired accuracy is reached. Hence, under the selected target region we obtain a pixel by pixel age estimate which ultimately provides an age distribution for radio lobes. For our sample, we have calculated the source magnetic field strengths at 0.4 of equipartition (as discussed in section 2.2.4) and have run the BRATS package command *fitjpmodel*, *fitkpmodel*, and *fitjptribble* to perform the JP, the KP and the Tribble model fitting respectively.

# 2.3 Results

The sample consists of 5 FR type-I, 17 FR type-II, one head-tail source, and 5 sources with anomalous structures. For sources where a strong central core was present, the core flux was excluded from the age analysis as it is not described by the models of spectral ageing. The analysis evaluates model values by varying the parameter values for injection index, magnetic field strength, and the age intervals along with their respective redshifts.

Before executing spectral age fitting, as an initial check, we generate the spectral index maps for the targets using the BRATS *specindex* command. We are looking for discrepant spectral index values in order to identify any misalignment, identify regions where there are anomalies or artifacts around the source, and review the data quality before performing any computationally intensive spectral age fitting. The majority of the maps show the flattest spectral index value in the lobes for the locations which are, according to morphology, the hot-spots of the sources, and then the spectral index value steepens along the ejection axis towards the core. This is typical

spectral behavior for FR type-II sources. We can also see that some targets show the flattest spectral index values near the core and continue towards both edges of the lobes gradually increasing the spectral index value. This behavior is typical for FR type-I sources. We expect to see similar patterns for our sample in terms of age distribution, depending on the type of FR morphology we observe and simultaneously confirming our observation about the structure of the source (see Appendix A.1 for further discussion). Looking at the spectral index maps, we do not observe any anomalous data hence the radio maps are aligned properly and the quality of data is good enough to perform spectral analysis.

Using the spectral fitting commands in BRATS, we initially set the age range between 0 and 200 Myr, the magnetic field strength (Table 2.2) and the injection index of 0.5 prior to the execution. We investigated the use of the KP and the Tribble models by fitting both them and the JP model to two large, bright targets (10 and 14) and found (Table 2.4) that the maximum ages returned by the KP and the Tribble model were similar to but slightly larger than JP. Hence, we use the JP model only in what follows. The results of the JP model fitting are summarized in Table 2.3. Figure 2.1-2.7 presents the JP spectral age maps for the selected targets, with contours overlaid from the MeerKAT survey (at 8.2 arcsec) and a cross representing the host galaxy position. We choose to use the MeerKAT survey contours as it is the most sensitive for the given data set. From here on we will refer to sources of the sample by their target numbers, given in Table 2.2. Table 2.3 summarizes the age distribution statistics for the sample with median reduced  $\chi^2$  values. The table clearly shows that for our sample the average age and the median age are approximately the same for a given source, except for a few targets discussed in detail in Section 2.4.4. We also observe that the average minimum age is 2.25 Myr, 18 sources show a 0 Myr minimum age. Target 14 (Fig. 2.4b), that is observed to have a higher minimum age, is responsible for weighting the average minimum age towards a higher value, without it the average minimum age value falls to 0.96 Myr. As a check of the model fit we inspected the median reduced  $\chi^2$  values, as we have independent  $\chi^2$  values for each pixel for each source. We see that the worst fit is observed for target 22 (Fig. 2.6b). The images used for analysis for this source do not show any artifacts, missing structures in individual maps, or bad data quality. However, we also looked at plots of the flux density as a function of frequency together with the fitted models and we see that the scatter in the data points is substantially larger than what we would expect from the error bars. Other objects that have  $\chi^2$  value greater than 2 show similar behavior. We cannot accommodate for this by changing any parameters or assumptions, which means that the ages of these sources have systematic uncertainties that we cannot account for. For more typical sources the fits are generally good and any regions of high  $\chi^2$  are restricted to small regions of the source. The mean average age obtained for the sample is 10.2 Myr with a standard deviation of 17.7 Myr, similarly, the mean maximum age is 23.09 Myr with a standard deviation of 30.35 Myr.

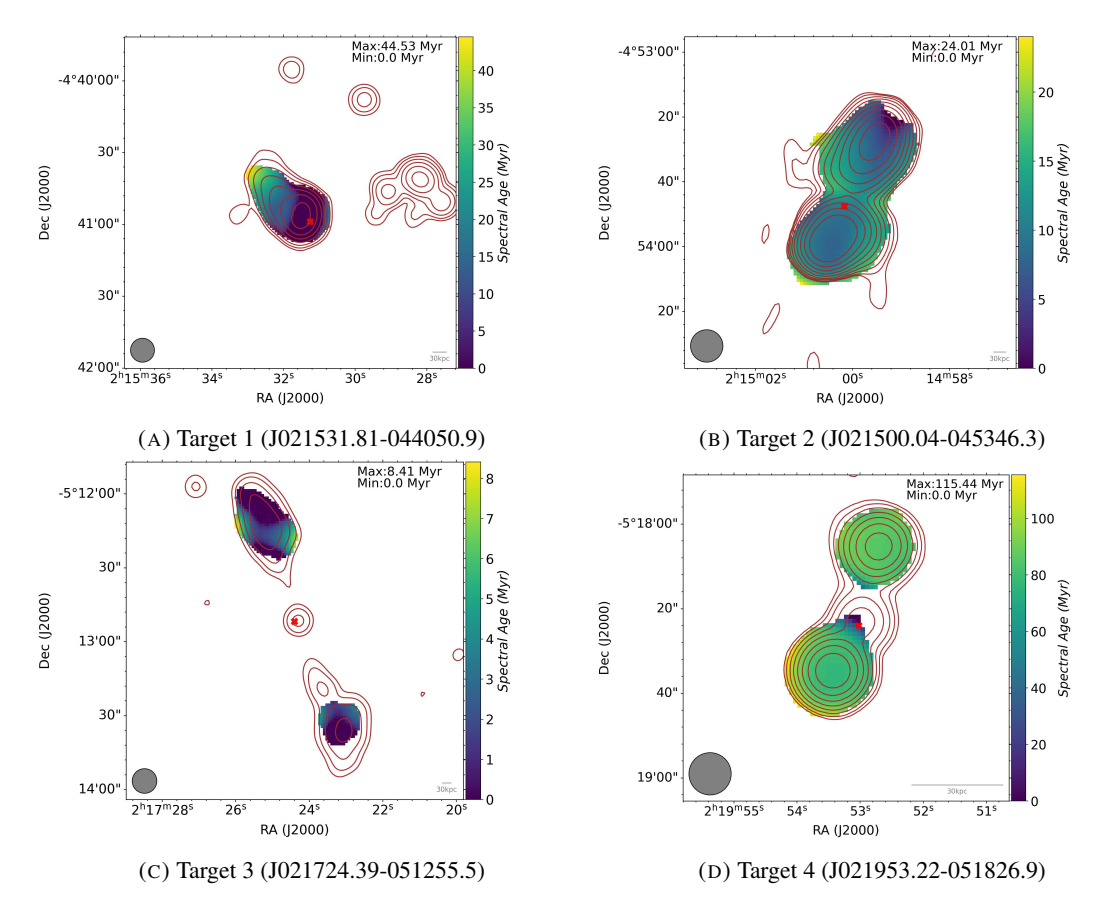


FIGURE 2.1: Spectral age maps of target 1 to target 4 with contours overlaid from the MeerKAT 1.2 GHz survey at 8.2 arcsec resolution and host galaxy position marked with a cross. The grey solid circle represents circular PSF beam of size 10 arcsec.

Tamhane et al. (2015) studied morphology, magnetic field strength, and energetics of a giant radio galaxy (target 27 in our sample, Fig. 2.7c) using radio and X-ray data and found that the age of the AGN was 8 Myr for magnetic field strength of 3.3  $\mu$ G and injection index of 0.5. These estimates are similar to ours (oldest age of 8.6 Myr with an average age of 6.4 Myr); this consistency between their results and ours further supports the analysis used in this chapter.

In the next sections we look at the results for our sample in terms of different source aspects and parameters. We also look at the images presented in Fig. 2.1-2.7, noting any anomalous behavior we observe and their suggested explanation for such abnormalities.

# 2.3.1 Morphology

Figure 2.1a shows the spectral age distribution for target 1 where the morphology in the spectral age map shows an increasing flux gradient towards the northern part of the source and indicates that the source morphology is that of a head-tail source, where the core is moving with respect to its environment and causing the ejected plasma to bend towards the movement axis. Hence we can only measure the size of a single lobe. The map shows a hot-spot near the southern region

TABLE 2.3: Estimates of the age values obtained after performing the analysis using the JP model for our sample. The table columns consists of values for recorded minimum age (Min age), maximum age (Max age), median age, average age, and median  $\chi^2$  reduced.

Target	Min age (Myr)	Max age (Myr)	Median age (Myr)	Average age (Myr)	Median $\chi^2_{red}$
1	$0.00^{+4.96}_{-0.00}$	$44.53^{+0.00}_{-5.77}$	$10.48^{+1.00}_{-0.96}$	$11.64^{+0.43}_{-0.45}$	0.46
2	$0.00^{+3.56}_{-0.00}$	$24.01^{+1.59}_{-1.36}$	$11.10^{+0.28}_{-0.01}$	$11.23^{+0.09}_{-0.10}$	1.49
3	$0.00^{+1.80}_{-0.00}$	$8.41^{+1.75}_{-1.81}$	$1.19_{-0.15}^{+0.14}$	$1.65^{+0.07}_{-0.07}$	0.89
4	$0.00^{+26.08}_{-0.00}$	$115.44_{-7.39}^{+7.62}$	$83.92^{+0.04}_{-0.01}$	$82.57^{+0.50}_{-0.53}$	0.79
5	$0.00^{+8.47}_{-0.00}$	$101.19^{+20.65}_{-12.62}$	$11.28^{+0.10}_{-1.16}$	$20.96^{+0.48}_{-0.47}$	1.43
6	$0.00^{+3.47}_{-0.00}$	$8.71^{+1.12}_{-1.30}$	$0.59^{+0.45}_{-0.44}$	$2.16_{-0.09}^{+0.09}$	1.21
7	$0.00^{+8.62}_{-0.00}$	$46.95^{+10.31}_{-13.02}$	$0.51^{+0.01}_{-0.01}$	$4.60^{+0.28}_{-0.26}$	0.96
8	$1.10^{+0.58}_{-1.10}$	$3.70^{+0.24}_{-0.22}$	$2.49^{+0.01}_{-0.00}$	$2.50^{+0.01}_{-0.01}$	2.08
9	$0.00^{+7.04}_{-0.00}$	$20.49_{-2.39}^{+2.17}$	$10.98^{+0.03}_{-0.46}$	$10.59^{+0.17}_{-0.16}$	0.9
10	$0.00^{+3.22}_{-0.00}$	$24.98^{+0.93}_{-1.28}$	$13.47^{+0.00}_{-0.45}$	$13.24^{+0.08}_{-0.08}$	1.96
11	$0.00^{+19.80}_{-0.00}$	$36.95^{+7.48}_{-9.02}$	$0.48^{+0.01}_{-0.45}$	$3.75^{+0.28}_{-0.27}$	0.91
12	$4.25^{+5.81}_{-4.25}$	$19.26^{+3.37}_{-3.30}$	$12.01^{+0.23}_{-0.02}$	$11.87^{+0.14}_{-0.13}$	0.26
13	$4.49^{+1.03}_{-1.27}$	$8.26^{+1.09}_{-1.07}$	$5.55^{+0.13}_{-0.01}$	$5.73^{+0.03}_{-0.03}$	0.33
14	$36.95^{+5.88}_{-6.29}$	$87.05^{+4.60}_{-3.22}$	$53.05^{+0.90}_{-0.09}$	$55.83^{+0.27}_{-0.27}$	0.92
15	$0.00^{+1.25}_{-0.00}$	$4.09_{-1.03}^{+0.71}$	$2.79^{+0.01}_{-0.00}$	$2.43^{+0.05}_{-0.05}$	1.27
16	$0.00^{+4.22}_{-0.00}$	$7.36_{-3.09}^{+2.24}$	$4.65^{+0.14}_{-0.30}$	$4.16_{-0.13}^{+0.13}$	0.51
17	$3.89^{+0.79}_{-0.90}$	$5.80^{+0.73}_{-0.77}$	$4.39^{+0.01}_{-0.08}$	$4.43^{+0.01}_{-0.01}$	0.53
18	$0.00^{+1.50}_{-0.00}$	$0.20^{+1.96}_{-0.20}$	$0.00^{+0.01}_{-0.00}$	$0.05^{+0.01}_{-0.01}$	1.78
19	$1.80^{+0.26}_{-0.22}$	$2.80^{+0.20}_{-0.20}$	$2.19^{+0.01}_{-0.01}$	$2.17^{+0.01}_{-0.01}$	0.44
20	$0.00^{+0.83}_{-0.00}$	$3.81^{+0.68}_{-0.86}$	$0.05^{+0.00}_{-0.04}$	$0.46^{+0.03}_{-0.03}$	1.05
21	$3.50^{+1.06}_{-1.71}$	$9.89^{+0.54}_{-0.55}$	$6.02^{+0.01}_{-0.09}$	$6.10^{+0.03}_{-0.03}$	1.05
22	$1.40^{+0.90}_{-1.40}$	$8.89^{+0.45}_{-0.46}$	$3.50^{+0.00}_{-0.00}$	$3.74^{+0.04}_{-0.04}$	2.71
23	$2.70^{+0.76}_{-0.95}$	$5.80^{+0.35}_{-0.36}$	$3.49^{+0.01}_{-0.00}$	$3.61^{+0.02}_{-0.02}$	0.55
24	$0.00^{+2.61}_{-0.00}$	$8.01^{+1.08}_{-1.38}$	$3.90^{+0.09}_{-0.01}$	$3.87^{+0.07}_{-0.07}$	0.58
25	$0.00^{+4.89}_{-0.00}$	$17.76^{+4.20}_{-3.54}$	$1.25^{+0.24}_{-0.01}$	$3.24^{+0.11}_{-0.11}$	0.73
26	$0.00^{+3.31}_{-0.00}$	$5.99^{+1.55}_{-2.37}$	$2.09^{+0.14}_{-0.14}$	$1.90^{+0.05}_{-0.04}$	0.50
27	$0.00^{+1.81}_{-0.00}$	$8.59^{+0.81}_{-0.91}$	$6.39^{+0.01}_{-0.17}$	$6.06^{+0.02}_{-0.02}$	0.19
28	$2.99^{+1.63}_{-2.99}$	$7.64^{+1.33}_{-1.60}$	$5.10^{+0.15}_{-0.01}$	$5.08^{+0.05}_{-0.05}$	0.14

TABLE 2.4: Minimum age, maximum age, average age, median age and median $\chi^2_{red}$ value	ues
for JP, Tribble, and KP model comparing two sources.	

Target	Model	Min age (Myr)	Max age (Myr)	Median age (Myr)	Mean age (Myr)	Median $\chi^2_{red}$
10	JP	$0.00^{+3.22}_{-0.00}$	$24.98^{+0.93}_{-1.28}$	$13.47^{+0.00}_{-0.45}$	$13.24^{+0.08}_{-0.08}$	1.96
	Tribble KP	$0.00^{+3.29}_{-0.00}$ $0.00^{+2.92}_{-0.00}$	$27.44^{+2.17}_{-2.36}$ $31.35^{+16.03}_{-5.03}$	$13.97^{+0.00}_{-0.04} \\ 12.08^{+0.02}_{-0.01}$	$13.99_{-0.10}^{+0.10}$ $12.16_{-0.08}^{+0.08}$	1.93 1.91
14	JP	36.95 <sup>+5.88</sup> <sub>-6.29</sub>	87.05 <sup>+4.60</sup> <sub>-3.22</sub>	53.05 <sup>+0.90</sup> <sub>-0.09</sub>	55.83 <sup>+0.27</sup> <sub>-0.27</sub>	0.92
14	Tribble KP	$38.02_{-6.64}^{+6.24}$ $32.98_{-6.05}^{+5.03}$	$96.97^{+5.09}_{-4.63}$ $115.56^{+0.00}_{-19.82}$	$56.05^{+0.90}_{-0.09}$ $48.41^{+1.03}_{-0.06}$	$59.45_{-0.30}^{+0.30}$ $52.14_{-0.32}^{+0.32}$	0.86 0.81

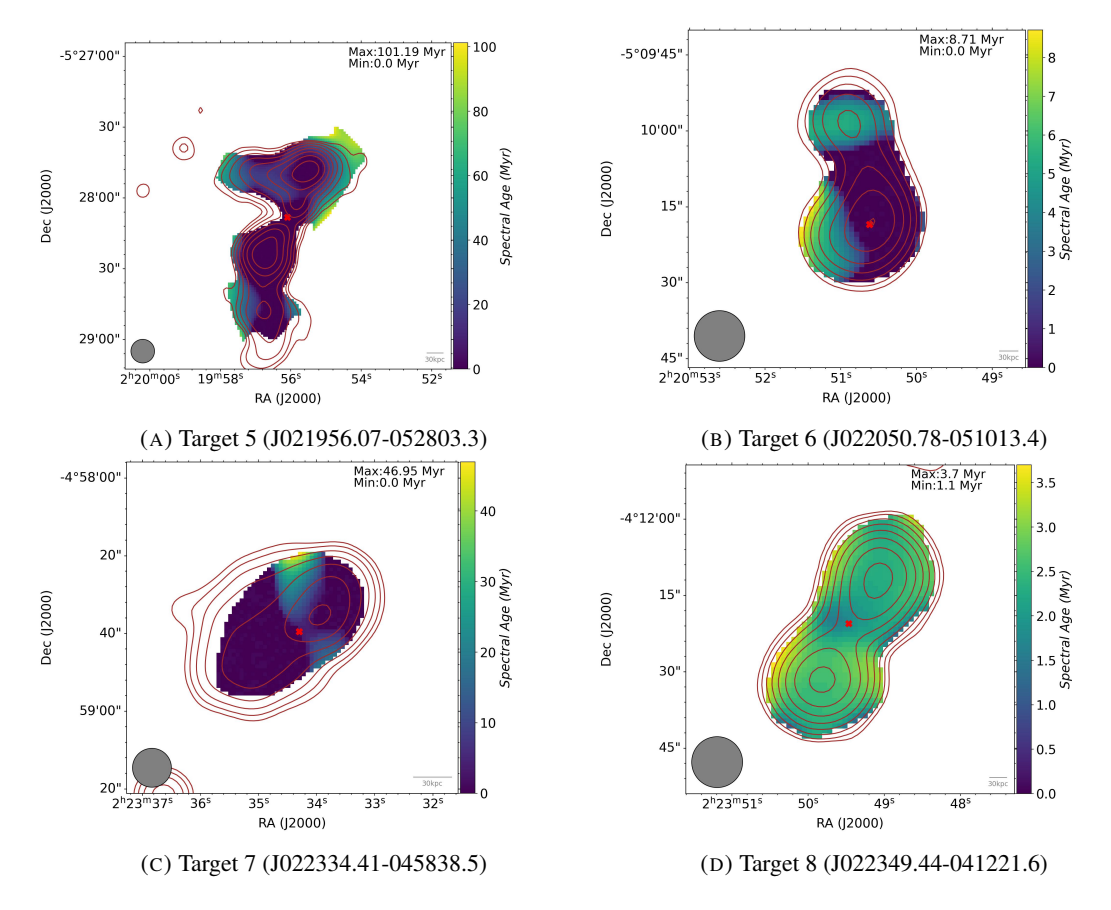


FIGURE 2.2: Spectral age maps of target 5 to target 8 with contours overlaid from the MeerKAT 1.2 GHz survey at 8.2 arcsec resolution and host galaxy position marked with a cross. The grey solid circle represents circular PSF beam of size 10 arcsec.

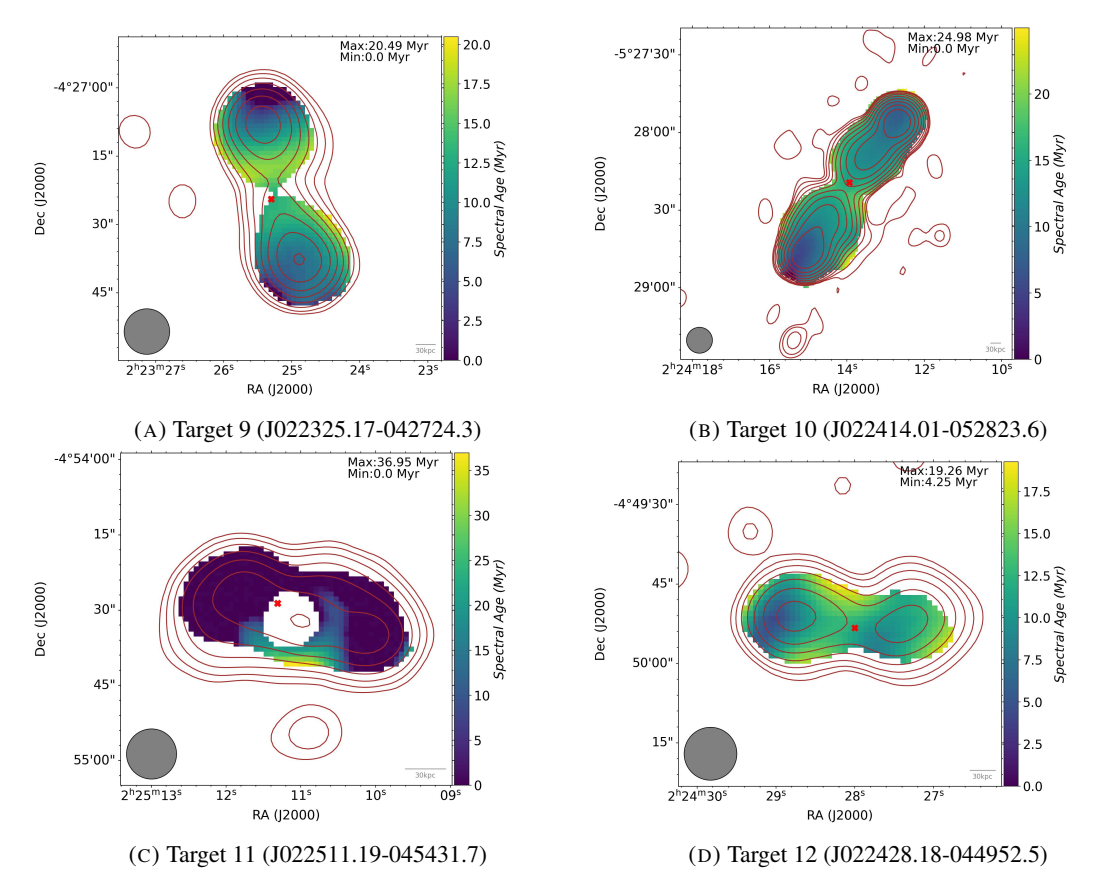


FIGURE 2.3: Spectral age maps of target 9 to target 12 with contours overlaid from the MeerKAT 1.2 GHz survey at 8.2 arcsec resolution and host galaxy position marked with a cross. The grey solid circle represents circular PSF beam of size 10 arcsec.

of the source. This region has an age which is consistent with zero which eventually grows to higher values exhibiting an increase in age of the source lobes towards the northern region. Figure 2.1b shows the spectral age distribution for target 2, where we observe hot-spots near the center of each lobe and the age eventually increases radially outwards and towards the core. This type of morphology is indicative of an FR type-II source. We see that the MeerKAT contours converge near the hot-spots with the host galaxy being near the center of the source where we expect the core to be, further confirming the morphology of the source. Similar morphology and features are observed for target 3 (Fig. 2.1c), 4 (Fig. 2.1d), 7 (Fig. 2.2c), 8 (Fig. 2.2d), 9-12 (Fig. 2.3a, Fig. 2.3b, Fig. 2.3c, Fig. 2.3d), 13 (Fig. 2.4a), 15 (Fig. 2.4c), 16 (Fig. 2.4d), 19 (Fig 2.5c), 21-23 (Fig. 2.6a, Fig. 2.6b, Fig 2.6c), 26 (Fig. 2.7b), and 27 (Fig. 2.7c).

Figure 2.4b shows the spectral age distribution for target 14 which has the lowest age values along the ejection axis. The age morphology indicates that the plasma flows out along the ejection axis with no termination point and then eventually spreads outwards perpendicular to the ejection axis, these are characteristics of FR-type I sources. For target 5 (Fig. 2.2a, see Section 2.3.5), 6 (Fig. 2.2b), 17 (Fig. 2.5a) and 28 (fig. 2.7d) we observe similar morphology and features, hence these sources would also be expected to be FR type I.

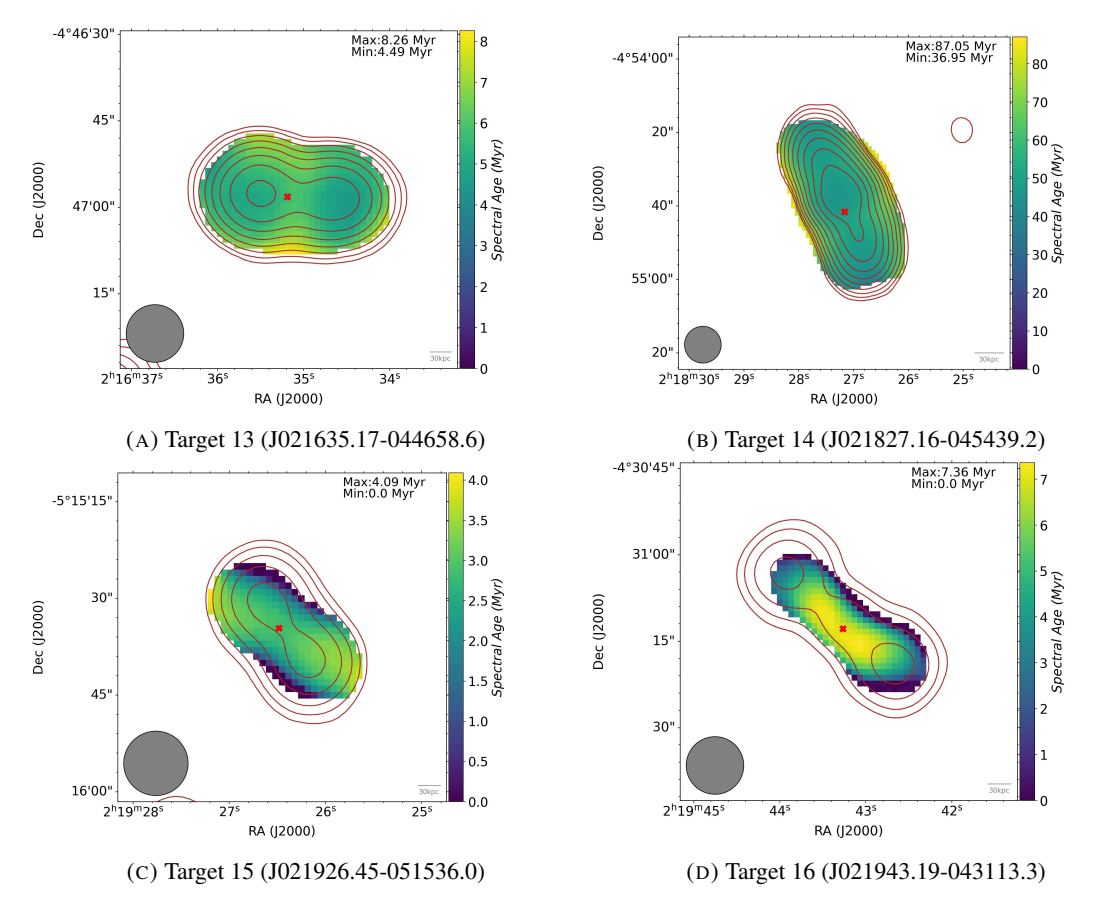


FIGURE 2.4: Spectral age maps of target 13 to target 16 with contours overlaid from the MeerKAT 1.2 GHz survey at 8.2 arcsec resolution and host galaxy position marked with a cross. The grey solid circle represents circular PSF beam of size 10 arcsec.

#### 2.3.2 Resolution and sensitivity

For target 3 (in Fig. 2.1c) we observe ages consistent with zero near the edge of the two lobes which indicate the hot-spot regions for the source. Furthermore, regions around the edge of the southern lobe and the top-right part of the northern lobe are missing in the analysis, as our age estimates are limited by the least resolved and lower sensitivity flux density maps. Although the hot-spots do emerge where the contour converges, clearly seen in the northern lobe. Similarly, for target 11 (Fig. 2.3c), due to the varying quality of the data and lower resolution for the maps, we are missing parts of the source near the boundary of the source and observe some age gradient around the centre. Hence, for some sources, we have lost some parts of the structure due to poorly resolved maps and low-sensitivity surveys.

#### 2.3.3 Beam size and source size

For sources like target 4 (Fig. 2.1d), 8 (Fig. 2.2d), 12 (Fig. 2.3d), 13 (Fig. 2.4a), 19 (Fig. 2.5c), and 21-23 (Fig. 2.6a, Fig. 2.6b, Fig.2.6c) we do not observe any zero value region although we

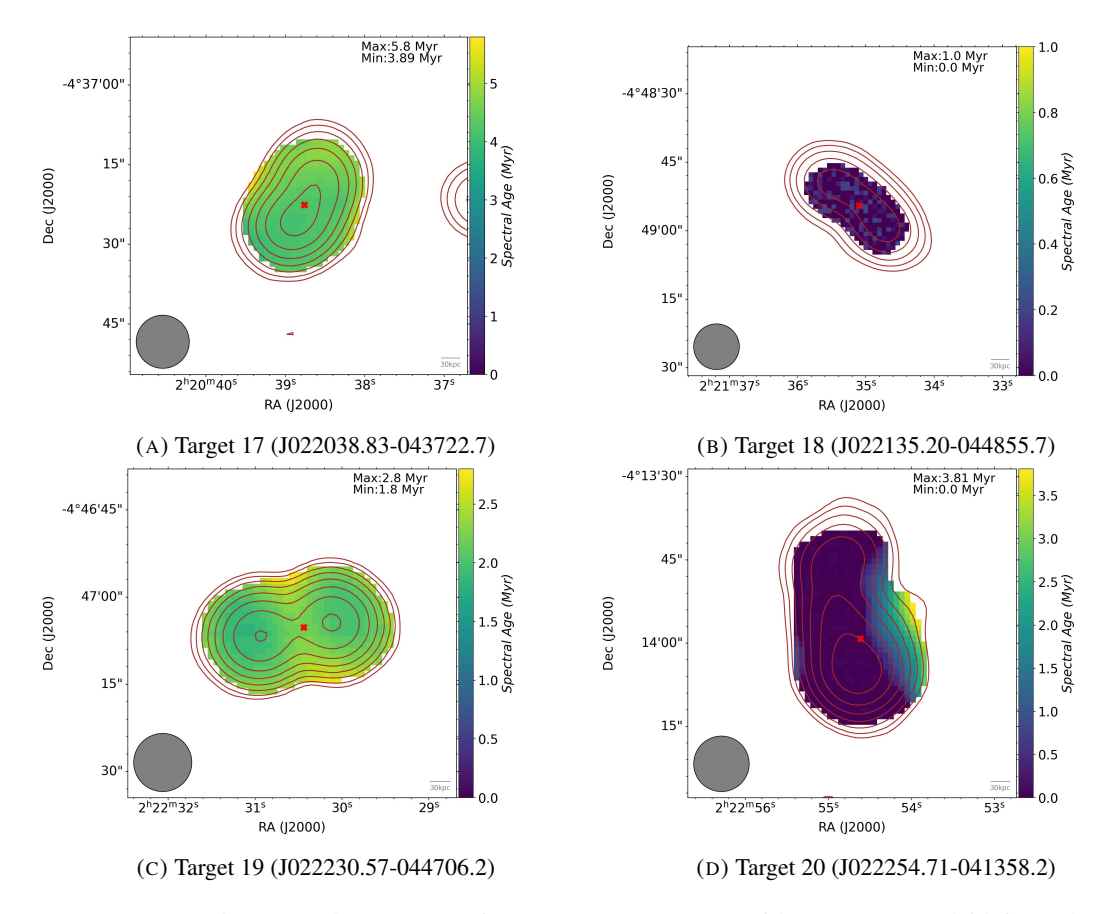


FIGURE 2.5: Spectral age maps of target 17 to target 20 with contours overlaid from the MeerKAT 1.2 GHz survey at 8.2 arcsec resolution and host galaxy position marked with a cross. The grey solid circle represents circular PSF beam of size 10 arcsec.

do see a lowest age region near the centre of the two lobes, also the region where the contours converge and the age eventually increases radially outwards. They also show much flatter age gradients than any other sources. We do not observe a sharp age gradient for the sources that either have a large beam size or a small source size. In other words, the size of the source is small with respect to the larger beam size, which gives us a lower age gradient, hence the lack of detailed age distribution. We can say the same for the FR type-I, target 17 (Fig. 2.5a) and 28 (Fig. 2.7d). For all of these sources it is plausible that the low resolution of our observations, relative to the source size, means that we cannot detect a consistent zero value region that may really be present. Even where low-age regions are detected, poorly resolved sources with beam size comparable to source size produce a less detailed age distribution map and a flatter age gradient.

#### 2.3.4 Source environment

Target 7 (Fig. 2.2c), at first glance, looks like a head-tail source, but if that were the case we would have observed the host galaxy position at the north-west end where the surface brightness

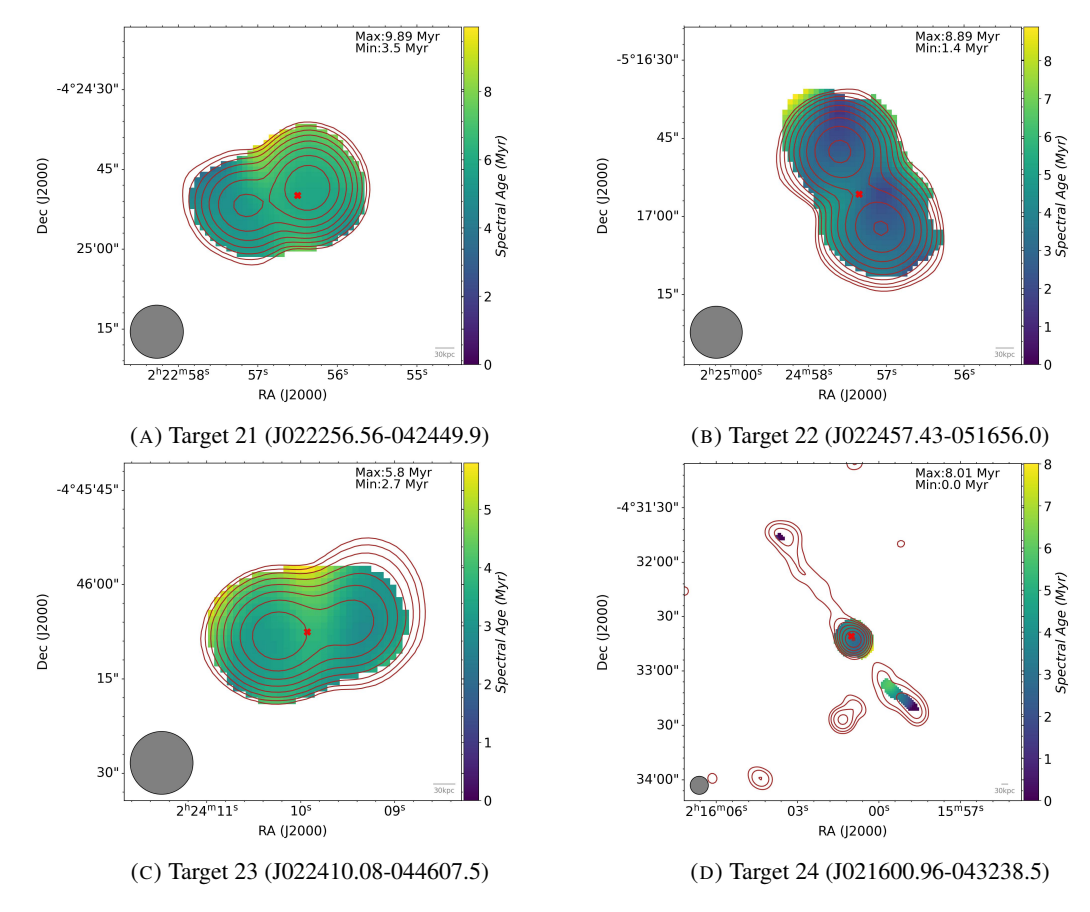


FIGURE 2.6: Spectral age maps of target 21 to target 24 with contours overlaid from the MeerKAT 1.2 GHz survey at 8.2 arcsec resolution and host galaxy position marked with a cross. The grey solid circle represents circular PSF beam of size 10 arcsec.

is highest. In fact the most plausible host galaxy is in the middle of the source. Further investigation reveals that there is another galaxy present near the south-east region, where the values are consistent with zero, which may be responsible for underestimating the age values near the south-east edge.

For target 26 (Fig. 2.7b), the two structures seen at the western and the eastern corner of the map can be classified as the lobes of the source with the core sitting in the middle of the two lobes along the ejection axis. For the two lobes we see that the lowest age regions are near the inner edge of the western lobe and on the outer edge of the eastern lobe, from which the plasma ages gradually and moves into the surrounding. The structure of the two lobes does not look similar to those seen in the previous examples, for which one of the reasons could be the external pressure applied by the surrounding ICM and IGM which restricts the uniform expansion of the plasma. We would have to study the host galaxy and its environment in detail to provide more information.

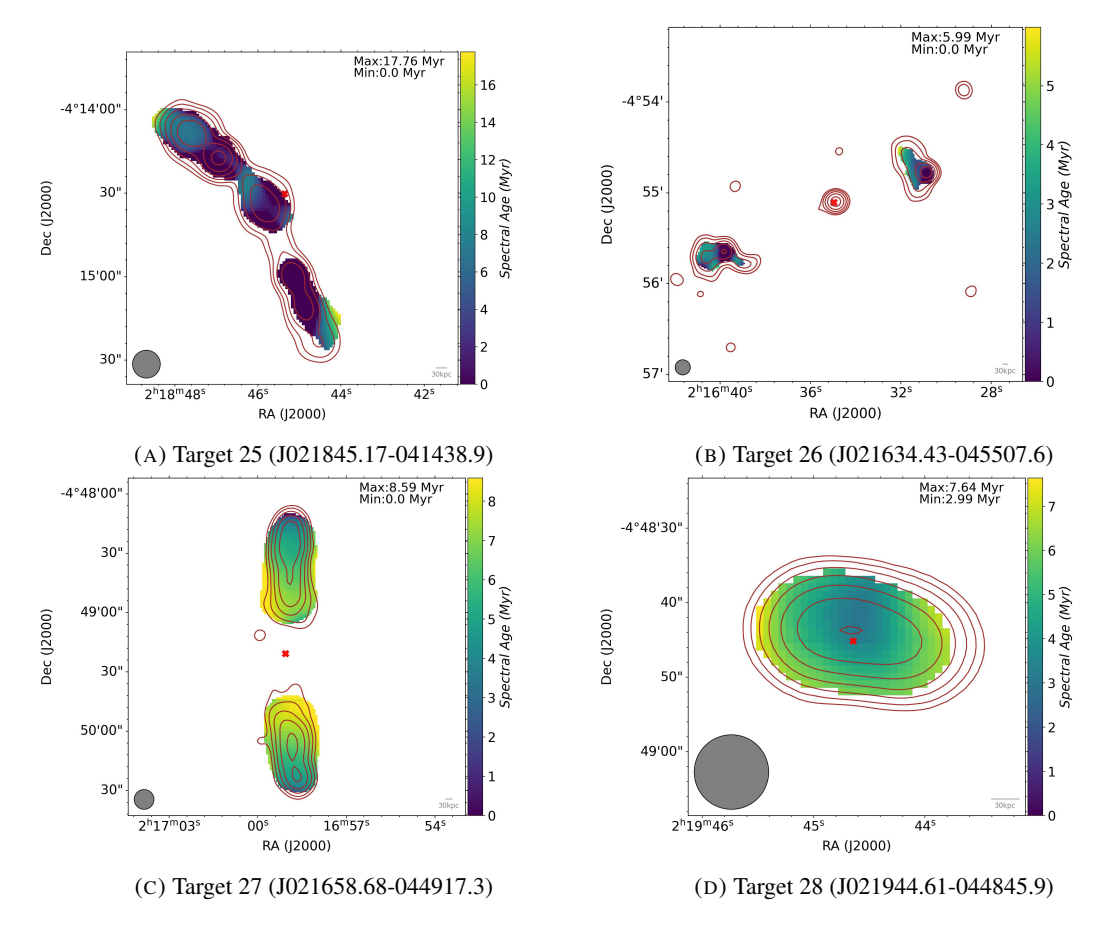


FIGURE 2.7: Spectral age maps of target 25 to target 28 with contours overlaid from the MeerKAT 1.2 GHz survey at 8.2 arcsec resolution and host galaxy position marked with a cross. The grey solid circle represents circular PSF beam of size 10 arcsec.

#### 2.3.5 Anomalous sources

Figure 2.2a shows the spectral age distribution for target 5 from which we obtain age estimates using flux densities from four radio maps. We exclude the radio flux densities from the GMRT survey at 420 MHz, 460 MHz, and 610 MHz as this map has lower signal-to-noise and a lot of artifacts around the source. Excluding the maps for the source allows us to include emission from the entire structure of the lobes and the source. Another noticeable feature of the age map is the giant zero-age region around the center of the lobes. The possible explanation for such a distribution can come from the calibration errors for the maps corresponding to different frequencies or the quality of data obtained during observation. It is difficult for us to point out a specific hot-spot region however, it should lie in the zero-age region. Furthermore, we also notice that the age estimates increase outwards from the zero-age region. The spectral age distribution is consistent with a source with the characteristics of FR-type I. Hence it is safe to say that the source is plausibly an FR type I source.

Figure 2.5b shows the spectral age distribution for target 18 where we observe that the entire source is filled with zero age values, corresponding to a flat spectrum everywhere in the source.

We looked for emission near the source in the sensitive MeerKAT data but did not find any evidence of contaminating sources that could be responsible for such behavior. As we do not see any clear morphology type, it is difficult to categorise the source. High resolution data would be needed to understand the behavior of this source.

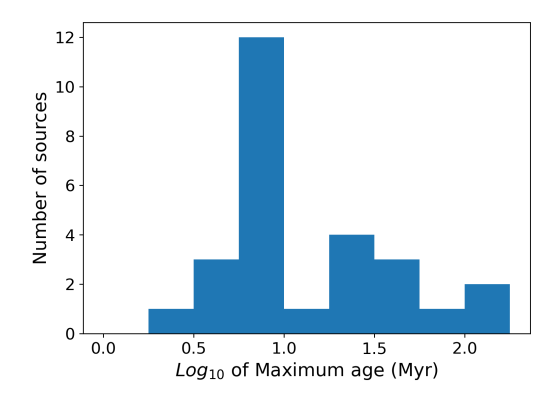
Figure 2.5d shows the spectral age distribution for target 20 which does not show any age distribution with the zero-age region spread across the source. This is not something we expect for any type of morphology and hence points towards problems with the data quality. In order to check the flux maps in our analysis, we excluded maps from the GMRT survey at 610 MHz, 460 MHz, and 420 MHz as the data are of poor quality at these frequencies. We still observe similar behavior in our analysis and thus we can conclude that either the source type is different or the data quality is improper for our analysis.

Figure 2.6d shows the spectral age distribution for target 24 which does not show any prominent structure looking at the age distribution. In the MeerKAT contours, we can see the structure of lobes emerging from the core (marked host galaxy position) with visible jet structure. These are characteristics of an FR type-II. From the age distribution map, we do not clearly see the lobe in the southern region and most of the northern lobe is missing. This is most likely due to the data quality from the maps other than MeerKAT. We see that most of the structure seen in the MeerKAT map is missing in other maps i.e. the GMRT survey and the LOFAR survey. For this reason, we only include maps with the best data quality, hence we exclude the data from the GMRT survey with frequencies at 320 MHz, 420 MHz, and 460 MHz. From the age map, we can see a zero-age region in the southern region and the age gradually increases towards the core which further confirms our classification of the source as FR type-II. For this analysis, we include the core as we also want to look at the age distribution around the core which increases radially outwards around the core.

Figure 2.7a shows the spectral age distribution for target 25 which shows an increasing age gradient around the core. The morphology is characteristic of a wide-angle tail type source where the age gradient grows away from the core. Another possible reason for such an age distribution could be a short time difference between AGN switch off and switch on where plasma injection was cut off. We also know that data quality plays a vital role so data from 144 MHz (LOFAR) and 610 MHz (GMRT) had to be removed. Data from more representative maps should be able to solve the problem and point out the reason for the anomaly.

#### 2.4 Discussion

In this study we have analyzed a total of 28 sources in the XMM-LSS field using the MeerKAT survey at 1.28 GHz, the LOFAR survey at 144 MHz, and the GMRT survey at 320 MHz, 370



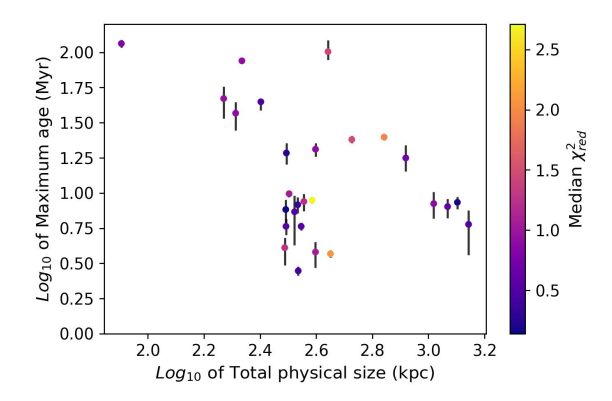


FIGURE 2.8: Left histogram shows maximum age distribution for the sample with bin size of  $10^{0.25}$  Myr, where the x-axis represents logarithmic values of age intervals and y-axis represents the number of sources within the interval. Right plot shows the relationship between the total physical size versus the maximum age of the sources in the sample, color coded by median of  $\chi^2_{red}$ . Target 18 is not included in the plot as the age is not reliable. We note that the errors are uncertainties on the age of the maximum age pixel on the source and as such are just indicative of the uncertainties on the true source maximum age.

MHz, 420 MHz, 460 MHz, and 610 MHz. We used the JP model of spectral aging to evaluate the age distribution over other models as this model is computationally least expensive and corresponds well with the physical description of the AGN activity. We assume the injection index for our sample to be 0.5 and obtain the magnetic field values by assuming that they are 0.4 times the equipartition value. In the next few sections we will first discuss the factors affecting our analysis. We explore the different observations made in section 2.3 and suggest ways in which future observations could be made so as to overcome the limitations of our study.

#### 2.4.1 Resolution limits

The minimum size of a source we use to select our sample is greater than 10 arcsec and we find that for a beam size of 10 arcsec, the sizes of some sources, such as target 15-17 (Fig. 2.4c, Fig. 2.4d, Fig. 2.5a), 19 (Fig. 2.5c), 21 (Fig. 2.6a), 23 (Fig. 2.6c), and 28 (Fig. 2.7d), are too small to give a detailed age distribution. We recommend that the source size should be around 4 times greater (per lobe) than the beam size to get a detailed age distribution, as we see in our sample for the target 1 (Fig. 2.1a), 3 (Fig. 2.1c), 10 (Fig. 2.3b), 26 (Fig. 2.7b), and 27 (Fig. 2.7c). Also, the lobe size needs to be around 1.5 times greater than the beam size to observe a reasonable age gradient, as we see for target 12 (Fig. 2.3d), 13 (Fig. 2.4a), 15 (Fig. 2.4c), 16 (Fig. 2.4d), and 19 (Fig. 2.5c) (see Table 2.2 for lobe sizes). As the resolution is low for these sources, it makes it difficult for us to obtain a detailed age distribution and determine the type of the source, that is, if it is FR type-I or FR type-II. This also means that the resolution of the radio maps plays a significant part in the spectral age analysis where the lowest resolution map

becomes the limiting factor. In order to study such small-sized sources in our sample in greater detail, high-resolution maps at a range of different frequencies are required.

#### 2.4.2 Sensitivity and redshift limits

We find that for targets 5 (Fig. 2.2a), 6 (Fig. 2.2b), 15 (Fig. 2.4c), 16 (Fig. 2.4d), 20 (Fig. 2.5d), 24 (Fig. 2.6d), 25 (Fig. 2.7a) and 27 (Fig. 2.7c) we have to exclude data from one or more frequencies in order to increase the spatial regions under analysis as the excluded maps lack emission detected clearly at other frequencies. This also means that while selecting sources for our analysis, survey sensitivities and image fidelity impose limitations. High-sensitivity surveys help us detect fainter and more extended emission which allows us to determine the radio source category and provide more spatial regions for analysis. Lack of structure and emission in any one of the maps limits the region under analysis making it difficult for us to obtain a detailed age distribution. Missing redshifts (as discussed in Section 2.2.2) can also limit our analysis.

#### 2.4.3 Injection index

In our analysis, we have assumed the injection index to be a constant at 0.5. From previous studies, we know that this is not likely to be true for all of the sources in the sample as each source is affected by different ICM, IGM, and pressure conditions which can affect the particle distribution upon injection. For our analysis we did not account for the changing injection index as more low-frequency data would be required to help constrain the injection index value for each source; we used a constant injection index value of 0.5 as this is the lowest possible value we can observe for any source as predicted by shock theory (Bell, 1978). Increasing the injection index would mean that we would obtain lower age estimates for a given region which could eventually pull regions to zero age. From Table 4.4, we can see that the age values decrease as we increase the injection index values. Two of the targets (target 2 and 27) are FR-type II and target 14 is FR-type I. The maximum ages of these sources reduce by 6-8% every time we increase the injection index value by 0.1. Thus a minimum injection index of 0.5 should produce age values that are oldest for the region under analysis which in turn helps us find the oldest possible age for the source.

#### 2.4.4 What are the age estimates?

For our sample, the highest recorded age is 115 Myr while we do observe the lowest age of 0 Myr for a few pixels in 18 out of 28 sources, especially for hot-spots, which is expected as this is where the particles are accelerated and the spectral index is flattest. The average age for the sample is 10.2 Myr and the mean of maximum ages recorded is 23.09 Myr. Using our

Target	Injection index	Min age (Myr)	Max age (Myr)	Mean age (Myr)	Median age (Myr)	Median $\chi^2_{red}$
		3 56	1 50		10.28	
	0.5	$0.00^{+3.56}_{-0.00}$	$24.01^{+1.59}_{-1.36}$	$11.23^{+0.09}_{-0.10}$	$11.10_{-0.01}^{+0.28}$	1.49
2	0.6	$0.00^{+3.02}_{-0.00}$	$22.51^{+1.52}_{-1.59}$	$8.80^{+0.10}_{-0.10}$	$8.69^{+0.02}_{-0.27}$	1.31
	0.7	$0.00^{+2.53}_{-0.00}$	$20.71^{+1.72}_{-1.49}$	$6.28^{+0.10}_{-0.11}$	$6.00^{+0.29}_{-0.02}$	1.24
	0.8	$0.00^{+2.14}_{-0.00}$	$19.19^{+1.54}_{-1.86}$	$4.02^{+0.11}_{-0.10}$	$3.28^{+0.03}_{-0.29}$	1.37
	0.5	26.05+5.89	97.05+4.60	55 o2+0.27	52.05+0.90	0.02
	0.5	$36.95^{+5.89}_{-6.29}$	$87.05^{+4.60}_{-3.22}$	$55.83^{+0.27}_{-0.27}$	$53.05^{+0.90}_{-0.09}$	0.92
14	0.6	$21.95^{+6.80}_{-8.83}$	$80.05^{+4.50}_{-4.17}$	$45.42^{+0.31}_{-0.31}$	$42.95^{+0.00}_{-0.90}$	0.63
	0.7	$0.00^{+11.23}_{-0.00}$	$72.95^{+3.66}_{-4.74}$	$34.08^{+0.47}_{-0.38}$	$30.96^{+0.07}_{-0.92}$	0.52
	0.8	$0.00^{+10.02}_{-0.00}$	$65.05^{+4.29}_{-4.81}$	$21.65^{+0.44}_{-0.42}$	$17.99^{+0.96}_{-0.04}$	0.47
	0.5	0.00+1.81	0.50+0.81	c oc+0.02	c 20±0.01	0.10
	0.5	$0.00^{+1.81}_{-0.00}$	$8.59^{+0.81}_{-0.91}$	$6.06^{+0.02}_{-0.02}$	$6.39^{+0.01}_{-0.17}$	0.19
27	0.6	$0.00^{+1.32}_{-0.00}$	$8.01^{+1.03}_{-0.82}$	$5.48^{+0.02}_{-0.02}$	$5.79^{+0.00}_{-0.01}$	0.17
	0.7	$0.00^{+1.20}_{-0.00}$	$7.61^{+1.06}_{-0.82}$	$4.89^{+0.03}_{-0.03}$	$5.19^{+0.00}_{-0.01}$	0.15
	0.8	$0.00^{+0.74}_{-0.00}$	$7.19^{+0.98}_{-0.87}$	$4.29^{+0.03}_{-0.03}$	$4.61^{+0.00}_{-0.02}$	0.14

TABLE 2.5: Minimum age, maximum age, average age, median age and median  $\chi^2_{red}$  values for increasing injection index of target 2, 14 and 27.

results from the sample we can construct a histogram of the maximum age from each source and observe the distribution of the oldest age in our sample. The histogram shown in Figure 2.8 (left), provides us with the oldest age estimates giving us information about when the AGN was first switched on. We see that the sample peaks at a maximum age range of around 5 Myr to 9 Myr and the number then falls off with increasing age.

From Table 2.3, we see that the average age and the median age for a given source is usually the same for our sample with exceptions such as target 5 (Fig. 2.2a), 6 (Fig. 2.2b), 7 (Fig. 2.2c), 11 (Fig. 2.3c), 20 (Fig. 2.5d), and 25 (Fig. 2.7a). We observe a very large zero age region for these sources which is responsible for the difference seen in the estimates of the median age and the average age. We are not sure why we observe these large zero-age regions for these sources. Some of the reasons we point out in terms of data are bad data quality, calibration error, and artifacts which are imposing limitations on our analysis and results. Other effects are physical and include low AGN switch-off switch-on time, or source morphology other than classical FR type-I and FR type-II. This means that the difference in the age estimates of the median age and the average age cannot be narrowed down to one specific reason and neither can it be solved by changing parameter values and assumptions; in general, better data will be required.

#### 2.4.5 What can we say about extended emissions?

We can see in Fig. 2.1-2.7 the age distribution maps and the MeerKAT contours overlaid on the age distribution maps which show radio-emitting regions that have not been accounted for in the

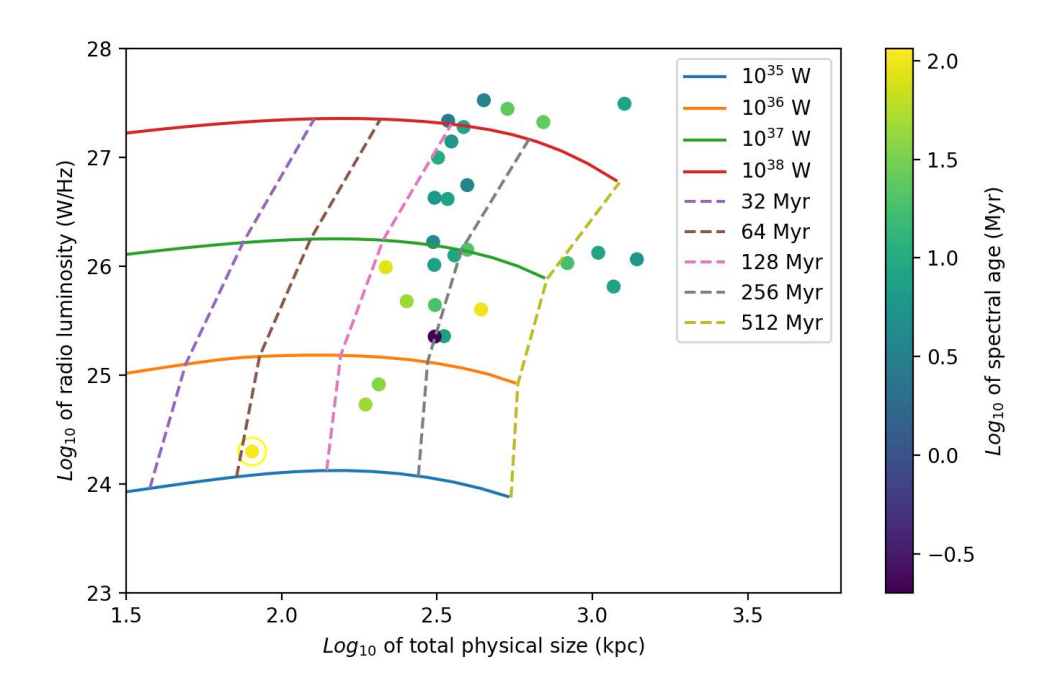


FIGURE 2.9: Radio luminosity versus total physical size relation color coded by maximum age obtained for our sample where, the ring marks the oldest source. The solid lines are model relations between radio luminosity and physical size for given jet powers between 10<sup>35</sup> and 10<sup>38</sup> W, presented by Hardcastle et al. 2019. The dashed lines connect locations of constant dynamical age in these models and so indicate the expected locations of sources with those dynamical ages on the plot. Note that the physical sizes plotted for the sources in our sample are projected sizes since we do not know their orientation with respect to the plane of the sky but this will give rise to only a small offset in their plotted positions.

spectral age fitting. Although we cannot estimate the ages of material in these regions, since we only have detection at single frequency, they may well be older than the material that we can see. We do not see this excess emission as we are limited by the lowest sensitivity map in our data, which is usually the LOFAR or the GMRT image. This means, in reality, the source can be older than what we obtain through our analysis and we may start seeing a larger number of old sources as we start using high-sensitivity maps, particularly at low frequency, in future work.

#### 2.4.6 What is the total size and age correlation?

The scatter plot given in Figure 2.8 (right) shows the relation between the total projected physical size of the sources and their respective evaluated oldest age values. The usual consensus is that the greater the physical size of the source, the higher the age values that should be observed. However, the plot shows if anything, an opposite relation where we see that as the age of the sources increases the total physical size of the source decreases. This could be due to the surface brightness limits for our sample as it can be biased against larger, older sources which are hard to see in all wavelengths. Also due to sensitivity and resolution limits, we cannot determine the

age for small sources, less than 10 arcsec for our sample, which creates another bias. This might be the reason why we see empty regions near the top right and bottom left corners of the plot. Again, more sensitive and high-resolution low-frequency data are needed to increase the sample size and overcome these biases.

#### 2.4.7 What can we say about the spectral age model?

Hardcastle et al. (2019) compared the actual size distribution of the sources to the size distribution obtained using dynamical models by assuming a lifetime distribution. In these models there is a direct relationship between the age of the source and its physical size; large RLAGN sources must have older ages. We used their dynamical modeling (which assumes a group environment with  $M_{500} = 2.5 \times 10^{13} M_{\odot}$ , typical for low redshift radio galaxies) to compare with the age of our sources in the sample (Fig. 2.9) and we can see that there is a discrepancy between the spectral age and the ages obtained by dynamical modeling, where the model lines are taken from Hardcastle et al. (2019). For example, we see that the target 4 (Fig. 2.1d), the oldest source in our sample, in Fig 2.9 lies near the 64 Myr curve which is far from the value of 115 Myr that we estimate using spectral analysis. This kind of discrepancy is also observed for other sources in our sample. In general, we see that the spectral ages that we measure are significantly lower than would be expected from their position on the plot of Fig. 2.9. This disagrees with the inferences drawn by Hardcastle et al. (2019) and indicates that there might be processes that either spectral or dynamical or both types of modeling do not account for, as also concluded by previous studies such as Harwood et al. (2016); Turner et al. (2018); Mahatma et al. (2020), although in our work we have not been able to account for the different environments of our sources, since in general we have no information on the host galaxy environment. This discrepancy potentially has important implications for determining the jet powers for powerful RLAGN which will affect the modeling of feedback.

## 2.4.8 What is the relationship between the age distribution maps and the source morphology?

From the age distribution map, we see that most of the maximum ages evaluated are near the outskirts or near the boundary of the lobes where one can suspect that the maximum age might be overestimated or highly uncertain due to missing data from low resolution and less sensitive maps or bad data quality. On the other hand, almost all of the sources show regions that are only detected in the sensitive MeerKAT data which means that there could be older material that is not included in our analysis. Furthermore, the age distribution map of the sources can also be used to infer the Fanaroff-Riley classification of the source as shown in Appendix A.1.

#### 2.5 Summary and Conclusions

We have used the data from the early science release MIGHTEE survey, the GMRT survey, and the LOFAR survey to evaluate the age of the sources for our sample, where we used the Jaffe-Perola (JP) model (Jaffe and Perola, 1973) to perform spectral age analysis, incorporating data from frequencies of 144 MHz, 320 MHz, 370 MHz, 420 MHz, 460 MHz, 610 MHz, and 1284 MHz. For the first time, we have been able to create and evaluate the age of a relatively large size of 28 sources in a single survey field, due to MeerKAT's high resolution and high sensitivity observations which were used as a reference to find extended sources and perform the spectral age study. We also determined the age distribution of the sources and the distribution of the maximum age for our sample.

Our sample's age distribution maps show sources of various sizes and structures, some of which exhibit peculiar characteristics. Some of this can be a result of the quality of the data. For two sources parts of the structure were missing from the analysis, suggesting limitations arising due to lower resolution and less sensitive flux density maps. Around 10 sources show no zero age regions in the age distribution maps along with some showing a flatter age gradient; these sources are all poorly resolved and so we conclude that the low resolution of our study is preventing us from isolating the regions of current particle acceleration. We had to exclude information from some frequencies as they were of poor quality and restricted us from analyzing emissions from the entire structure of the source. We have observed anomalies for 5 different sources in our sample, most of which correspond to the use of bad quality data or poor detection in one or more images. Hence, we note that our sample is limited by the least resolved maps, the availability of redshifts, the survey sensitivities, and the size of the sources.

We summarize the key findings related to the questions posed in Section 2.1.3, in the order they appear in that section:

- i we see that the oldest source in our sample is observed to be 115 Myr old and the youngest source has an age of 2.8 Myr, the mean of the sample is 23.09 Myr and the median is 8.71 Myr. We observe the maximum age distribution to peak at values between 5 Myr to 9 Myr which correlates well with the median age values for our sample.
- ii Most sources (17 sources) in our sample can be classified as FR-type II but there are 5 sources that can be classified as FR-type I and one source which is classified as a Head-tail source, using the spectral index plots and drawing inferences from the age distribution plots.
- iii As we overlaid the MeerKAT contours over the age distribution maps, we observe excess emission that has not been accounted for in the analysis, which means there is most likely older material beyond our region of analysis and our estimates of the maximum age are very probably giving us lower limits of age for the sources. We suggest use of high sensitivity

low-frequency maps in future analysis which can help estimate much older age values for a given source. We also observe that from a detailed age distribution observation, we can clearly classify the morphology of a source (see Appendix A.1).

- iv We can conclude from this study that the beam size and the source size plays a vital role in giving us a detailed age distribution map along with well constrained age estimates. The size of the source should be at least 4 times bigger than the beam size to observe detailed age distribution or the beam size should be such that we can accommodate a minimum of 4 but preferably more than 5 beams over the entire source.
- v For our sample, we observe no clear relation between the total size of the sources and their age, contrary to what would be expected in dynamical models. We point out the use of small sample, resolution, sensitivity, and surface brightness limits as the factors that may give rise to this observation. Furthermore, we have observed a discrepancy between spectral age and dynamical age analysis where we see that spectral ages are significantly lower than what we would expect for dynamical ages. This can be an indication that there might be processes that either or both the models do not account for but further investigation is necessary as these discrepancies in ages could invalidate analysis used to infer the magnitude of jet power and therefore of AGN feedback.

Overall, the model and the analysis also require us to make assumptions about the parameters of the spectral ageing model (such as the injection index and the magnetic field strength) that depend on the data availability and the data quality. We have pointed out different limiting factors that are affecting the analysis and discussed the possible ways to overcome the limitations. The present study tries to draw its conclusion from a sample of 28 sources, which is larger than the samples used before in any other study and has highlighted some important aspects to consider when attempting such analysis on large samples of radio galaxies in the future. The superMIGHTEE survey in the full XMM-LSS area with the uGMRT (Lal, Taylor, et al., submitted) will provide multi-frequency radio data for a much larger sample, while in the long term the Square Kilometer Array (SKA) is expected to generate very large quantities of radio images that can be used in this way.

### Chapter 3

# Spectral Index, Redshift, and Radio Luminosity Correlation

#### 3.1 Introduction

Radio galaxies and radio-loud quasars are believed to be powered by accretion of matter onto the supermassive black holes located at the centre of the host galaxy. Distant radio sources are among the most massive, luminous and largest objects in the universe (see review by Miley and De Breuck 2008). These distant objects are called high-redshift radio galaxies (HzRGs) and are known for their kpc-scale jets and lobes, clumpy optical morphology (Villar-Martín et al., 2003; Reuland et al., 2003), and high stellar masses (Seymour et al., 2007; De Breuck et al., 2010). The radio emission from these objects is due to the synchrotron process, in which flat spectral indices ( $\alpha \approx -0.5$ ) are associated with newly accelerated particles and steep spectra  $(\alpha \lesssim -1.0)$  imply that there have been strong effects of radiative ageing. Selection on the basis of an ultra steep spectrum (USS) has been used to find almost all HzRG, where USS is defined as  $\alpha \lesssim -1.4$  and we adopt the convention in which flux density  $S_v \propto v^{\alpha}$ ; we will refer to this relation as the spectral index equation. Often found in protocluster environments (Pentericci et al., 2000; Venemans et al., 2007), HzRGs have been a topic of interest since the 1960s, when Minkowski (1960) used the association of bright emission lines and the bright radio source 3C 295, to determine its redshift of z = 0.5. Since then many HzRG sources or candidates have been identified (Rawlings et al., 1996; De Breuck et al., 1998, 1999; Miley and De Breuck, 2008); the most recent HzRG to be discovered on the basis of its steep radio spectrum was found by Saxena et al. (2018) at z = 5.72 with an ultra-steep spectral index value,  $\alpha = -1.4$  between 150 MHz and 1.4 GHz.

Early studies like those of Tielens et al. (1979) and Blumenthal and Miley (1979) first showed that USS sources had smaller angular sizes, implying that they were located farther away, and

also recognized the association of redshift with spectral index. Later, more studies began exploring the underlying causes of this correlation; possibilities included star formation rates, K-correction for steep spectral index, luminosity dependency, galaxy cluster richness, etc. (e.g.; Chambers et al. 1990; Krolik and Chen 1991; Athreya et al. 1998, Klamer et al. 2006; Vernstrom et al. 2018). It was realised early on that one plausible reason for the relationship between spectral index and redshift (hereafter the  $\alpha$ -z relation) was inverse Compton scattering losses, which differentially affect high-z sources due to the higher energy density in cosmic microwave background photons at high z (Krolik and Chen, 1991). Morabito and Harwood (2018) used models including redshift dependent inverse Compton losses to simulate HzRGs and explore the spectral index redshift correlation, and compared their simulated sample to that of De Breuck et al. (2000) who used objects from the 3CR survey (Spinrad et al., 1985) and the Molonglo Reference Catalog (MRC) survey (McCarthy et al., 1996). Morabito and Harwood (2018) found that the  $\alpha$ -z correlation existed in their sample, as also reported by De Breuck et al. (2000), and suggested that the spectral index criterion used to find USS can be relaxed to  $\alpha < -0.9$  or < -0.8. Ker et al. (2012) also confirmed the presence of the  $\alpha$ -z correlation in high-frequency and low-frequency selected samples, although they do point out that the  $\alpha$ -z relation is weak and that the intrinsic scatter on  $\alpha$  is dominant, arguing that 50% of the measured gradient was contributed by K-correction.

However, investigations carried out by e.g. Gopal-Krishna (1988) and Onuora (1989) revealed that a correlation also exists between radio luminosity and spectral index. Onuora (1989) compared different radio luminosity ranges for given redshift bins and observed that with increasing radio luminosity spectral index values become steeper, irrespective of the redshift bin. Similarly, Gopal-Krishna (1988) analyzed two samples at 408 MHz of flux densities above 10 Jy and near 1 Jy. They observed different median redshifts for the two samples but similar luminosities and concluded that a spectral index to redshift correlation might not exist for higher redshifts (z > 1). Furthermore, the study hints at a correlation between the luminosity and the spectral index of the sample, especially for intermediate-strength source sample (1 Jy sample). Blundell et al. (1999), among others, argue that the luminosity-spectral index correlation is fundamental with the  $\alpha$ -z correlation being merely a by-product. Clearly, evidence has for some time pointed to the  $\alpha$ -z correlation taking a secondary role to other correlations with  $\alpha$  such as radio luminosity. Some authors have bypassed the ultra-steep spectrum criterion entirely in selecting high-z radio galaxies (e.g. Jarvis et al., 2009).

The aim of the current study is to explore the spectral index correlation with redshift and radio luminosity at different frequency ranges using high-sensitivity surveys like MeerKAT International GHz Tiered Extragalactic Exploration (MIGHTEE, Jarvis et al. 2016) and superMIGHTEE (Lal, Taylor, et al., submitted), which allow us to probe a much wider range of luminosities than earlier studies. With the inception of new and improved telescopes, we can make use of

high resolution and high sensitivity surveys to study the relation in greater detail. For the analysis we make use of the first MIGHTEE survey data release 1 (Hale et al., 2024). Along with these data, we use the survey carried out by Hale et al. (2019) using the Low Frequency Array survey (LOFAR), the Giant Meter-wave Radio Telescope survey (GMRT, Smolčić et al. 2018) and the early science superMIGHTEE GMRT survey (Lal, Taylor, et al., submitted).

Using these surveys, we can explore the relation between the spectral index, luminosity and the redshift. Within this chapter we therefore aim to answer the following questions using the spectral index analysis at increasing redshift bins for our sample:

- i What is the observed relationship between the spectral index and redshift?
- ii What is the observed relationship between the radio luminosity and spectral index?
- iii What is the observed trend for two-frequency and multi-frequency analysis?
- iv Does sample size affect our observations from the two analyses?
- v What can we infer from the comparison of previous studies to our study?
- vi What are the physical processes that create the spectral index redshift correlation and the radio luminosity spectral index correlation?

Section 3.2 describes the data processing steps to get the sample of sources used for our study. In Section 3.3 we discuss the results obtained from our analysis. The conclusions derived from the analysis are given in Section 3.4. In this study we use a cosmology in which  $H_0 = 70$  km s<sup>-1</sup> Mpc<sup>-1</sup>,  $\Omega_m = 0.3$  and  $\Omega_{\Lambda} = 0.7$ .

#### 3.2 Data reduction and analysis

#### 3.2.1 Data description

MIGHTEE (Jarvis et al., 2016) is providing radio continuum, spectral line, and polarization information for four well-studied extragalactic deep fields: the Cosmological Evolution Survey (COSMOS), *XMM-Newton* Large-Scale Structure (XMM-LSS), Extended Chandra Deep Field-South Survey (ECDFS), and European Large-Area Infrared Space Observatory Survey (ELAIS) S1 fields, using observations with the South African MeerKAT telescope (see Jonas 2009; Jonas and MeerKAT Team 2016). MeerKAT is equipped to observe in three bands, namely UHF (544 – 1088 MHz), L-band (856 – 1712 MHz), and S-band (1750 – 3500 MHz). The dense core region of dishes (three-quarters of the collecting area) spans over 1 km in diameter while the rest spreads out to provide a maximum baseline of 8km. The MIGHTEE L-band survey

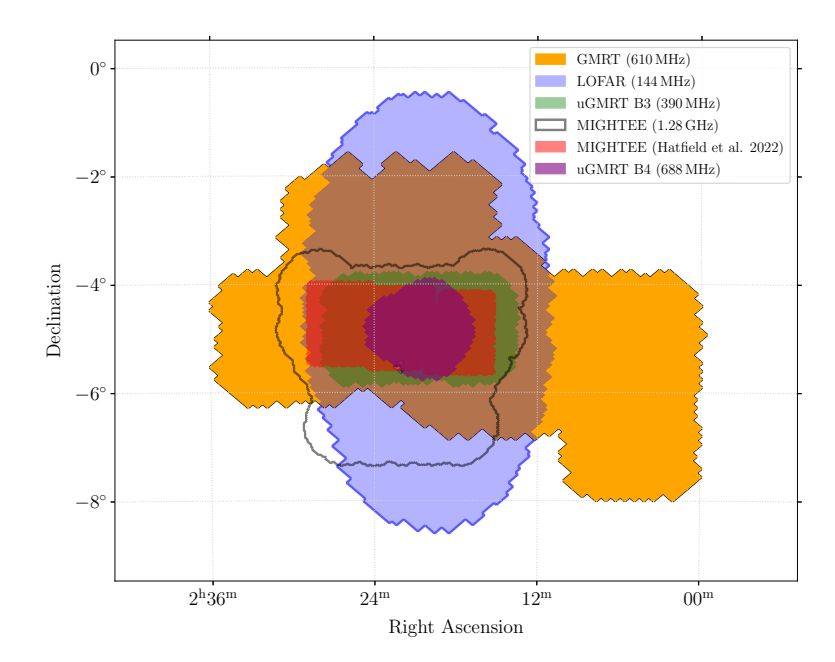


FIGURE 3.1: Plot showing the positions of the data from different surveys (see text for details) which will be used in the sample. Note that most of the positions for MIGHTEE are for sources that are matched to the photometric redshift catalogue, and so are limited to the sky coverage of the optical survey (Hatfield et al., 2022). All MIGHTEE positions including those with a spectroscopic catalogue match are within the grey line denoting the MIGHTEE survey coverage.

will cover  $\sim 20~\text{deg}^2$  over the four extragalactic deep fields at a central frequency of  $\sim 1284~\text{MHz}$  with  $\sim 1000~\text{h}$  of observations with the L-band receivers. The MIGHTEE data release 1 detects around 70,000 radio sources present in the XMM-LSS field in the form of a catalogue made from images at a resolution of 5 arcsec (see Hale et al. 2024 and Heywood et al. 2022 for more information about the MIGHTEE survey and details of the data processing steps). The MIGHTEE images at this resolution have a central median rms sensitivity of 3.6  $\mu$ Jy beam $^{-1}$ .

We combine the MIGHTEE data with other observations of the field. LOFAR has made a survey of the XMM-LSS field using the High-Band Array (HBA) at 120-168 MHz which covers almost the entire area currently observed by MIGHTEE, but at significantly lower sensitivity for a typical radio spectral index of  $\sim -0.7$ . The observations in the field reach a central rms of 280  $\mu$ Jy beam<sup>-1</sup> at 144 MHz and provide a resolution of  $7.5 \times 8.5$  arcsec (Hale et al. 2019). The XMM-LSS was also observed with the GMRT, Smolčić et al. (2018), in a 610-MHz radio continuum survey covering a 25 deg<sup>2</sup> area in the XMM-LSS field and towards the XXL-N field. The rms noise level achieved in the XMM-LSS field is between 40  $\mu$ Jy beam<sup>-1</sup> and 200  $\mu$ Jy beam<sup>-1</sup> and the resolution of the mosaic is around 6.5 arcsec. In addition, we use DR1 maps from the superMIGHTEE GMRT survey (Lal, Taylor, et al., submitted), where the observations target the MIGHTEE XMM-LSS early science region (Heywood et al., 2022). The region used in this study is covered by a mosaic of 4 pointings at GMRT band 3 and 5 pointings at band 4 with a total solid angle of 6.22 deg<sup>2</sup> and 2.16 deg<sup>2</sup>, with rms sensitivities of 16  $\mu$ Jy beam<sup>-1</sup> and 8  $\mu$ Jy beam<sup>-1</sup> respectively. The band-3 radio frequency covers the range 300 to 500 MHz

and band-4 covers 550-900 MHz, out of which we use broad-band data centred at 390 MHz for band-3 and at 688 MHz for band-4. The resolution of both is 10 arcsec (Lal, Taylor, et al., submitted). Fig. 3.1 shows a plot of source positions for the five surveys that will be used in this study, indicating their different sky coverages.

#### 3.2.2 Data extraction

Due to MIGHTEE's high sensitivity, the data obtained from the survey makes it our obvious choice for selecting the radio sources. An advantage of this is that we have the capacity to detect steep-spectrum sources since the MIGHTEE data are much more sensitive than those at the other bands used here. We restrict our analysis to MIGHTEE sources with catalogued deconvolved major axes less than 10 arcsec, which makes it likely that we will be able to obtain a good optical counterpart by simple positional cross-matching. We selected radio sources in the XMM-LSS field that had redshift information. We used the photometric redshift information in the XMM-LSS, reported by Hatfield et al. (2022) and spectroscopic redshift information reported by Vaccari (2015, 2022), to find redshifts of the sources by cross-matching the photometric and spectroscopic catalogues with the MIGHTEE survey by setting the match radius within 2 arcsec, as the positional accuracy for MIGHTEE sources is expected to be better than this; we verified that the distribution of observed offsets deviates from a Rayleigh distribution for larger offsets than 2 arcsec. The cross-match of MIGHTEE with the two redshift catalogues produced a unified MIGHTEE parent sample. We obtain around 1,870 sources that have spectroscopic redshift values available and for the rest we use the photometric redshifts. The cross-match after the union gives 35,478 sources after filtering sources that do not have any redshift information available. For larger sources, visual inspection would be needed to obtain optical counterparts (Pinjarkar et al., 2023). This is approximately 50% less than the number of sources in the DR1 MIGHTEE survey, as we are limited by the area of coverage of the photometric redshift information given by Hatfield et al. (2022) and, in addition, some radio sources do not have an optical counterpart in either redshift catalogue. There are 34,961 sources from the MIGHTEE DR1 survey within the Hatfield et al. (2022) area coverage, of which 96.8% have an optical counterpart with a redshift estimate: we are therefore not significantly biased by the missing objects (as also seen for the COSMOS field by Whittam et al. 2024). Our selection of compact radio sources allows us to capture the total flux density of a source in the absence of a catalogue that associates components of extended sources. Most high redshift sources are expected to be compact (Blundell and Rawlings, 1999), so this limitation should not cause a strong bias in our analysis. We return to the question of the effect of extended sources below, in Section 3.3.1. We note that for the faintest sources we may be affected by source blending, in which a catalogued radio source is composed of emission from two unrelated physical objects.

Survey	Frequency (MHz)	Area (deg <sup>2</sup> )	No. of Sources	RMS Depth (µJy/beam)	No. crossmatch
MIGHTEE	1280	14.4	69,059	3.6	35,478
LOFAR	140	27	3,200	280	602
GMRT	610	25	6,570	200	764
uGMRT-B3	390	6.22	6,226	16	3,219
uGMRT-B4	688	2.16	7,243	8	4,851

TABLE 3.1: Survey information used to obtain the sample for the spectral index, redshift, and luminosity analysis. The area column gives the area covered by the survey, next is the number of sources in the catalogue for each survey, where the MIGHTEE crossmatch number is the number of sources obtained after cross-matching with the redshift information as described in the text and for the other surveys the number of crossmatches is the total number of sources obtained for each survey after matching them with the optically crossmatched MIGHTEE data. For MIGHTEE we quote the central frequency, but use the effective frequency for each source in our analysis.

We cross-matched the radio co-ordinates of our sample with optical counterparts and redshifts to the radio co-ordinates of sources in the LOFAR survey, the GMRT survey and the super-MIGHTEE uGMRT band-3 and band-4 survey using a cross-match radius of 2 arcsec to ensure consistency with the radio-optical cross-match carried out previously. The number of sources with crossmatches at each frequency is given in Table 3.1. The number of sources reported by the LOFAR and GMRT surveys is lower than the other surveys as they are less sensitive. Only a source with at least one detection at one of the other surveys in addition to MIGHTEE will be considered further in this work. We note that as we are selecting only compact sources in MIGHTEE, and the resolution of all the surveys used are within a factor 2 of each other, we should be seeing the same emission at each frequency.

#### 3.2.3 Parameters and analysis

To find the relationship between the spectral index and redshift for our sample we use the spectral index equation for two given flux densities at two different frequencies. The other variable that we investigate for our sample is the radio luminosity of the sources, computed using the formula

$$L_{V_{ref}} = 4\pi S_{V_{obs}} \left(\frac{V_{ref}}{V_{obs}}\right)^{\alpha} D_L^2 (1+z)^{-1-\alpha}$$
(3.1)

where,  $v_{ref}$  is a reference frequency for emission which we take to be 1300 MHz and  $v_{obs}$  is the effective frequency which varies across the image due to the shape of the primary beam and which we take from the MIGHTEE effective frequency map (Hale et al., 2024).  $L_{v_{ref}}$  is the radio luminosity at 1300 MHz,  $S_{v_{obs}}$  is the total flux density at a given effective frequency and  $D_L$  is the luminosity distance. We use the flux densities from MIGHTEE and from the other surveys to evaluate  $\alpha$ , using the broadest frequency range available for each source, and so calculate the radio luminosities for our sample; this means that our luminosity calculations are not completely homogeneous but they do make use of the best information that we have

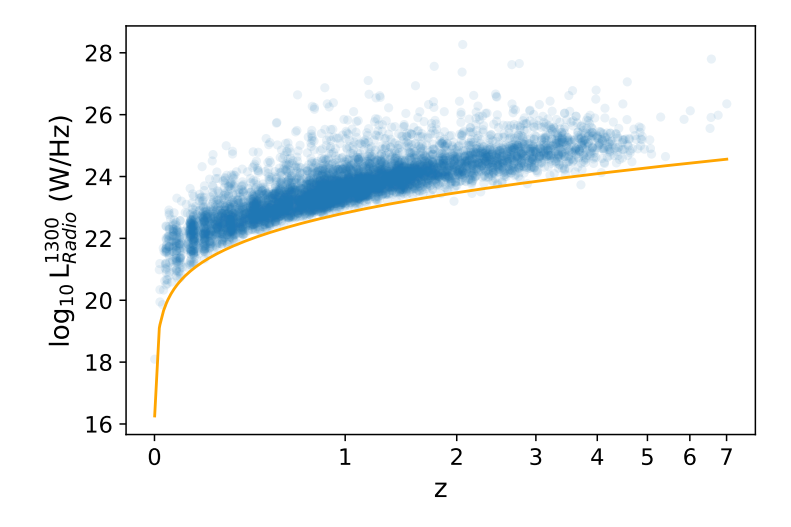


FIGURE 3.2: Luminosity versus redshift plot for optically identified MIGHTEE sources with a counterpart at at least one other frequency. The orange line shows the lower limit on luminosity as a function of redshift given the sensitivity of the survey (assuming a  $5\sigma$  limit of  $18~\mu$ Jy). Note that the objects with  $z\gtrsim 6$  are likely photometric redshift outliers (Hatfield et al., 2022) and we do not consider them in further analysis.

available for each source. Fig. 3.2 shows the 1300 MHz luminosity of the sample sources as a function of redshift. We can see that the luminosity increases with increasing redshift, as expected, but the scatter in luminosity is large at all redshifts. Thus in this sample the low flux limit allows us to investigate luminosity and redshift dependencies of observed quantities.

For our parent MIGHTEE sample the redshift values lie between 0 and 7 (see Fig. 3.3, left panel) and more than half of the sources lie within the redshift range of 0-1. The distribution shown in Fig. 3.3 (left panel) is obtained for each frequency where the MIGHTEE sources have the highest number of sources as compared to the number of sources with matches in other surveys. In addition, Fig. 3.3 (right panel), shows the flux density distribution for the different frequencies, where we can see that the distribution progressively shifts to higher fluxes as we move to lower frequencies. This is the expected behaviour for the dataset, as the sensitivities of the surveys increase with increasing frequency and hence is a good sanity check before we begin the analysis. As various combinations of the LOFAR, the GMRT and the MIGHTEE surveys of the field discussed above will be used further we will refer to the sample with crossmatches in at least one other frequency range as GLaMS (GMRT, LOFAR and MIGHTEE samples).

It is important to note that our GLaMS sample will contain star-forming galaxies as well as AGN, as we do not have any information that allows us to separate the two classes. At these frequencies both classes of object are dominated by synchrotron radiation and will show qualitatively similar radio spectral indices in many cases. However, above a 1.3 GHz luminosity of  $\sim 10^{23}$  W Hz<sup>-1</sup> we expect AGN to dominate the population (Mauch and Sadler, 2007; Whittam et al., 2022, 2024) and above  $10^{24}$  W Hz<sup>-1</sup> there will be essentially no star-forming galaxies (Tadhunter, 2016). Rather than applying a low-luminosity cutoff, in plots involving luminosity we indicate

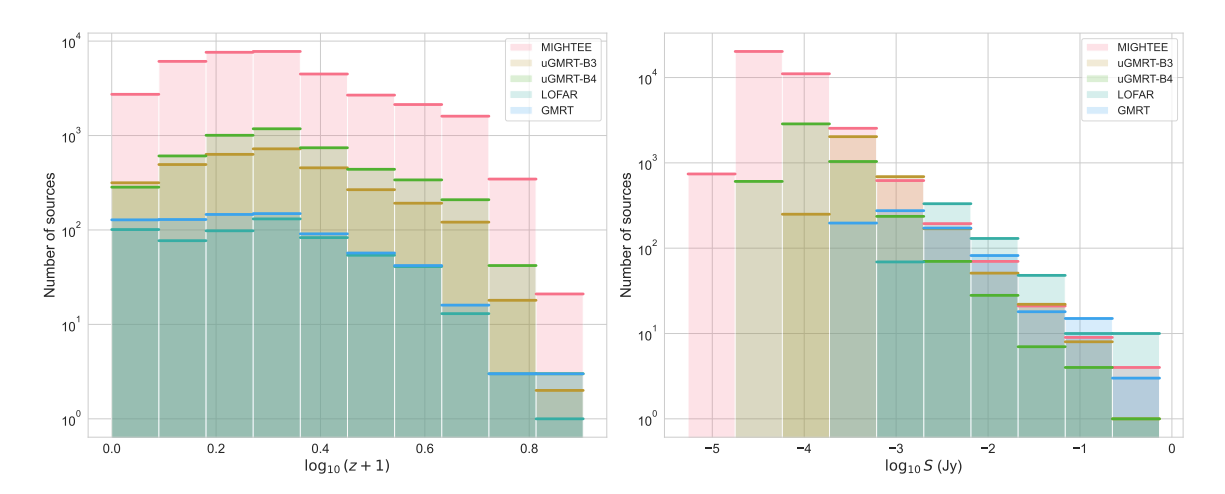


FIGURE 3.3: Redshift and flux density distribution (left and right plots respectively) for MIGHTEE survey, LOFAR survey, GMRT survey, uGMRT-B3 survey, and uGMRT-B4 survey.

the position of  $L_{1300} = 10^{23} \text{ W Hz}^{-1}$  so that the reader can be aware of the point below which star-forming galaxies are likely to dominate.

In Fig. 3.4, we show flux density versus spectral index plots where we create a grid that consists of all possible flux densities and spectral indices that can be observed by the MIGHTEE survey. For these points in the grid we evaluate the area under the plot where other frequencies can observe sources observed in the MIGHTEE survey. The solid line in the plot shows the boundary of the undetectable region for the respective survey for the given rms noise of the survey. The plots are overlaid with the sources that are observed in the GLaMS sample where we can see, as expected, that all of the sources lie in the detectable region with the exception of some sources from the GMRT survey. We note that for the GMRT survey the rms noise over the survey area varies from 40  $\mu$ Jy beam<sup>-1</sup> to up to 200  $\mu$ Jy beam<sup>-1</sup> and as we have used  $5\sigma$  as the detection limit with  $\sigma$  being measured in the centre of the GMRT fields for simplicity, some sources are expected to lie in the non-detectable region of the plot due to better sensitivity than we assume. We can see from the plots that we expect to be biased against inverted spectrum sources but we are not biased against steep spectrum sources; moreover, we can see that few observed sources have spectral indices close to the limits imposed by the sensitivity of the survey. This means that we can observe sources that are steep spectrum and faint for the surveys used in this study without worrying about the selection bias; we will argue later that the bias against inverted-spectrum sources does not affect our conclusions. Our only remaining bias is that we only consider relatively compact MIGHTEE sources: thus some extended sources, which might be preferentially steep-spectrum, are excluded from our analysis (Laing and Peacock, 1980). Consideration of these sources requires full optical identification for extended MIGHTEE sources, which is in progress but not available at the time of writing of this chapter. However, there is a relatively small number of these sources in the survey (Pinjarkar et al., 2023).

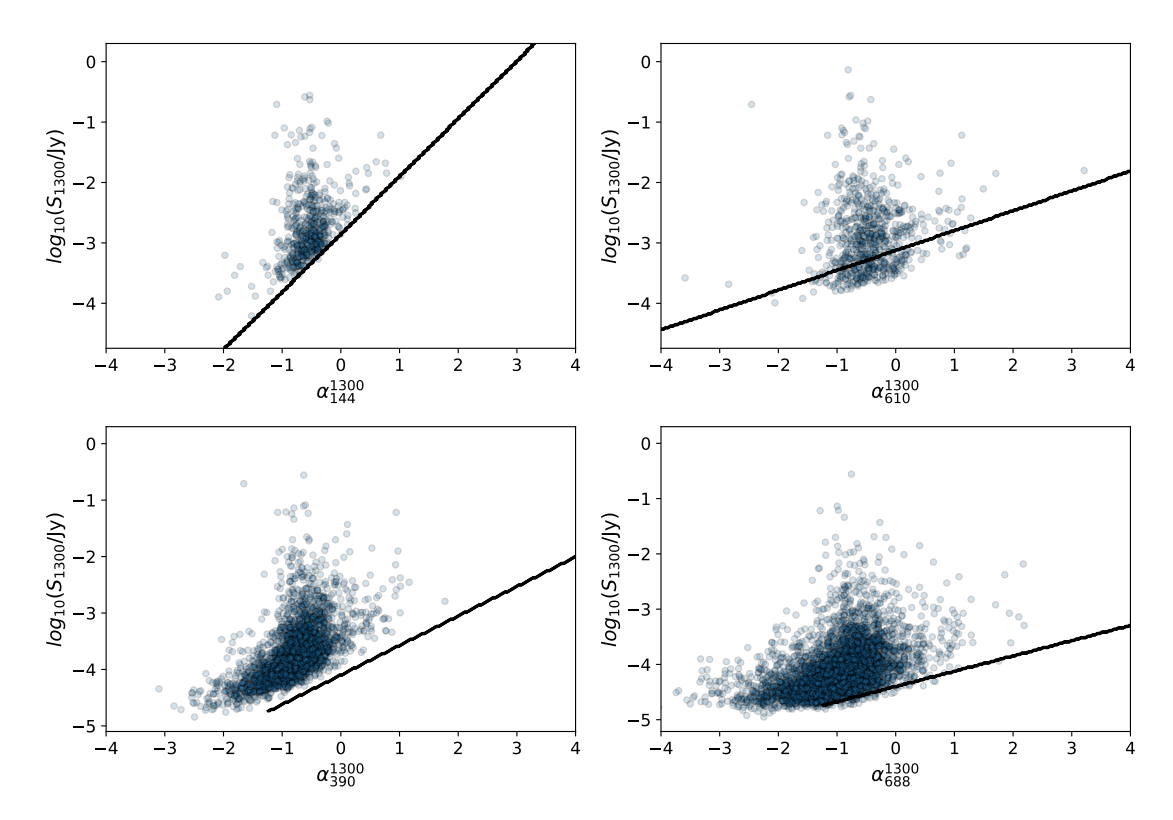


FIGURE 3.4: Plots showing the observed distribution of MIGHTEE flux density and spectral index, and the line separating observable from unobservable parts of this parameter space, for each of the other surveys used. The top left panel shows LOFAR, the top right the GMRT survey, and the bottom panels show the two SuperMIGHTEE bands, 3 and 4 to left and right respectively. The black line is the part of the plot below which sources are excluded by the sensitivity of the corresponding survey. The sources from the GLaMS sample are plotted for their respective frequencies. It can be seen that a broad range of spectral indices can be measured, other than for the faintest sources, and that our principal bias is against inverted-spectrum sources of which there are not many in the parent population (as can be seen from the higher-flux regions of these plots in which the bias is not present).

Our approach in the remainder of the chapter is to consider all of the data without trying to impose any further selection. This has the advantage that we can extract the maximum information from sensitive surveys like the B4 and B3 superMIGHTEE data. Trends seen across many different combinations of frequencies can be considered robust even when the samples considered are not identical.

#### 3.2.4 Data from legacy radio surveys

Legacy radio surveys with much higher flux limits than provided by MIGHTEE were the source of the original discovery of the  $\alpha$ -z relation and so it is important to compare our results with a consistent analysis of objects from those surveys. We use data from the revised Third Cambridge Catalogue of Radio Sources (3CRR; Laing et al. 1983) and a subsample of bright sources from the Molonglo Reference Catalog identified with galaxies and quasars (Kapahi et al., 1998b,a) to compare with the results obtained from our sample.

The 3CRR¹ catalog consists of radio sources along with their redshifts, observed by the 3C and Fourth Cambridge Survey (4C) at 178 MHz, along with spectral index, calculated between 178 MHz and 750 MHz. The catalogue contains 173 sources. We use NASA Extragalactic Database (NED) to search sources obtained from the 3CRR catalogue. We extract flux densities at 365 MHz by using the Texas survey (Douglas et al., 1996), as the observed frequency for the survey falls in the frequency range we use to get our sample. There are 96 sources in the 3CRR sample with flux densities for frequencies 178 MHz, 365 MHz, and 750 MHz. Similarly, we use the above sample to select sources with flux densities at 1.4 GHz by using the sample obtained by Pauliny-Toth et al. (1966), as this frequency is close to the MIGHTEE survey frequency used in our sample². This leaves us with 90 sources in the sample where the source photometric information is available for frequencies at 178 MHz, 365 MHz, 750 MHz, and 1400 MHz. These frequencies are similar to what we use to get our MIGHTEE sample and can be used further to evaluate spectral index and radio luminosities that can be compared with our sample calculations.

Kapahi et al. (1998b,a) defined a bright subsample of the Molonglo Reference Catalog (MRC) consisting of 557 sources of which 446 are radio galaxies and 111 are radio quasars. A full multi-frequency data compilation for these sources is not available. We therefore obtained photometric data for these sources from NED using the 'data products' section given in NASA's ADS website. These data consist of the source names, their redshifts and their respective flux densities at different frequencies. We use these frequencies to obtain the spectral index values for different frequency ranges. This analysis of the 3CRR and MRC sources means that we have the information required to compare the results from our sample and those used by previous studies in a consistent way with frequencies that are matched to those available in GLaMS. The number of MRC sources available depends on the combination of frequencies used but is at most 355.

#### 3.3 Results and Discussion

#### 3.3.1 Two-frequency analysis

In this section we show and discuss the various combinations of two point analysis at different frequencies and frequency ranges. We show the overall distribution of the spectral index for the GLaMS sample for pairs of frequency ranges in Fig. 3.5. In Fig. 3.6, we present spectral index versus redshift for the different values of spectral index obtained by using various combinations

https://3crr.extragalactic.info/field\_info.html

<sup>&</sup>lt;sup>2</sup>We use these observations in preference to those from more modern interferometric surveys as they are readily accessible without additional data analysis and are not affected by issues such as missing short spacings or limited surface brightness sensitivity.

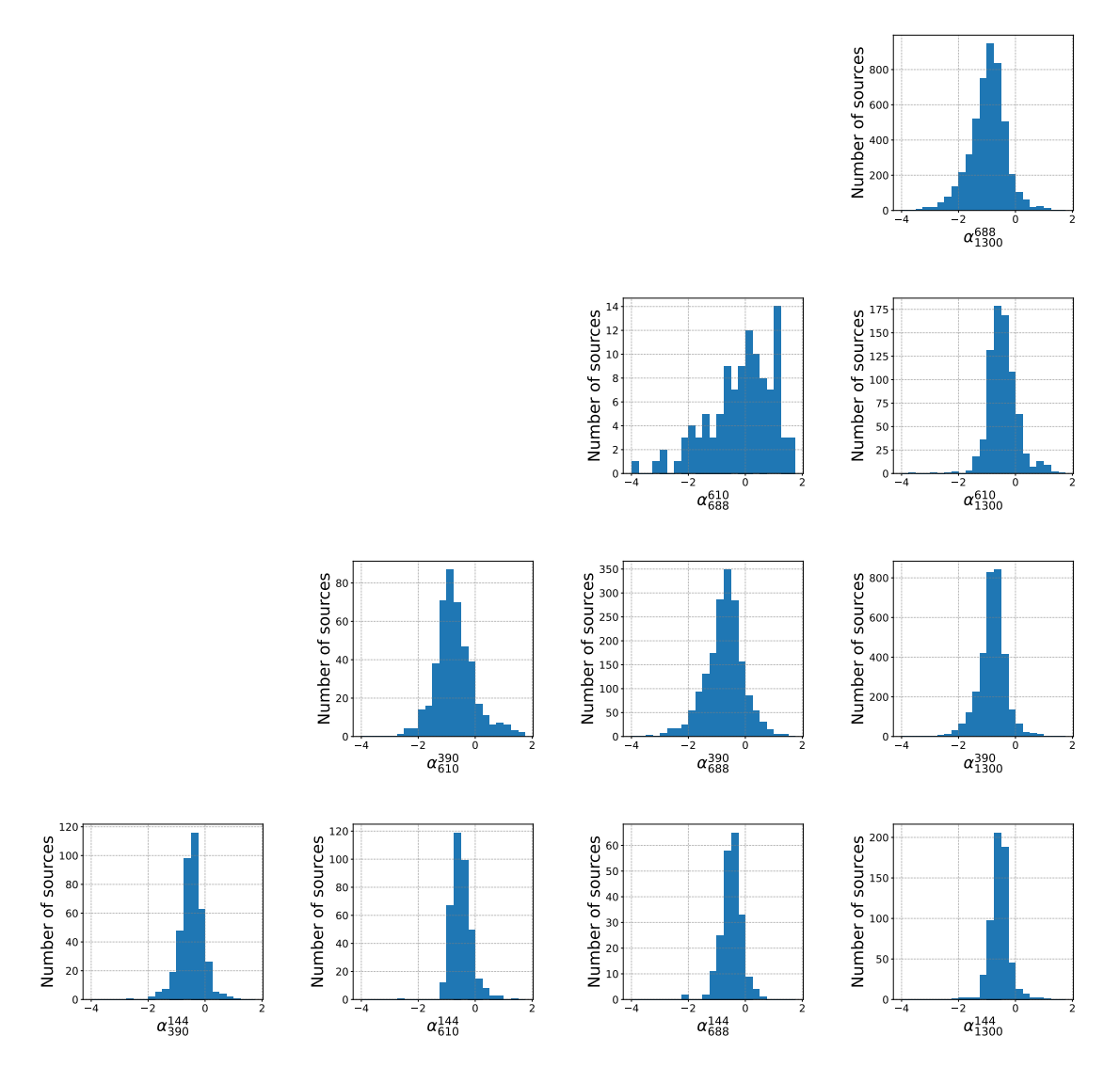


FIGURE 3.5: The distribution of the spectral index for each detected source where the spectral index is calculated for flux densities measured at 144 MHz (LOFAR), 390 MHz (uGMRT band-3), 610 MHz (GMRT), 688 MHz (uGMRT band-4), and 1.3 GHz (MIGHTEE).

of frequencies, while the number of sources in the GLaMS sample are given in Table 3.2. The errors on the spectral index are obtained using error propagation of flux density errors for each source in the sample. We bin all the detected sources for a given frequency pair in redshift and evaluate the mean spectral index values, where uncertainties are calculated using the standard error on the mean. In Table 3.2, we also report the Spearman rank correlation along with their *p*-values for each frequency pair. These correlation values are obtained by using the mean binned values.

We compare results for various frequency ranges, which include both results for the smallest frequency difference such as GMRT 610-MHz to uGMRT band-4 at 688 MHz, and results from the largest frequency difference, i.e. LOFAR 144 MHz to MIGHTEE 1300 MHz. We repeat the same analysis for the sample obtained from the 3CRR survey and the MRC survey to present a comparison with the data from previous studies. The plots in Fig. 3.6 show the mean of the

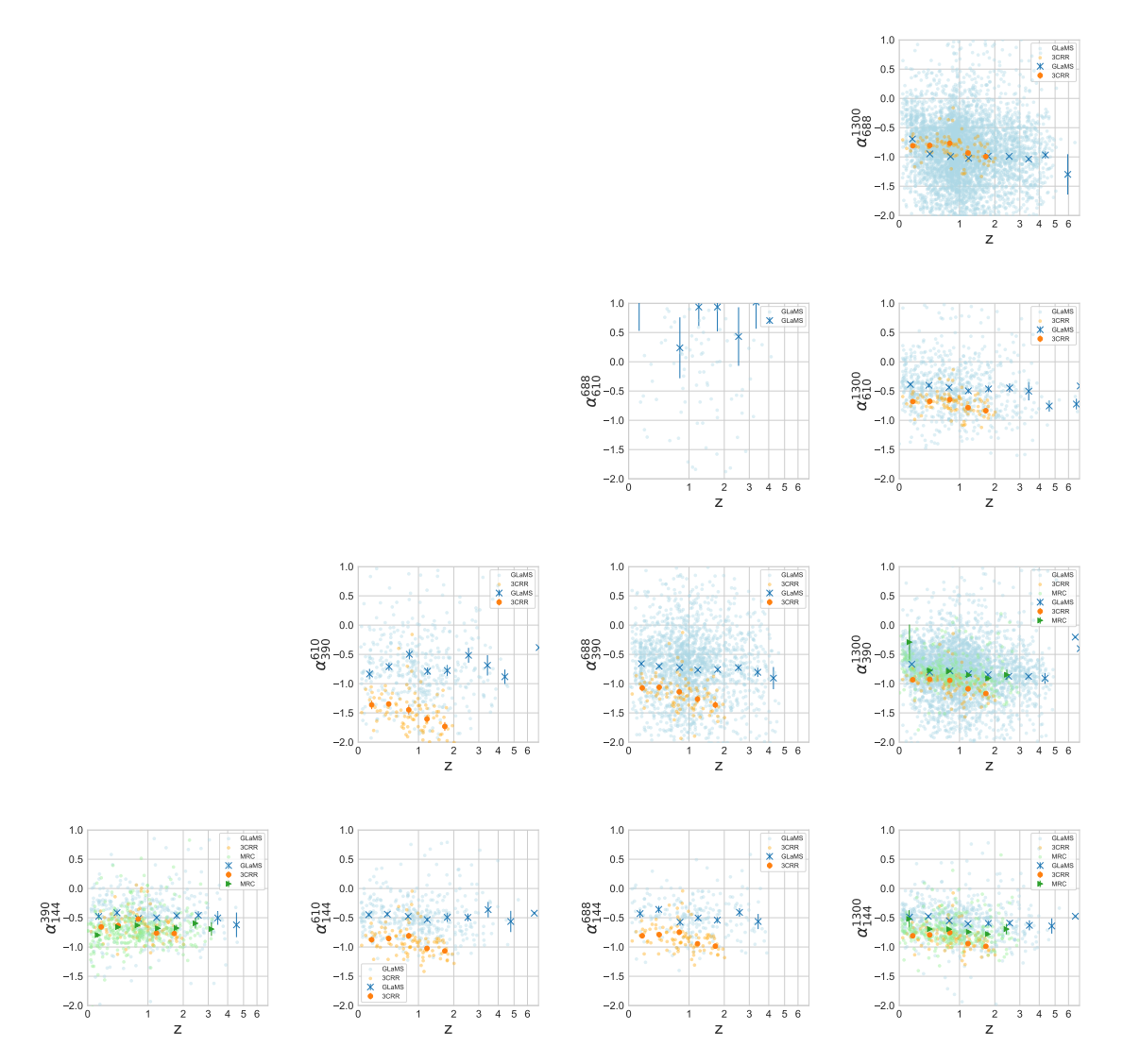


FIGURE 3.6: The correlation of the average spectral index with the redshift of the sources where the spectral index is calculated for flux densities measured at 144 MHz (LOFAR), 390 MHz (uGMRT band-3), 610 MHz (GMRT), 688 MHz (uGMRT band-4), and 1.3 GHz (MIGHTEE). Individual data points are also plotted without errors in order to indicate the spread of the data. The MRC sample is not present for some plots as the sample size for these frequencies is very low. Error bars indicate the  $1\sigma$  error on the weighted mean.

spectral index as a function of redshift. Frequency range pairs such as uGMRT-B4 - MIGHTEE, uGMRT-B3 - MIGHTEE, and uGMRT-B3 - B4 have the highest number of sources as the frequency ranges are from the sensitive uGMRT and MIGHTEE survey whereas pairs such as LOFAR - uGMRT-B3 and LOFAR - GMRT both contain data from the less sensitive LOFAR survey. In all of the plots of Fig. 3.6 we can see that the spectral index values for GLaMS are comparatively flatter than the spectral index values observed for the 3CRR survey and the MRC spectral index values lie in between the two, especially for the frequency ranges with 200 or more objects. We also observe an offset between the  $\alpha$  values of GLaMS, 3CRR, and MRC sample, for the same redshift bins. We note from Table 3.2 that the GLaMS sample shows lower

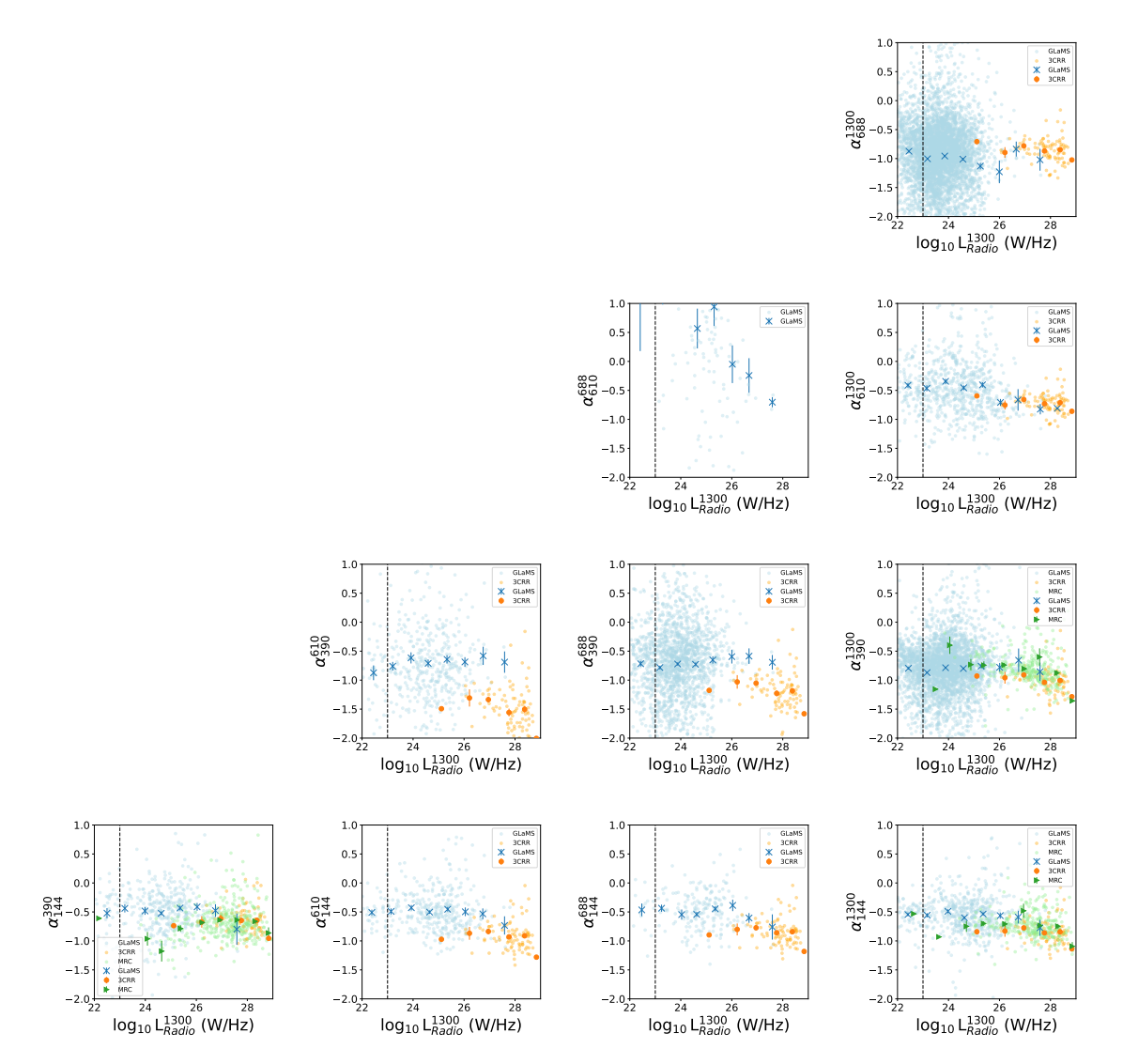


FIGURE 3.7: The correlation of the spectral index with the luminosity of the sources from MIGHTEE at 1.3 GHz where the spectral index is calculated for flux densities measured at 144 MHz (LOFAR), 390 MHz (uGMRT band-3), 610 MHz (GMRT), 688 MHz (uGMRT band-4), and 1.3 GHz (MIGHTEE). Luminosity is calculated as described in Section 3.2.3. Comments as in Fig. 3.6. The vertical dotted line shows the radio luminosity value above which AGN start to dominate.

correlation values between spectral index and redshift than 3CRR, except for the uGMRT B3-B4, GMRT-MIGHTEE, and uGMRT B4-MIGHTEE correlations, although uGMRT B3-B4 and GMRT-MIGHTEE still show an offset between GLaMS and 3CRR spectral index values.<sup>3</sup>

We also note that the p-values for the  $\alpha$ -z relation in GLaMS exceed the 5% threshold for all frequency pairs – there is no statistically significant  $\alpha$ -z correlation in the binned GLaMS data. This is not true for the 3CRR sample where at least three frequency pairs, corresponding to uGMRT B3 - MIGHTEE uGMRT B3 - uGMRT B4, and uGMRT B3 - GMRT, show p-values

<sup>&</sup>lt;sup>3</sup>The GMRT to uGMRT-B4 pair in Fig. 3.6 is shown for completeness, but is not reliable because of the very close frequencies for these objects.

Survey	Frequency Range (MHz)	$N_{GLaMS}$	N <sub>3CRR</sub>	$N_{MRC}$	$ ho_{GLaMS}^{\alpha-z}\left(\mathbf{p} ight)$	$ \rho_{3CRR}^{\alpha-z}(\mathbf{p}) $	$\rho_{MRC}^{\alpha-z}(\mathbf{p})$	$ ho_{GLaMS}^{lpha-L}\left(\mathbf{p} ight)$	$ \rho_{3CRR}^{\alpha-L}(\mathbf{p}) $	$ ho_{MRC}^{\alpha-L}$ (p)
LOFAR - MIGHTEE	144-1300	602	90	288	-0.312 (0.402)	-0.600 (0.284)	-0.428 (0.396)	-0.619 (0.101)	-0.714 (0.110)	-0.266 (0.487)
LOFAR - uGMRT B4	144-688	210	90	-	-0.321 (0.482)	-0.600 (0.284)	-	-0.428 (0.289)	-0.314 (0.544)	-
LOFAR - GMRT	144-610	378	90	-	-0.016 (0.966)	-0.600 (0.284)	_	-0.476 (0.232)	-0.314 (0.544)	-
LOFAR - uGMRT B3	144-390	397	90	355	-0.428 (0.289)	-0.600 (0.284)	0.178 (0.701)	-0.023 (0.955)	-0.028 (0.957)	0.083 (0.831)
uGMRT B3 - MIGHTEE	390-1300	3219	90	309	-0.018 (0.960)	-0.890(0.037)	-0.828 (0.041)	0.333 (0.419)	-0.771 (0.072)	-0.350 (0.355)
uGMRT B3 - uGMRT B4	390-688	1790	90	-	-0.904 (0.002)	-0.890 (0.037)	_	0.690 (0.057)	-0.771 (0.072)	-
uGMRT B3 - GMRT	390-610	446	90	-	0.266 (0.487)	-0.890 (0.037)	-	0.571 (0.138)	-0.771 (0.072)	-
GMRT - MIGHTEE	610-1300	764	90	-	-0.600 (0.066)	-0.600 (0.284)	_	-0.750 (0.019)	-0.600 (0.207)	-
GMRT - uGMRT B4	610-688	159	90	-	-0.357 (0.431)	-	-	-0.904 (0.002)	-	-
uGMRT B4 - MIGHTEE	688-1300	4851	90	-	-0.616 (0.076)	-0.600 (0.284)	-	-0.357 (0.385)	-0.600 (0.207)	-

TABLE 3.2: Number of sources in the analysis at each frequency range and correlation coefficients between spectral index, luminosity and redshift for different pairs of frequencies in the GLaMS catalogue. We use the effective frequency for the MIGHTEE sample wherever required and report the average frequency of the MIGHTEE survey in the table. The number of sources for GLaMS, 3CRR, and MRC sample are given in columns  $N_{GLaMS}$ ,  $N_{3CRR}$ , and  $N_{MRC}$ , respectively. The correlation between spectral index and redshift is given by columns  $\rho_{GLaMS}^{\alpha-z}$  (p),  $\rho_{3CRR}^{\alpha-z}$  (p), and  $\rho_{MRC}^{\alpha-z}$  (p). The correlation between spectral index and radio luminosity is given by columns  $\rho_{GLaMS}^{\alpha-L}$  (p),  $\rho_{3CRR}^{\alpha-L}$  (p), and  $\rho_{MRC}^{\alpha-L}$  (p). The values in the brackets give the p-value of the correlation, where we take a correlation with p < 0.05 to be statistically significant. We only show MRC sources where the number of sources in the MRC sample is greater than 20.

less than 5% implying a significant correlation. The MRC sources behave consistently with 3CRR, at least at the frequencies where we have sufficient data to make the comparison.

In order to understand the discrepancy observed in Fig. 3.6, between the GLaMS sample and the 3CRR sample, we look at the luminosities of the samples, as we know that the selections made in the older samples are dominated by luminous sources. Fig. 3.7 shows plots of spectral index and the radio luminosity of the sources in the GLaMS sample, the 3CRR sample, and the MRC sample. The spectral index values for sources are averaged for a radio luminosity bin size of 0.5 decades of radio luminosity for both sets of observations. From all the plots in Fig. 3.7, we can see that all the 3CRR sample contains only luminous sources, i.e. higher than  $L_{1300}$   $10^{25}$ W Hz<sup>-1</sup>. In addition, we also see for all plots that the 3CRR sample shows a downward trend, which indicates that as the luminosity increases the spectral index steepens. Further, when we look at the GLaMS sample and its arrangement in the plots we can see that the trend from the 3CRR sample is continued to lower luminosities by the GLaMS sources, following a similar slope to that exhibited by the 3CRR sample for most plots, except for uGMRT B4 - B3 and GMRT 610 - B3, where the two samples are offset from each other. From Table 3.2, we observe that the correlation values in the GLaMS sample are mostly closer to the values found for the 3CRR samples, for examples, LOFAR - MIGHTEE, LOFAR - uGMRT B4, LOFAR - GMRT, GMRT - MIGHTEE, and the uGMRT B4 - MIGHTEE. Out of these, GMRT - MIGHTEE, and GMRT - uGMRT B4 show significant correlations with p < 0.05. We also observe that the uGMRT B3-B4, uGMRT B3-MIGHTEE, and uGMRT B3-GMRT pairs shows a positive correlation with luminosity, although looking at the plot in Fig. 3.7, we can see that the mean spectral indices are almost constant with luminosity for the frequency pairs (noting that the sample size for uGMRT B3-GMRT is low and the data show high scatter). In addition, the plots of the three pairs show lower number of sources at higher radio luminosity bins for GLaMS, which could shift the average spectral index to flatter values and be responsible for overall positive correlation. Overall, both from the individual data points and the mean values, we see that in most cases the trend in the GLaMS sample is continued by the 3CRR sample and almost all of them show a slight downward progression in the sense that higher luminosities imply steeper spectra. The same is also evident from the background scatter shown in the plots. The vertical dotted line shown in the plots represents the boundary before which the dominance of SFGs is prominent. From the plots, only one or two data points fall within the limit and hence the presence of SFGs in our sample does not affect our overall result.

The results of studies such as those of Gopal-Krishna (1988), Onuora (1989), and Blundell et al. (1999), also suggest a relationship between luminosity and spectral index, but our work extends the luminosity dependence to even lower luminosities and to much larger sample sizes. In our analysis we have observed a statistically significant luminosity-spectral index correlation for some frequency pairs, although the relationship is not very prominent until we look at the background scatter. Blundell et al. (1999) proposed that the spectral index/luminosity relation effect can give rise to an apparent spectral index/redshift relation, as luminosity is a function of spectral index and redshift for flux limited samples. For a given source at high redshift, the luminosity of the source needs to be high enough to be detected in the survey, depending on the instrument's flux limits. As we cannot observe low-luminosity sources below some threshold at higher redshifts, the spectral index to redshift correlation becomes more evident in such cases, which shows up for surveys like 3CRR but is not seen in the GLaMS sample where low-luminosity sources are seen at all redshifts. However, there are other effects, such as selection of sources, that can mask this one: in this chapter we have only selected compact sources and effects from extended sources have not been included in the analysis.

The study of steep-spectrum radio sources by De Breuck et al. (2000) is widely cited as showing a strong spectral index/redshift correlation, with an almost linearly increasing correlation between the steepness of the spectrum and the redshift for their sample. They present flux densities and spectral indices for 147 sources at frequencies of 325 and 1400 MHz, very close to our uGMRT B3 and MIGHTEE observing frequencies respectively, which allows a direct comparison. As shown in Fig. 3.8 (top row), we do observe the same for the GLaMS sample over the same frequency range, although the trend is comparatively flatter in the GLaMS sample and there is an offset between the spectral index values for a given redshift. As above, we note that one of the major differences between the GLaMS sample and the De Breuck et al. (2000) sample is that the GLaMS sample consists of low luminosity sources as compared to those studied by De Breuck et al. (2000), also shown in Fig. 3.8, in the bottom row. We see from the same figures that the slope of either the luminosity or redshift correlations from the GLaMS sample is flatter than that of the De Breuck et al. (2000) sample. This reinforces the point already seen from the 3CRR and MRC sources above: there is a trend for spectra to be steeper at higher redshift in both the GLaMS sample and the comparison samples, but they are not the same trend.

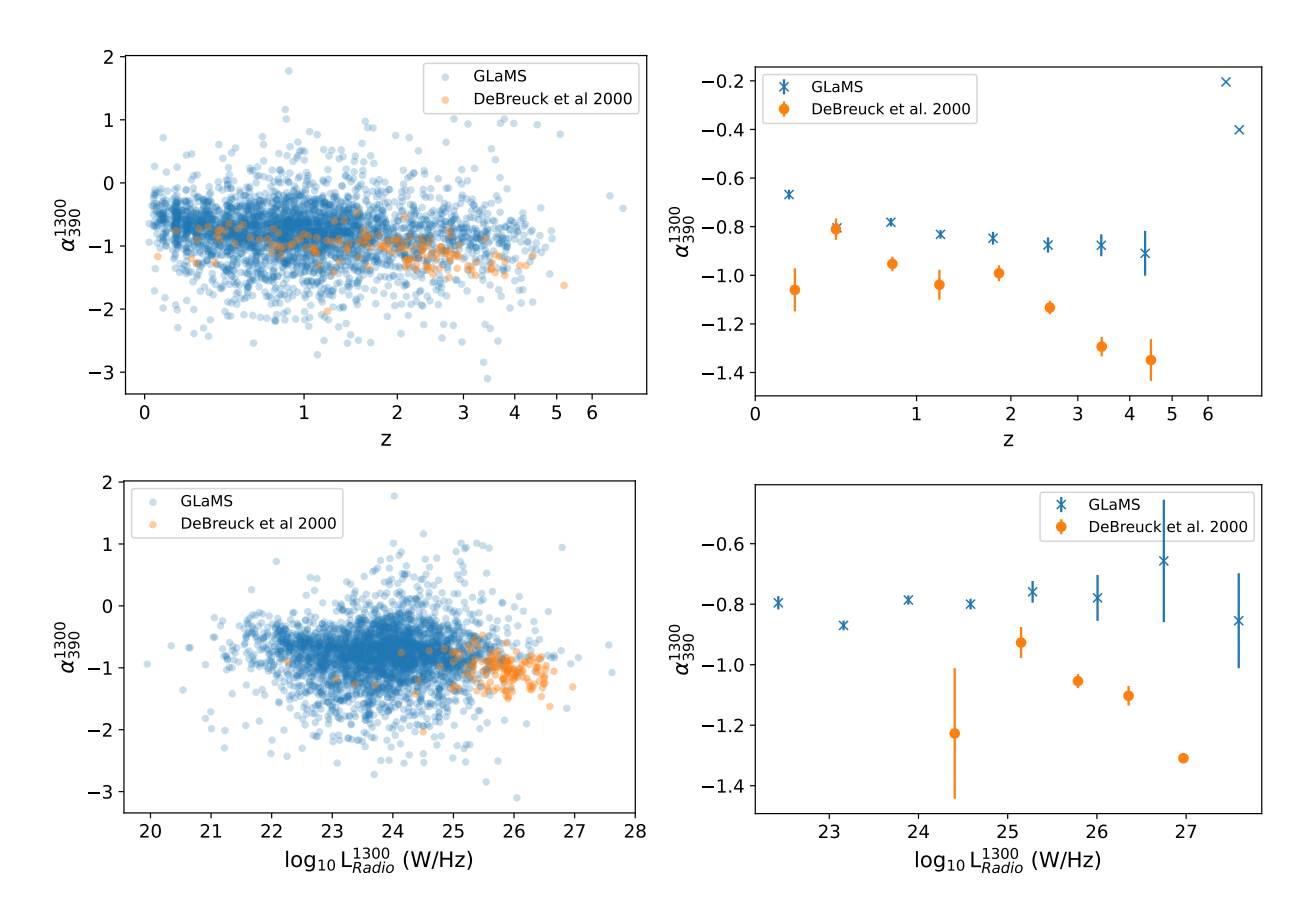


FIGURE 3.8: Top row: the relationship between the spectral index and the redshift, comparing the observations of sources obtained by De Breuck et al. (2000) and the GLaMS sample: on the left we show the distribution of individual sources and on the right the average values in matched bins in redshift are shown. Bottom row: the same relationship between radio luminosity and spectral index, with a radio luminosity bin size of 1 decade in radio luminosity for both the samples.

Finally, we considered the possibility that the systematic offset in the  $\alpha$ -z relations between the GLaMS objects and earlier samples might be due to the fact that the latter include extended sources whereas our study does not. We cannot include extended sources in our sample but we can test the effects of excluding them in the case of the 3CRR sample, where largest angular size measurements are available for all sources. When this test is carried out we see no clear difference between the trends for the small-source subset of 3CRR and the whole sample, and the  $\alpha$ -z offset is still clearly visible. Full details of this test and its results are presented in Appendix A.2.

#### 3.3.2 Multi-frequency analysis

In this section we explore the multi-frequency spectral index relation with the redshift and the radio luminosity, where Fig.3.9 shows the plots of spectral index versus redshift on the left and spectral index versus radio luminosity on the right. As stated in Section 3.1, using flux from multiple frequencies as input points we can fit a power law to all the flux measurements to get

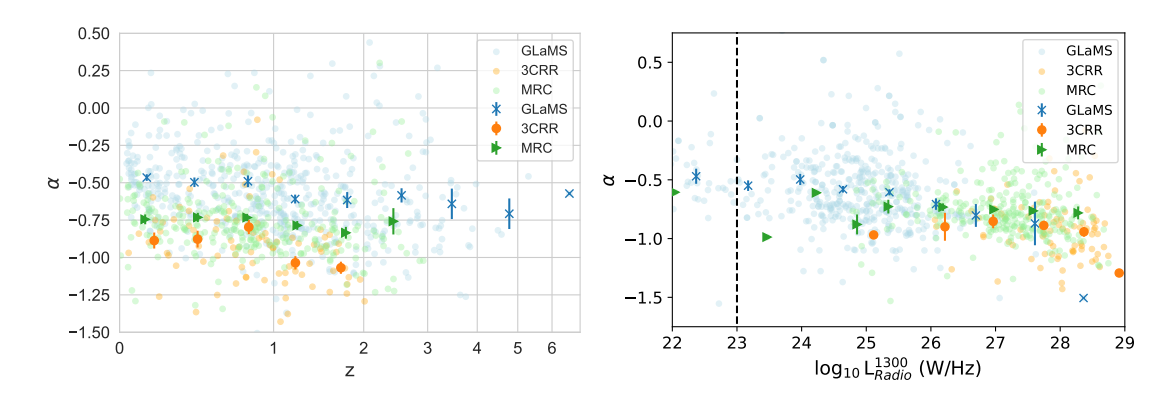


FIGURE 3.9: Left: correlation between the spectral index and the redshift (left) obtained by evaluating spectral index using flux from three or more frequencies. Right: correlation between the radio luminosity and the spectral index (right) for the same data. The vertical dotted line shows the radio luminosity value after which AGN start to dominate.

Sample	Number of Sources	$ \rho^{\alpha-z}(\mathbf{p}) $	$ \rho^{\alpha-L}(p) $
GLaMS	522	-0.683 (0.042)	-0.809 (0.014)
3CRR	90	-0.600 (0.284)	-0.257 (0.622)
MRC	287	-0.657 (0.156)	-0.283 (0.460)

TABLE 3.3: Correlation analysis for each sample for the spectral index, redshift, and luminosity. We use effective frequency for the MIGHTEE sample and the number of sources for GLaMS, 3CRR, and MRC sample are given in column 'Number of Sources', respectively. The correlation between spectral index and redshift is given by column  $\rho^{\alpha-z}$  (p). The correlation between spectral index and radio luminosity is given by column  $\rho^{\alpha-L}$  (p). The values in the bracket give the p-value of the correlation.

the spectral index based on multiple data points. We do this using the SCIPY function (Virtanen et al., 2020) curve\_fit in linear space taking account of the error bars, i.e.  $\chi^2$  minimization. We force the fits to include the LOFAR survey and the MIGHTEE survey by selecting only sources that have data at the respective frequencies. We do this because they represent the largest frequency range we have for our sample and the MIGHTEE survey is the most sensitive survey we have in our sample. We also select sources that also have flux values present for at least one of the other three surveys, i.e. the GMRT survey and the uGMRT band 3 and band 4 survey. By selecting sources with flux values at three or more frequencies we obtain spectral index values obtained from multiple bands, which allows us to improve the accuracy of the broad-band alpha values <sup>4</sup>. The number of sources obtained using this method for the three samples is given in Table 3.3; the number of GLaMS sources is significantly reduced by the requirement to include LOFAR data in the analysis. We use the 90 sources from the 3CRR survey as we have values at all the frequencies. For MRC we do the same by selecting sources at the respective frequency

<sup>&</sup>lt;sup>4</sup>We explicitly chose not to determine a spectral index for all sources for which three, or even two frequencies were available, but to require the frequency coverage to span the 144-1300 MHz range given by LOFAR and MIGHTEE. This is because any given pair of frequencies suffers from bias as shown in Fig. 3.4; a sample constructed using all available pairs of frequencies would have a *flux-dependent* bias and that could result in spurious correlations in the α-z or α-L plots.

range used in the 3CRR sample where we ignore the frequency band between 600 MHz and 800 MHz as requiring these would reduce the sample size to less than 10. The spectral index values shown in the plots of Fig.3.9 are averaged for a redshift bin size of 0.1 in  $\log_{10}(1+z)$  for the left panel and a radio luminosity bin size of 0.5 decades in  $\log_{10}(L_{1300})$  for the right panel. In Table 3.3, we also report the Spearman correlation for the spectral index versus redshift and spectral index versus luminosity plots.

From Fig.3.9, we find a similar trend between the spectral index and redshift to the one that we observed in the two point frequency analysis. We can see that the GLaMS data show evolution with *z*, although we again observe an offset between the 3CRR and GLaMS spectral index values with the MRC objects lying between the two. For the 3CRR sample, the spectral index tends to steepen with increasing redshift and the steepening is comparatively stronger than for GLaMS or MRC. For the MRC sample, we see a trend similar to the 3CRR sample at least for the first few data points after which the scatter increases. This is also representative of the correlation values observed in Table 3.3. The spectral index of the MRC sample is also intermediate between the spectral index of the GLaMS and the 3CRR sample which suggests a dependency of these apparent trends on the luminosity. To confirm this we can look at the right plot of Fig. 3.9 and the correlation values in Table 3.3, where we can see clearly that the data points from the three samples lie on the same trend of steeper spectrum for higher luminosity. This is a clear indication that a relationship between luminosity and spectral index exists, as discussed in the previous section.

#### **3.3.3** Interpretation of the correlations

From both the preceding subsections we have seen weak but significant correlations between redshift and spectral index, and luminosity and spectral index, for the GLaMS sources. However, the GLaMS sources show systematically flatter spectral indices than 3CRR or MRC sources at the same redshift, while plots of spectral index against luminosity show broadly similar trends of steeper spectra with higher luminosity in all three samples. We interpret the fact that all the samples seem to lie on the same spectral index/luminosity trend in terms of a direct relationship between luminosity and spectral index.

What could cause this relationship? Blundell et al. (1999) pointed out that a relationship between luminosity and spectral index that persists over a wide range of frequencies is most easily explained in terms of the injection index, i.e. the spectral index of particles when they are originally detected. The most powerful radio AGN are FRII sources where the main location of particle acceleration is the hotspots, and in these we expect higher jet powers to equate to higher magnetic field strengths and synchrotron photon densities, and thus to higher radiative and inverse-Compton losses, so that qualitatively the energy spectrum of particles escaping from

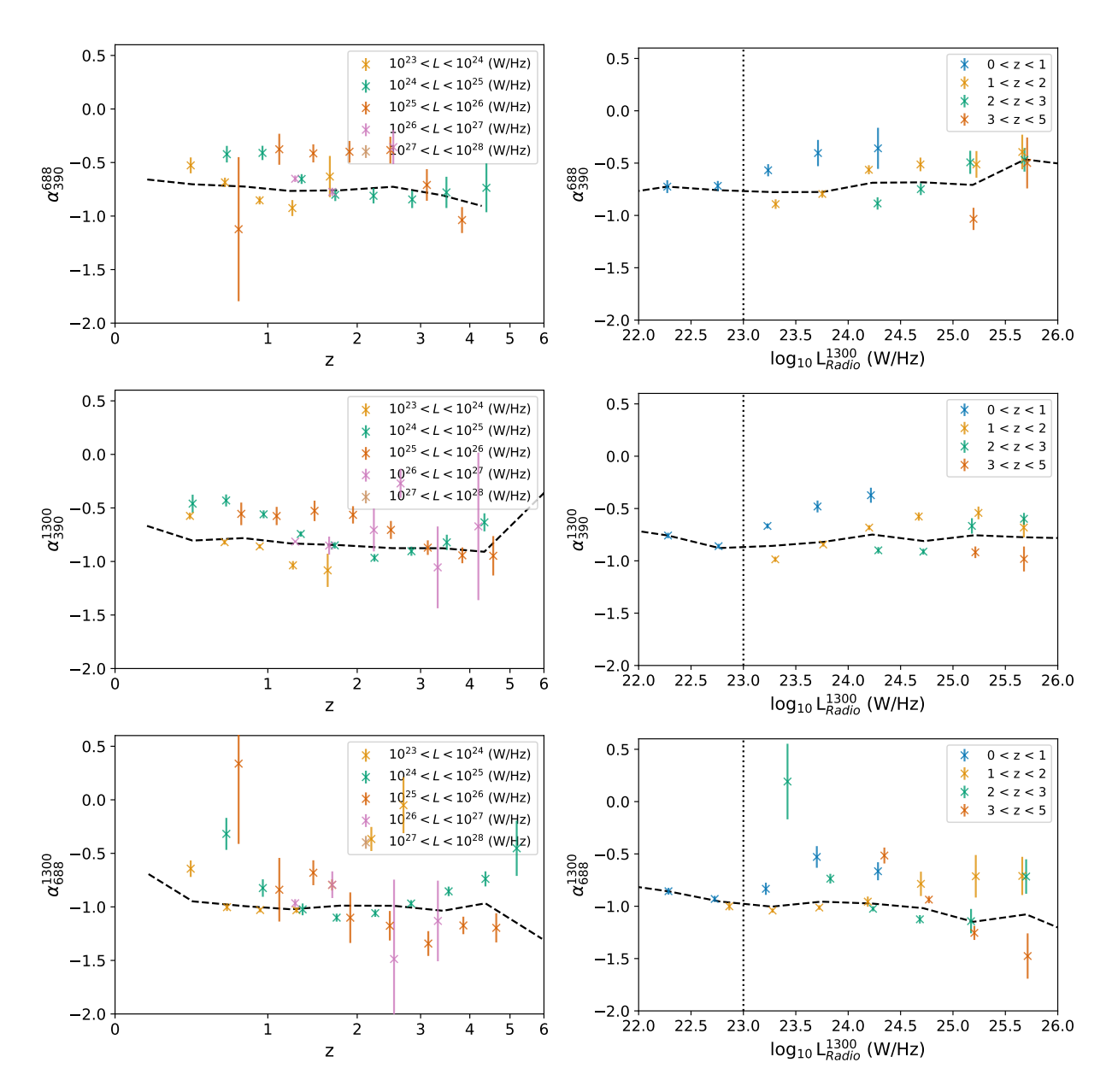


FIGURE 3.10: Left column: the relationship between the two-point spectral index and the redshift, filtered for different range of radio luminosities. Right column: relationship between spectral index and radio luminosity, filtered for different ranges of redshifts. The black dashed line represents the mean of  $\alpha$  as seen for the frequency pairs in Fig 3.6 and 3.7, averaging over all GLaMS sources at these frequencies. The vertical dotted line shows the radio luminosity value above which AGN start to dominate.

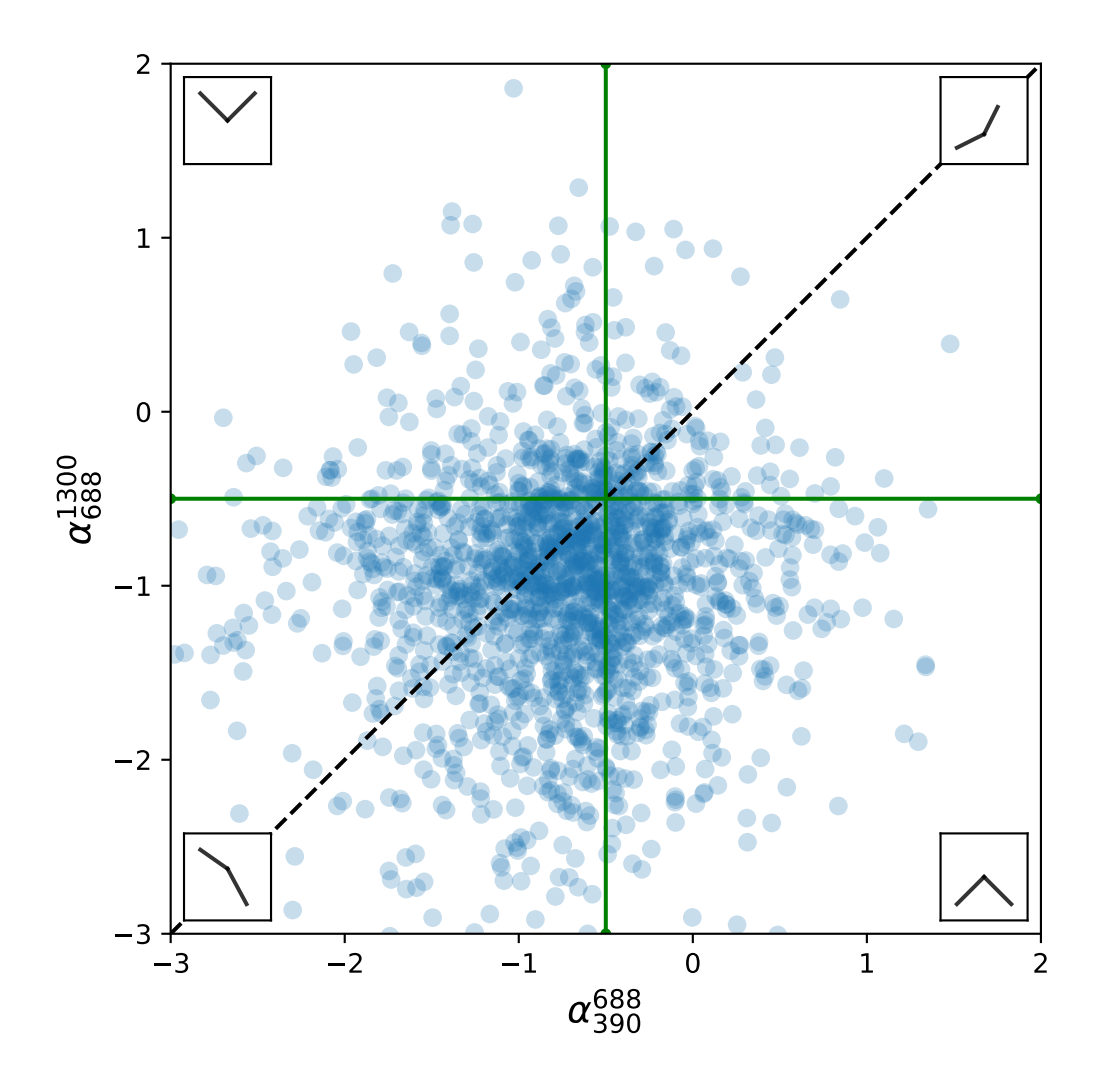


FIGURE 3.11: Plot showing correlation between the spectral index obtained for frequency range uGMRT B3 - B4 and uGMRT B4 - MIGHTEE, divided into quadrants at a spectral index of -0.5 which is the flattest value expected for optically thin synchrotron emission. The four small plots on each quadrant illustrate the respective spectral curve. The dashed line shows the line of equality of spectral index at the two frequencies.

the hotspot might be expected to steepen with increasing jet power, while potentially still being flatter at the lowest energies. They argued that the non-detection of optical synchrotron emission from the most powerful hotspots is evidence that the synchrotron spectra may be steeper in those systems (cf. Meisenheimer et al., 1997; Brunetti et al., 2003). Since then the widespread detection of X-ray synchrotron from lower-power hotspots (Hardcastle et al., 2004) has provided evidence that the overall synchrotron spectrum, including the high-energy cutoff, depends on jet power in some way. Further evidence supporting this general picture comes from the observation that the pairs of hotspots in double-double radio galaxies have the same spectral indices, despite their very different dynamics (Konar and Hardcastle, 2013), which can only be explained in terms of a direct jet power/hotspot spectrum relationship.

In an effort to explore the spectral index, redshift, and luminosity relationship for the GLaMS

sources in more detail we have generated  $\alpha$ -z and  $\alpha$ -L plots for the frequency pairs that have the largest sample sizes and are most sensitive, that is, the uGMRT B3 - B4, uGMRT B4 - MIGHTEE, and the uGMRT B3 - MIGHTEE pairs. For these plots we filter samples in different redshift ranges for the  $\alpha$ -L plots and filter samples in different radio luminosity ranges for the  $\alpha$ -z plots in order to separate out the redshift and luminosity effects. The plots are shown in Fig. 3.10. These plots show that the picture is more complicated than is consistent with a simple luminosity/spectral index relationship. In fixed luminosity bins (left column) we see a steepening spectral index as a function of redshift in almost every bin, though this is more prominent at the two lower frequencies, and is only modest in magnitude (e.g. sources in the bin  $10^{25}$  to  $10^{26}$  W Hz<sup>-1</sup> have typical spectral indices that steepen from -0.5 to -0.9 between z = 1 and z = 4). Moreover, in a given redshift range (right column), more luminous sources tend to have *flatter* spectra, which is the opposite of what would be predicted by the Blundell et al. (1999) model or what is expected from the offset between 3CRR and GLaMS sources.

The steepening of spectral index with redshift and luminosity is consistent with the expected effect of inverse-Compton losses and higher radiative losses, combined with the fact that we observe at higher rest-frame frequencies at higher redshifts<sup>5</sup>. However, we are not sure why low luminosity sources are steeper-spectrum than high luminosity sources, especially for the uGMRT B3 - B4 and uGMRT B3 - MIGHTEE pairs. Most of the sources driving these trends are much lower in luminosity than the sources discussed by Blundell et al. (1999), and it may be that particle acceleration operates differently in these low-luminosity objects, or that they have a larger fraction of sources affected by self-absorption or free-free absorption. At the lowest luminosities, many may not be AGN at all. In Fig. 3.11, we show a scatter plot of the spectral indices for the two frequency ranges discussed above. We can see that there are around 542 sources in the quadrant where the spectrum turns down at low frequencies, consistent with the idea that one or both of the absorption processes are important for a significant fraction of our sample. To take this analysis further it will also be important to consider the full population of MIGHTEE sources by including the extended objects when they have all been identified, to include a full coverage of physical sizes in our sample, although as discussed above we have reason to believe that our results are not driven by the missing extended sources in GLaMS.

Finally, we checked the robustness of our results by conducting the same analysis using only sources that have flux density greater than  $10^{-4}$  and  $10^{-3.5}$  Jy for uGMRT B4 and B3 respectively. As we can see from Fig.3.4, at these flux limits the sensitivity limit intersects the spectral index line at a spectral index of 1 which essentially removes any bias against inverted-spectrum sources. We find qualitatively similar results after conducting this analysis and conclude that the bias against inverted spectrum sources does not have a significant effect on our results.

<sup>&</sup>lt;sup>5</sup>In our sample there may also be more subtle effects such as a bias against physically large sources at low redshift due to our angular size cutoff; exploring the effects of these will have to await the availability of a full optical identification for the larger MIGHTEE sources.

#### 3.4 Conclusions

We have used the data from five different surveys carried out in the XMM-LSS field to look at the spectral index behavior of radio sources as a function of redshift and luminosity. We used two point spectral index analysis and multi-frequency spectral index analysis to revisit the correlation between spectral index, luminosity and redshift for much larger samples than have hitherto been available and over a wide range of different combinations of frequency. As investigated by different studies, discussed in Section 3.1, it has been observed that there is a positive correlation between the spectral index and the redshift, i.e. the spectral index of the sources become steeper with increasing redshift. In the past, this correlation has been used to identify steep spectrum sources, especially for high redshift radio galaxies. However, the correlation has largely been explored for bright sources such as those from the 3CRR and MRC surveys (De Breuck et al., 2000; Morabito and Harwood, 2018).

From the results obtained using the two-point analysis and multi-frequency analysis for the three samples, we can answer the questions presented in the Section 3.1, which are as follows:

- i We observe that for our sample the spectral index increases weakly but significantly in many cases with redshift. However, we also observe an offset between the mean spectral index values obtained from GLaMS and 3CRR: at the same redshift, the more luminous 3CRR sources show systematically steeper spectra.
- ii We observe a weak but again significant correlation between the radio luminosity and averaged spectral index for most frequency pairs, although some pairs, such as LOFAR MIGHTEE and GMRT MIGHTEE, show a more prominent increasing trend. The more luminous 3CRR and MRC sources that we compare with lie on the same trend.
- iii In the two-point analysis we constructed ten different plots using different combinations of the frequency ranges obtained from the surveys for the two correlations. For all the plots we can see a correlation for the GLaMS sources but a stronger and more rapidly increasing trend for the 3CRR sample for the spectral index versus the redshift. By contrast, the trend between the luminosity and the spectral index is consistent with same continued slopes for the three samples in most of the pairs of frequencies we used. Due to the low number of sources in the MRC sample we observe a significant scatter in the plots. Very similar results are obtained in the multi-frequency analysis.
- iv For the two-point analysis, the largest sample size is 4851 sources and the smallest sample size is 159 sources although the trend observed for these are more tightly constrained for almost all the large sample plots in GLaMS. The smaller samples lead to large uncertainties when binned by luminosity or redshift. A sample size of more than 500 sources is ideal to analyse such correlations if sensitive data are used.

- v Attempting to disentangle the redshift and luminosity relations in the GLaMS sample, we find evidence for relationships between spectral index and both redshift and luminosity: in fixed luminosity bins there is a clear redshift dependence at some frequencies, while in fixed redshift bins there is a luminosity dependence.
- vi As argued by Blundell et al. (1999), the relationship between spectral index and luminosity seen in luminous sources could be due to the injection index of the sources, where high power sources have high jet energy densities with stronger magnetic fields, leading to higher synchrotron losses and hence steeper spectra. This would be consistent with the very clear offset between the spectral indices of GLaMS and 3CRR sources at a fixed redshift and the continuity of the spectral index values between GLaMS and 3CRR at high luminosities. However, there is clearly also evidence for a direct relationship between spectral index and redshift at a fixed luminosity, which could be explained qualitatively in terms of increased inverse-Compton losses together with the higher rest-frame frequency of observation. The fact that spectral index in some bands shows a positive correlation with luminosity (higher luminosity gives flatter spectrum) at fixed redshift is a puzzle in this scenario, but is probably driven by the presence of many very low-luminosity sources in our sample. We would not necessarily expect the low-luminosity sources, which will be of FRI-type, to obey the same relation as the sources discussed by Blundell et al. (1999), which are all powerful FRII sources with hotspots.

Further investigations are required, where we can explore samples from more sensitive surveys and also include extended sources in the analysis to form a complete sample, but our basic conclusion is that at high luminosities the radio luminosity is the driver of the observed steep spectra, with any direct correlation with redshift being a weaker effect. Thus we predict that ultra-steep-spectrum selection will become less and less effective to select high-redshift sources as it is applied to fainter sources with intrinsically lower luminosities.

Other studies, such as those of An et al. (2021) and An et al. (2024), suggest no strong or obvious correlations between radio spectral index and redshift. These studies found results using a sample that contains SFGs and argue that including AGN does not affect their statistical results on the radio spectral index. Large sample sizes (> 1000) are important to analyze such correlations, as data from sensitive surveys gives larger samples and gives rise to less noisy plots. We have observed that the quality of the relationship is also improved by making use of as broad a frequency range as possible. For the XMM-LSS survey, more sensitive data at low frequencies could further help to reduce the scatter and increase the number of sources. Further investigation of these correlations could also be carried out using the LoTSS wide-area survey of the northern sky (Shimwell et al., 2022), where spectral index measurements are in principle available for large numbers of optically identified sources (Hardcastle et al., 2023). Extension of

the MIGHTEE survey to a wider range of frequencies would also allow us to expand the scope of this work.

### **Chapter 4**

# **Revisiting Barthel's Unification Scheme**

#### 4.1 Introduction

#### 4.1.1 Quasars and radio galaxies

The ultimate source of the luminosity of Active Galactic Nuclei (AGN) is accretion onto the central supermassive black hole. For radiatively efficient (RE) objects (Hardcastle, 2018b) this is thought to take place through a geometrically thin accretion disk<sup>1</sup>. Dissipation in the disk leads to continuum radiation in the optical through UV and, via Compton scattering, the X-ray. The hard radiation field ionizes material both close to and far away from the central black hole, giving rise to the broad-line region (BLR) and narrow-line region (NLR), respectively.

This picture is more or less independent of the orientation of the disk with respect to the line of sight, but it has been known for some time that there exist 'type II' AGN which have a narrow-line region of a luminosity comparable to those seen in normal, or 'type I', AGN, but do not have the strong optical/UV continuum emission or broad-line emission of the type Is. The generally accepted explanation (Antonucci, 1993) is that an anisotropic obscuring structure, the 'torus', surrounds the accretion disk, obscuring a direct view of the continuum emission and BLR from certain lines of sight (Kormendy and Richstone, 1995; Magorrian et al., 1998; Ferrarese and Merritt, 2000) while the NLR largely lies on larger scales than the torus and so is seen from all viewing angles. The clinching argument for this picture originally was the detection of the BLR in polarized emission in type II objects, showing that it is present but not directly observable

<sup>&</sup>lt;sup>1</sup>There are many reasons to believe that the standard picture of these disks is lacking important physics (Antonucci, 2023); here we use the term 'disk' simply as a shorthand for the geometrically thin structure that seems likely to exist without subscribing to any particular model for the origin of the continuum emission.

(Antonucci, 1984; Antonucci and Miller, 1985). Since then, the strong obscuration seen in the X-ray spectrum of type II objects and the detection of mid-IR emission consistent with obscuration via the torus have provided additional support to this 'orientation-based unification' picture (Whysong and Antonucci, 2004; Ogle et al., 2007; Hardcastle et al., 2009; Netzer, 2015).

AGN with strong jet-driven radio emission (hereafter radio-loud AGN, or RLAGN) add a complication but also allow additional tests of orientation-based unified models. While some RLAGN behave as more or less standard type I or type II AGN with the addition of strong radio emission (the so-called narrow-line radio galaxies, NLRG, being type II and radio-loud quasars being type I) there exists a numerically dominant population of what are commonly known as low-excitation radio galaxies (LERG), which have been known for many years (Hine and Longair, 1979). These objects do not show any of the apparatus of the type I/II standard AGN, including, crucially, no evidence for an obscuring torus that might hide it (Whysong and Antonucci, 2004; Hardcastle et al., 2009). LERGs are thought to accrete through a geometrically thick and optically thin, radiatively inefficient accretion disk (e.g. Narayan and Yi, 1995), producing very little radiation while still having potentially highly energetic radio jets, and it now seems clear that these 'radiatively inefficient' AGN are the result of accretion below some critical Eddington-scaled accretion rate threshold (Best and Heckman, 2012; Mingo et al., 2014). LERGs must therefore be excluded from any consideration of a radio-loud orientation-based unified model (Hardcastle et al., 1999).

If LERGs are excluded, though, RLAGN have a number of advantages in tests of unified models. Firstly, low-frequency radio emission is (almost) isotropic, and so allows us to select samples that are unbiased with respect to orientation. Secondly, jets are relativistically beamed (Laing, 1988; Garrington et al., 1988) and appear to emerge more or less perpendicular to the torus, so that quasars show stronger, more one-sided jets, apparently faster bulk motions on parsec scales, and more prominent cores than NLRG. These key facts led Barthel (1989) to propose the original radio-loud orientation-based unified model, with a critical angle of  $\sim 45^{\circ}$  to the line of sight separating quasars and NLRG. We explore the consequences of this model in the next subsection.

#### 4.1.2 Consequences of the unification model

The orientation based scheme proposed by Barthel (1989) considers radio galaxies and quasars to be derived from the same AGN population, which means that they are intrinsically indistinguishable. This also means that their observed sizes are affected by geometrical projection: quasars, which are at smaller angles to the line of sight, should be systematically smaller than radio galaxies, as was indeed the case for Barthel's sample. Another aspect of the scheme is that the relative numbers of radio galaxies and quasars are dependent on the critical angle that

separates quasars from radio galaxies. The unified model assumes that there is intrinsically no bias in the distribution of angles to the line of sight, so that if  $\theta$  is the angle to the line of sight, then  $p(\theta) = \sin \theta$ . It is thus more probable for a source to be close to the plane of the sky than for it to be aligned along our line of sight. If we consider a critical angle  $\theta_c$  such that sources are classified as quasars if  $\theta < \theta_c$  and radiatively efficient radio galaxies otherwise, then the ratio of the numbers of quasars  $(N_Q)$  to radio galaxies  $(N_R)$  is given by:

$$\frac{N_Q}{N_R} = \frac{\int_0^{\theta_c} \sin\theta d\theta}{\int_{\theta_c}^{\pi/2} \sin\theta d\theta} = \frac{1 - \cos\theta_c}{\cos\theta_c}$$
(4.1)

This means that we can evaluate the critical angle from a given sample using the number of quasars and radio galaxies.

If radio galaxies and quasars were intrinsically all of constant length  $(L_0)$  and appeared when projected to have a length  $L_0 \sin \theta$ , then the mean apparent lengths of quasars  $(\bar{L}_Q)$  would be given by:

$$\bar{L}_{Q} = \frac{\int_{0}^{\theta_{c}} L_{0} \sin^{2}\theta d\theta}{\int_{0}^{\theta_{c}} \sin\theta d\theta}$$
(4.2)

and the mean apparent lengths of radio galaxies ( $\bar{L}_R$ ) would be given by:

$$\bar{L}_R = \frac{\int_{\theta_c}^{\pi/2} L_0 \sin^2 \theta d\theta}{\int_{\theta_c}^{\pi/2} \sin \theta d\theta}$$
(4.3)

Using Eq.(4.2) and Eq.(4.3), and assuming that the distributions of intrinsic lengths are identical, we can derive the predicted size ratio between quasars and radio galaxies, obtaining:

$$\frac{\bar{L}_{Q}}{\bar{L}_{R}} = \frac{2\left(\theta_{C} - \frac{\sin(2\theta_{C})}{2}\right)\cos(\theta_{C})}{\left(\cos(\theta_{C}) - 1\right)\left(2\theta_{C} - \sin(2\theta_{C}) - \pi\right)} \tag{4.4}$$

where the assumed constant length disappears, so that the size ratio should also hold under any distribution of intrinsic lengths that is the same for radio galaxies and quasars.

However, the above analysis, which is essentially that of Barthel (1989), assumes that radio AGN behave like one-dimensional rods (the 'stick model'). Barthel argued that the lengths of radio galaxies and quasars in the 3CRR sample are in agreement with this model. In reality, however, we know that quasars and radio galaxies have a non-zero axial ratio; that is, they have finite width for a given length. This means that these galaxies would be better described as cylinders rather than rods (see Fig. 4.1). In this model the lobe width becomes the width of the cylinder (2r), where r is the radius of the cylinder. The length of the source  $(L_0)$  becomes the height of the cylinder. It follows that the apparent length or projected length of the source can be given by:

$$L_{proj} = L_0 \sin \theta + 2r \cos \theta \tag{4.5}$$

If we define axial ratio,  $a = 2r/L_0$ , then the mean apparent length of the quasars in the cylindrical model is given by:

$$\bar{L}_{Q} = \frac{\int_{0}^{\theta_{c}} L_{0} \sin^{2}\theta d\theta + a \int_{0}^{\theta_{c}} L_{0} \cos\theta \sin\theta d\theta}{\int_{0}^{\theta_{c}} \sin\theta d\theta}$$
(4.6)

whereas the mean apparent length for the radio galaxies for the cylindrical configuration is given by:

$$\bar{L}_{R} = \frac{\int_{\theta_{c}}^{\pi/2} L_{0} \sin^{2}\theta d\theta + a \int_{\theta_{c}}^{\pi/2} L_{0} \cos\theta \sin\theta d\theta}{\int_{\theta_{c}}^{\pi/2} \sin\theta d\theta}$$
(4.7)

Hence, the ratio of the mean of the linear sizes for the quasars and radio galaxies is given by:

$$\frac{\bar{L}_Q}{\bar{L}_R} = \frac{2\left(a\sin^2\left(\theta_C\right) + \theta_C - \frac{\sin\left(2\theta_C\right)}{2}\right)\cos\left(\theta_C\right)}{\left(\cos\left(\theta_C\right) - 1\right)\left(-a\cos\left(2\theta_C\right) - a + 2\theta_C - \sin\left(2\theta_C\right) - \pi\right)} \tag{4.8}$$

Fig. 4.2 shows the number ratio and length ratio for the two models for different values of critical angle where the axial ratio takes fixed values of 0 (stick model), 1/3, and 2/3.

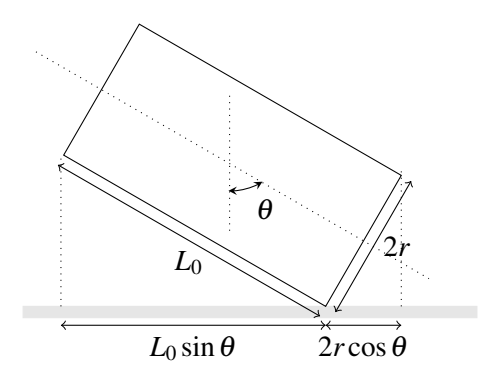


FIGURE 4.1: Representation of the cylindrical model for a source tilted at angle  $\theta$  from the line of sight.

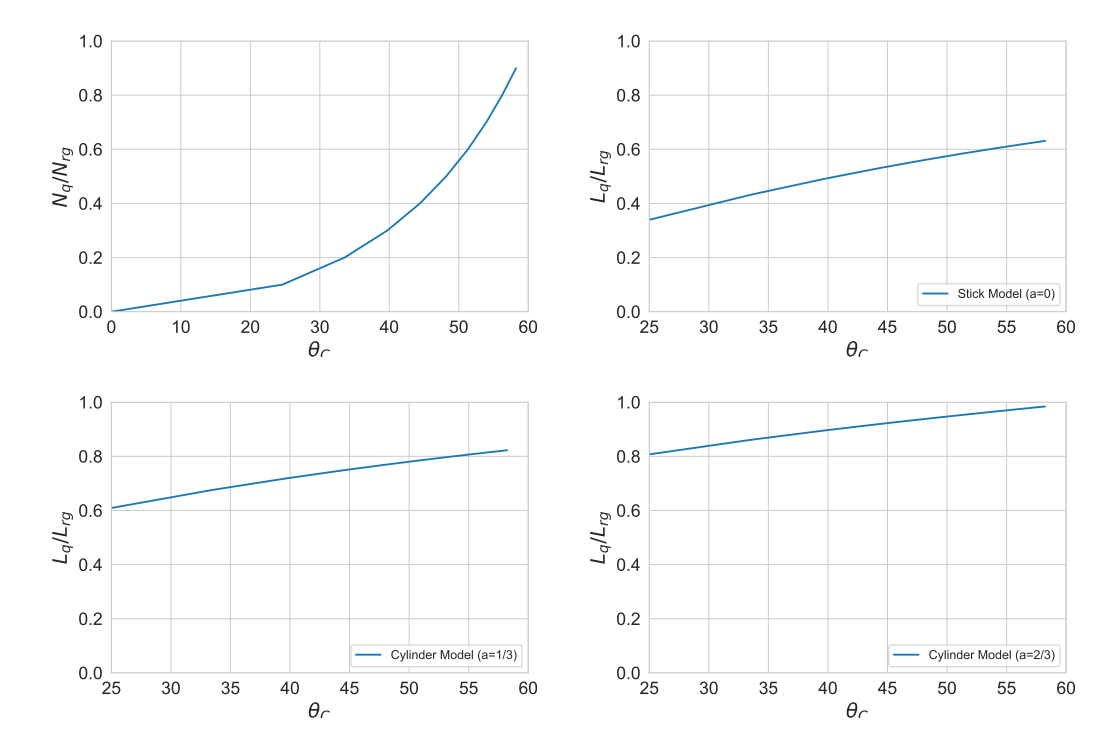


FIGURE 4.2: Quasar versus radio galaxy diagnostics in different models. The top row shows plots of (left) the numbers ratio (quasar to radio galaxy) and (right) the mean length ratio (quasar to radio galaxy) as a function of the critical angle. The top right-hand plot uses the stick model to calculate the length ratio, i.e. the assumption is that the axial ratio is zero. The bottom row shows length ratio (quasar to radio galaxies) versus critical angle plots using the cylindrical model, where the value of axial ratio for the two plots is 1/3 (left) and 2/3 (right). Note the strong dependence of measured length ratio on the axial ratio.

#### 4.1.3 Previous tests of unified models

TABLE 4.1: Previous studies that support Barthel's unification schemes with their respective conclusions.  $N_q$  and  $N_{rg}$  are number of quasars and number of radio galaxies (RG)

Study	$N_q$	$N_{rg}$	Test/Objective	Conclusions	Remarks
Barthel (1989)	17	33	Investigate relativistic beaming in quasi-stellar radio sources by examine large and small scale radio morphology	All radio loud quasars are beamed towards observer and powerful RGs are unbeamed parent population	Only powerful sources are used in the sample.
Onuora (1991)	30	66	Explore angular- diameter relation taking into account Barthel's scheme	Radio galaxies have different angular diameter-redshift relation than quasars which is an orienta- tion effect	Non random steep spectrum bright sources $(P_{178} > 10^{26})$ W Hz <sup>-1</sup> sr <sup>-1</sup>
Gopal- Krishna and Kulka- rni (1992)	308	127	Compare linear size and redshift of radio sources only for large sources	The evolution of linear sizes is indistinguishable for quasars and RG's	The redshift bins size is 0.1 to 2
Saikia and Kulka- rni (1994)	44	70	Test the unification scheme and explore the quasar fraction	Size ratios and critical angles are consistent with unified scheme	Two redshift bins considered have linear size ratio of 0.90 and 0.45
Hong and Wan (1995)	41	2	Investigate individ- ual angles to line of sight and linear sizes	Individual quasars and RG's are ob- served at $> 40^{\circ}$ and $< 50^{\circ}$ respectively	VLBI data is used and very low number of RG's
Saikia et al. (1995)	39	42	Test the unification scheme and investigate the source sizes	The expected size ratio and the observed size ratio are similar Radio axes of	The redshift is from 0 to 2 and only bright sources are used.
Ubachuk (2002)	wu 132	76	Measure and compared angle to line of sight for individual sources	quasars are close to the line of sight and radio axes of radio galaxies are close to the plane of the sky (median of $Q \approx 28^{\circ}$ and $RG \approx 51^{\circ}$ )	Compact steep spectrum sources are used in sample.
Morabito et al. (2017)	16	44	Measured critical angle and linear size ratio	The critical angle observed is 42.8° and linear size ratio is 0.32	Sample from LO-FAR for sources at power greater than $10^{25.5}WHz^{-1}$

Barthel's proposal was not the first to suggest that different classes of AGN could be unified: for example, Orr and Browne (1982) had already explored the role of beaming in unifying flat-and steep-spectrum radio-loud quasars, and Lawrence (1987) had already discussed in detail possible unification of all AGN based on orientation and relativistic beaming. Barthel's work,

TABLE 4.2: Previous studies that provide evidence against Barthel's unification schemes with their respective conclusions.  $N_q$  and  $N_{rg}$  are number of quasars and number of radio galaxies (RG)

Study	$N_q$	$N_{rg}$	Test/Objective	Conclusions	Remarks
Fanti et al. (1990)	46	93	Explore properties of different classes of CSS	The difference in CSS radio galaxy and quasar morphology is not explained by projection	The linear size distributions for quasars and RG's are similar
Singal (1993)	32	99	Compare the linear size ratios for expected and observed values	Discrepancy between observed and ex- pected size ratio for three redshift bins	Large mismatch at lower redshift bin
Singal (1996)	188	934*	Test the unification scheme by exploring the quasar fraction for different flux den- sities	Systematic decrease in quasar fraction; no drop in RG and Quasar observed size ratios	Samples are from multiple surveys for decreasing flux levels
Singal and Laxmi Singh (2013)	93	381	Test and observe source sizes, their flux level and red- shift trends	Observed quasar sizes are not systematically smaller than RGs for same flux level and redshift	The sample (MRC) is compared with 3CRR
Singal (2014)	45	85	Test the unification scheme and investi- gate the source sizes and other parameters	The source sizes are not systematically smaller and there are discrepancies between observed and expected ratio	Sample is obtained for FR type-II sources

and in particular the fact that it predicted different size distributions for quasars and radio galaxies, enabled new observational tests of unification. Studies such as those of Onuora (1991) and Gopal-Krishna and Kulkarni (1992) found different linear size or angular size trends for quasars and radio galaxies. Other studies (e.g. Saikia and Kulkarni, 1994; Hong and Wan, 1995; Ubachukwu, 2002) found that the fraction of quasars present in the sample or the individual angles of the sources in the sample were consistent with Barthel's proposed scheme. Similarly, Best (1996); Morganti et al. (1997); Lähteenmäki and Valtaoja (1999), have explored different properties of AGN and confirmed their consistency with the unified scheme. All of these studies support the idea that quasars lie at lower values of the angle to the line of sight than radio galaxies. By contrast, other studies (e.g. Fanti et al., 1990; Saripalli et al., 2005) found evidence against the unification model by studying the galaxy environments, size distribution, and or evolution of galaxies, although some of these were affected by a failure to realize that LERGs do not participate in the unified model. Most importantly in the context of this chapter, a number of studies (Singal, 1993, 1996; Singal and Laxmi Singh, 2013; Singal, 2014) have carried out a comparison between the expected and observed linear size ratios for the quasar and radio galaxy samples and observed discrepancies between the two. They also found varying critical angles at different redshifts (again, to some extent affected by including LERGs in their sample) and hence concluded that Barthel's unified scheme as originally proposed does not hold. A brief description of the studies and the sample sizes used by different investigations previously, either supporting Barthel's unified scheme or presenting evidence against it, are presented in Tables 4.1 and 4.2.

It is important to note here that the basic assumption for the effect of projection on measured size considered in all of the studies presenting evidence against the unified models is based on the simple 'stick' model, although, as discussed above, this is not realistic and real sources have finite axial ratio. The number of sources in samples used for testing the unification model is usually very small, and has never been more than  $\sim 500$ .

#### 4.1.4 This chapter

Our aim in the present study is to explore the unification model by studying a sample of quasars and radio galaxies from deep radio observations and to interpret the results using simulated samples that assume a cylindrical model for the projection of the lobes. For this study we will be using the data from the LOw Frequency Array Two-Metre Sky Survey deep field observations (LoTSS-DF: Tasse et al. 2021), AGN selection from optical and IR photometry (Best et al., 2023) and the Sloan Digital Sky Survey (SDSS) data release 16 (Lyke et al., 2020) to select quasars and differentiate them from the radio galaxies. For the simulation of the effects of projection we will make use of the study conducted by Mullin et al. (2008), who explored the morphological properties of Fanaroff–Riley II (FRII) quasars and radio galaxies with z < 1. We hope to answer the following questions in this study:

- i What are the observed critical angles and sample sizes for different redshift bins?
- ii What are the mean and median size ratios of quasars to radio galaxies at different redshift bins produced using the stick model?
- iii What can be concluded from the size ratio ranges and how do the observed values compare to the results of Monte Carlo simulation based on the cylindrical model?
- iv What constraints can be placed on the unification model in general from Monte Carlo simulations in the cylindrical model, taking account of realistic size and axial ratio distributions for the sources?
- v What can we say about the previous studies that performed similar tests and how do they compare with our results?
- vi What can we conclude about the validity of the unification scheme from our results? Do any of our observations challenge the unification model?

In Section 4.2 we explore the data in detail and outline the sample selection process. In Section 4.3, we discuss the results from our study in detail, and compare our results with those of previous studies and with our simulations. In Section 4.4 we summarize our results and give answers to the above questions. In this study we use a cosmology in which  $H_0 = 70 \text{ km s}^{-1} \text{ Mpc}^{-1}$ ,  $\Omega_m = 0.3$  and  $\Omega_{\Lambda} = 0.7$ .

#### 4.2 Data Reduction and Analysis

#### 4.2.1 Data description

For our study we will be using the data from the LOFAR LoTSS deep field surveys (Best et al., 2023), providing source classifications for  $\approx 80,000$  sources. These are the deepest lowfrequency surveys yet carried out and are combined with deep multi-wavelength data spanning from the ultra-violet to far infrared, with an optical identification rate that approaches 100 per cent. Best et al. (2023) carried out spectral energy distribution (SED) fitting to the broad-band photometric data, which allow us to assess the contribution from the AGN and to identify galaxies that host radiative AGN. The deep radio survey covers the European Large Area ISO Survey Northern Field 1 (ELAIS-N1) field, the Boötes field, the Lockman Hole field and the North Ecliptic Pole (NEP) which total to 35 deg<sup>2</sup> of sky area. The LOFAR telescope has a resolution of 6 arcsec at 144 MHz if only the Dutch baselines are used, which is further improved to 0.3 arcsec with international stations included. The first data release (DR1) of the LoTSS Deep fields was focused on the ELAIS-N1 field, the Lockman field, and the Boötes field, and used only Dutch baselines, reaching an rms noise level below 20  $\mu$ Jy beam<sup>-1</sup>. The catalogue produced for each of these fields includes fluxes from ultraviolet to mid-infrared wavelengths obtained using optical ground based surveys and Spitzer surveys, and far-IR wavelengths obtained from Herschel data using the XID+ Bayesian tool (Kondapally et al., 2021). The total number of sources present in the catalogue is 81,951, out of which 31,610 and 31,162 sources are from the ELAIS-N1 and Lockman Hole fields, respectively, and the remaining 19,179 sources are from the Boötes field. These sources were then further classified into different classes, such as star-forming galaxies, Radio-quiet AGN, LERGs and HERGs, by Best et al. (2023). We refer to the value-added Best et al. catalogue as the LoTSS-DF catalogue in what follows.

To select a sample of quasars and radio galaxies from the above catalogue we also use the Sloan Digital Sky Survey (SDSS) Data release 16 which gives the largest available quasar catalogue (Lyke et al., 2020). The catalogue for the quasars was generated from the superset catalog and contains around 750,000 sources.

To carry out a test of the predictions of the unified model regarding source size with the LoTSS-DF survey we need two things: a catalogue of radiatively efficient radio galaxies and quasars,

selected in as closely matched a manner as possible, and linear size measurements for all of these objects. We describe how we obtain these in the following subsections.

#### 4.2.2 Radio selection

From the LoTSS-DF survey we obtain source information in three different fields, namely, the Boötes field, the Lockman Hole field and the ELAIS-N1 field with a total of 14,493 objects classified by Best et al. (2023) as RLAGN. We use the size information given by the LoTSS-DF catalogue although many sources are unresolved at the 6 arcsec resolution of LoTSS – only 1,293 RLAGN sources are resolved. The number of resolved sources for the Lockman, ELAIS-N1 and Boötes fields are 697, 340 and 256 respectively.

#### 4.2.3 Identification of quasars and narrow-line radio galaxies

Crucial to tests of unified models is a method for selecting quasars. Traditionally these were identified as objects that have broad lines in optical spectra and star-like appearance in optical images, but this method requires optical spectroscopy, which is often not available for large homogeneously selected samples. Most quasars, especially ones at high redshifts, are observed to be much bluer and redder in the optical and infrared respectively than the old stellar population that dominates massive normal galaxies. In addition, quasars also show time dependent stochastic aperiodic variability, at least of the order 10% for a year time scale. Some studies have used colour-colour plots (e.g., Warren et al. 2000; Richards et al. 2002; Croom et al. 2004; Stern et al. 2005; Maddox et al. 2012) and time dependent variability (e.g., Koo et al. 1986; de Vries et al. 2003; Vanden Berk et al. 2004; Sesar et al. 2007; Kozłowski et al. 2010; Schmidt et al. 2010; MacLeod et al. 2011) to select quasars. Using only the colour selection method has limitations, such as misidentification of true quasars and a high false positive rate. Similarly, the variability only selection method is limited by factors such as the contribution of the host galaxy to the luminosity, or reduced continuum due to Ly $\alpha$  absorption, and in addition requires multi-epoch observations. To overcome such effects, Peters et al. (2015) investigated the selection of quasars using both the colour and variability methods by using distinctive quantifiable characteristics of colour and variability. They found that by using the two methods the quasar completeness and efficiency reaches 97%, better than either method separately. Chaussidon et al. (2023) presented a quasar selection method in which they use three optical bands and two infrared bands. By using the optical bands and infrared bands, the excess emission from the infrared allows a clear segregation of quasars from optically similar stars and galaxies.

For the LoTSS-DF catalogue, the first step in the selection process of the quasar sample from the catalogues is to select radiatively efficient sources, as we know that they exhibit intrinsically quasar-like characteristics. In order to select quasars from these objects, we use the SDSS catalogue to define a color space where the quasars are in and then use that color space to get the quasar sample. Hence, initially, by cross-matching the LoTSS-DF RLAGN catalogue and the SDSS parent catalogue, SDSS catalogue containing 177 sources is obtained. From the Best et al. (2023) filtered LoTSS-DF catalogue, the numbers of radiatively efficient RLAGN sources for Lockman, ELAIS-N1, and Boötes field are 710, 510, and 524; the respective SDSS catalogue number of sources are 88, 52, and 36, respectively.

As we know that the sources in the LoTSS-DF catalogue are all radiatively efficient AGN, we can select quasars and assume that the rest of the sample are narrow-line radio galaxies. To do this we make use of flux information from different optical and infrared bands to construct colour-colour plots. We use the sources from the SDSS catalogue as quasar references to identify the region in colour-colour space that contains quasars, dividing the SDSS cross matched LoTSS-DF catalogue into 3 different redshift bins ( $z \le 1$ , 1 < z < 2, and  $z \ge 2$ ) since we know that observed colours will be redshift-dependent. The LoTSS-DF catalogue is used to test for unification in the ELAIS-N1 field, along with the Lockman and ELAIS-N1 fields combined sample as well. We perform the analysis on the Lockman field using more accurate length measurements, details of which are discussed in Section 4.2.5. In addition, we do not use the Boötes field in the analysis; the reasons for this choice are discussed in the upcoming section. Table 4.3 shows the number of sources in the sample for each redshift bin after we select the radiatively efficient sources.

Peters et al. (2015) used g, r, and i optical bands to construct a colour-colour plot and showed that it allows them to distinguish quasars from non-quasars. They also explored the colour-colour plots using the u band and report that the selection is much worse as the u band is affected by Ly $\alpha$  absorption. Similarly, Chaussidon et al. (2023) in their study used three optical bands g, r, and z, and two infrared bands W1 and W2, to construct a colour-colour plot where the colours obtained for the y-axis are given by; flux(grz) - flux(W). The relation used for flux(grz) = [flux(g)]+0.8\*flux(r) + 0.5\*flux(z)] and relation used for flux(W) = [0.75\*flux(W1) + 0.25\*flux(W2)]. Using the above colour-colour plots from the two studies we can select quasars from the different redshift bins. To maximize the number of sources we can include in our sample, we use optical band values from the different surveys present in the catalogue. If the g, r, i, and z colours are reported by the Hyper-Suprime-Cam (HSC) survey, we use those, otherwise we use the values reported by Red-sequence Cluster Survey (RCS). If both are not available then we use the values reported by the Panoramic Survey Telescope and Rapid Response Sysytem (Pan-STARRS-1) survey. We do the same for the two infrared bands, where if the values are available from the Spitzer Wide-Area Infrared Extragalactic Survey (SWIRE) then we use those, otherwise we use the values from the Spitzer Extragalactic Representative Volume Survey (SERVS).

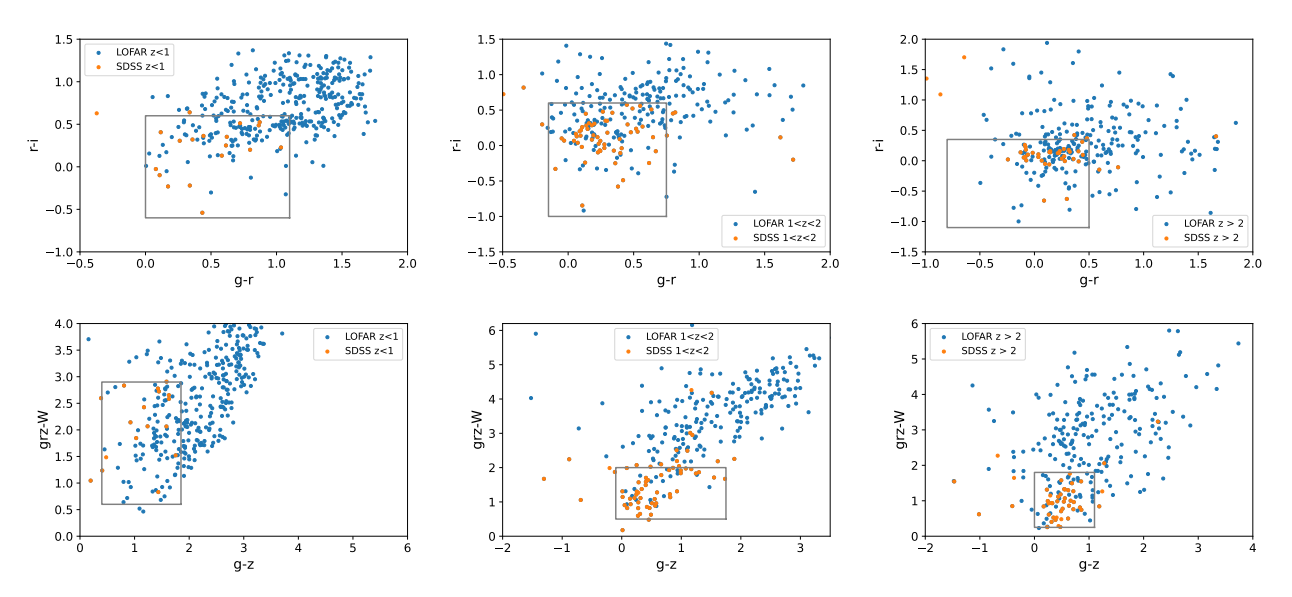
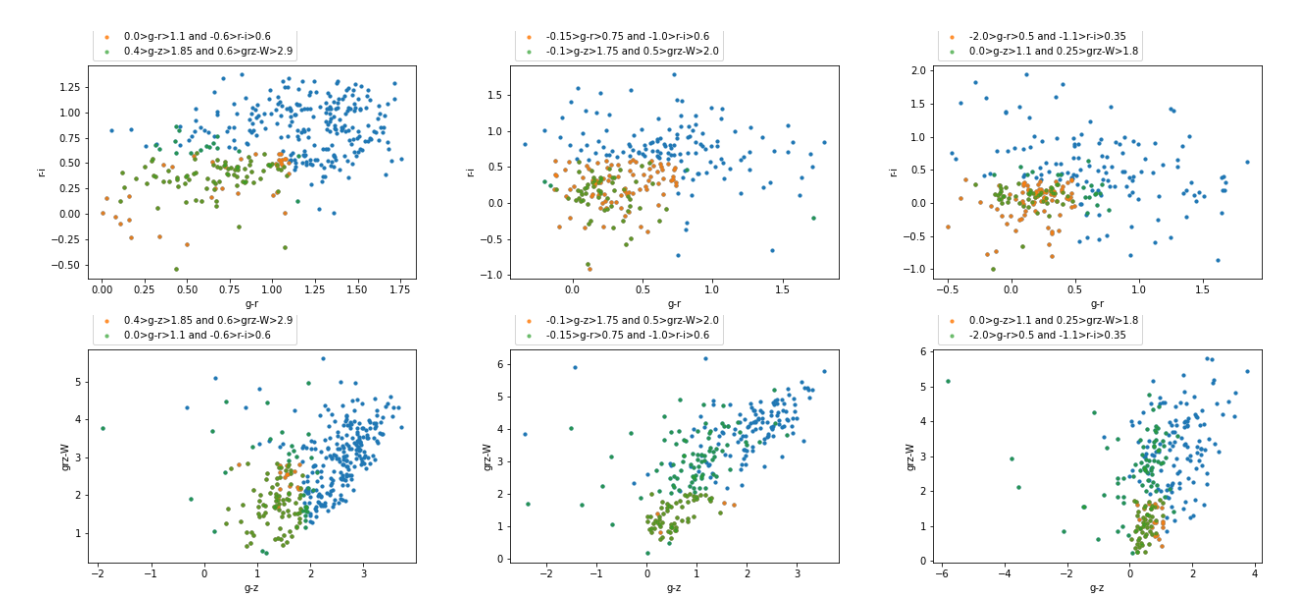


FIGURE 4.3: Top row shows colour-colour plot for the g-r-r-i bands and the bottom row shows colour-colour plots for the g-r-g/r2-W bands. The sample comes from the three redshift bins of the LoTSS-DF and the SDSS survey. The first column contains the z < 1 sample, the second column shows sources with 1 < z < 2 and the third column contains sources with z > 2.

#### 4.2.4 Sample Analysis

Using the above process we obtained a sample for the three redshift bands and for three different fields; these samples can be used to identify quasars and radio galaxies. We started by making the two colour-colour plots, namely; g-r versus r-i and the g-z versus grz-W for each redshift bin, where the known SDSS DR16 quasars are labelled as 'SDSS' (see Fig.4.3). For each redshift bin we can observe the line of separation for the two plots or identify a boxed regions using the two plots, where the quasars clump together. This region was defined separately for each redshift bin and two samples were created where the first sample only contained quasars (sources inside the box) and radio galaxies obtained by selecting sources using the g-r versus r-i plot. The other sample consists of quasars (sources inside the box) and radio galaxies obtained by selecting sources using the g-z versus grz-W plot. Next we checked if we have correctly identified the sources as quasars by overlaying the sources from the two plots for each redshift bin in order to see if the quasars that lie in the boxed region of the g-r versus r-i plot showed up in the boxed quasar region of the g-z versus grz-W plot and vice versa. The plots are shown in Fig.4.3 and Fig.4.4 with the colour-colour plots observed for the three redshift bins. Fig.4.3 shows the colour-colour plots with the LoTSS-DF and SDSS sample overlay which can be used to define the boxed regions and Fig.4.4 shows the sample comparison that was done by overlaying the sources on each other that are obtained from the boxed regions. We note that we use the same boxed regions for analysis of samples in the different fields listed above, in order to preserve consistency. We repeated the process for each field and combination of fields. We observe that for the Boötes field the optical bands available for the other two fields, such as g, r, and i, were



not present in the catalogue; we use these colours to extract quasars from the sample in each redshift bin. For this reason we were not able to use the field for the analysis. Hence, for our final sample we use only the Lockman Hole and ELAIS-N1 observations. Fig. 4.3 and 4.4 show the plots obtained by using the combined field information from the LoTSS-DF and the SDSS catalogue. We can see from the plots given in Fig.4.4 that the samples selected using the *g-r* versus *r-i* plot agree well with the sample selected using *g-z* versus *grz-W* plot. Accordingly, we extracted the quasars and radio galaxies by using the boxed regions from the *g-r* versus *r-i* plot, which can be further used to evaluate the total observed length of the sources, number of quasars and radio galaxies in each redshift bin, and the critical angle between the source axis and the line of sight.

#### 4.2.5 Sub-sample with accurate lengths

Sweijen et al. (2022), and submitted, have measured the angular length distribution of bright radio sources in the Lockman hole field on scales down to sub-arcsecond resolution, making use of the long baselines of the International LOFAR telescope (ILT). The sizes in the study are measured using a combination of high, intermediate, and standard resolution radio images where the sizes of resolved sources are primarily determined using gaussian fitting. In addition floodfill technique is applied to intermediate and high resolution resolution radio images to measure sizes for complex or irregular morphologies. The study measures sizes of 2,192 sources. Such high accuracy measurements will be useful for our study as we will otherwise be working with

sources that are unresolved in many cases. Hence, we use the size measurements reported by Sweijen et al. (2025), for the Lockman Hole field as we have high accuracy and sensitive measurements for this field. We create a separate catalogue (or a sub sample) where we join the LoTSS-DF catalogue and the catalogue created by Sweijen et al. (2025) to get accurate source sizes: this catalogue will be referred to as LoTSS-DFL from here on and contains 1005 sources. The LoTSS-DFL catalogue is essentially a subsample that will contain sources from LoTSS-DF catalogue (the initial Best et al. (2023) created catalogue) but with accurate length measurements obtained by Sweijen et al. (2025). As LoTSS-DF catalogue has already been matched with SDSS, we obtain the corresponding SDSS sources for the LoTSS-DFL catalogue. We will use the LoTSS-DFL catalogue when we want to conduct tests and analysis on the Lockman field alone.

As described in sections above, we first select for radiatively efficient sources where the selection reduces the number of sources in the LoTSS-DFL catalogue to 165 sources and the corresponding sources for the SDSS catalogue is 88. We emphasize that the LoTSS-DF catalogue alone presents challenges to tests of unified models due to the relatively small fraction of resolved sources, and hence, analysis using length measurements from a resolved catalogue can bear more reliable results and we are also limited by availability of accurate length measurements in the other fields. The LoTSS-DFL catalogue is divided in three redshift bins, in the same way as LoTSS-DF, where the number of sources in each bin is given in Table 4.3. Next, we segregate quasars and radio galaxies for different redshift bins using the color-color plots and the method given in Section 4.2.3 and 4.2.4, where we use the same quasar boxed regions to select sources. This process produces a final sub-sample that consists of sources that have accurately measured source sizes, and will be used in the testing as a stand alone analysis for the unification scheme.

#### 4.2.6 Simulation of source population

Mullin et al. (2008) present the relationship between the lobe axial ratio and the largest lobe linear size of the source for a sample of 98 3C sources obtained from a pointed survey with the Very Large Array (VLA) and the Multi-Element Radio-Linked Interferometer (MERLIN), observing that axial ratio depends on length, in the sense that larger sources tend to have smaller axial ratios. Using this relationship we can simulate a sample with an intrinsic size and axial ratio distribution similar to the distribution observed by Mullin et al. (2008), assuming the cylindrical projection model discussed in Section 4.1. First we defined the intrinsic (unprojected) length of the source to be distributed log-normally ( $\mu = 5.38$ ,  $\sigma = 1.07$ ), based on the fact that the maximum and minimum projected lengths of Mullin's sources lie between values close to  $\sim 10$  and  $\sim 2000$  kpc. Next, we know that the cosine of the angle to the line of sight  $\theta$  is uniformly distributed, and so we get the distribution of  $\theta$  by using the formula:  $\cos \theta = (1 - u)$  where u is a uniformly distributed variable. We use the measured critical angle (from the observed number

TABLE 4.3: Number of sources in the sample from the LOFAR and SDSS catalogue after filtering for radiatively efficient sources and the three redshift bins. For the Lockman Hole field we report sources from both the LoTSS-DFL and LoTSS-DF catalogue and for the other two fields we will use the LoTSS-DF catalogue. The first columns contains the fields, second column gives the redshift bins, the  $N_{\rm LOFAR}$  column shows the total number of sources in the LoTSS-DF/LoTSS-DFL catalogue, and the  $N_{\rm SDSS}$  column shows the total number of sources in the SDSS catalogue.)

Field	Redshift bins	$N_{ m LOFAR}$	$N_{ m SDSS}$
Lockman	$z \leq 1$	235	11
(LoTSS- DF)	1 < z < 2	207	43
	$z \ge 2$	268	34
ELAIS- N1	$z \le 1$	200	10
	1 < z < 2	127	26
	$z \ge 2$	183	16
Boötes	$z \le 1$	219	3
	1 < z < 2	119	20
	$z \ge 2$	106	13
Lockman	$z \le 1$	51	11
(LoTSS- DFL)	1 < z < 2	57	43
	$z \ge 2$	57	34

of quasars and radio galaxies) to select quasars and radio galaxies in the simulations. By using the axial ratio and the actual length of the source we obtain the projected length of the source, which is given by

$$L_{proj} = aL\cos(\theta) + L\sin\theta \tag{4.9}$$

where  $a = \frac{2r}{L}$ , L is the actual (intrinsic) length of the source, and 2r is the width of the lobe (cf. Eq. 4.5). However, we know that axial ratio cannot be a constant for a given sample and instead should follow some distribution. For this, we compare the distribution of the axial ratio versus the linear size obtained by Mullin et al. (2008) to the axial ratio versus the linear size plot obtained by simulation to model the distribution of the axial ratio. We can do this by adjusting the parameters of the distribution of axial ratio that we obtain comparing the plots from Mullin et al. (2008). We observe a cut off in the observed axial ratio distribution greater than 0.1 in the Mullin et al. (2008) sample, which becomes a constraint for our simulation. The distribution comparison shows that the axial ratio has a dependency on the actual source lengths, and we use the Rayleigh's distribution to model its scatter. The distribution is given by;  $a = (1.605 + 0.0046l) \times R(x, \sigma = 0.75)$ , where  $R(x, \sigma = 0.75)$  is Rayleigh's distribution with scale factor ( $\sigma$ ) of 0.75 and x is a random value. Now for each source in the simulation we can generate their projected lengths, true axial ratio and use them to get the projected axial ratio. We

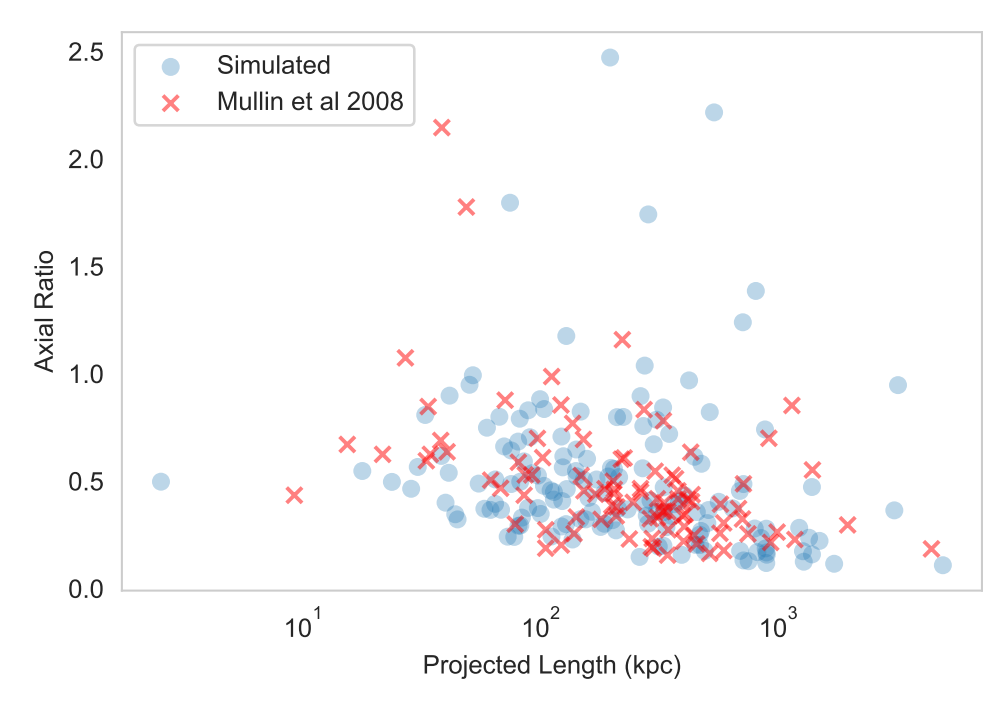


FIGURE 4.5: Actual length of the sources versus the axial ratio of the source, comparing the results of our simulation with 150 sources and the distribution observed by Mullin et al. (2008). We see good agreement between the two distributions.

.

truncate this distribution so as to avoid generating any source that has an axial ration less than 0.1. The observed distribution of lobe length and axial ratio from simulation using the above parameters is overlaid on the Mullin et al. (2008) data in Fig. 4.5. The simulated distribution agrees well with the Mullin et al. (2008) observations where we used the Kolmogorov-Smirnov test to compare the two distributions for varying parameter values. The parameters that generated highest statistic value and the lowest p-value were used. Hence, we use these parameters for the unification tests.

We also note that the LoTSS-DF has a resolution of 6 arcsec which means that length measurements would be accurate for a source having angular size greater than 6 arcsec. Therefore, we also take into account the resolution constraints of the survey. We do this by estimating Gaussian kernel density for the redshift distribution obtained from the LoTSS-DF catalogue. We can use this to resample and generate random redshift values that lie within the same distribution as seen in LoTSS-DF catalogue. Using the simulated redshift values we can get angular sizes of sources in the simulation. Next, we look at the angular size distribution of sources from the LoTSS-DF catalogue in order to match the simulated sources to observed ones with finite resolution. Based on the sample we choose to analyze we reassign the angular sizes of sources smaller than some critical value to have an angular size drawn from the distribution observed in LoTSS-DF catalogue for unresolved sources for the given sample. We do this for the different samples that are

TABLE 4.4: Critical angle, expected linear size ratio of the stick model and observed linear size ratio for sources in different redshift bins. For Lockman alone we use the more accurate length measurements obtained by Sweijen et al. (2025) (the LoTSS-DFL catalogue) and for the rest we use the lengths measured in the LoTSS-DF catalogue. The first columns contains the fields used for the analysis, the second column gives the redshift bins, the  $N_q$  and  $N_{rg}$  columns show the number of quasars and radio galaxies,  $\theta_c$  is the measured critical angle (ref. Eq. 4.1),  $Ra_{exp}^{St}$  is the expected length ratio for the stick model (ref. Eq. 4.4),  $Ra_{obs}^{mean}$  and  $Ra_{obs}^{median}$  are the observed mean and median length ratios for the sample respectively,  $Ra_{obs}^{Cy}$  is the length ratio for the cylindrical model where the values lying in the 95% confidence region are presented, and  $Ra_{3\sigma}$  is the length ratio for the cylindrical model where the values lie in the  $3\sigma$  interval for 1000 iterations.) We do not use truncation for the simulations done to match the Lockman field.

Field	Redshift bins	$N_q$	$N_{rg}$	$\theta_c$	$Ra_{exp}^{St}$	Ra <sub>obs</sub> <sup>mean</sup>	$Ra_{obs}^{median}$	$Ra_{95}^{Cy}$	$Ra_{3\sigma}^{Cy}$
Lockman	$z \le 1$	16	23	53.86°	0.60	0.35	0.83	0.41-1.97	0.25-2.73
	1 < z < 2	27	18	66.42°	0.68	1.74	1.69	0.44-1.92	0.27-2.96
	$z \ge 2$	14	17	56.74°	0.62	1.54	1.22	0.35-2.09	0.25-4.32
ELAIS- N1	$z \le 1$	63	124	48.46°	0.56	0.89	0.64	0.59-1.25	0.42-1.41
	1 < z < 2	58	57	$60.28^{\circ}$	0.64	0.54	1.02	0.55-1.46	0.37-1.91
	$z \ge 2$	64	53	63.06°	0.66	0.90	0.95	0.56-1.43	0.40-2.20
Both fields	$z \le 1$	115	249	46.83°	0.55	0.74	0.66	0.64-1.08	0.54-1.25
	1 < z < 2	143	129	61.68°	0.65	0.82	1.09	0.67-1.25	0.55-1.52
	$z \ge 2$	126	141	58.12°	0.63	1.07	1.02	0.67-1.21	0.52-1.43
Both fields	$0.25 \le z \le 1.75$	142	347	44.80°	0.53	1.01	1.16	0.64-1.05	0.51-1.17

used for the analysis discussed in the section below. We can divide the simulated data points into quasars and radio galaxies by defining a critical angle which is chosen based on the critical angle observed in the corresponding observational data. We note that the resolution truncation will be used when comparing to the results from the LoTSS-DF catalogue only.

#### 4.3 Results

As stated in Eq. 4.1 and Eq. 4.4, we can find the critical angle and the ratio of lengths for the sample of quasar and radio galaxies for the three redshift bins in different fields. We used the two fields for which the data distinguishing between quasar and non-quasar radiative AGN are available, i.e. the Lockman field and the ELAIS-N1 field. We also report results observed by combining the two fields, where the length values for the Lockman Hole field are taken from the LoTSS-DF catalogue. This gives us a larger sample size to analyze. Table 4.4 shows values of the critical angles and the linear size ratios for different redshift bins. The table also reports a

fourth row consisting of sources from different redshift ranges, which will be discussed in detail in Section 4.3.2. As we have used the length measurements derived from Sweijen et al. (2022), which are accurate up to sub-arcsec precision, for the Lockman field, comparison simulations do not use the resolution truncation.

#### 4.3.1 Critical Angle and Sample Size

For all three redshift bins, in the Lockman field, ELAIS-N1 field, and both field observations, we can see that the critical angle estimated from the numbers of sources is above  $45^{\circ}$ , and the largest value is as high as  $66^{\circ}$ . This differs from the critical angle of  $\sim 45^{\circ}$  obtained by Barthel (1989): in other words, there are more quasars than would be expected. Taken at face value, this means that we should be able to observe quasars at much higher angles than expected, i.e. sources of much greater sizes can be classified as quasars rather than radio galaxies if the orientation based model holds.

The smallest sample size is observed for the Lockman field, where the number of quasars is higher than that of radio galaxies for the 1 < z < 2 redshift bin. This leads to a higher critical angle value compared to other two redshift bins in the Lockman field. We note that the number of quasars and radio galaxies are similar. For the ELAIS-N1 field the sample size is much higher than we obtain for the Lockman field, which is expected as we are not limited by the use of the high-resolution data. We see that the sample size is highest for the  $z \le 1$  redshift bin and the difference between the number of quasars and radio galaxies is also largest. We also note that the critical angle is much closer to 45° for this bin in the field. In the results obtained for the analysis of both fields, where we use data from the Lockman field and ELAIS-N1 field combined, we have the largest sample size, but, we observe that the gap between the number of quasars and radio galaxies is still not large, except for the z < 1 redshift bin, and as expected this bin shows a critical angle value much closer to  $45^{\circ}$  as compared to the critical angle seen in the ELAIS-N1 field for the same bin. Even with the higher total sample size provided by combining the two fields we observe critical angles greater than 60°, which means that we can potentially still observe quasars in greater numbers than would be expected. This prompted us to explore the completeness of the samples that we are using, and we discuss this in the next section.

#### 4.3.2 Construction of an unbiased sample

After investigating the results obtained for the different fields and our original fixed redshift bins, we also looked at the luminosity and redshift distribution of the entire quasar and radio galaxy sample using both the Lockman and ELAIS-N1 fields (see Fig.4.6). We know that the quasars' and radio galaxies' radio luminosity should not depend on their orientation and, in particular,

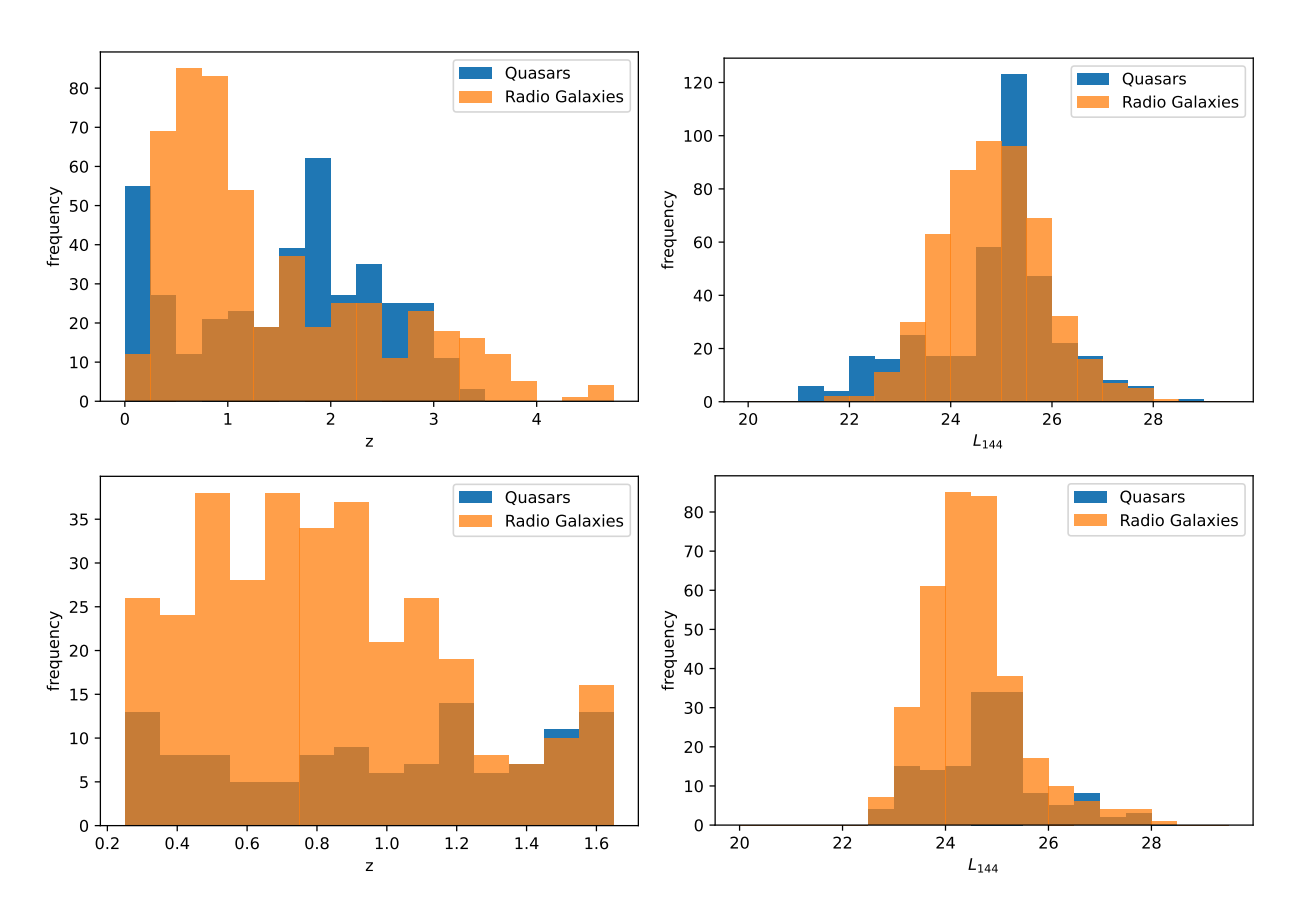


FIGURE 4.6: Top row shows the distribution of the redshift and the luminosity using the full sample of quasars and radio galaxies obtained from the three redshift bins combining both ELAIS-N1 and Lockman data. Bottom row shows the distribution of the redshift and the luminosity for the subsample of these quasars and radio galaxies between z = 0.25 and z = 1.75.

the distribution of the two should be similar. As a check of this, we combined the quasar and radio galaxy samples from the three redshift bins and constructed a redshift and luminosity distribution plot for the combined sample. We can see from Fig. 4.6, the redshift distribution that at very low redshift (z = 0 to 0.25), the number of quasars is much higher than the number of radio galaxies. Most likely this indicates contamination of the sample by radio-quiet quasars; the galaxy counterparts of these objects are hard to identify since they may not show an AGN excess over the expected radio emission from star formation. We also see a varying distribution of the numbers of quasars and radio galaxies over the entire redshift range where the fraction of quasars increases at higher redshifts. This could be due to incompleteness of the optical counterparts for the radio survey as galaxies are systematically harder to detect than quasars at higher redshift. Inspecting the plots, for the total sample a range that shows roughly uniform redshift distribution for galaxies and quasars is from z = 0.25 to z = 1.75. When we plot the luminosity distribution for the total sample we can similarly see a shift in the luminosity peaks and non-uniform distribution of the quasars and radio galaxies, particularly in the sense that there are a number of low-luminosity quasars without radio galaxy counterparts.

We therefore also extracted the quasars and radio galaxies in the range 0.25 < z < 1.75 to form

a sub-sample of quasars and radio galaxies that is as free as we can make it from biases such as incomplete surveys or anomalous distribution. In Figure 4.6, we can see that for these redshifts the distribution is quite uniform and the number of radio galaxies is higher over the redshift range, as expected. We can also see from the luminosity plot for this redshift range that the radio galaxies and quasars have similar distributions. When we run the statistics to check the critical angle, as shown in Table 4.3, we can see that the number of sources for quasars and radio galaxies in this range is much higher than any other range in the table where the gap between the number of quasars and radio galaxies is the widest observed as compared to others. We can also see that the critical angle is very close to the expected critical angle of 45°. These results point out that completeness of data is important and affects the critical angle estimation for any sample for any given redshift bin. Other past studies that found large critical angles may have been affected by this type of bias.

#### 4.3.3 Mean Length Ratio

A widely used metric for testing unified models, based on the work of Barthel (1989), is the ratio of the mean or median lengths of quasars and radio galaxies, where we can compare predicted values from Eq.(4.4) with the observed lengths of the sources in the sample. We can see from Table 4.4, that the size ratio expected from the stick model measured using the equation lies between 0.55 and 0.68 which implies that the lengths of the quasars should be around half the lengths of the radio galaxies. The observed mean and median values of the ratio in the two fields and their combination show much higher values than this: in fact the ratio is above 1 for the samples in the Lockman field at 1 < z < 2 and  $z \ge 2$  bins, meaning that the lengths of quasars are greater than the radio galaxies, which is clearly not expected in any model in which quasars are more projected. Even for large sample sizes we can see the ratio to be close to or above 1 for some bins. One can point towards the use of complete data, as done in the 'both fields' row in the  $0.25 \le z \le 1.75$  redshift bin, and the use of high-resolution observations for more accurate length measurements, as reported in the Lockman field row of Table 4.4, but even these two show mean and median length ratio values greater than 1 which on the face of it is inconsistent with the simple unified model using simple length projection (the 'stick model').

However, if we consider the cylindrical model for the scheme, the typical size ratios will always be larger than the stick model predicts, and may very well be close to unity for large axial ratios. Given the small numbers of sources in typical samples and the broad distribution of observed axial ratios, we cannot necessarily rule out the unified model simply due to an observed quasar/radio galaxy mean size ratio > 1.

We can find the range of expected length ratio values for the samples used in the study by running the simulation (described in Section 4.2.6), which uses the same parameters as seen in

Table 4.5: Predicted range of length ratio at  $3\sigma$  (99.86 per cent confidence) using the cylindrical model simulation for a given critical angle and 10,000 iterations. The rows give increasing sample sizes and columns show assumed critical angles where each critical angle column reports length ratio values obtained with and without resolution truncation.

	45°		55°		65°	
Critical Angle Sample size	Non Truncated	Truncated	Non Truncated	Truncated	Non Truncated	Truncated
500	0.56 - 1.20	0.52 - 1.21	0.62 - 1.26	0.61 - 1.26	0.63 - 1.34	0.64 - 1.35
600	0.58 - 1.16	0.55 - 1.17	0.64 - 1.21	0.63 - 1.24	0.66 - 1.30	0.66 - 1.29
700	0.61 - 1.14	0.58 - 1.13	0.65 - 1.21	0.65 - 1.21	0.68 - 1.25	0.68 - 1.26
800	0.62 - 1.12	0.60 - 1.12	0.65 - 1.16	0.67 - 1.17	0.70 - 1.23	0.68 - 1.24
900	0.62 - 1.09	0.62 - 1.10	0.68 - 1.14	0.67 - 1.18	0.72 - 1.22	0.70 - 1.23
1000	0.63 - 1.08	0.63 - 1.08	0.69 - 1.12	0.69 - 1.13	0.72 - 1.20	0.72 - 1.20

Table 4.4; this allows us to produce a sample that is matched to the observations in terms of critical angle and sample size for a given distribution of lengths and axial ratios. For a large number of iterations of the same parameter conditions, we can produce different samples of sources and obtain the predicted range of length ratios by looking at different intervals. In order to make a comparison of the observed results with the cylindrical model and examine the possible length ratio ranges after which unification model might fail, we report length ratio ranges at the 95% confidence interval and  $3\sigma$ , shown in Table 4.4 columns,  $Ra_{95}^{Cy}$  and  $Ra_{3\sigma}$ . We do this to show the extent of possible length ratio values that could be obtained for a model that takes varying axial ratio into account. If the observed ratio of sizes were out of the  $3\sigma$  range, we could say that the unification model could be rejected at that confidence level. However, we can see that the observed mean median values lie within the 95% confidence range for all samples in the table, except the  $0.25 \le z \le 1.75$  redshift bin row. For this sample, which is the best we have available, the observed median value lies close to the  $3\sigma$  upper range expected from simulation, which indicates that we are close to but not actually at the point where we would have to conclude that the unification model could be rejected. We note that the range in columns  $Ra_{95}^{Cy}$  and  $Ra_{3\sigma}$  is wider for small sample sizes, as expected, so that the probability of rejecting the unification model is lower for small sample sizes. But as the sample size increases the range decreases and the expected length ratio starts converging. We explore the effects of sample size in Section 4.3.4, where we discuss results from simulations.

#### 4.3.4 Simulation Analysis of Length Ratios

In this section we explore the distributions of length ratios observed for different sample sizes and critical angles. The unification scheme predicts that critical angle could be somewhere near  $45^{\circ}$ , and a reasonable starting point for simulations is a sample size of 500 as seen in Table 4.4 for the 'Both Fields' row at  $0.25 \le z \le 1.75$  bin. Hence, we start by setting the critical angle to  $45^{\circ}$  and incrementing it by  $10^{\circ}$ . Similarly, we start with a sample size of 500 and increment it by  $10^{\circ}$  for each critical angle producing length ratio values for 10,000 iteration and observing their

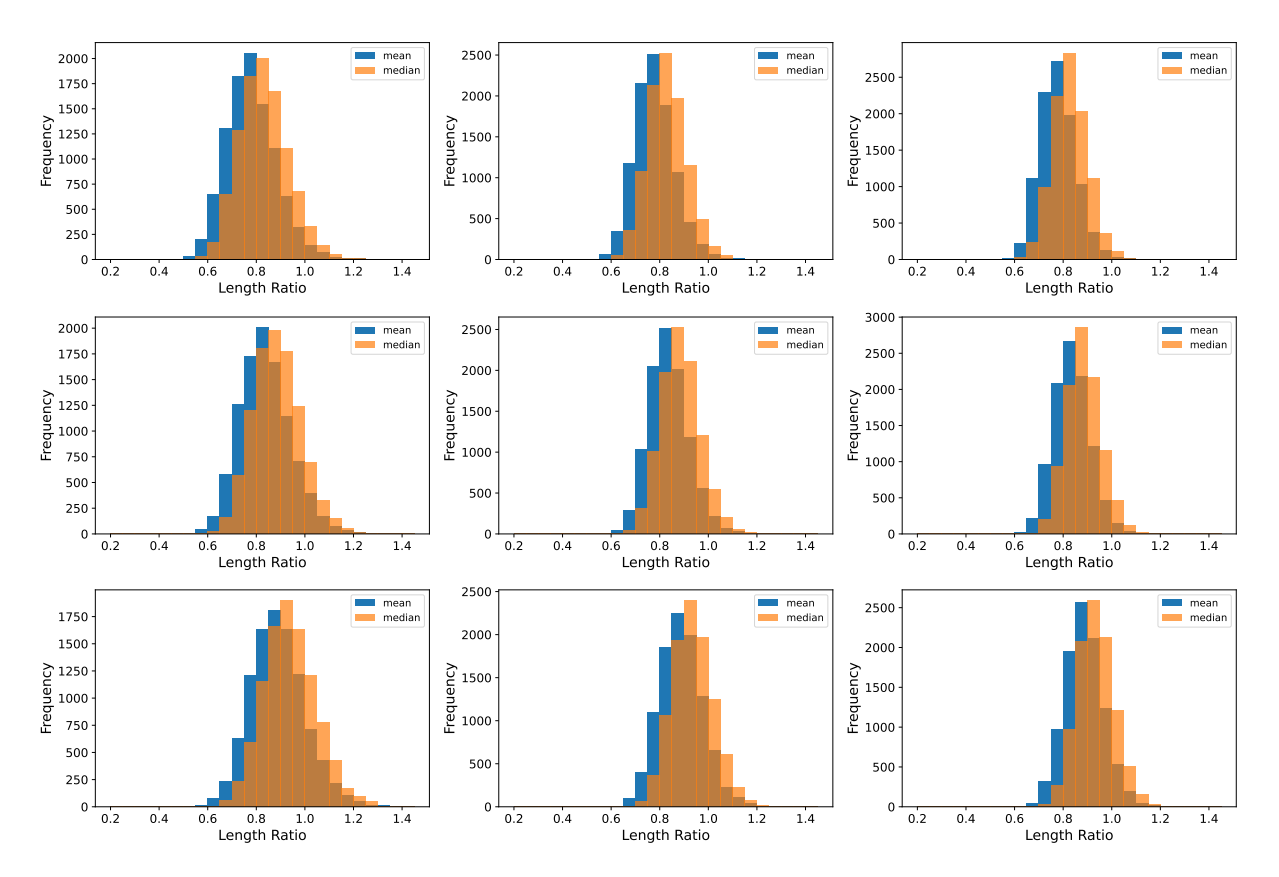


FIGURE 4.7: Distribution of ratios for average quasar linear size to average radio galaxy linear size for a sample size of 500, 800, and 1000 for different critical angles of  $45^{\circ}$ ,  $55^{\circ}$ , and  $65^{\circ}$ , with 10000 simulations. The three columns represent the distributions for three sample sizes (500, 800, 1000) and the three rows represent the distribution at the three critical angles ( $45^{\circ}$ ,  $55^{\circ}$ ,  $65^{\circ}$ )

distribution. For each sample size and critical angle pair we can obtain length ratio ranges at  $3\sigma$  confidence, giving the range outside which the unification model could be rejected. We report these values in Table 4.5, where for each critical angle there are two sub-columns showing length ratio values obtained with and without truncation. We note that in this section we only discuss the simulation results that do not involve the resolution truncation, i.e. the 'Non Truncated' column of each critical angle in the table. We assume that the sample is complete and contains only resolved sources, which could be useful for future survey comparisons that will produce high resolution data. In addition, in Fig.4.7, we plot the distribution of length ratios for 10000 iterations with the different critical angles and increasing sample sizes as described above.

We observe from the table that for the lowest critical angle of 45° and sample size of 500, we obtain the widest length ratio range. As we increase the sample size for a given critical angle the range starts converging to a central value. Similarly, we see that as we increase the critical angle for a given sample size the range starts shifting to the right, i.e. we obtain much higher length ratio ranges. This is expected as we move to higher critical angles, since the number of quasars of larger sizes increases and hence so does the length ratio. From Table 4.5 we can see that as the sample size increases the length ratio range converges. In addition, Fig. 4.7 shows

that all distributions peak at values between 0.8 and 0.9, which means that for an optimal sample size there are high chances of observing length ratios between these values. Hence, it is clear from the analysis that changing the critical angle and sample size changes the length ratio at which we can reject the unification scheme, if we use the cylindrical model. For the redshift range  $0.25 \le z \le 1.75$ , Table 4.4 shows a length ratio that is close to being inconsistent with unification, where the critical angle is close to  $45^{\circ}$  and sample size close to 500.

In the next section we explore the resolution effects in detail and also the possible reasons behind different length range observations. The key conclusion from this section is that the ranges of length ratio that would allow a rejection of the model are different for different sample sizes and critical angles, even if the sample is unbiased and all sources are well resolved.

#### 4.3.5 Effects of Resolution

In this section we explore the effects of observing at a finite resolution on the length ratio range. We do this to understand how the quality of the data can affect the outcome of the test. In this section we discuss the values obtained after applying the resolution truncation, assuming that the sample is complete. We report the values in Table 4.5 under the 'Truncated' column for each critical angle and compare the values observed in the 'Non Truncated' columns. From the two sub-column observations we can observe that the values are quite similar. There are few changes in the size ratio ranges between the two pairs of columns in each critical angle although where they differ it is usually in the sense that truncation makes the range of possible ratios larger. In principle, truncation should have some effect on the size ratios of these observations, but we note that the angular size distribution at which we place the angular size selection is limited by the model, which is built by replicating data obtained from a sample of bright sources (Mullin et al., 2008) that contains axial ratio distribution information that is crucial for building the model. The 3CRR sources used by Mullin et al. (2008) may not be well matched to the LoTSS data, which are taken from a survey of higher sensitivity and therefore include many lower-luminosity sources. This is why when we compare the fraction of objects that fall below the truncation cut in the simulation versus the objects present in the LoTSS sample, it is only around 20% to 30% which is too low to show any major effect on the size ratios, and contrasts with the unresolved fraction of 93% seen in the data. Overall, the simulated 'Truncated' observations show similar trends to the 'Non Truncated' observations, with minor changes in the expected length ratio ranges. The difference seen in length ratio value with truncation for the 'Both fields'  $0.25 \le z \le 1.75$  bin, which is the best sample so far available to us, could be different (and most likely would be less constraining of the model) if a sample observed at high angular resolution with axial ratio information is used to build a model that could represent the actual LoTSS sources that we observe. This work is beyond the scope of the current chapter but could be carried out using the high-resolution observations by Sweijen et al. (2022) and de Jong et al. (2024).

#### 4.3.6 Implications for previous tests of unified models

We have discussed previous studies of the orientation based unification scheme in Section 4.1.3, where we briefly summarized the different conclusions presented by different investigations. We have seen that some studies present evidence in support of Barthel's unification scheme and some studies present evidence against it. However, in all of the investigations previously carried out, we can note that the number of sources used is consistently low. For almost all studies in Table 4.1 and 4.2, the total number of sources is less than 200 for the entire range of redshift used. There are a few exceptions, such as the work of Gopal-Krishna and Kulkarni (1992) in Table 4.1, Singal (1996), and Singal and Laxmi Singh (2013) in Table 4.2, where previous work has a sample size that is comparable to the sample size that we would consider appropriate to perform the unification test. However, these studies have other problems, In the study performed by Gopal-Krishna and Kulkarni (1992), the radio galaxy sample comes from a complete flux-limited catalogue, which is not true for the quasar sample, where more than half of the quasars are at low redshift (z < 1.5) and the sources are not homogeneously selected. For the study conducted by Singal (1996), the sources are homogeneously selected from different surveys, such as 3CRR, MQC, and B3, and are thus obtained by selection from different fluxlimited samples. Hence, the total number of sources might be high but the comparisons are made for different homogeneously selected sources from different surveys, which cannot be considered as a single total sample but rather different samples for which a similar analysis is made. Similarly, in the study of Singal and Laxmi Singh (2013), the sources in the sample come from two different surveys, that is the 3CRR survey and the MRC survey. The number of sources in each sample from the two surveys are smaller than the number quoted in our simulation outcomes.

Overall, the number of sources used in the samples from previous studies often have considerably lower sample size with respect to the sample size of more than 800 sources that we propose to be necessary to test for orientation based unification scheme, and/or do not use a uniform selection. From the results of the simulations described in this study, we can see that a small sample size results in a wider predicted length ratio range, and hence a higher probability of obtaining size ratios greater than 1 simply because of the random scatter imposed by the intrinsic distribution in radio galaxy axial ratio. Such results would on the face of it imply that the size of the quasars are systematically greater than radio galaxies, which would be inconsistent with a unified model, but we have shown that they are not unexpected when the cylindrical projection model and a realistic axial ratio distribution are used, especially when the sample size is small. If a large homogeneously selected sample is used, then there is a low probability in the

unified model of observing a large size ratio, although as the results from simulations suggest, this might still not be enough to reject the model as the rejection ranges are different for any given critical angle and sample size. Our simulations show that the stick configuration used by many previous studies does not give reliable expected size ratio values and leads to unrealistically small expectations for the size ratio. Once we move to a cylindrical configuration and take into account a realistic distribution in source axial ratio we start to notice that expected size ratio measurements could be much higher. This is expected for an orientation based theory because as the source, which has a cylinder-like shape, is tilted towards the observer, the diameter of the lobe will come to dominate what is seen projected on the sky. Hence we conclude that sample size plays a pivotal role in establishing the validity of the orientation based unification scheme. As noted in the above discussion, the sample sizes used in many previous investigations are not high enough to give reliable results; for these small samples, the probability of obtaining length ratios greater than 1 simply by chance is relatively high, which means that observed length ratios greater than 1 would still not be enough to reject the unification scheme. So in general previous studies neither support nor rule out unified models at any high significance level. We emphasise, however, that analysis based on length ratios that purports to support the unified model, such as the original work of Barthel (1989), must also be discounted given the small sample size.

#### 4.4 Conclusions

In this study we have used the LOFAR Deep Field data (Best et al., 2023) to obtain a sample of AGN that can be used to test the unification model of Barthel (1989). The sample consists of quasars and radio galaxies which are selected based on the colour plots obtained using the g, r, i, and z optical bands along with the W1 and W2 infrared bands. By using the colour-colour plot relations investigated by Peters et al. (2015); Chaussidon et al. (2023) we constructed colour-colour plots and compared them with the SDSS-DR16 quasars catalogue (Lyke et al., 2020) to obtain colour limits that were used to segregate quasars from radio galaxies. We have constructed different samples using the LoTSS data, making use of the measurements of Sweijen et al. 2022 to get accurate lengths for the Lockman Hole field. The sample we used is limited to the Lockman Hole and ELAIS-N1 fields and is separated in different redshift bins. We have used these samples to evaluate the critical angle and the size ratios for quasar and radio galaxy separation using the stick model and the cylinder model, and compared these results with values predicted by simulations. Also, we obtained various length ratio ranges for varying sample size and critical angles from observed results and uniformly incremented parameter values by using simulations.

In the analysis we have also run simulations to obtain the critical angles for the different redshift bins and their respective linear size ratios. For the simulation we assume that the sources have a cylindrical configuration where the length of the cylinder is the actual length of the source and the lobe width is the diameter of the cylinder. According to the orientation of the sources the cylindrical model implies that both the intrinsic length and width (or axial ratio) are involved in calculating the projected sizes of the sources. For 1000 different iterations of the simulation and varying the sample size of each simulation we obtain the expected linear size ratios at a given critical angle. We compare the results obtained from the simulation and the results obtained from the deep field sample to test the validity of the orientation based unification scheme. An important point to note here is that according to the orientation based unification of AGN, the quasars and radio galaxies, if derived from the same population, should be intrinsically indistinguishable. Hence, the results should show that the observed sizes are only affected by geometrical projection. Because the scheme relies on the orientation to distinguish between a quasar and radio galaxy there should also exist a critical angle that separates the two types. Hence, the critical angle plays a crucial role in the analysis. Further, we have also explored the effects of resolution on length ratio ranges and compared our results with previous investigations.

Keeping the orientation based unification scheme conclusions in mind and incorporating the results from the observed and simulated data, we can answer the questions raised in Section 4.1:

- i In our results, we observed that for the two fields together and individually, the critical angles are greater than 45° and overall go as high as 66°. We note that the sample size also varies between the different fields and a small or large sample size still produces varying critical angles. The angles vary for different redshift bins but do not show any trend with redshift. We observe that for some bins in the fields the number of quasars and radio galaxies are similar to each other or even that there are sometimes larger numbers of quasars than radio galaxies, which leads to the large critical angles. Using our best attempt at selection of an unbiased sample, as shown for the redshift bin  $0.25 \le z \le 1.75$  in Table 4.4, we obtain a critical angle close to  $45^{\circ}$  in our sample of observation. We conclude that high values of critical angle may be the results of selection effects, and complete and unbiased data are required to make reliable measurements.
- ii From the critical angle values obtained from observed data, we obtain expected ratios of the quasar to radio galaxy linear sizes that are around 0.5 to 0.6 for any redshift bin in the fields, using the stick model. These values are not close to the observed mean or median values of linear size ratios. The linear size ratios sometimes show values greater than 1, for both mean and median observations. These values seem alarming as ratios greater than 1 mean that the typical size of the quasars in the sample is greater than the size of the galaxies in the sample, which is not expected for orientation based unification. This is true even for our most carefully selected sample.
- iii We take into account the cylinder model which considers the axial ratio of a source, and run a Monte-Carlo simulation for the sample sizes and critical angles observed in the different

fields. We obtain a size ratio range that predicts the required value of length ratio that can be used to reject the unification scheme. This range is dependent on critical angle and sample size, where the means of the ranges typically lie between 0.8-0.9. The predicted  $3\sigma$  ranges for the different fields and redshift ranges are greater than 1 for almost all observations, which shows that quasars can show sizes greater than radio galaxies with finite probability when the non-zero value and broad distribution of the axial ratios of the sources are taken into account. For our observations the mean and median length ratio lie well within the  $3\sigma$  length ratio range, meaning that unified models cannot be rejected, and only one of the redshift bin,  $0.25 \le z \le 1.75$ , is close to value of rejection. We argue that in order to test the orientation based scheme the width of sources should be taken into account and size ratio greater than 1 cannot be used to reject the scheme; size ratios greater than 1 do not rule out the unified model with high confidence as long as they lie within the  $3\sigma$  range shown in this study for different critical angles and sample sizes. However, the larger the sample size, the higher the probability of rejecting the unified model for a given observed size ratio, so long as the data are complete and homogeneously selected.

- iv Modeling reveals that the axial ratio distribution is dependent on the true length distribution of the sources and in addition has scatter that we model using a Rayleigh distribution where we have used data from the work of Mullin et al. (2008) to model the axial ratio dependence on length. Furthermore, in our modeling for the cylindrical configuration we truncated the projected axial ratio to be less than 0.1 to observe consistency with the Mullin et al. (2008) data. In our simulation we are able to account for resolution effects, where we reassign the angular size of a source to be drawn from a Gaussian, depending on the sample used. We observe that the fraction of unresolved sources obtained by simulation is around 20% to 30%, whereas the fraction of unresolved sources in the LoTSS-DF data is around 93%. Such a small fraction compared to the LoTSS data gives rise to the negligible change seen in size ratio range with and without resolution truncation. Hence, we conclude that for more accurate simulation results and size ratio ranges we require axial ratio information that is representative of LoTSS sources. In future work we will attempt to derive this information from large numbers of LoTSS sources observed at high resolution.
- v Previous studies have presented statistical tests of the orientation based unification scheme, similar to the tests that we have performed, that provide evidence either against or in support of the scheme. However, an aspect common to all these studies is the use of small samples from less sensitive surveys than are now available; in addition, some use non-homogeneous selection, and some have incomplete data. These investigations have all relied on the stick model of projection to draw their conclusions, but we have argued that the cylinder model is a much more realistic representation of the sources for orientation based unification testing. Many studies have proposed that the unified model should be rejected if size ratios greater than 1 are observed, but as we have shown, this should be updated to a size ratio range

that is a function of the critical angle, sample size and assumed axial ratio distribution. If we compare the results obtained from our observed data and the data used in the previous investigations, the discrepancy in the length ratios or the observation of high scattering in the critical angles is common. Our results show that when we increase the sample size and use complete samples, the chances of observing such discrepancy decreases and size ratio range is better constrained.

vi From the results of the observed data alone we might be able to come to a conclusion that the orientation based unification of AGN does not hold. We have observed ambiguous values for the critical angle and ratio of the lengths for the two types of sources, although simulations suggest that there are different acceptable ratio ranges that can validate the unification scheme. Hence, varying values of length ratio are not surprising, even if they are greater than 1. As for critical angles, we determine that complete samples are required to obtain reasonable estimates, where unbiased selection of quasars and radio galaxies is possible. We also note that by increasing the sample size we can obtain better constrained estimates of length ratios and reduce the chances of observing discrepancy in ratios. Furthermore, the analysis used for simulation, apart from size distribution of the sources and the shape of the sources, considers resolution restrictions. The resolution constraint does not seem to affect the results to a large extent, but this could be due to the use of only luminous sources to construct the linear size distribution model. We do not take into account the evolutionary process of the AGN, the luminosity dependencies or the fact that there are still other types of sources, such as the LERGs, that might be affecting the AGN population and its properties. We suggest to use large sample sizes for such tests with more accurate and sensitive surveys to at least reduce the bias due to the selection or geometry of the sources. The use of large, complete samples in different redshift bins will give more accurate and reliable results that can shed more light on the unification of AGNs without worrying about the errors due to geometry or the selection.

## **Chapter 5**

# **Summary and Conclusions**

In this thesis I have explored three different methods used to understand the properties of RLAGN. In Chapter 2 I measured and studied the spectral age distribution of different RLAGNs on a pixel by pixel basis; in Chapter 3 I investigated the correlation observed between spectral index and redshift, and spectral index and luminosity, later comparing them with observations made in previous studies; and in Chapter 4 I inspected the orientation based unification scheme for radiatively efficient AGNs by testing and investigating parameters like critical angle and size ratios using sample observations and simulations of different configurations. For all three studies I have used large datasets which are of arcsecond resolution and high sensitivity. The highest sensitivity data used is from the MIGHTEE survey, presented in Chapters 2 and 3, which has also acted as a reference catalog to select and inspect sources in the studies based on it. In addition, for these two studies, using combination of surveys and different selection criteria I was able to produce samples of sizes that have not been used before, helping me to derive statistically significant results and constraining parameters. For the study described in Chapter 4, I have used deep field data from yet another sensitive survey, the LoTSS Deep Field survey, which has sub-arcsecond resolution and has data in several fields, of which I make use of the Lockman Hole and ELAIS-N1. In the following sections I highlight and summarize the take-away points from the three studies and the physical implications of these projects for AGNs.

## 5.1 Spectral Age Distribution analysis

This study revolves around the evaluation of spectral age values on a pixel by pixel basis for a sample of RLAGNs selected using MIGHTEE early science data for the XMM-LSS field, with the help of software designed for the purpose (BRATS). The study uses multi-wavelength information to calculate spectral age of the sources using the JP model (Jaffe and Perola, 1973) and also compares the values of most resolved sources in the sample with other models, such as

KP and Tribble (Kardashev, 1962; Tribble, 1993). The study provides a detailed investigation of the spectral age distribution of the sources obtained using the JP model and also note different morphologies observed in the sample. The study also answers some other key questions with respect to resolution, sample size, model use case and validity, and data sensitivity. In the end, the study attempts to compare the spectral age values obtained for the sample to the projected dynamical age values that could be observed for a given radio luminosity and physical size. Below I summarize the key points from this work:

- The study uses data from four surveys, MeerKAT MIGHTEE, LOFAR, GMRT, and uGMRT, by using radio maps that provide data at multiple frequencies, such as 144, 320, 370, 420, 460, 610, and 1284 MHz. The differences in the data are due to resolution and sensitivity of each survey where the most sensitive data comes from the MIGHTEE survey, with rms noise of 4.5 μJy/beam.
- 2. The sample size obtained using the study is of 28 sources in the XMM-LSS field, where there are 17 sources that can be categorized as FR-II, 5 sources as FR-I, one source is a Head-Tail source, and 5 sources that show anomalous morphologies.
- 3. The spectral age analysis makes use of the BRATS software, which takes in the radio maps from different frequencies, their redshift and the magnetic field strengths measured using the PYSYNCH code. The software also has different capabilities to obtain spectral age such as choice of model, evaluation of injection index, and maximum age limit. I have used these parameters, along with model type to evaluate the age of the sources in the sample; the output of the software is spectral age maps, together with their errors and  $\chi^2$  values.
- 4. For a sample of 28 sources with different types of morphologies, the spectral age maps in the results are able to show the age distribution in the region of the sources aligned with the structure observed for FR-I and FR-II, where FR-IIs show highest age values near the central region of the source and FR-Is show highest age values furthest away from the center of the source. The age maps also clearly show zero age regions or minimum age regions near the hotspots for FR-IIs and near the center for FR-Is, at least for sources that are highly resolved and have low beam size. The oldest source observed in the study is 115 Myr and the youngest source is 2.8 Myr, and the mean and median is 23.09 Myr and 8.71 Myr respectively. In the study I also show the distribution of the maximum age observed in each source for the sample where the distribution peaks near 5-9 Myr, which also correlates with the median age of the sample.
- 5. The 5 anomalous morphologies observed in the sample are flagged to an extent where we are not able to draw any conclusion on the processes that might lead to such structures,

although I do make some speculations about the possible reasons that could lead to observation of such structures, which include quality of data, part of structure missing from analysis attributing to limitations due to use of low sensitivity data from surveys such as LOFAR and GMRT at 610 MHz. In addition, I have also excluded information from the analysis, such as excluding the region of the cores, as they are not part of the aged structure, and outer edges of the sources, as the poor quality from some of the frequencies prevented me from analyzing emission from the entire region of the structure.

- 6. In the spectral age maps I also overlay the contours obtained from the MIGHTEE survey to check for the amount of emission that is part of the analysis. As observed for all the sources there is a outer region of the source that is not part of the analysis, which happens due to use of low sensitivity surveys as the region selected from the BRATS software considers only pixels that have information in all the frequencies provided. One of the conclusions drawn from the observation relates to the use of sensitive data from all the frequencies, where the data of the lowest sensitivity becomes the limiting factor. The same applies to the resolution, since in the BRATS software the radio images are smoothed and regridded to the lowest resolution present, so that use of low resolution maps can drastically change pixel by pixel analysis, thereby producing low resolution age maps.
- 7. Another parameter that plays a crucial role in producing quality outputs and obtaining age maps is the combination of the beam size and the source size. In the study, my analysis suggests that the size of the source should be at least four times bigger than the beam size, or the beam size should be such that we can accommodate a minimum of four but preferably more than five beams over the entire source. If the source is big enough then a low resolution would still be enough to produce a detailed age map.
- 8. I conduct a similar analysis but use different models of spectral ageing for a select few sources that show good resolved structure and are large in size. The analysis using different spectral ageing models do not show large deviations from what is observed using the JP model, where the age values of the Tribble model lie between the values for the JP and KP models, aligned with expectation and observations from previous studies (Harwood et al., 2013, 2017). Although the Tribble model is physically the most realistic out of the three, I refrain from using it as it is computationally costly and JP model is able to provide lower limits on the age of the sources. In addition, observations in Chapter 2 Table 2.4 show that the median values obtained using Tribble model and the JP model vary by only 3% to 5%. These small differences should not impact the results obtained for the spectral age analysis.
- 9. With respect to comparisons made between the projected dynamical age of the sources at different radio luminosities and physical size, the sample in the study does not show any

clear relationship between spectral age and the total size of the source. However, in the study I have also pointed out that there are resolution, sensitivity, sample size, and surface brightness limits, and the sample size used in the study is still low to conclude anything that can be statistically significant to obtain a relation between physical size and the age of the sources. Further, there are also age differences in terms of spectral age calculations and dynamical age calculations, which point out the discrepancy observed between the two methods and suggest that some processes might not be accounted for in either or both of the methods.

10. The results from the study can now be used to place constraints on jet power as we now have lower limits on spectral age for sources in a field. These evaluated powers of the sources can then be used to obtain the correlation between jet powers and the quantitative effect they have in the environment. Hence, the results from the study can be used in future to answer open questions, such as, the effect an AGN has on the environment.

Overall from the spectral age analysis of the 28 source sample from the XMM-LSS field using the MIGHTEE survey as reference, the conclusion can be made that the age of the sources are distributed at over a wide range and there are many limiting factors that can alter ability to obtain detailed age distribution maps. Mainly, the resolution and sensitivity of the multiple frequency data used cause major limitations and so I conclude that more sensitive data, such as MIGHTEE, but for multiple wavelengths is required to obtain more constrained age values. In addition to this, the resolution of the radio maps also plays vital role in deciding the morphology of the source and the area under analysis. Other parameters include sample size, beam size, source size and the overall quality of the data plays a key role. The study has successfully highlighted the key points to be considered while conducting such an analysis with the use of appropriate parameters, along with expectations regarding the use of models and the data limits. This study not only conducted spectral age analysis for the highest number of sources in a sample for a given field but it also lays down important aspects of the analysis that could be helpful in future work, e.g. with the Square Kilometer Array, when better survey of high sensitivity at multiple wavelengths are available. The study is also a stepping stone towards constraining the jet powers of the sources which is useful in understanding the feedback mechanism that affects the hosts and environments of these sources.

### 5.2 Spectral index, redshift and Radio luminosity correlation

Chapter 3 is about exploring the relation between spectral index, redshift, and radio luminosity where I investigate the way in which the spectral index changes as a function of redshift and radio luminosity. The study performed stems from the observations from previous studies, such

as (De Breuck et al., 1998), that spectral index and redshift are correlated for high redshift radio galaxies. This correlation hypothesizes that as we move to higher redshifts we observe sources with steeper spectral index, which has been useful in selecting high-redshift sources in the past. The correlation that was initially observed by De Breuck et al. (1998) used surveys such as 3CRR and MRC, known to be two of the more complete surveys at the time. However, these early surveys had low sensitivity as compared to the recent surveys used in this study. Due to the low sensitivity of surveys, 3CRR and MRC only contained sources that were highly luminous, which raised the possibility that they were biased towards sources that were steep spectrum, whereas recent surveys such as MIGHTEE, superMIGHTEE, GMRT and or LOFAR, are much more sensitive and can detect low luminosity sources too. This led to the question of whether we can observe the same correlation between spectral index and redshift as observed previously and whether the correlation is actually due to other factors, such as radio luminosity. In order to explore the relationship between the three parameters, spectral index, redshift, and radio luminosity, I have used the MIGHTEE, LOFAR, GMRT, and superMIGHTEE survey which give data at 5 different frequencies 144, 390, 610, 688, and 1400 MHz; I call the resulting multifrequency survey GLaMS. The sources selected have source size less than 10 arcsec, so that the selection only consists of compact sources, as the highest resolution used in the parent surveys is 5 arcsec. The selection is made by keeping MIGHTEE as a reference catalog, as it has the highest sensitivity, and I have used spectroscopic redshift wherever possible. This multi-wavelength information grants the ability to explore the spectral index versus redshift and spectral index versus radio luminosity relation over different frequency ranges, including both broad-band and multiple pairs of frequencies. Below I summarize some of the key observations and note the conclusions that can be made after conducting the analysis.

- 1. The study uses multiple frequencies to observe if any trend exits between spectral index and redshift  $(\alpha$ -z), and spectra index and radio luminosity  $(\alpha$ -L), for which I have conducted analysis by obtaining spectral index values using a combination of pairs of frequencies and broad-band analysis. Using different pairs of frequencies helps in understanding and observing the trends showed by  $\alpha$ -z and  $\alpha$ -L plots, where each frequency comes from a survey of varying sensitivity and different sample sizes. In the study I have also conducted similar analysis using multiple wavelengths, by requiring the presence of data from LOFAR and MIGHTEE, and including the best available data from other surveys, which helps observing trends in  $\alpha$ -z and  $\alpha$ -L with overall contribution from best available data.
- 2. The trends in the  $\alpha$ -z plots for paired and multiple frequencies overall suggest that there exists a positive correlation between the parameters, where for some cases the correlation is weak but many show a positive trend. However, when the observations are compared with the results of previous studies, an offset is observed between the values for the 3CRR

survey (prominently used by previous studies) and the GLaMS samples, in the sense that at the same redshift the sources from 3CRR show systematically steeper spectra. In addition, in the ten plots of various combinations of frequencies, the sample from 3CRR mainly shows a more rapidly and strongly increasing trend with redshift as compared to GLaMS samples.

- 3. Conducting similar analysis, when observing the trends for α-L plots, it is seen that there is a weak but significant correlation between averaged spectral index and radio luminosity for most frequency pairs, but here we observe a continued trend from GLaMS sample to 3CRR sample. The plots also reveal that the GLaMS sample contains less luminous sources which were absent from the surveys like 3CRR which within the plots only appear at higher luminosities, with the MRC sample lying in between the samples from GLaMS and 3CRR. The continued trend is an indication of the consistency in the correlation that ranges from low luminosity to high luminosity, which is contrary to the offset observed in the α-z plots. Similar results are observed in the multi-frequency analysis where the α-z plot shows offset between recent and previous samples and α-L shows continued trend.
- 4. As the study uses different pairs of frequencies, which come from surveys of different sensitivities, different sample sizes from the ten pairs and multiple-frequency dataset is used to conduct the analysis, where the largest sample size is of 4851 sources and the lowest is of 159 sources. In the study, results from the larger sample size pairs tend to show better constraints when binned in redshift and radio luminosity.
- 5. The observations show positive trends in  $\alpha$ -z and  $\alpha$ -L and in order to further understand the combined effects of the three parameters, I have constructed plots which present the  $\alpha$ -z trend for different fixed luminosity ranges. Similarly, plots of  $\alpha$ -L are constructed for different fixed redshift ranges. This helps in disentangling the combined effects observed between spectral index, redshift and radio luminosity, showing that in fixed luminosity bins there is a clear redshift dependence at some frequencies, while in fixed redshift bins there is a luminosity dependence.
- 6. A physical explanation of the spectral index and luminosity correlation can be attributed to the injection index of the sources where high power sources have high jet energy densities and strong magnetic fields, as also explained by (Blundell and Rawlings, 1999). This means that the higher energy sources will have higher synchrotron losses leading to steeper spectra which is able to explain the offset observed for 3CRR and GLaMS sample in α-z, and the continued trend observed for α-L. However, there is also another trend that shows clear relationship between spectral index and redshift when different fixed luminosity ranges are used, which could be due to inverse-Compton losses coupled with the higher rest frame frequency at higher z.

7. The study draws attention to the need for careful use of  $\alpha$ -z correlation in order to select sources to understand the HzRG population. The study argues against the use of  $\alpha$ -z correlation as it can be an effect of  $\alpha$ -L correlation. Hence, in order to understand the properties of AGNs at high redshifts steep spectrum selection should not be primary criterion and the presence of low luminosity sources should also be taken into account.

The study in Chapter 3 has clearly highlighted the inherent relationship that exists between the three parameters where all three, spectral index, redshift, and radio luminosity could be affecting the observed trends. In the study I have also pointed out how the inclusion of lower luminosity sources can affect the correlations observed, along with the use of multi-wavelength data. Although there is no one clear explanation of as to why the entangled correlation is observed, different physical factors do seem to affect the correlation which change over the broad range of frequencies used. Several speculations and suggestions have been made in the study which include the use of appropriate samples and data of higher sensitivity, as flux limit biases that can come into the picture while selecting sources and evaluating spectral index values for different samples.

#### 5.3 Testing orientation-based unification schemes

Barthel (1989) proposed a scheme that could unify radiatively efficient AGNs as a single population which were observed as different objects due to effects like projection and relativistic beaming. Several studies after that have set out to verify the validity of the scheme, testing the scheme using different methods and sample sizes. As we have entered an era of surveys that are advanced enough to observe fainter objects than before and produce large datasets, it was rational to test the scheme again but using recent LoTSS deep field data. The catalog we use (Best et al., 2023) provides data for three different fields along with information in the infrared, radio, and optical, from which I have used data from two fields and their respective color information to select sources for the analysis. In the analysis and testing of the unified model, I have broadly looked at two parameters that are typically used to validate the unification scheme, the critical angle and the size ratios. In addition to the observations, I have also explored the two different source shape configuration, namely, the 'stick model' and the 'cylindrical model', to understand the influence of axial ratio on the model parameters. In order to verify and test the scheme using the cylindrical model, I have developed a simulation that generates sources of varying lengths and axial ratios; the results of the model are dependent on the distribution of axial ratio, true lengths, redshift and angle to the line of sight. The model is used to produce a distribution of source sizes for a given critical angle and sample size, two important factors in the actual observations for unification testing. Based on the analysis run using simulation, the actual observed sample using the LoTSS deep field data, and the sample sizes obtained using

color-color plot selection method, important conclusions have been drawn in the study. Below I have summarized some of the key points to be noted from the analysis and conclusions derived after the analysis.

- 1. In the selection and segregation of the sources into quasars and radio galaxies, color plots that use color in the optical and infrared are used, along with the condition that sources are identified as radiatively efficient in the catalog and lie in the Lockman Hole and ELAIS-N1 fields. The analysis does not use the Boötes field as sufficient information in the optical and infrared was missing. To segregate the sources after filtering the data, SDSS-DR16 data is used as a reference, as this has identified quasars in the two fields, and its results can be used to confine the area where quasars are found in the two color plots. After all these steps, the number of the sources in the sample are cut down to a small number compared to the sources in the catalog. This points out the first limitation of using the method, availability of high-quality data that can be used to systematically and homogeneously select sources, so that proper sample sizes can be obtained for quasars and radio galaxies.
- 2. In the analysis along with using sample from different fields, use of accurate source sizes is also being made, where source sizes accurate up to sub-arcseconds is available for the Lockman Hole field. Analysis including the accurate sizes and different combinations of fields at different redshift ranges have been conducted where three major parameters are being observed, the critical angle, source size ratios and the sample sizes. The analysis results suggest different critical angles for the different redshift ranges and field combinations, where the lowest critical angle observed is 44.80° and largest is 66.42°. These values are very far apart given that the expectation is that the critical angle to be close to 45°, which is obtained in the results but only when the sample is constructed with the best available completeness. This leads to another key conclusion that the sample used should not only be homogeneously selected but also complete, which is not the case in many of the previous studies. Here, other observations made also include the fact that the sample of sources with accurate sizes used in the Lockman field analysis is very small. Other fields and combinations of fields in different redshift ranges show varying sample sizes for quasars and radio galaxies where in some cases the number of quasars and radio galaxies are equal or even sometimes the number of quasars is greater, reflecting selection biases. Overall, the conclusion is that the samples used for such tests should be complete and no clear dependency on the redshift ranges should be observed.
- 3. In the same analysis that uses various redshift ranges and fields, the mean and median source size ratios do not agree well with the ones predicted by the stick model. The stick model predicts the size ratios to be close to 0.5-0.6, but the size ratios obtained in the samples are far off, some even showing values greater than one, meaning that the

sizes of the quasars are greater than those of the radio galaxies. This type of observation, although contrasting with the simplest predictions of unified models, is not surprising, as we know that the results of the stick model are dependent on critical angle which is further dependent on the ratio of number of quasars to radio galaxies, which in the sample used is small and mostly incomplete. In addition, if the samples are incomplete, i.e. we are missing radio galaxies or quasars, then there might be biases in the sense that overall size distribution might change due to unaccounted radio galaxies or quasars in the sample. However, even the one sample that we believe to be most nearly complete used in the analysis also shows size ratios deviating from the stick model predicted values.

- 4. Owing to the discrepancies observed in the stick model, in the study I have also studied samples using simulation that uses Monte-Carlo method of simulation to produce samples at different source sizes, using the sample size and critical angle. The important element of the simulation is the use of axial ratio, that derives from the fact that sources are not one dimensional stick type shape, but are more like a cylindrical shaped objects, so that the finite width of the sources also shows up in the projected sizes of the sources which are used for unified model tests. The modeling of the cylindrical configuration used data provided by Mullin et al. (2008) to obtain the distribution of projected axial ratio and lengths of the sources in their sample. The modeling grants the ability to produce a distribution of size ratios, where the size ratio ranges at the 99% confidence interval can be obtained for the sample sizes and critical angles observed by the samples at different redshift ranges and fields. Overall the intervals show that the mean/median source size ratios observed for the LoTSS data lie well within these ranges, where the range basically describes the values above or below which the unification model could be rejected. It is worth noting in the analysis that the previously thought threshold of size ratio being greater than 1 to reject the model has no special significance here, since due to the introduction of axial ratio the possibility of obtaining size ratios greater than 1 is present and does not imply an automatic inconsistency with the model.
- 5. I have not restricted the analysis to the observed sample sizes and critical angles, but have also performed simulations for regularly varying sample sizes and critical angles, varying from 500 to 1000 and 45° to 65° for 10,000 iterations. For the given number of iterations, I also observe the distribution of the size ratios in the analysis that usually peak between 0.8 and 0.9. However, the model developed has its own caveats with respect to the data used to develop the model and in particular the size ratios. The two limitations of the model presented in the study is (i) the ability to only produce sources that have axial ratios grater than 0.1 as the distribution below axial ratio of 0.1 is not known for the data present by Mullin et al. (2008) and (ii) restricting the simulation from producing sources that have apparent sizes less than 6 arcsecs, as this is the resolution of the bulk of the LoTSS data. The restriction takes into account the redshift distribution of the LoTSS data

and resamples them to get similar redshift distribution, which are further used to obtain the angular sizes of the sources where any size less than 6 arcsecs is regenerated until size greater than 6 arcsecs is obtained. These angular size distribution are then compared and matched with angular size distribution of the LoTSS data to generate sources that match match with the actual data and can be used in testing and comparison the actual versus predicted observations. From the model of the cylindrical configuration another key observation and conclusion is obtained that relates to the resolution of the survey and the data used to develop the model. Using data that have higher resolution for a much larger sample size to obtain complete axial ratio distribution would improve the results of future analysis.

- 6. Further to the limitations discussed in the study, in the analysis I have also included simulation observations that show size ratio ranges obtained using the resolution truncation and without it. Not surprisingly, the ranges of the size ratio for all different sample sizes and critical angles is close to one another; this effect arises due to the fact that we use Mullin et al. 2008 data which is based on the physical sizes and axial ratios of the 3CRR sources and is not representative of the LoTSS sources. The number of unresolved to resolved sources obtained through simulation is around 20 to 30% whereas for the LoTSS sample the fraction is around 93%. This vast difference in production of resolved sources by the simulation undermines the effects of the resolution truncation, producing size ratio ranges close to one another.
- 7. Finally in the study I have also compared the source sizes used by the previous studies and their results to the results obtained in the unification study in the thesis. Different studies have claimed the unified models to be valid and some have rejected it, but on the whole these studies have used samples that are not complete, or homogeneously selected and importantly do not have large enough sample size to successfully reject the model in the presence of a distribution of intrinsic source axial ratio.
- 8. In the study we conclude that the orientation based unification scheme is not ruled out by our new data or by any existing analysis as the size ratios are well within the critical limits. As this study incorporates the use of cylindrical configuration, it makes the model mimic the real projection effects and hence, further helps bolster the testing criterion. Such robust testing is useful in placing strong confidence towards use of AGN feedback and its underlying processes in modeling of galaxy evolution, star formation rates, and other phenomenon.

Overall I conclude that it is important in these studies to use complete data where the sources are selected systematically and homogeneously, and most importantly to use the cylindrical model which is more realistic and produces reasonable results to validate the existence of unification

scheme. In order to further improve the quality of simulations and to draw firm conclusions, a greater sample size for the axial ratio distribution is needed with accurate length measurements of the projected lengths, which can only come from higher resolution data. We also note that apart from the resolution restrictions, the analysis mainly uses luminous sources to build the linear size distribution, and that effects due to AGN evolution, luminosity dependency, and or contamination by others type of sources such as LERGs can also be affecting the AGN population and its properties.

#### 5.4 Conclusion and Future Work

The spectral age analysis performed in Chapter 2, investigation of spectral index, redshift and luminosity correlation explored in Chapter 3, and the orientation-based unification schemes tests performed in Chapter 4, all give insights into the physical properties of RLAGNs. I have successfully shown how multi-frequency data can be used to perform the analysis conducted in this thesis and what conclusions can be drawn from using big datasets. The three studies underscore the importance of using high resolution and sensitive data available at multiple frequencies, in addition to the effects of selection which plays an important role while analyzing and interpreting the outcomes of the analysis.

In the three studies use of high resolution data at multiple frequencies has surfaced as one of the key factors that can affect the three analyses. Although, we have high resolution data, such as MIGHTEE, we are still limited by the lowest resolution dataset available, as seen in Chapter 2. Similar observations were made in Chapter 4, where resolution truncation was applied. Not only for analysis, but high resolution data is also useful in selection of sources, as seen in Chapter 2. In addition to resolution, the sensitivity of the surveys also plays a key role in the three analyses. High sensitivity data is vital in terms of observation of extended emission from AGN structure, as seen in Chapter 2, detection of less luminous sources, as seen in Chapter 3, and overall for obtaining larger sample sizes for the analysis, as seen in all three studies. Sensitivity is seen to play a key role in Chapters 2 and 3, where the least sensitive dataset can be limiting for analysis of outer regions of AGN structure which are seen in surveys, such as MIGHTEE, but excluded due to less sensitive surveys, such as GMRT and LOFAR. Furthermore, sensitivity also affects the selection of sources in the sample; depending on the survey sensitivity, sample size of the analysis changes, further affecting the interpretations drawn from them. Effects of sensitivity also show up in the selection biases which can have an effect on the type of population of sources selected. Overall, the three studies have proved that use of large dataset can be vital in conducting such analysis, especially if data from multiple frequencies is involved, given that data from multiple frequencies has high resolution and sensitivity, in order to produce large unbiased samples.

Specific to the analysis performed in the three studies and the physics behind the observed phenomenon, in the thesis, I have also successfully highlighted the importance of use of large sample size. Given that the studies involve use of multi-frequency data, generation of large sample size can be particularly difficult. This is where future surveys, such as SKA, would be useful, due to their ability to observe in wider frequency range and large collecting area, the survey will have high sensitivity and resolution providing quality data at multiple frequencies. The large sample size will prove essential to constrain physical parameters of AGNs, such as their age and power distribution, parameter correlations, sizes and various test parameters. Hence, large sample size coupled with high resolution and high sensitivity datasets obtained at multiple frequencies are essential in order to obtain well constrained, statistically significant results that can prove helpful in understanding the physics behind the AGN phenomenon, and in turn the effects on their surrounding and host galaxies. In addition to this, other notable factors highlighted in the studies are optical identification and multi wavelength information; especially useful for obtaining redshifts of sources and segregation of the population of AGNs. Finally, the bigger the better is in-fact true for multi frequency exploration of RLAGN, especially the ones explored in the thesis, in the sense that high resolution and sensitivity data would result in a quality sample which would in turn produce reliable, significant and quality results.

Given that the three studies were limited by some factors, such as use of less sensitive and lower resolution surveys, unavailability of redshifts, accurate measures of source size, etc, in future similar analysis can be performed with the help of high sensitive and resolution survey, such as those that will be provided by the SKA, that would be able to overcome these limitations. With the availability of better quality data in multiple frequencies, in future, I would want to perform spectral age analysis for a much larger sample which can be used to compare with the dynamical age model and help give insights into the discrepancies between both models. I would also be interested to understand more about the ambiguous sources seen in the sample of spectral age analysis, in Chapter 2, to understand the possible reason behind such structures, and if there could be more explored for such sources in terms of their age, the physical processes responsible for such structure, and any other effects coming into play. Even with the unavailability of better data from future surveys, such as SKA, a more immediate future work would also involve measuring the source size and width from the current high resolution LoTSS data, refereed to in Chapter 4, to further rerun the analysis and compare the results. Continued further, with the availability of the more accurate source sizes and higher resolved sources, from surveys such as SKA, I would like to continue to perform unification test but with angular sizes and axial ratio distributions obtained from a larger sample size which are representative, which would also be helpful in building a better cylindrical model for the test. This would give better constraints on the size ratios which are critical to a test of the unification scheme validity.

## Appendix A

# **Appendix**

#### A.1 Spectral age distribution versus distance

This section shows error maps and age distribution plot for each source that is visualized in a different way. Figure A.1 shows error distribution for each source. Figure A.2 shows the correlation between the age distribution to the size distribution of pixels for each source. For each pixel in the source that reports an age value, we calculate the distance of that pixel from the core of the source and hence obtain an array of distances that correlate to their respective age. The aim is to understand the pattern we obtain for a well sampled source in the pixel space for different FR types. For example, for target 1 (fig 2.1a), we see that pixel number density increases with increasing age and size. Hence, we expect to see linear relationship for Head-Tail sources. As for well resolved and sampled FR-type II sources we can see clear double arcs along the y axis, for example target 10, target 27 (Fig. 2.1c and 2.7c). These sources show increase in age as we reach close to core, which is represented by a downward curve of the pixel density in the plot. With sources like target 14, target 17 (fig 2.4b and 2.5a); which show FRtype I morphology, we see an arc that starts from low age and ends at higher age with increasing distance from the core. We can observe an upward curve of the pixel density in the plots. The Figure also shows some plots with 'FLAGGED' title which is due to anomalous behavior seen in the age distribution plots. These distinct patterns can be used as training datasets to obtain filters for autonomous selection and classification of the sources. Although this is just one of the thought applications, more exploration can be done into the method for future use.

## A.2 $\alpha$ -z and $\alpha$ -L for compact 3CRR sources

In figure A.3 and A.4 we show the  $\alpha$ -z and  $\alpha$ -L plots where the sample using the 3CRR data is also filtered for sources having largest angular sizes less than 20 arcsec (consistent with being

Appendix 131

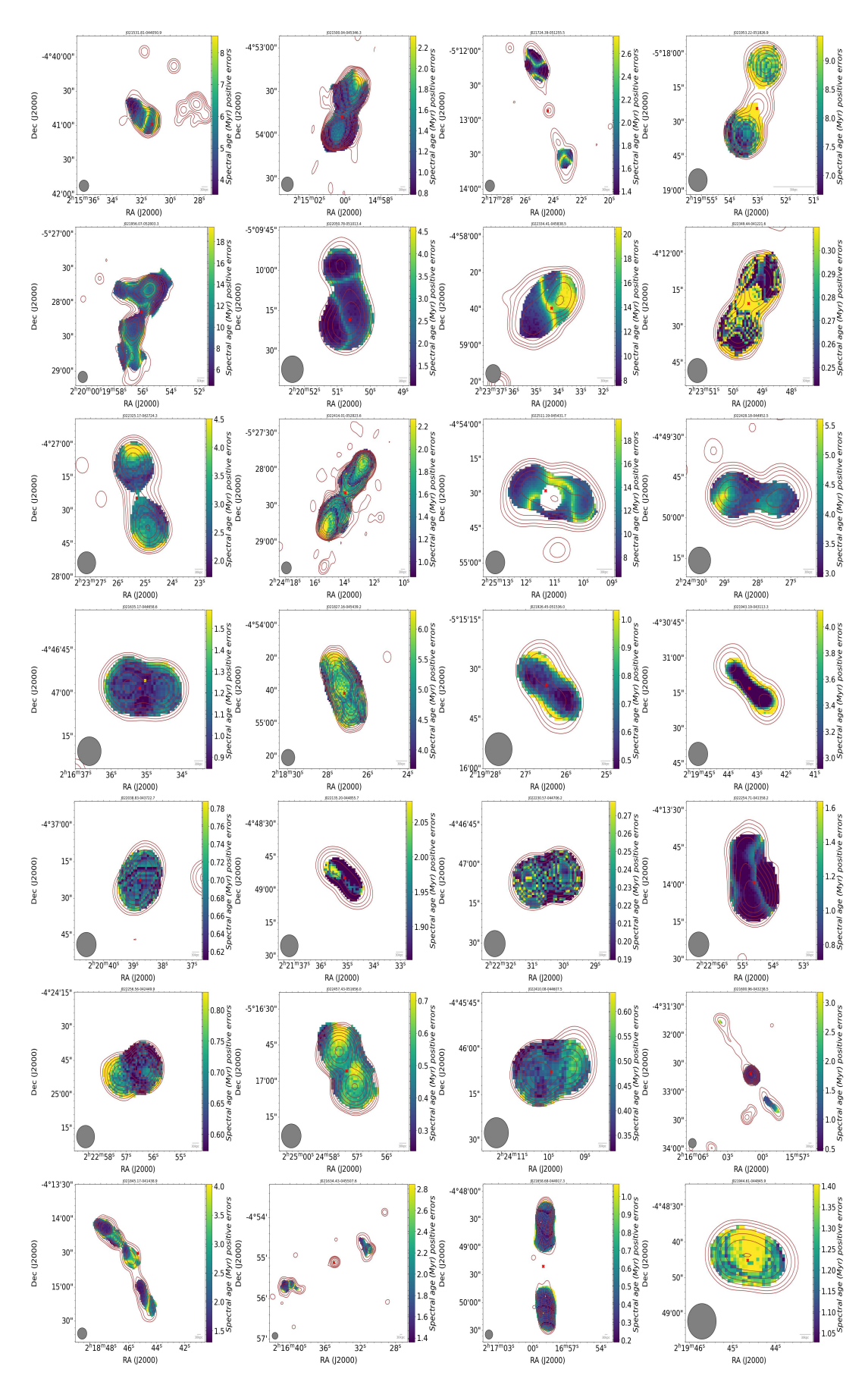


FIGURE A.1: Positive error distribution of age for each source.

Appendix 132

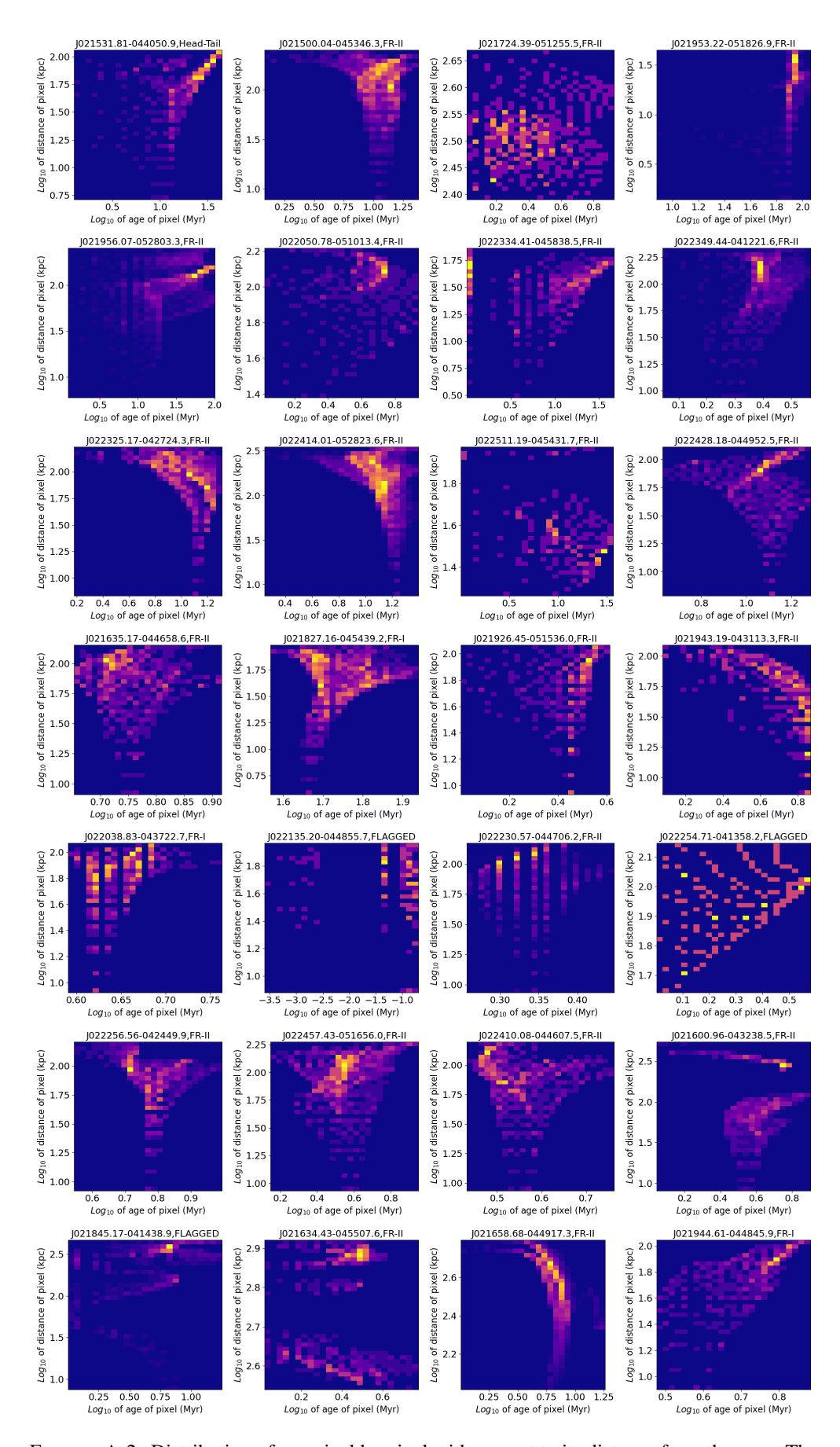


FIGURE A.2: Distribution of age pixel by pixel with respect to its distance from the core. The x-axis is age of the source in logarithmic scale and y-axis is the distance of the corresponding pixel from the core of the source in logarithmic scale. The title in each plot gives source IAU name and morphology.

Appendix 133

unresolved with DC\_Maj < 10 arcsec since DC\_Maj is the FWHM of a Gaussian). The number of sources after filtering for angular sizes is 55 which is around 61 per cent of the non filtered 3CRR sample used in the analysis above. We observe that this does not affect the overall position of the 3CRR sources with respect to the plots shown in the main body of the paper.

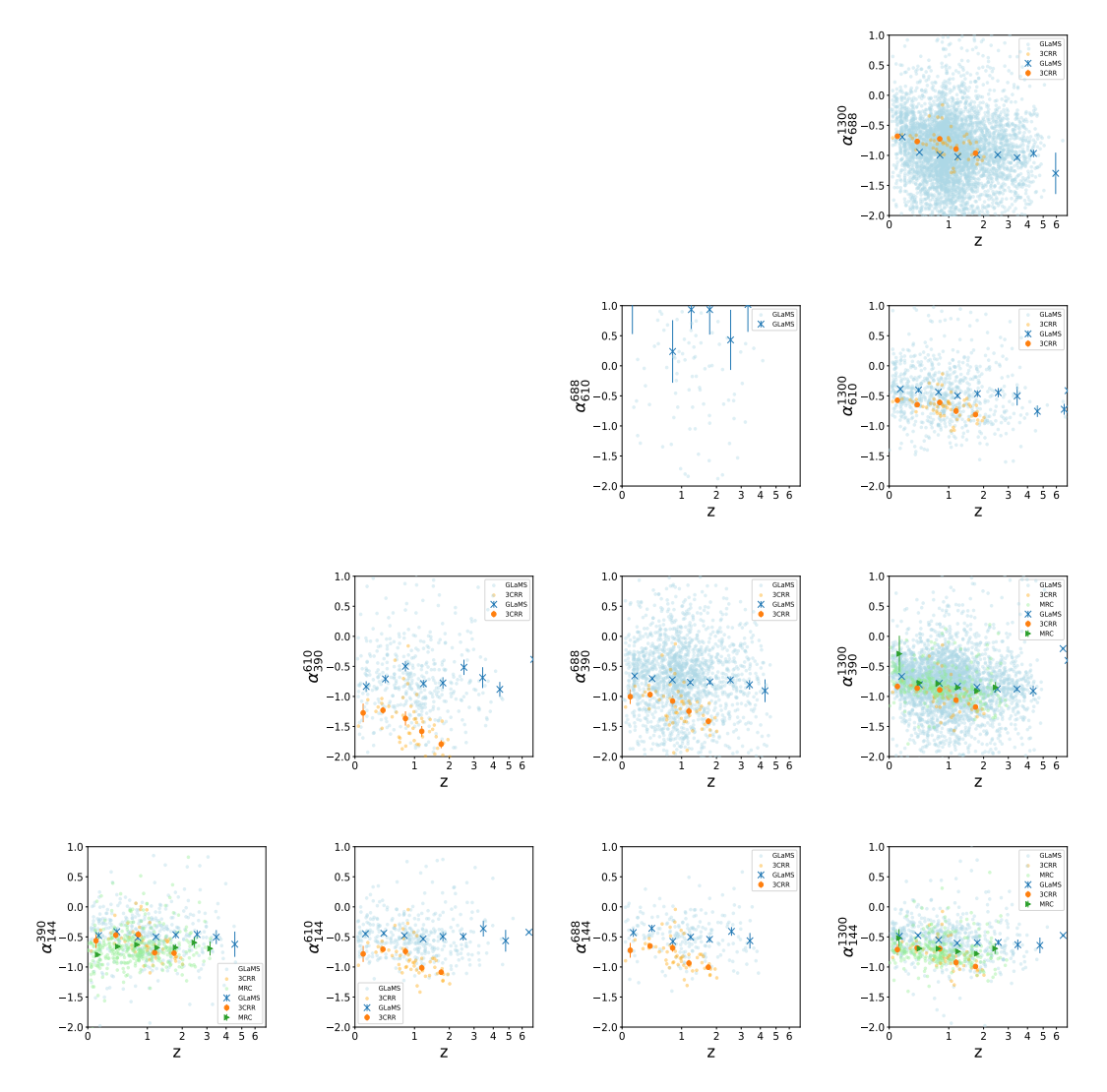


FIGURE A.3: The correlation of the average spectral index with the redshift of the sources where the spectral index is calculated for flux densities measured at 144 MHz (LOFAR), 390 MHz (uGMRT band-3), 610 MHz (GMRT), 688 MHz (uGMRT band-4), and 1.3 GHz (MIGHTEE). Individual data points are also plotted without errors in order to indicate the spread of the data. The MRC sample is not present for some plots as the sample size for these frequencies is very low. Error bars indicate the  $1\sigma$  error on the weighted mean. The sources in 3CRR sample are selected by filtering sources having angular size less than 10 arcsec

Appendix 134

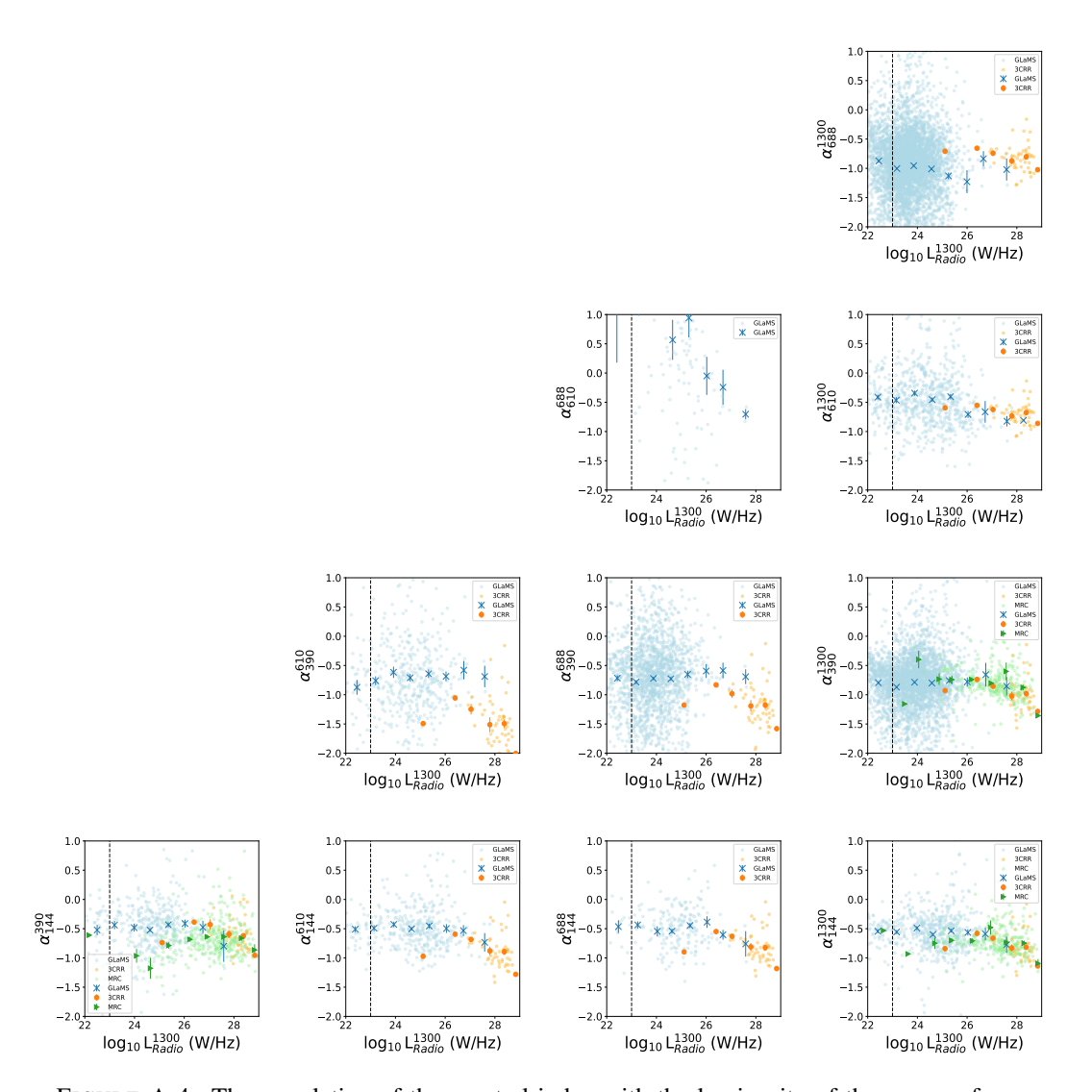


FIGURE A.4: The correlation of the spectral index with the luminosity of the sources from MIGHTEE at 1.3 GHz where the spectral index is calculated for flux densities measured at 144 MHz (LOFAR), 390 MHz (uGMRT band-3), 610 MHz (GMRT), 688 MHz (uGMRT band-4), and 1.3 GHz (MIGHTEE). Luminosity is calculated as described in Section 3.2.3. Comments as in Fig. 3.6. The vertical dotted line shows the radio luminosity value above which AGN start to dominate. The sources in 3CRR sample are selected by filtering sources having angular size less than 10 arcsec

- Albareti, F.D., Allende Prieto, C., Almeida, A., et al., 2017. The 13th Data Release of the Sloan Digital Sky Survey: First Spectroscopic Data from the SDSS-IV Survey Mapping Nearby Galaxies at Apache Point Observatory. ApJ, 233(2):25.
- Alberts, S., Rujopakarn, W., Rieke, G.H., et al., 2020. Completing the Census of AGN in GOODS-S/HUDF: New Ultradeep Radio Imaging and Predictions for JWST. <u>ApJ</u>, 901(2):168.
- Alexander, P. and Leahy, J.P., 1987. Ageing and speeds in a representative sample of 21 classical double radio sources. MNRAS, 225:1.
- Alfvén, H. and Herlofson, N., 1950. Cosmic Radiation and Radio Stars. <u>Physical Review</u>, 78(5):616.
- An, F., Vaccari, M., Best, P.N., et al., 2024. Radio spectral properties of star-forming galaxies between 150 and 5000 MHz in the ELAIS-N1 field. MNRAS, 528(3):5346.
- An, F., Vaccari, M., Smail, I., et al., 2021. Radio spectral properties of star-forming galaxies in the MIGHTEE-COSMOS field and their impact on the far-infrared-radio correlation. MNRAS, 507(2):2643.
- Angel, J.R.P. and Stockman, H.S., 1980. Optical and infrared polarization of active extragalactic objects. Annual Review of Astronomy and Astrophysics, 18:321.
- Antonucci, R., 1993. Unified models for active galactic nuclei and quasars. Annual Review of Astronomy and Astrophysics, 31:473.
- Antonucci, R.R.J., 1984. Optical spectropolarimetry of radio galaxies. ApJ, 278:499.
- Antonucci, R.R.J., 2023. A Walk through AGN Country—For the Somewhat Initiated! Galaxies, 11(5):102.
- Antonucci, R.R.J. and Miller, J.S., 1985. Spectropolarimetry and the nature of NGC 1068. <u>ApJ</u>, 297:621.
- Appenzeller, I., 2013. Introduction to Astronomical Spectroscopy.

Arons, J., Kulsrud, R.M., and Ostriker, J.P., 1975. A multiple pulsar model for quasi-stellar objects and active galactic nuclei. ApJ, 198:687.

- Athreya, R.M., Kapahi, V.K., McCarthy, P.J., et al., 1998. Large rotation measures in radio galaxies at Z ¿ 2. A&A, 329:809.
- Baade, W., 1956. Polarization in the Jet of Messier 87. ApJ, 123:550.
- Baade, W. and Minkowski, R., 1954. Identification of the Radio Sources in Cassiopeia, Cygnus A, and Puppis A. ApJ, 119:206.
- Baldi, R.D. and Capetti, A., 2008. Recent star formation in nearby 3CR radio-galaxies from UV HST observations. A&A, 489(3):989.
- Baldry, I.K., Glazebrook, K., Brinkmann, J., et al., 2004. Quantifying the Bimodal Color-Magnitude Distribution of Galaxies. ApJ, 600(2):681.
- Barthel, P.D., 1989. Is Every Quasar Beamed? ApJ, 336:606.
- Becker, R.H., White, R.L., and Helfand, D.J., 1995. The FIRST Survey: Faint Images of the Radio Sky at Twenty Centimeters. ApJ, 450:559.
- Begelman, M.C., Blandford, R.D., and Rees, M.J., 1984. Theory of extragalactic radio sources. Reviews of Modern Physics, 56(2):255.
- Bell, A.R., 1978. The acceleration of cosmic rays in shock fronts I. MNRAS, 182:147.
- Bennett, A.S., 1962. The preparation of the revised 3C catalogue of radio sources. MNRAS, 125:75.
- Best, P.N., 1996. Radio source asymmetries and unified schemes. <u>Vistas in Astronomy</u>, 40(1):185.
- Best, P.N., 2004. The environmental dependence of radio-loud AGN activity and star formation in the 2dFGRS. MNRAS, 351(1):70.
- Best, P.N., 2007. Feedback from radio-loud AGN. NAR, 51(1-2):168.
- Best, P.N., 2009. Radio source populations: Results from SDSS. <u>Astronomische Nachrichten</u>, 330(2):184.
- Best, P.N., Carilli, C.L., Garrington, S.T., et al., 1998. Deep radio observations of 3C 324 and 3C 368: evidence for jet-cloud interactions. MNRAS, 299(2):357.
- Best, P.N. and Heckman, T.M., 2012. On the fundamental dichotomy in the local radio-AGN population: accretion, evolution and host galaxy properties. MNRAS, 421(2):1569.

Best, P.N., Kauffmann, G., Heckman, T.M., et al., 2005. The host galaxies of radio-loud active galactic nuclei: mass dependences, gas cooling and active galactic nuclei feedback. MNRAS, 362(1):25.

- Best, P.N., Kondapally, R., Williams, W.L., et al., 2023. The LOFAR Two-metre Sky Survey: Deep Fields data release 1. V. Survey description, source classifications, and host galaxy properties. MNRAS, 523(2):1729.
- Best, P.N., Longair, M.S., and Rottgering, H.J.A., 1997. A jet-cloud interaction in 3C 34 at redshift z=0.69. MNRAS, 286(4):785.
- Bicknell, G.V., 1995. Relativistic Jets and the Fanaroff-Riley Classification of Radio Galaxies. ApJ, 101:29.
- Bîrzan, L., Rafferty, D.A., McNamara, B.R., et al., 2004. A Systematic Study of Radio-induced X-Ray Cavities in Clusters, Groups, and Galaxies. ApJ, 607(2):800.
- Bîrzan, L., Rafferty, D.A., Nulsen, P.E.J., et al., 2012. The duty cycle of radio-mode feedback in complete samples of clusters. MNRAS, 427(4):3468.
- Blake, G.M., 1970. Observations of Extragalactic Radio Sources Having Unusual Spectra. Astrophysical Letters, 6:201.
- Blandford, R., Meier, D., and Readhead, A., 2019. Relativistic Jets from Active Galactic Nuclei. Annual Review of Astronomy and Astrophysics, 57:467.
- Blandford, R.D. and Königl, A., 1979. Relativistic jets as compact radio sources. ApJ, 232:34.
- Blandford, R.D. and Rees, M.J., 1974. A "twin-exhaust" model for double radio sources. MNRAS, 169:395.
- Blumenthal, G. and Miley, G., 1979. Spectral index dependent properties of steep spectrum radio sources. A&A, 80:13.
- Blundell, K.M. and Rawlings, S., 1999. The inevitable youthfulness of known high-redshift radio galaxies. <u>Nature</u>, 399(6734):330.
- Blundell, K.M. and Rawlings, S., 2000. The Spectra and Energies of Classical Double Radio Lobes. AJ, 119(3):1111.
- Blundell, K.M., Rawlings, S., and Willott, C.J., 1999. The Nature and Evolution of Classical Double Radio Sources from Complete Samples. <u>AJ</u>, 117(2):677.
- Bock, D.C.J., Large, M.I., and Sadler, E.M., 1999. SUMSS: A Wide-Field Radio Imaging Survey of the Southern Sky. I. Science Goals, Survey Design, and Instrumentation. <u>AJ</u>, 117(3):1578.

Boehringer, H., Voges, W., Fabian, A.C., et al., 1993. A ROSAT HRI study of the interaction of the X-ray emitting gas and radio lobes of NGC 1275. MNRAS, 264:L25.

- Bolton, J.G., 1948. Discrete Sources of Galactic Radio Frequency Noise. <u>Nature</u>, 162(4108):141.
- Bolton, J.G., Gardner, F.F., and Mackey, M.B., 1964. The Parkes catalogue of radio sources, declination zone -20° to -60°. Australian Journal of Physics, 17:340.
- Bolton, J.G. and Stanley, G.J., 1948. Variable Source of Radio Frequency Radiation in the Constellation of Cygnus. Nature, 161(4087):312.
- Bolton, J.G., Stanley, G.J., and Slee, O.B., 1949. Positions of Three Discrete Sources of Galactic Radio-Frequency Radiation. Nature, 164(4159):101.
- Bower, R.G., Benson, A.J., Malbon, R., et al., 2006. Breaking the hierarchy of galaxy formation. MNRAS, 370(2):645.
- Brandt, W.N. and Hasinger, G., 2005. Deep Extragalactic X-Ray Surveys. Annual Review of Astronomy and Astrophysics, 43(1):827.
- Bridle, A.H. and Perley, R.A., 1984. Extragalactic Radio Jets. Annual Review of Astronomy and Astrophysics, 22:319.
- Brunetti, G., Mack, K.H., Prieto, M.A., et al., 2003. In-situ particle acceleration in extragalactic radio hot spots: observations meet expectations. MNRAS, 345(3):L40.
- Burbidge, G.R., 1956. On Synchrotron Radiation from Messier 87. ApJ, 124:416.
- Burbidge, G.R., 1959. Estimates of the Total Energy in Particles and Magnetic Field in the Non-Thermal Radio Sources. <u>ApJ</u>, 129:849.
- Burbidge, G.R., 1961. Galactic Explosions as Sources of Radio Emission. Nature, 190(4781):1053.
- Burch, S.F., 1977. The variation of spectral index across the radio galaxy 3C 452. MNRAS, 180:623.
- Capetti, A., Massaro, F., and Baldi, R.D., 2017. FRIICAT: A FIRST catalog of FR II radio galaxies. <u>A&A</u>, 601:A81.
- Carilli, C.L., Perley, R.A., Dreher, J.W., et al., 1991. Multifrequency Radio Observations of Cygnus A: Spectral Aging in Powerful Radio Galaxies. ApJ, 383:554.
- Carilli, C.L., Röttgering, H.J.A., van Ojik, R., et al., 1997. Radio Continuum Imaging of High-Redshift Radio Galaxies. ApJ, 109(1):1.

Celotti, A., Ghisellini, G., and Chiaberge, M., 2001. Large-scale jets in active galactic nuclei: multiwavelength mapping. MNRAS, 321(1):L1.

- Ceraj, L., Smolčić, V., Delvecchio, I., et al., 2020. The XXL Survey. XLIII. The quasar radio loudness dichotomy exposed via radio luminosity functions obtained by combining results from COSMOS and XXL-S X-ray selected quasars. A&A, 642:A125.
- Chambers, K.C., Miley, G.K., and van Breugel, W.J.M., 1988. 4C 40.36: A Radio Galaxy at a Redshift of 2.3. ApJ, 327:L47.
- Chambers, K.C., Miley, G.K., and van Breugel, W.J.M., 1990. 4C 41.17: A Radio Galaxy at a Redshift of 3.8. ApJ, 363:21.
- Chambers, K.C., Miley, G.K., van Breugel, W.J.M., et al., 1996. Ultra–Steep-Spectrum Radio Sources. II. Radio, Infrared, Optical, and HST Imaging of High-Redshift 4C Objects. <u>ApJ</u>, 106:247.
- Chaussidon, E., Yèche, C., Palanque-Delabrouille, N., et al., 2023. Target Selection and Validation of DESI Quasars. ApJ, 944(1):107.
- Chiaberge, M., Macchetto, F.D., Sparks, W.B., et al., 2002. The Nuclei of Radio Galaxies in the Ultraviolet: The Signature of Different Emission Processes. ApJ, 571(1):247.
- Ching, J.H.Y., Croom, S.M., Sadler, E.M., et al., 2017. Galaxy And Mass Assembly (GAMA): the environments of high- and low-excitation radio galaxies. MNRAS, 469(4):4584.
- Clarke, D.A., Bridle, A.H., Burns, J.O., et al., 1992. Origin of the Structures and Polarization in the Classical Double 3C 219. <u>ApJ</u>, 385:173.
- Colla, G., Fanti, C., Fanti, R., et al., 1973. The B2 catalogue of radio sources third part. A&A Supp., 11:291.
- Condon, J.J., Cotton, W.D., Greisen, E.W., et al., 1998. The NRAO VLA Sky Survey. AJ, 115(5):1693.
- Condon, J.J., Kellermann, K.I., Kimball, A.E., et al., 2013. Active Galactic Nucleus and Starburst Radio Emission from Optically Selected Quasi-stellar Objects. ApJ, 768(1):37.
- Croom, S.M., Smith, R.J., Boyle, B.J., et al., 2004. The 2dF QSO Redshift Survey XII. The spectroscopic catalogue and luminosity function. MNRAS, 349(4):1397.
- Croston, J.H., Hardcastle, M.J., and Birkinshaw, M., 2005. Evidence for radio-source heating of groups. MNRAS, 357(1):279.
- Croston, J.H., Hardcastle, M.J., Kharb, P., et al., 2008. Chandra Evidence for AGN Feedback in the Spiral Galaxy NGC 6764. ApJ, 688(1):190.

Croston, J.H., Hardcastle, M.J., Mingo, B., et al., 2011. A Large-scale Shock Surrounding a Powerful Radio Galaxy? ApJ, 734(2):L28.

- Croston, J.H., Kraft, R.P., Hardcastle, M.J., et al., 2009. High-energy particle acceleration at the radio-lobe shock of Centaurus A. MNRAS, 395(4):1999.
- Croton, D.J., Springel, V., White, S.D.M., et al., 2006. The many lives of active galactic nuclei: cooling flows, black holes and the luminosities and colours of galaxies. MNRAS, 365(1):11.
- Davies, J.J., Crain, R.A., McCarthy, I.G., et al., 2019. The gas fractions of dark matter haloes hosting simulated ∼L\* galaxies are governed by the feedback history of their black holes. MNRAS, 485(3):3783.
- De Breuck, C., Brotherton, M.S., Tran, H.D., et al., 1998. Discovery of an Ultra-Steep-Spectrum, Highly Polarized Red Quasar at Z = 1.462. AJ, 116(1):13.
- De Breuck, C., Seymour, N., Stern, D., et al., 2010. The Spitzer High-redshift Radio Galaxy Survey. ApJ, 725(1):36.
- De Breuck, C., van Breugel, W., Röttgering, H., et al., 1999. Searches for High Redshift Radio Galaxies. In H.J.A. Röttgering, P.N. Best, and M.D. Lehnert, editors, <u>The Most Distant Radio Galaxies</u>, page 477.
- De Breuck, C., van Breugel, W., Röttgering, H.J.A., et al., 2000. A sample of 669 ultra steep spectrum radio sources to find high redshift radio galaxies. A&A Supp., 143:303.
- de Jong, J.M.G.H.J., van Weeren, R.J., Sweijen, F., et al., 2024. Into the depths: Unveiling ELAIS-N1 with LOFAR's deepest sub-arcsecond wide-field images. <u>A&A</u>, 689:A80.
- de Vries, W.H., Becker, R.H., and White, R.L., 2003. Long-Term Variability of Sloan Digital Sky Survey Quasars. AJ, 126(3):1217.
- Delhaize, J., Heywood, I., Prescott, M., et al., 2021. MIGHTEE: are giant radio galaxies more common than we thought? MNRAS, 501(3):3833.
- Delvecchio, I., Smolčić, V., Zamorani, G., et al., 2017. The VLA-COSMOS 3 GHz Large Project: AGN and host-galaxy properties out to  $z \lesssim 6$ . A&A, 602:A3.
- Dent, W.A., 1965. Quasi-Stellar Sources: Variation in the Radio Emission of 3C 273. Science, 148(3676):1458.
- Dewdney, P.E., Hall, P.J., Schilizzi, R.T., et al., 2009. The Square Kilometre Array. <u>IEEE</u> Proceedings, 97(8):1482.
- Di Matteo, T., Springel, V., and Hernquist, L., 2005. Energy input from quasars regulates the growth and activity of black holes and their host galaxies. Nature, 433(7026):604.

Donley, J.L., Koekemoer, A.M., Brusa, M., et al., 2012. Identifying Luminous Active Galactic Nuclei in Deep Surveys: Revised IRAC Selection Criteria. ApJ, 748(2):142.

- Douglas, J.N., Bash, F.N., Bozyan, F.A., et al., 1996. The Texas Survey of Radio Sources Covering -35.5 degrees < declination < 71.5 degrees at 365 MHz. AJ, 111:1945.
- Drouart, G., Rocca-Volmerange, B., De Breuck, C., et al., 2016. Disentangling star formation and AGN activity in powerful infrared luminous radio galaxies at 1; z; 4. A&A, 593:A109.
- Dunn, R.J.H., Fabian, A.C., and Taylor, G.B., 2005. Radio bubbles in clusters of galaxies. MNRAS, 364(4):1343.
- DuPuy, D., Schmitt, J., McClure, R., et al., 1969. Optical Observations of BL Lac = VRO 42.22.01. ApJ, 156:L135.
- Edge, D.O., Shakeshaft, J.R., McAdam, W.B., et al., 1959. A survey of radio sources at a frequency of 159 Mc/s. Memoirs of the Royal Astronomical Society, 68:37.
- Ellison, S.L., Patton, D.R., and Hickox, R.C., 2015. Galaxy pairs in the Sloan Digital Sky Survey XII. The fuelling mechanism of low-excitation radio-loud AGN. MNRAS, 451:L35.
- Fabian, A.C., 1994. Cooling Flows in Clusters of Galaxies. Annual Review of Astronomy and Astrophysics, 32:277.
- Fabian, A.C., 2012. Observational Evidence of Active Galactic Nuclei Feedback. Annual Review of Astronomy and Astrophysics, 50:455.
- Fanaroff, B.L. and Riley, J.M., 1974. The morphology of extragalactic radio sources of high and low luminosity. <u>MNRAS</u>, 167:31P.
- Fanti, R., Fanti, C., Schilizzi, R.T., et al., 1990. On the nature of compact steep spectrum radio sources. A&A, 231:333.
- Fath, E.A., 1909. The spectra of some spiral nebulae and globular star clusters. <u>Lick Observatory</u> Bulletin, 149:71.
- Ferrarese, L. and Merritt, D., 2000. A Fundamental Relation between Supermassive Black Holes and Their Host Galaxies. ApJ, 539(1):L9.
- Gaibler, V., Khochfar, S., Krause, M., et al., 2012. Jet-induced star formation in gas-rich galaxies. MNRAS, 425(1):438.
- Galametz, A., Grazian, A., Fontana, A., et al., 2013. CANDELS Multiwavelength Catalogs: Source Identification and Photometry in the CANDELS UKIDSS Ultra-deep Survey Field. ApJ, 206(2):10.

Garon, A.F., Rudnick, L., Wong, O.I., et al., 2019. Radio Galaxy Zoo: The Distortion of Radio Galaxies by Galaxy Clusters. AJ, 157(3):126.

- Garrington, S.T., Conway, R.G., and Leahy, J.P., 1991. Asymmetry depolarization in double radio sources with one sided jets. MNRAS, 250:171.
- Garrington, S.T., Leahy, J.P., Conway, R.G., et al., 1988. A systematic asymmetry in the polarization properties of double radio sources with one jet. <u>Nature</u>, 331(6152):147.
- Gaspari, M., Brighenti, F., and Temi, P., 2012. Mechanical AGN feedback: controlling the thermodynamical evolution of elliptical galaxies. MNRAS, 424(1):190.
- Gaspari, M., Ruszkowski, M., and Oh, S.P., 2013. Chaotic cold accretion on to black holes. MNRAS, 432(4):3401.
- Gaspari, M., Temi, P., and Brighenti, F., 2017. Raining on black holes and massive galaxies: the top-down multiphase condensation model. MNRAS, 466(1):677.
- Ghisellini, G. and Celotti, A., 2001. The dividing line between FR I and FR II radio-galaxies. A&A, 379:L1.
- Gilmour, R., Gray, M.E., Almaini, O., et al., 2007. Environmental dependence of active galactic nuclei activity in the supercluster A901/2. MNRAS, 380(4):1467.
- Ginzburg, V.L., 1951. Cosmic rays as a source of galactic radio emission. <u>Akademiia Nauk</u> SSSR Doklady, 76:377.
- Gopal-Krishna, 1988. An investigation of the redshift-dependence of the radio spectral index among powerful double radio sources. A&A, 192:37.
- Gopal-Krishna and Kulkarni, V.K., 1992. The unification of radio galaxies and quasars and their linear size evolution. A&A, 257:11.
- Greenstein, J.L. and Schmidt, M., 1964. The Quasi-Stellar Radio Sources 3C 48 and 3C 273. ApJ, 140:1.
- Griffith, M.R. and Wright, A.E., 1993. The Parkes-MIT-NRAO (PMN) Survey. I. The 4850 MHz Surveys and Data Reduction. <u>AJ</u>, 105:1666.
- Gürkan, G., Hardcastle, M.J., Jarvis, M.J., et al., 2015. Herschel-ATLAS: the connection between star formation and AGN activity in radio-loud and radio-quiet active galaxies. MNRAS, 452(4):3776.
- Hale, C.L., Heywood, I., Jarvis, M.J., et al., 2024. MIGHTEE: The continuum survey data release 1. MNRAS.

Hale, C.L., Williams, W., Jarvis, M.J., et al., 2019. LOFAR observations of the XMM-LSS field. A&A, 622:A4.

- Hardcastle, M., 2018a. Interpreting radiative efficiency in radio-loud AGNs. <u>Nature Astronomy</u>, 2:273.
- Hardcastle, M.J., 2018b. A simulation-based analytic model of radio galaxies. MNRAS, 475(2):2768.
- Hardcastle, M.J., Alexander, P., Pooley, G.G., et al., 1999. FR II radio galaxies with z<sub>i</sub>0.3 II. Beaming and unification. MNRAS, 304(1):135.
- Hardcastle, M.J., Birkinshaw, M., and Worrall, D.M., 1998. Magnetic field strengths in the hotspots of 3C 33 and 111. MNRAS, 294:615.
- Hardcastle, M.J., Ching, J.H.Y., Virdee, J.S., et al., 2013. Herschel-ATLAS/GAMA: a difference between star formation rates in strong-line and weak-line radio galaxies. MNRAS, 429(3):2407.
- Hardcastle, M.J. and Croston, J.H., 2020. Radio galaxies and feedback from AGN jets. <u>NAR</u>, 88:101539.
- Hardcastle, M.J., Evans, D.A., and Croston, J.H., 2006. The X-ray nuclei of intermediate-redshift radio sources. MNRAS, 370(4):1893.
- Hardcastle, M.J., Evans, D.A., and Croston, J.H., 2007. Hot and cold gas accretion and feedback in radio-loud active galaxies. Monthly Notices of the Royal Astronomical Society, 376(4):1849.
- Hardcastle, M.J., Evans, D.A., and Croston, J.H., 2009. The active nuclei of z < 1.0 3CRR radio sources. MNRAS, 396(4):1929.
- Hardcastle, M.J., Harris, D.E., Worrall, D.M., et al., 2004. The Origins of X-Ray Emission from the Hot Spots of FR II Radio Sources. <u>ApJ</u>, 612(2):729.
- Hardcastle, M.J., Horton, M.A., Williams, W.L., et al., 2023. The LOFAR Two-Metre Sky Survey. VI. Optical identifications for the second data release. A&A, 678:A151.
- Hardcastle, M.J. and Looney, L.W., 2001. 85-GHz BIMA observations of the double-hotspot radio galaxy 3C20. MNRAS, 320(3):355.
- Hardcastle, M.J., Pierce, J.C.S., Duncan, K.J., et al., 2025. Radio AGN selection in LoTSS DR2. MNRAS, 539(2):1856.
- Hardcastle, M.J., Williams, W.L., Best, P.N., et al., 2019. Radio-loud AGN in the first LoTSS data release. The lifetimes and environmental impact of jet-driven sources. A&A, 622:A12.

Harwood, J.J., Croston, J.H., Intema, H.T., et al., 2016. FR II radio galaxies at low frequencies - I. Morphology, magnetic field strength and energetics. MNRAS, 458(4):4443.

- Harwood, J.J., Hardcastle, M.J., and Croston, J.H., 2015. Spectral ageing in the lobes of cluster-centre FR II radio galaxies. MNRAS, 454(4):3403.
- Harwood, J.J., Hardcastle, M.J., Croston, J.H., et al., 2013. Spectral ageing in the lobes of FR-II radio galaxies: new methods of analysis for broad-band radio data. MNRAS, 435(4):3353.
- Harwood, J.J., Hardcastle, M.J., Morganti, R., et al., 2017. FR II radio galaxies at low frequencies II. Spectral ageing and source dynamics. MNRAS, 469(1):639.
- Hatfield, P.W., Jarvis, M.J., Adams, N., et al., 2022. Hybrid photometric redshifts for sources in the COSMOS and XMM-LSS fields. MNRAS, 513(3):3719.
- Heald, G.H., Pizzo, R.F., Orrú, E., et al., 2015. The LOFAR Multifrequency Snapshot Sky Survey (MSSS). I. Survey description and first results. A&A, 582:A123.
- Heckman, T.M., 1980. An Optical and Radio Survey of the Nuclei of Bright Galaxies Activity in the Normal Galactic Nuclei. A&A, 87:152.
- Hey, J.S., Parsons, S.J., and Phillips, J.W., 1946. Fluctuations in Cosmic Radiation at Radio-Frequencies. Nature, 158(4007):234.
- Heywood, I., Jarvis, M.J., Hale, C.L., et al., 2022. MIGHTEE: total intensity radio continuum imaging and the COSMOS/XMM-LSS Early Science fields. MNRAS, 509(2):2150.
- Hine, R.G. and Longair, M.S., 1979. Optical spectra of 3CR radio galaxies. <u>Monthly Notices</u> of the Royal Astronomical Society, 188(1):111.
- Hlavacek-Larrondo, J., McDonald, M., Benson, B.A., et al., 2015. X-Ray Cavities in a Sample of 83 SPT-selected Clusters of Galaxies: Tracing the Evolution of AGN Feedback in Clusters of Galaxies out to z=1.2. <u>ApJ</u>, 805(1):35.
- Hong, X.y. and Wan, T.s., 1995. A statistical test of the unified model of active galactic nuclei. CAA, 19(3):277.
- Hota, A., Sirothia, S.K., Ohyama, Y., et al., 2011. Discovery of a spiral-host episodic radio galaxy. MNRAS, 417(1):L36.
- Hoyle, F., 1966. On the Nature of the Quasi-stellar Sources. Nature, 209(5025):751.
- Hoyle, F. and Fowler, W.A., 1963a. Nature of Strong Radio Sources. Nature, 197(4867):533.
- Hoyle, F. and Fowler, W.A., 1963b. On the nature of strong radio sources. MNRAS, 125:169.
- Hubble, E.P., 1926. Extragalactic nebulae. ApJ, 64:321.

Ineson, J., Croston, J.H., Hardcastle, M.J., et al., 2013. Radio-loud Active Galactic Nucleus: Is There a Link between Luminosity and Cluster Environment? ApJ, 770(2):136.

- Ineson, J., Croston, J.H., Hardcastle, M.J., et al., 2015. The link between accretion mode and environment in radio-loud active galaxies. MNRAS, 453(3):2682.
- Ineson, J., Croston, J.H., Hardcastle, M.J., et al., 2017. A representative survey of the dynamics and energetics of FR II radio galaxies. MNRAS, 467(2):1586.
- Jaffe, W.J. and Perola, G.C., 1973. Dynamical Models of Tailed Radio Sources in Clusters of Galaxies. A&A, 26:423.
- Jansky, K.G., 1933. Radio Waves from Outside the Solar System. Nature, 132(3323):66.
- Janssen, R.M.J., Röttgering, H.J.A., Best, P.N., et al., 2012. The triggering probability of radio-loud AGN. A comparison of high and low excitation radio galaxies in hosts of different colors. A&A, 541:A62.
- Jarvis, M., Taylor, R., Agudo, I., et al., 2016. The MeerKAT International GHz Tiered Extragalactic Exploration (MIGHTEE) Survey. In MeerKAT Science: On the Pathway to the SKA, page 6.
- Jarvis, M.J., Rawlings, S., Eales, S., et al., 2001. A sample of 6C radio sources designed to find objects at redshift z<sub>6</sub>4 III. Imaging and the radio galaxy K-z relation. MNRAS, 326(4):1585.
- Jarvis, M.J., Teimourian, H., Simpson, C., et al., 2009. The discovery of a typical radio galaxy at z = 4.88. MNRAS, 398(1):L83.
- Jenkins, C.R., 1982. Radio observations of early-type galaxies. MNRAS, 200:705.
- Jennison, R.C. and Das Gupta, M.K., 1953. Fine Structure of the Extra-terrestrial Radio Source Cygnus I. Nature, 172(4387):996.
- Johnston-Hollitt, M., Dehghan, S., and Pratley, L., 2015. Using Tailed Radio Galaxies to Probe the Environment and Magnetic Field of Galaxy Clusters in the SKA Era. In <u>Advancing</u> Astrophysics with the Square Kilometre Array (AASKA14), page 101.
- Jonas, J. and MeerKAT Team, 2016. The MeerKAT Radio Telescope. In MeerKAT Science:

  On the Pathway to the SKA, page 1.
- Jonas, J.L., 2009. MeerKAT The South African Array With Composite Dishes and Wide-Band Single Pixel Feeds. <u>IEEE Proceedings</u>, 97(8):1522.
- Joye, W.A. and Mandel, E., 2003. New Features of SAOImage DS9. In H.E. Payne, R.I. Jedrzejewski, and R.N. Hook, editors, <u>Astronomical Data Analysis Software and Systems</u> XII, volume 295 of Astronomical Society of the Pacific Conference Series, page 489.

Kapahi, V.K., Athreya, R.M., Subrahmanya, C.R., et al., 1998a. The Molonglo Reference Catalog 1 Jy Radio Source Survey. III. Identification of a Complete Quasar Sample. <u>ApJ</u>, 118(2):327.

- Kapahi, V.K., Athreya, R.M., van Breugel, W., et al., 1998b. The Molonglo Reference Catalog 1 Jy Radio Source Survey. II. Radio Structures of Galaxy Identifications. ApJ, 118(2):275.
- Kardashev, N.S., 1962. Nonstationarity of Spectra of Young Sources of Nonthermal Radio Emission. Soviet Astronomy, 6:317.
- Kataoka, J. and Stawarz, Ł., 2005. X-Ray Emission Properties of Large-Scale Jets, Hot Spots, and Lobes in Active Galactic Nuclei. ApJ, 622(2):797.
- Katz-Stone, D.M. and Rudnick, L., 1998. A Spectral Analysis of 3C 67 and 3C 190. In J.A. Zensus, G.B. Taylor, and J.M. Wrobel, editors, <u>IAU Colloq. 164</u>: Radio Emission from <u>Galactic and Extragalactic Compact Sources</u>, volume 144 of <u>Astronomical Society of the Pacific Conference Series</u>, page 181.
- Kauffmann, G., Heckman, T.M., Tremonti, C., et al., 2003. The host galaxies of active galactic nuclei. MNRAS, 346(4):1055.
- Kellermann, K.I., Sramek, R., Schmidt, M., et al., 1989. VLA Observations of Objects in the Palomar Bright Quasar Survey. <u>AJ</u>, 98:1195.
- Kelly, B.C., Bechtold, J., and Siemiginowska, A., 2009. Are the Variations in Quasar Optical Flux Driven by Thermal Fluctuations? ApJ, 698(1):895.
- Ker, L.M., Best, P.N., Rigby, E.E., et al., 2012. New insights on the z– $\alpha$  correlation from complete radio samples. MNRAS, 420(3):2644.
- Khabibullina, M.L., Mikhailov, A.G., Sotnikova, Y.V., et al., 2023. Radio Properties of High-Redshift Galaxies at  $z \ge 1$ . Astrophysical Bulletin, 78(4):443.
- Kiepenheuer, K.O., 1950. Cosmic Rays as the Source of General Galactic Radio Emission. Physical Review, 79(4):738.
- Kimball, A.E., Kellermann, K.I., Condon, J.J., et al., 2012. The Two-Component Radio Luminosity Function of QSOs: Star Formation and AGNs. In <u>American Astronomical Society Meeting Abstracts #219</u>, volume 219 of <u>American Astronomical Society Meeting Abstracts</u>, page 109.05.
- Klamer, I.J., Ekers, R.D., Bryant, J.J., et al., 2006. A search for distant radio galaxies from SUMSS and NVSS III. Radio spectral energy distributions and the z- $\alpha$  correlation. MNRAS, 371(2):852.

Knight, C.A., Rogers, A.E.E., Shapiro, I.I., et al., 1971. Detection of double-source structure in the nucleus of the quasi-stellar radio sources 3C 279. In <u>Bulletin of the American</u> Astronomical Society, volume 3, page 416.

- Konar, C. and Hardcastle, M.J., 2013. Particle acceleration and dynamics of double-double radio galaxies: theory versus observations. MNRAS, 436(2):1595.
- Kondapally, R., Best, P.N., Hardcastle, M.J., et al., 2021. The LOFAR Two-meter Sky Survey: Deep Fields Data Release 1. III. Host-galaxy identifications and value added catalogues. A&A, 648:A3.
- Koo, D.C., Kron, R.G., and Cudworth, K.M., 1986. Quasars to B ¿ 22.5 in selected area 57: a catalog of multicolor photometry, variability and astrometry. PASP, 98:285.
- Kormendy, J. and Richstone, D., 1995. Inward Bound—The Search For Supermassive Black Holes In Galactic Nuclei. Annual Review of Astronomy and Astrophysics, 33:581.
- Kozłowski, S., Kochanek, C.S., Udalski, A., et al., 2010. Quantifying Quasar Variability as Part of a General Approach to Classifying Continuously Varying Sources. ApJ, 708(2):927.
- Kraft, R.P., Birkinshaw, M., Hardcastle, M.J., et al., 2007. A Radio through X-Ray Study of the Hot Spots, Active Nucleus, and Environment of the Nearby FR II Radio Galaxy 3C 33. <u>ApJ</u>, 659(2):1008.
- Kraft, R.P., Vázquez, S.E., Forman, W.R., et al., 2003. X-Ray Emission from the Hot Interstellar Medium and Southwest Radio Lobe of the Nearby Radio Galaxy Centaurus A. <u>ApJ</u>, 592(1):129.
- Krause, M.G.H., Shabala, S.S., Hardcastle, M.J., et al., 2019. How frequent are close supermassive binary black holes in powerful jet sources? MNRAS, 482(1):240.
- Krolik, J.H. and Chen, W., 1991. Steep Radio Spectra in High-Redshift Radio Galaxies. <u>AJ</u>, 102:1659.
- Lähteenmäki, A. and Valtaoja, E., 1999. Total Flux Density Variations in Extragalactic Radio Sources. III. Doppler Boosting Factors, Lorentz Factors, and Viewing Angles for Active Galactic Nuclei. ApJ, 521(2):493.
- Laing, R.A., 1988. The sidedness of jets and depolarization in powerful extragalactic radio sources. Nature, 331(6152):149.
- Laing, R.A., Jenkins, C.R., Wall, J.V., et al., 1994. Spectrophotometry of a Complete Sample of 3CR Radio Sources: Implications for Unified Models. In G.V. Bicknell, M.A. Dopita, and P.J. Quinn, editors, <u>The Physics of Active Galaxies</u>, volume 54 of <u>Astronomical Society of the Pacific Conference Series</u>, page 201.

Laing, R.A. and Peacock, J.A., 1980. The relation between radio luminosity and spectrum for extended extragalactic radio sources. MNRAS, 190:903.

- Laing, R.A., Riley, J.M., and Longair, M.S., 1983. Bright radio sources at 178 MHz: flux densities, optical identifications and the cosmological evolution of powerful radio galaxies. MNRAS, 204:151.
- Large, M.I., Mills, B.Y., Little, A.G., et al., 1981. The Molonglo Reference Catalogue of radio sources. MNRAS, 194:693.
- Lawrence, A., 1987. Classification of active galaxies and the prospect of a unified phenomenology. PASP, 99:309.
- Le Brun, A.M.C., McCarthy, I.G., Schaye, J., et al., 2014. Towards a realistic population of simulated galaxy groups and clusters. MNRAS, 441(2):1270.
- Le Fevre, O., Deltorn, J.M., Crampton, D., et al., 1996. Clustering around the Radio Galaxy MRC 0316-257 at Z = 3.14. ApJ, 471:L11.
- Ledlow, M.J. and Owen, F.N., 1996. 20 CM VLA Survey of Abell Clusters of Galaxies. VI. Radio/Optical Luminosity Functions. AJ, 112:9.
- Ledlow, M.J., Owen, F.N., Yun, M.S., et al., 2001. A Large-Scale Jet and FR I Radio Source in a Spiral Galaxy: The Host Properties and External Environment. ApJ, 552(1):120.
- Lilly, S.J., 1988. Discovery of a Radio Galaxy at a Redshift of 3.395. ApJ, 333:161.
- Lin, Y.T., Hsieh, B.C., Lin, S.C., et al., 2017. First Results on the Cluster Galaxy Population from the Subaru Hyper Suprime-Cam Survey. III. Brightest Cluster Galaxies, Stellar Mass Distribution, and Active Galaxies. ApJ, 851(2):139.
- Lin, Y.T., Shen, Y., Strauss, M.A., et al., 2010. On the Populations of Radio Galaxies with Extended Morphology at z < 0.3. ApJ, 723(2):1119.
- Longair, M.S., 1980. Radio Astronomers, X-Ray Astronomers and the Space Telescope. In M.S. Longair and J.W. Warner, editors, <u>Scientific Research with the Space Telescope</u>, page 241.
- Longair, M.S., 2010. High energy astrophysics. Cambridge university press.
- Longair, M.S., Ryle, M., and Scheuer, P.A.G., 1973. Models of extended radiosources. MNRAS, 164:243.
- Lyke, B.W., Higley, A.N., McLane, J.N., et al., 2020. The Sloan Digital Sky Survey Quasar Catalog: Sixteenth Data Release. ApJ, 250(1):8.

Lynden-Bell, D., 1969. Galactic Nuclei as Collapsed Old Quasars. Nature, 223(5207):690.

- Machalski, J., Chyży, K.T., Stawarz, Ł., et al., 2007. A method for estimating the dynamical age of FR II-type radio sources from multi-frequency data. A&A, 462(1):43.
- MacLeod, C.L., Brooks, K., Ivezić, Ž., et al., 2011. Quasar Selection Based on Photometric Variability. ApJ, 728(1):26.
- Maddox, N., Hewett, P.C., Péroux, C., et al., 2012. The large area KX quasar catalogue I. Analysis of the photometric redshift selection and the complete quasar catalogue. MNRAS, 424(4):2876.
- Magliocchetti, M., 2022. Hosts and environments: a (large-scale) radio history of AGN and star-forming galaxies. AAPR, 30(1):6.
- Magliocchetti, M., Maddox, S.J., Wall, J.V., et al., 2000. The redshift distribution of FIRST radio sources at 1mJy. MNRAS, 318(4):1047.
- Magorrian, J., Tremaine, S., Richstone, D., et al., 1998. The Demography of Massive Dark Objects in Galaxy Centers. AJ, 115(6):2285.
- Mahabal, A., Kembhavi, A., and McCarthy, P.J., 1999. Effective Radii and Color Gradients in Radio Galaxies. ApJ, 516(2):L61.
- Mahatma, V.H., Hardcastle, M.J., Croston, J.H., et al., 2020. Investigating the spectral age problem with powerful radio galaxies. MNRAS, 491(4):5015.
- Maltby, P., Matthews, T.A., and Moffet, A.T., 1963. Brightness Distribution in Discrete Radio Sources.IV. a Discussion of 24 Identified Sources. ApJ, 137:153.
- Mannering, E.J.A., Worrall, D.M., and Birkinshaw, M., 2011. The host galaxies of radio-loud active galactic nuclei: colour structure. MNRAS, 416(4):2869.
- Mao, M.Y., Owen, F., Duffin, R., et al., 2015. J1649+2635: a grand-design spiral with a large double-lobed radio source. MNRAS, 446(4):4176.
- Matthews, T.A., Morgan, W.W., and Schmidt, M., 1964. A Discussion of Galaxies Indentified with Radio Sources. <u>ApJ</u>, 140:35.
- Matthews, T.A. and Sandage, A.R., 1963. Optical Identification of 3C 48, 3C 196, and 3C 286 with Stellar Objects. ApJ, 138:30.
- Mauch, T. and Sadler, E.M., 2007. Radio sources in the 6dFGS: local luminosity functions at 1.4 GHz for star-forming galaxies and radio-loud AGN. MNRAS, 375(3):931.
- McCarthy, I.G., Schaye, J., Bower, R.G., et al., 2011. Gas expulsion by quasar-driven winds as a solution to the overcooling problem in galaxy groups and clusters. MNRAS, 412(3):1965.

McCarthy, P.J., Kapahi, V.K., van Breugel, W., et al., 1996. The Molonglo Reference Catalog/1 Jansky Radio Source Survey. I. Radio Galaxy Identifications. ApJ, 107:19.

- McMullin, J.P., Waters, B., Schiebel, D., et al., 2007. CASA Architecture and Applications. In R.A. Shaw, F. Hill, and D.J. Bell, editors, <u>Astronomical Data Analysis Software and Systems</u> XVI, volume 376 of Astronomical Society of the Pacific Conference Series, page 127.
- McNamara, B.R. and Nulsen, P.E.J., 2007. Heating Hot Atmospheres with Active Galactic Nuclei. Annual Review of Astronomy and Astrophysics, 45(1):117.
- McNamara, B.R. and Nulsen, P.E.J., 2012. Mechanical feedback from active galactic nuclei in galaxies, groups and clusters. New Journal of Physics, 14(5):055023.
- Meisenheimer, K., Roser, H.J., Hiltner, P.R., et al., 1989. The synchrotron spectra of radio hot spots. A&A, 219:63.
- Meisenheimer, K., Yates, M.G., and Roeser, H.J., 1997. The synchrotron spectra of radio hot spots. II. Infrared imaging. A&A, 325:57.
- Merloni, A. and Heinz, S., 2008. A synthesis model for AGN evolution: supermassive black holes growth and feedback modes. MNRAS, 388(3):1011.
- Merloni, A., Rudnick, G., and Di Matteo, T., 2004. Tracing the cosmological assembly of stars and supermassive black holes in galaxies. MNRAS, 354(3):L37.
- Miley, G. and De Breuck, C., 2008. Distant radio galaxies and their environments. <u>AAPR</u>, 15(2):67.
- Mingo, B., Croston, J.H., Best, P.N., et al., 2022. Accretion mode versus radio morphology in the LOFAR Deep Fields. MNRAS, 511(3):3250.
- Mingo, B., Croston, J.H., Hardcastle, M.J., et al., 2019. Revisiting the Fanaroff-Riley dichotomy and radio-galaxy morphology with the LOFAR Two-Metre Sky Survey (LoTSS). MNRAS, 488(2):2701.
- Mingo, B., Hardcastle, M.J., Croston, J.H., et al., 2014. An X-ray survey of the 2 Jy sample I. Is there an accretion mode dichotomy in radio-loud AGN? MNRAS, 440(1):269.
- Minkowski, R., 1960. A New Distant Cluster of Galaxies. ApJ, 132:908.
- Miraghaei, H. and Best, P.N., 2017. The nuclear properties and extended morphologies of powerful radio galaxies: the roles of host galaxy and environment. MNRAS, 466(4):4346.
- Mo, W., Gonzalez, A., Brodwin, M., et al., 2020. The Massive and Distant Clusters of WISE Survey. VIII. Radio Activity in Massive Galaxy Clusters. ApJ, 901(2):131.

Mohan, N. and Rafferty, D., 2015. PyBDSF: Python Blob Detection and Source Finder. Astrophysics Source Code Library, record ascl:1502.007.

- Morabito, L.K. and Harwood, J.J., 2018. Investigating the cause of the  $\alpha$ -z relation. MNRAS, 480(2):2726.
- Morabito, L.K., Sweijen, F., Radcliffe, J.F., et al., 2022. Identifying active galactic nuclei via brightness temperature with sub-arcsecond international LOFAR telescope observations. MNRAS, 515(4):5758.
- Morabito, L.K., Williams, W.L., Duncan, K.J., et al., 2017. Investigating the unification of LOFAR-detected powerful AGN in the Boötes field. MNRAS, 469(2):1883.
- Morganti, R., Oosterloo, T.A., Reynolds, J.E., et al., 1997. A study of cores in a complete sample of radio sources. MNRAS, 284(3):541.
- Mulcahy, D.D., Mao, M.Y., Mitsuishi, I., et al., 2016. Discovery of a low-luminosity spiral DRAGN. A&A, 595:L8.
- Mullin, L.M., Riley, J.M., and Hardcastle, M.J., 2008. Observed properties of FRII quasars and radio galaxies at z < 1.0. MNRAS, 390(2):595.
- Myers, S.T. and Spangler, S.R., 1985. Synchrotron aging in the lobes of luminous radio galaxies. ApJ, 291:52.
- Naab, T. and Ostriker, J.P., 2017. Theoretical Challenges in Galaxy Formation. Annual Review of Astronomy and Astrophysics, 55(1):59.
- Narayan, R. and Yi, I., 1995. Advection-dominated Accretion: Underfed Black Holes and Neutron Stars. ApJ, 452:710.
- Netzer, H., 2015. Revisiting the Unified Model of Active Galactic Nuclei. Annual Review of Astronomy and Astrophysics, 53:365.
- Norris, R.P., Hopkins, A.M., Afonso, J., et al., 2011. EMU: Evolutionary Map of the Universe. PASA, 28(3):215.
- Northover, K.J.E., 1973. The radio galaxy 3C 66. MNRAS, 165:369.
- Ogle, P., Antonucci, R., and Whysong, D., 2007. Mid infrared spectra of radio galaxies and quasars.
- Onuora, L.I., 1989. The Variation of Spectral Index with Luminosity for Radio Galaxies. APSS, 162(2):349.
- Onuora, L.I., 1991. Radio Source Orientation and the Angular Diameter–Redshift Relation. ApJ, 377:36.

Orr, M.J.L. and Browne, I.W.A., 1982. Relativistic beaming and quasar statistics. MNRAS, 200:1067.

- Orrù, E., Murgia, M., Feretti, L., et al., 2010. Low-frequency study of two giant radio galaxies: 3C 35 and 3C 223. A&A, 515:A50.
- Osterbrock, D.E., 1989. Astrophysics of gaseous nebulae and active galactic nuclei.
- Pace, C. and Salim, S., 2014. Satellites of Radio AGN in SDSS: Insights into AGN Triggering and Feedback. ApJ, 785(1):66.
- Pacholczyk, A.G. and Roberts, J.A., 1971. Radio Astrophysics: Nonthermal Processes in Galactic and Extragalactic Sources. Physics Today, 24(9):57.
- Padovani, P., 2016. The faint radio sky: radio astronomy becomes mainstream. AAPR, 24(1):13.
- Pascarelle, S.M., Windhorst, R.A., Keel, W.C., et al., 1996. Sub-galactic clumps at a redshift of 2.39 and implications for galaxy formation. Nature, 383(6595):45.
- Paterno-Mahler, R., Blanton, E.L., Brodwin, M., et al., 2017. The High-redshift Clusters Occupied by Bent Radio AGN (COBRA) Survey: The Spitzer Catalog. ApJ, 844(1):78.
- Pauliny-Toth, I.I.K. and Kellermann, K.I., 1966. Variations in the Radio-Frequency Spectra of 3c 84, 3c 273, 3c 279, and Other Radio Sources. ApJ, 146:634.
- Pauliny-Toth, I.I.K., Wade, C.M., and Heeschen, D.S., 1966. Positions and Flux Densities of Radio Sources. ApJ, 13:65.
- Peacock, J.A. and Gull, S.F., 1981. Multifrequency models for the cosmological evolution of extragalactic radio sources. MNRAS, 196:611.
- Pentericci, L., Röttgering, H.J.A., Miley, G.K., et al., 1999. HST images and properties of the most distant radio galaxies. A&A, 341:329.
- Pentericci, L., Van Reeven, W., Carilli, C.L., et al., 2000. VLA radio continuum observations of a new sample of high redshift radio galaxies. A&A Supp., 145:121.
- Peters, C.M., Richards, G.T., Myers, A.D., et al., 2015. Quasar Classification Using Color and Variability. ApJ, 811(2):95.
- Peterson, B.M., Ferrarese, L., Gilbert, K.M., et al., 2004. Central Masses and Broad-Line Region Sizes of Active Galactic Nuclei. II. A Homogeneous Analysis of a Large Reverberation-Mapping Database. <a href="https://example.com/apping-patabase">ApJ, 613(2):682</a>.
- Peterson, J.R., Kahn, S.M., Paerels, F.B.S., et al., 2003. High-Resolution X-Ray Spectroscopic Constraints on Cooling-Flow Models for Clusters of Galaxies. ApJ, 590(1):207.

Pierce, J.C.S., Tadhunter, C.N., Ramos Almeida, C., et al., 2019. Do AGN triggering mechanisms vary with radio power? - I. Optical morphologies of radio-intermediate HERGs. MNRAS, 487(4):5490.

- Pinjarkar, S., Hardcastle, M.J., Harwood, J.J., et al., 2023. Spectral age distribution for radio-loud active galaxies in the XMM-LSS field. MNRAS, 523(1):620.
- Pizzolato, F. and Soker, N., 2005. On the Nature of Feedback Heating in Cooling Flow Clusters. ApJ, 632(2):821.
- Rafferty, D.A., McNamara, B.R., Nulsen, P.E.J., et al., 2006. The Feedback-regulated Growth of Black Holes and Bulges through Gas Accretion and Starbursts in Cluster Central Dominant Galaxies. ApJ, 652(1):216.
- Ramos Almeida, C., Bessiere, P.S., Tadhunter, C.N., et al., 2012. Are luminous radio-loud active galactic nuclei triggered by galaxy interactions? MNRAS, 419(1):687.
- Randall, S.W., Nulsen, P.E.J., Jones, C., et al., 2015. A Very Deep Chandra Observation of the Galaxy Group NGC 5813: AGN Shocks, Feedback, and Outburst History. ApJ, 805(2):112.
- Rawlings, S., Lacy, M., Blundell, K.M., et al., 1996. A radio galaxy at redshift 4.41. Nature, 383(6600):502.
- Reber, G., 1940. Notes: Cosmic Static. ApJ, 91:621.
- Reber, G., 1944. Cosmic Static. ApJ, 100:279.
- Rees, M.J., 1966. Appearance of Relativistically Expanding Radio Sources. <u>Nature</u>, 211(5048):468.
- Rengelink, R.B., Tang, Y., de Bruyn, A.G., et al., 1997. The Westerbork Northern Sky Survey (WENSS), I. A 570 square degree Mini-Survey around the North Ecliptic Pole. <u>A&A Supp.</u>, 124:259.
- Reuland, M., van Breugel, W., Röttgering, H., et al., 2003. Giant Ly $\alpha$  Nebulae Associated with High-Redshift Radio Galaxies. ApJ, 592(2):755.
- Richards, G.T., Fan, X., Newberg, H.J., et al., 2002. Spectroscopic Target Selection in the Sloan Digital Sky Survey: The Quasar Sample. AJ, 123(6):2945.
- Roettgering, H.J.A., West, M.J., Miley, G.K., et al., 1996. The optical counterparts and the environments of ultra-steep-spectrum radio sources. <u>A&A</u>, 307:376.
- Rowan-Robinson, M., Babbedge, T., Oliver, S., et al., 2008. Photometric redshifts in the SWIRE Survey. MNRAS, 386(2):697.

Rybicki, G.B. and Lightman, A.P., 1979. Radiative processes in astrophysics. J. Wiley and sons.

- Ryle, M., Smith, F.G., and Elsmore, B., 1950. A preliminary survey of the radio stars in the Northern Hemisphere. MNRAS, 110:508.
- Sabater, J., Best, P.N., Hardcastle, M.J., et al., 2019. The LoTSS view of radio AGN in the local Universe. The most massive galaxies are always switched on. A&A, 622:A17.
- Sabater, J., Best, P.N., and Heckman, T.M., 2015. Triggering optical AGN: the need for cold gas, and the indirect roles of galaxy environment and interactions. MNRAS, 447(1):110.
- Saikia, D.J., Jeyakumar, S., Wiita, P.J., et al., 1995. Compact steep-spectrum radio sources and unification schemes. MNRAS, 276(4):1215.
- Saikia, D.J. and Kulkarni, V.K., 1994. On the evidence against the unified scheme for radio galaxies and quasars. MNRAS, 270:897.
- Sakelliou, I., Peterson, J.R., Tamura, T., et al., 2002. High resolution soft X-ray spectroscopy of M 87 with the reflection grating spectrometers on XMM-Newton. A&A, 391:903.
- Salpeter, E.E., 1964. Accretion of Interstellar Matter by Massive Objects. ApJ, 140:796.
- Sandage, A., 1965. The Existence of a Major New Constituent of the Universe: the Quasistellar Galaxies. ApJ, 141:1560.
- Saripalli, L., Hunstead, R.W., Subrahmanyan, R., et al., 2005. A Complete Sample of Megaparsec-sized Double Radio Sources from the Sydney University Molonglo Sky Survey. AJ, 130(3):896.
- Saxena, A., Jagannathan, P., Röttgering, H.J.A., et al., 2018. A search for faint high-redshift radio galaxy candidates at 150 MHz. MNRAS, 475(4):5041.
- Scheuer, P.A.G., 1974. Models of extragalactic radio sources with a continuous energy supply from a central object. MNRAS, 166:513.
- Schmidt, K.B., Marshall, P.J., Rix, H.W., et al., 2010. Selecting Quasars by Their Intrinsic Variability. ApJ, 714(2):1194.
- Schmidt, M., 1963. 3C 273: A Star-Like Object with Large Red-Shift. Nature, 197(4872):1040.
- Schmidt, M. and Green, R.F., 1983. Quasar evolution derived from the Palomar bright quasar survey and other complete quasar surveys. ApJ, 269:352.
- Scott, P.F. and Ryle, M., 1961. The number-flux density relation for radio sources away from the galactic plane. MNRAS, 122:389.

Sesar, B., Ivezić, Ž., Lupton, R.H., et al., 2007. Exploring the Variable Sky with the Sloan Digital Sky Survey. AJ, 134(6):2236.

- Seyfert, C.K., 1943. Nuclear Emission in Spiral Nebulae. ApJ, 97:28.
- Seymour, N., Stern, D., De Breuck, C., et al., 2007. The Massive Hosts of Radio Galaxies across Cosmic Time. ApJ, 171(2):353.
- Shakeshaft, J.R., Ryle, M., Baldwin, J.E., et al., 1955. A survey of radio sources between declinations—38° and +83°. Memoirs of the Royal Astronomical Society, 67:106.
- Shields, G.A., 1999. A Brief History of Active Galactic Nuclei. PASP, 111(760):661.
- Shimwell, T.W., Hardcastle, M.J., Tasse, C., et al., 2022. The LOFAR Two-metre Sky Survey. V. Second data release. A&A, 659:A1.
- Shimwell, T.W., Röttgering, H.J.A., Best, P.N., et al., 2017. The LOFAR Two-metre Sky Survey. I. Survey description and preliminary data release. A&A, 598:A104.
- Shimwell, T.W., Tasse, C., Hardcastle, M.J., et al., 2019. The LOFAR Two-metre Sky Survey. II. First data release. A&A, 622:A1.
- Sholomitsky, G.B., 1965. Variability of the Radio Source CTA-102. <u>Information Bulletin on Variable Stars</u>, 83:1.
- Shull, J.M., Smith, B.D., and Danforth, C.W., 2012. The Baryon Census in a Multiphase Intergalactic Medium: 30% of the Baryons May Still be Missing. ApJ, 759(1):23.
- Silk, J. and Rees, M.J., 1998. Quasars and galaxy formation. A&A, 331:L1.
- Simionescu, A., Werner, N., Böhringer, H., et al., 2009. Chemical enrichment in the cluster of galaxies Hydra A. A&A, 493(2):409.
- Simpson, C., Martínez-Sansigre, A., Rawlings, S., et al., 2006. Radio imaging of the Subaru/XMM-Newton Deep Field I. The 100-μJy catalogue, optical identifications, and the nature of the faint radio source population. MNRAS, 372(2):741.
- Singal, A.K., 1993. Evidence against the unified scheme for powerful radio galaxies and quasars. MNRAS, 262(2):L27.
- Singal, A.K., 1996. Differential number counts of radio galaxies and quasars: evidence against the unified scheme. MNRAS, 278:1069.
- Singal, A.K., 2014. Discordance of the Unified Scheme with Observed Properties of Quasars and High-excitation Galaxies in the 3CRR Sample. AJ, 148(1):16.

Singal, A.K. and Laxmi Singh, R., 2013. Unification Scheme of Radio Galaxies and Quasars Falsified by Their Observed Size Distributions. ApJ, 766(1):37.

- Slipher, V.M., 1917. Nebulae. Proceedings of the American Philosophical Society, 56:403.
- Smith, F.G., 1951. An Accurate Determination of the Positions of Four Radio Stars. <u>Nature</u>, 168(4274):555.
- Smolčić, V., Intema, H., Šlaus, B., et al., 2018. The XXL Survey. XXIX. GMRT 610 MHz continuum observations. A&A, 620:A14.
- Smolčić, V., Zamorani, G., Schinnerer, E., et al., 2009. Cosmic Evolution of Radio Selected Active Galactic Nuclei in the Cosmos Field. ApJ, 696(1):24.
- Somerville, R.S. and Davé, R., 2015. Physical Models of Galaxy Formation in a Cosmological Framework. Annual Review of Astronomy and Astrophysics, 53:51.
- Spinrad, H., 1982. Redshifts and spectroscopy of very distant radio galaxies with strong emission lines. PASP, 94:397.
- Spinrad, H., Djorgovski, S., Marr, J., et al., 1985. A third update of the status of the 3 CR sources: further new redshifts and new identifications of distant galaxies. PASP, 97:932.
- Spitzer, Lyman, J. and Saslaw, W.C., 1966. On the Evolution of Galactic Nuclei. ApJ, 143:400.
- Springel, V., Di Matteo, T., and Hernquist, L., 2005a. Modelling feedback from stars and black holes in galaxy mergers. MNRAS, 361(3):776.
- Springel, V., White, S.D.M., Jenkins, A., et al., 2005b. Simulations of the formation, evolution and clustering of galaxies and quasars. Nature, 435(7042):629.
- Stern, D., Assef, R.J., Benford, D.J., et al., 2012. Mid-infrared Selection of Active Galactic Nuclei with the Wide-Field Infrared Survey Explorer. I. Characterizing WISE-selected Active Galactic Nuclei in COSMOS. ApJ, 753(1):30.
- Stern, D., Eisenhardt, P., Gorjian, V., et al., 2005. Mid-Infrared Selection of Active Galaxies. ApJ, 631(1):163.
- Strateva, I., Ivezić, Ž., Knapp, G.R., et al., 2001. Color Separation of Galaxy Types in the Sloan Digital Sky Survey Imaging Data. AJ, 122(4):1861.
- Swarup, G., Ananthakrishnan, S., Kapahi, V.K., et al., 1991. The Giant Metre-Wave Radio Telescope. Current Science, 60:95.
- Sweijen, F., Pierce, J.C.S., Hardcastle, M.J., et al., 2025. The low-frequency size distribution of radio sources in the Lockman Hole. MNRAS, 540(1):416.

Sweijen, F., van Weeren, R.J., Röttgering, H.J.A., et al., 2022. Deep sub-arcsecond wide-field imaging of the Lockman Hole field at 144 MHz. Nature Astronomy, 6:350.

- Tadhunter, C., 2016. Radio AGN in the local universe: unification, triggering and evolution. AAPR, 24(1):10.
- Tamhane, P., Wadadekar, Y., Basu, A., et al., 2015. J021659-044920: a relic giant radio galaxy at  $z \sim 1.3$ . MNRAS, 453(3):2438.
- Tasse, C., Best, P.N., Röttgering, H., et al., 2008. Radio-loud AGN in the XMM-LSS field. II. A dichotomy in environment and accretion mode? A&A, 490(3):893.
- Tasse, C., Shimwell, T., Hardcastle, M.J., et al., 2021. The LOFAR Two-meter Sky Survey: Deep Fields Data Release 1. I. Direction-dependent calibration and imaging. A&A, 648:A1.
- Tavecchio, F., Maraschi, L., Sambruna, R.M., et al., 2000. The X-Ray Jet of PKS 0637-752: Inverse Compton Radiation from the Cosmic Microwave Background? ApJ, 544(1):L23.
- Terlevich, R. and Melnick, J., 1985. Warmers: the missing link between Starburst and Seyfert galaxies. MNRAS, 213:841.
- Thompson, A.R., Clark, B.G., Wade, C.M., et al., 1980. The Very Large Array. ApJ, 44:151.
- Tielens, A.G.G.M., Miley, G.K., and Willis, A.G., 1979. Westerbork Observations of 4C Sources with Steep Radio Spectra. A&A Supp., 35:153.
- Treister, E., Virani, S., Gawiser, E., et al., 2009. Optical Spectroscopy of X-Ray Sources in the Extended Chandra Deep Field South. ApJ, 693(2):1713.
- Tribble, P.C., 1993. Radio spectral ageing in a random magnetic field. MNRAS, 261:57.
- Turner, R.J., Rogers, J.G., Shabala, S.S., et al., 2018. RAiSE II: resolved spectral evolution in radio AGN. MNRAS, 473(3):4179.
- Ubachukwu, A.A., 2002. Statistical Tests of the Unification Scheme for High Luminosity Double Radio Sources. APSS, 279(3):251.
- Ulrich, M.H., Maraschi, L., and Urry, C.M., 1997. Variability of Active Galactic Nuclei. Annual Review of Astronomy and Astrophysics, 35:445.
- Urry, C.M. and Padovani, P., 1995. Unified Schemes for Radio-Loud Active Galactic Nuclei. PASP, 107:803.
- Vaccari, M., 2015. The Spitzer Data Fusion: Contents, Construction and Applications to Galaxy Evolution Studies. In <u>The Many Facets of Extragalactic Radio Surveys: Towards</u> New Scientific Challenges, page 27.

Vaccari, M., 2022. The Spitzer Spectroscopic Data Fusion - Merged Spectroscopic Redshift Catalogs in Spitzer Fields. In Zenodo dataset, volume 63, page 6368348.

- Vanden Berk, D.E., Wilhite, B.C., Kron, R.G., et al., 2004. The Ensemble Photometric Variability of ~25,000 Quasars in the Sloan Digital Sky Survey. ApJ, 601(2):692.
- Venemans, B.P., Röttgering, H.J.A., Miley, G.K., et al., 2007. Protoclusters associated with z ¿ 2 radio galaxies . I. Characteristics of high redshift protoclusters. A&A, 461(3):823.
- Vernstrom, T., Gaensler, B.M., Vacca, V., et al., 2018. Radio polarization properties of quasars and active galaxies at high redshifts. MNRAS, 475(2):1736.
- Villar-Martín, M., Vernet, J., di Serego Alighieri, S., et al., 2003. Kinematically quiet haloes around z-2.5 radio galaxies. Keck spectroscopy. MNRAS, 346(1):273.
- Virtanen, P., Gommers, R., Oliphant, T.E., et al., 2020. SciPy 1.0: Fundamental Algorithms for Scientific Computing in Python. Nature Methods, 17:261.
- Warren, S.J., Hewett, P.C., and Foltz, C.B., 2000. The KX method for producing K-band flux-limited samples of quasars. MNRAS, 312(4):827.
- Whitney, A.R., Shapiro, I.I., Rogers, A.E.E., et al., 1971. Quasars Revisited: Rapid Time Variations Observed Via Very-Long-Baseline Interferometry. Science, 173(3993):225.
- Whittam, I.H., Jarvis, M.J., Hale, C.L., et al., 2022. MIGHTEE: the nature of the radio-loud AGN population. MNRAS, 516(1):245.
- Whittam, I.H., Prescott, M., Hale, C.L., et al., 2024. MIGHTEE: Multi-wavelength counterparts in the COSMOS field. MNRAS, 527(2):3231.
- Whysong, D. and Antonucci, R., 2004. Thermal Emission as a Test for Hidden Nuclei in Nearby Radio Galaxies. ApJ, 602(1):116.
- Willott, C.J., Rawlings, S., Jarvis, M.J., et al., 2003. Near-infrared imaging and the K-z relation for radio galaxies in the 7C Redshift Survey. MNRAS, 339(1):173.
- Windhorst, R.A., Katgert, P., Kron, R.G., et al., 1982. Colors of radio galaxies at high redshifts. In D.S. Heeschen and C.M. Wade, editors, <a href="Extragalactic Radio Sources"><u>Extragalactic Radio Sources</u></a>, volume 97 of <a href="EAU Symposium"><u>IAU Symposium</u></a>, pages 427–430.
- Windhorst, R.A., Miley, G.K., Owen, F.N., et al., 1985. Sub-millijansky 1.4 GHz source counts and multicolor studies of weak rado galaxy populations. ApJ, 289:494.
- York, D.G., Adelman, J., Anderson, John E., J., et al., 2000. The Sloan Digital Sky Survey: Technical Summary. AJ, 120(3):1579.